SURFACE MICROMACHINED CAPACITIVE ACCELEROMETERS USING MEMS TECHNOLOGY

A THESIS SUBMITTED TO
THE GRADUATE SCHOOL OF NATURAL AND APPLIED SCIENCES
OF
THE MIDDLE EAST TECHNICAL UNIVERSITY

BY

REFET FIRAT YAZICIOĞLU

IN PARTIAL FULFILLMENT OF THE REQUIREMENTS FOR THE DEGREE OF
MASTER OF SCIENCE
IN
THE DEPARTMENT OF ELECTRICAL AND ELECTRONICS ENGINEERING

AUGUST 2003

Approval of Graduate School of Natural and Applied Science.

Prof. Dr. Canan ÖZGEN
Director

I certify that this thesis satisfies all the requirements as a thesis for the degree of Master of Science.

Prof. Dr. Mübeccel DEMİREKLER
Head of Department

This is to certify that we have read this thesis and that in our opinion it is fully adequate, in scope and quality, as a thesis for the degree of Master of Science.

Assoc. Prof. Dr. Tayfun AKIN
Supervisor

Examining Committee Members:

Prof. Dr. Ersin TULUNAY

Assoc. Prof. Dr. Tayfun AKIN

Assoc. Prof. Dr. İsmet ERKMEN

Dr. Ayşe Pınar KOYAZ

Dr. Volkan NALBANTOĞLU

ABSTRACT

SURFACE MICROMACHINED CAPACITIVE ACCELEROMETERS USING MEMS TECHNOLOGY

Yazıcıoğlu, Refet Fırat
M.Sc., Department of Electrical and Electronics Engineering
Supervisor: Assoc. Prof. Dr. Tayfun Akın

August 2003, 232 pages

Micromachined accelerometers have found large attention in recent years due to their low-cost and small size. There are extensive studies with different approaches to implement accelerometers with increased performance for a number of military and industrial applications, such as guidance control of missiles, active suspension control in automobiles, and various consumer electronics devices. This thesis reports the development of various capacitive micromachined accelerometers and various integrated CMOS readout circuits that can be hybrid-connected to accelerometers to implement low-cost accelerometer systems.

Various micromachined accelerometer prototypes are designed and optimized with the finite element (FEM) simulation program, COVENTORWARE, considering a simple 3-mask surface micromachining process, where electroplated nickel is used as the structural layer. There are 8 different accelerometer prototypes with a total of 65 different structures that are fabricated and tested. These accelerometer structures occupy areas ranging from 0.2 mm^2 to 0.9 mm^2 and provide sensitivities in the range of 1-69 fF/g.

Various capacitive readout circuits for micromachined accelerometers are designed and fabricated using the AMS 0.8 µm n-well CMOS process, including a single-ended and a fully-differential switched-capacitor readout circuits that can operate in both open-loop and close-loop. Using the same process, a buffer circuit with 2.26fF input capacitance is also implemented to be used with micromachined gyroscopes. A single-ended readout circuit is hybrid connected to a fabricated accelerometer to implement an open-loop accelerometer system, which occupies an area less than 1 cm^2 and weighs less than 5 gr. The system operation is verified with various tests, which show that the system has a voltage sensitivity of 15.7 mV/g, a nonlinearity of 0.29 %, a noise floor of 487 $\mu g/\sqrt{Hz}$, and a bias instability of 13.9 mg, while dissipating less than 20 mW power from a 5 V supply. The system presented in this research is the first accelerometer system developed in Turkey, and this research is a part of the study to implement a national inertial measurement unit composed of low-cost micromachined accelerometers and gyroscopes.

Keywords: Micro Electro Mechanical Systems (MEMS), Micromachined Accelerometer, Capacitive Readout Circuit.

ÖZ

MEMS TEKNOLOJİSİ İLE YÜZEY MİKROİŞLENMİŞ KAPASİTİF İVME ÖLÇERLER

Yazıcıoğlu, Refet Fırat
Yüksek Lisans, Elektrik ve Elektronik Mühendisliği Bölümü
Tez Yöneticisi: Doç. Dr. Tayfun Akın

Ağustos 2003, 232 sayfa

Mikroişlenmiş ivmeölçerler, düşük maliyetleri ve küçük boyutları sebebiyle son yıllarda büyük ilgi görmektedir. Füzelerde güdüm kontrolü, otomobillerde aktif süspansiyon kontrolü, ve çeşitli tüketici elektronik aygıtları gibi askeri ve endüstriyel uygulamalarda, daha yüksek performanslı ivmeölçerler yapabilmek için farklı açılardan, geniş çaplı araştırmalar yürütülmektedir. Bu tez çeşitli ivmeölçer yapılarını ve düşük maliyetli ivmeölçer sistemleri oluşturabilmek için ivmeölçerlere hibrit bağlanabilecek çeşitli entegre CMOS okuma devrelerini rapor etmektedir.

Çeşitli mikroişlenmiş ivmeölçerler COVENTORWARE sonlu eleman simulatorü ile elektro kaplanmış nikelin yapısal kaptan olarak kullanıldığı, 3 maskeli yüzey mikroişleme üretimine göre tasarlanmış ve optimize edilmiştir. Üretilmiş ve test edilmiş 65 değişik yapıdan oluşan 8 farklı ivmeölçer prototipi bulunmaktadır. Bu ivmeölçer yapıları, 0.2 mm^2 ile 0.9 mm^2 arasında değişen alanları kaplamaktadırlar ve 1-69 fF/g aralığında değişen kapasite hassasiyeti sağlamaktadırlar.

Açık döngü ve kapalı döngü olarak çalışabilen, bir tek çıkışlı ve bir tamamiyle fark gösteren anahtarlamalı kapasitör okuma devrelerini içeren çeşitli kapasitif okuma devreleri AMS 0.8 μm CMOS işleme ile dizayn edilip üretilmiştir. Aynı işlemeyi kullanarak, mikroişlenmiş jiroskoplarda kullanılmak üzere giriş kapasitesi 2.26 fF olan bir tampon devresi de oluşturulmuştur. 1 cm^2 den daha az alan kaplayan ve 5 gr. dan daha hafif olan açık döngülü bir ivmeölçer sistemi oluşturmak için tek çıkışlı okuma devresi, üretilen bir ivmeölçere hibrit bağlanmıştır. Sistemin 5 V kaynaktan 20 mW'dan daha az güç tüketirken, 15.7 mV/g orantı katsayısı, % 0.29 orantı katsayısı hatası, 487 $\mu g/\sqrt{Hz}$ gürültü seviyesi, ve 13.9 mg bias kararsızlığı olduğunu gösteren çeşitli testlerle sistemin çalışması onaylanmıştır. Bu araştırmada sunulan sistem Türkiye'de geliştirilen ilk ivmeölçer sistemidir, ve ivmeölçerler ve dönüölçerlerden oluşan düşük maliyetli ulusal ataletsel ölçüm birimi üzerine yapılan araştırmanın bir parçasıdır.

Anahtar Kelimeler: Mikro Elektro Mekanik Sistemler (MEMS), Mikroişlenmiş İvmeölçer, Kapasitif Okuma Devresi.

To my family and

to the memory of my grandmother Fatma Gözen

ACKNOWLEDGEMENTS

First of all I would like to thank my family for their support and patience. I would specially like to thank my advisor Prof. Tayfun Akın for his guidance and support, as well as, his friendly attitude.

I would like to thank Mr. Said Emre Alper for sharing his knowledge with me, performing electroplating and evaporation processes. I would like to acknowledge Mr. Selim Eminoğlu for his guidance with the circuit design and layout. I would like to thank Mr. Orhan Akar for his suggestions on the fabrication process and also for those bunches of wire bondings. I would like to thank Mr. Yusuf Tanrıkulu for SEM sessions and also wire bondings. I would like to acknowledge all the METU MEMS-VLSI group members for their friendly attitude and also for the nice research atmosphere. Also I would like to thank my dear friends Arda, Sencer, and Evren for their support and friendship. I would like to acknowledge TÜBİTAK-SAGE for providing their test facilities. Finally, I would like to acknowledge ASELSAN for SEM pictures.

TABLE OF CONTENTS

LIST OF TABLES

TABLE

LIST OF FIGURES

FIGURES

CHAPTER 1

INTRODUCTION

Accelerometers are defined as acceleration sensors that measure the linear acceleration along their sensitive axis. These devices have many application areas in the military and industrial fields, such as, activity monitoring in biomedical applications, active stabilization, robotics, vibration monitoring, navigation and guidance systems, and safety-arming in missiles. Until the introduction of MicroElectroMechanical Systems (MEMS), accelerometers were majorly utilized in the military applications, where cost is of little concern. With the advances in MEMS technology, micromachined accelerometers became the subject of extensive research and introduced to the cost sensitive commercial products. Being low cost, small size and having low power consumption, micromachined accelerometers are widely used for low-cost industrial applications, such as platform stabilization of video-cameras, shock monitoring of sensitive goods, electronic toys, robotics, and automotive applications [1-5].

Automotive industry led the way to high volume applications of the micromachined accelerometers. IC compatible micro fabrication processes enable the fabrication of these mechanical transducers together with their readout circuitry on the same substrate resulting in more reliable and higher performance accelerometers. There are several companies manufacturing micromachined accelerometers in high-volumes. One of the most successful products in the market is the ADXL series of the Analog Devices. Analog Devices have a variety of surface micromachined accelerometers, monolithically fabricated with its readout circuitry. This company is capable of producing 2 million accelerometers per month and has fabricated its 100 millionth MEMS product recently. Table 1.1 summarizes the application based market size for micromachined accelerometers, which totals up to an estimate of $4 billion per year [6]. For each of these applications, different accelerometers with different performance requirements are employed. Figure 1.1 shows the required performances of accelerometers for different application areas. Although there are a number of accelerometers in the market for some of these applications, there is still need for the high performance accelerometers that can meet the expectations of high performance inertial measurement units for military applications [6-8]. Furthermore, there are restrictions on purchasing of these high performance accelerometers, since they are considered as critical technology products. Therefore, there is a need for a national research to implement high performance accelerometers. This study reports the development of the various micromachined accelerometers that can be used for industrial and military applications, and this is the first national study for implementing micromachined accelerometers.

Table 1.1 The expected market size for micromachined accelerometers [6].

Applications	Price Per Axis	Number of Products Produced/Year	Expected Sales Volume/year
Cameras, Camcoders, Inertial Mouse, other Consumer Items	\$1-10	10^7-10^8	\$100M
Automotive, Marine, Industrial, etc.	\$10-100	10^5-10^8	\$4000M
Munitions, Fusing, etc.	\$100-500	10^4-10^7	\$500M
Autopilot, Stabilization, Rate Packages	\$100-1000	10^4-10^5	\$10M
1 nm/hr INS	\$5-10K	10^4-$6x10^4$	\$100M-300M

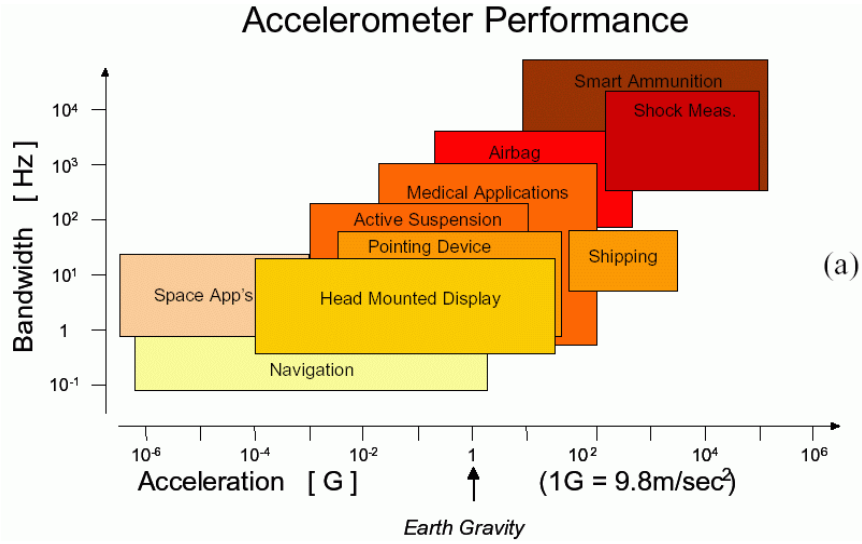

Figure 1.1 The application areas of accelerometers and required performances for these application areas [1].

This study includes the design and fabrication of various accelerometers and integrated readout circuits that are hybrid connected to the accelerometers to obtain an accelerometer system. Accelerometers are first designed using MATLAB and COVENTORWARE simulations in order to estimate their performance. Designed accelerometer structures are fabricated with a three-mask surface micromachining process, where electroplated nickel is used as the structural layer. Fabricated accelerometers are tested for comparing the characteristics of the fabricated accelerometers with the design values. Moreover, a single-ended and a fully-differential readout circuit capable of operating in both open and close loop are designed and fabricated using the AMS 0.8 µm n-well CMOS process to implement high performance accelerometer systems. After the operation of these circuits is verified, the single-ended readout circuit is hybrid connected to an accelerometer sample, and open-loop operation of micromachined accelerometer system is verified. This study also includes the development of an interface circuit for micromachined capacitive gyroscopes using the AMS 0.8 µm n-well CMOS process. This circuit can be used to implement a gyroscope with its control circuit, which is necessary for inertial measurement units that consist of accelerometers and gyroscopes. This circuit is attached to a micromachined gyroscope and its high performance operation is verified.

This chapter provides a brief review of micromachined accelerometers. Section 1.1 explains the operation principle of accelerometers. Section 1.2 describes the types of micromachined accelerometers according to their transduction mechanisms, and discusses on advantages and disadvantages of these transduction mechanisms. Section 1.3 briefly describes the accelerometers designed and fabricated in this study. Finally, Section 1.4 lists the objectives of this study and describes the organization of the thesis.

1.1 Basic Operation Principle of Accelerometers

Operation of accelerometers depends on Newton's second law of motion, which states that any object undergoing acceleration is responding to a force. Newton's second law can be expressed with Equation 1.1, where F is the force exerted on the body, m is the mass of the body, and a is the acceleration of the body.

$$F = m \times a \tag{1.1}$$

An accelerometer can be modeled by a mass-spring-damper system. Figure 1.2 shows the basic model of an accelerometer where seismic mass has a mass of m, suspension beams have an effective spring constant of k, and there is a damping factor of b. External acceleration displaces the seismic mass relative to the support frame. This displacement can be sensed with different transductions mechanisms. A detailed analysis of the mass-spring-damper system is given in Section 2.3.

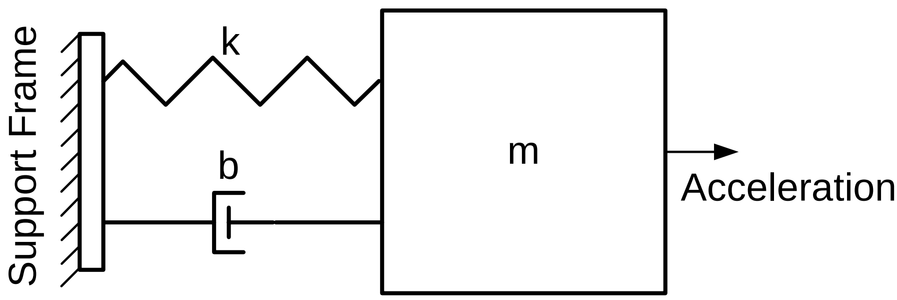

Figure 1.2 The basic model of an accelerometer.

1.2 Classification of Micromachined Accelerometers

Micromachined accelerometers can be classified into seven groups according to their transduction mechanisms:

- Piezoresistive
- Capacitive
- Tunneling Current
- Piezoelectric
- Optical
- Thermal
- Resonant

First six classes of accelerometers generally have stationary seismic masses under no acceleration, and transduction from mechanical to electrical domain is by means of measuring the deflection of the seismic mass. Whereas, last group of accelerometers have continuously resonating members in order to sense the external acceleration. Following subsections gives the basic descriptions of different types of accelerometers. Then, Section 1.3 explains the accelerometers designed and fabricated in this study, which is based on the capacitive transduction mechanism.

1.2.1 Piezoresistive Accelerometers

Piezoresistance is one of the most commonly used transduction mechanism for accelerometers. Basic description of piezoresistive effect can be summarized as the change in the resistance of the material due to mechanical strain. Figure 1.3 shows the general structure of a piezoresistive accelerometer. A basic accelerometer structure consists of a seismic mass, a beam, and a support. The piezoresistive material is generally diffused on the edge of the support beam and seismic mass, where the stress variation is maximum. When the device is subjected to an acceleration along its sensitive axis, the seismic mass tilts upwards or downwards, inducing mechanical stress on the beam. This stress causes a strain on the resistive element, where resistance change can be expressed as [9];

$$\frac{\Delta R}{R} = \pi_l \sigma_l + \pi_t \sigma_t \tag{1.2}$$

π_l is the longitudinal piezoresistive coefficient, π_t is the transversal piezoresistive coefficient, σ_l is the longitudinal stress, and σ_t is the transversal stress on the resistor.

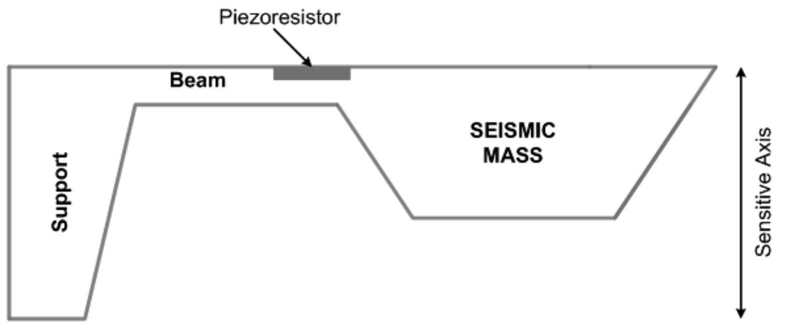

Figure 1.3 The cross section of a basic piezoresistive accelerometer consisting of a support, a beam, and a seismic mass. Seismic mass deflects upwards or downwards due to acceleration, resulting in a stress on the beam, which results in a change of the resistance of the piezoresistive element.

Generally, there are two different methods for fabricating the piezoresistive material. First one is using single crystalline P-type resistors fabricate on (100) plane in <110> direction, since the piezoresistive coefficients of the p-type resistors are highest at this direction [9-12]. The other one is using inversion layers of the MOS transistors as the piezoresistive element [13-15]. One of the proposed accelerometers in the literature having resistor-type piezoresistive elements is similar to the accelerometer structure shown in Figure 1.3, and it is sensitive to the z-axis acceleration. The accelerometer consists of a seismic mass and four supporting Si diaphragm bridges. Each bridge has a U-shaped p-type piezoresistor. The size of the accelerometer is 3mm x 4mm including the metal bonding pads. With the bridge sizes of 10 µm thick, 420 µm long, 170 µm wide, and under a bias voltage of 6 V, voltage sensitivity of the device is 286.8 µV per V/g and nonlinearity is ± 4% [9]. A different type of accelerometer having lateral sensitive axis (parallel to wafer surface) and ± 50 g range is given in references [12, 16]. Figure 1.4 shows the structure of this device. Deep reactive ion etching (DRIE) is used for the formation of the vertical sidewalls. The piezoresistors on the sidewalls of the beam are implemented with oblique ion implementation. With proof mass length, r, of 1mm, beam width, w, of 3 µm and bias voltage of 5 V, voltage sensitivity of the device is 3mV/g. Its nonlinearity is smaller than 1% and noise floor is $0.2\,\mathrm{mg}/\sqrt{\mathrm{Hz}}$.

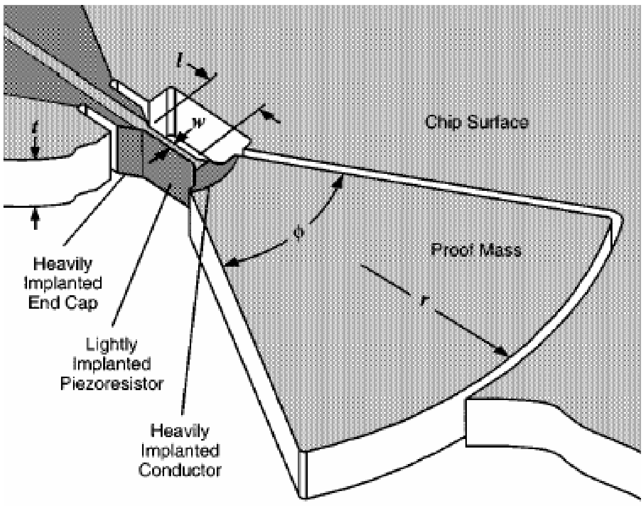

Figure 1.4 Structure of the lateral piezoresistive accelerometer from [12]. Lightly implanted piezoresistors at the sidewalls of the flexure is used for sensing the deflection of the seismic mass.

An accelerometer can be damaged, when the stress on the beam exceeds the maximum rupture point of the beam material requiring over-range protection. Figure 1.5 shows the structure of the over range protection mechanism. Movement of the mass is restricted, in order to make the device to have a high over-range protection. As shown in the Figure 1.5, bumpers on the bottom and top caps limit the deflection of the seismic mass under high accelerations. Under small accelerations, mass is free to move. However, for accelerations high enough to deflect the seismic mass more than the separation between the bumper and mass, d_o, the bumper limits the deflection of the mass resulting in higher operation range.

Main advantages of the piezoresistive accelerometers are the simplicity of their structures and their fabrication processes. In addition to that, resistive bridge creates low impedance readout node, which makes the readout circuit very easy. Moreover, they have a good DC response, which means that they can sense DC accelerations.

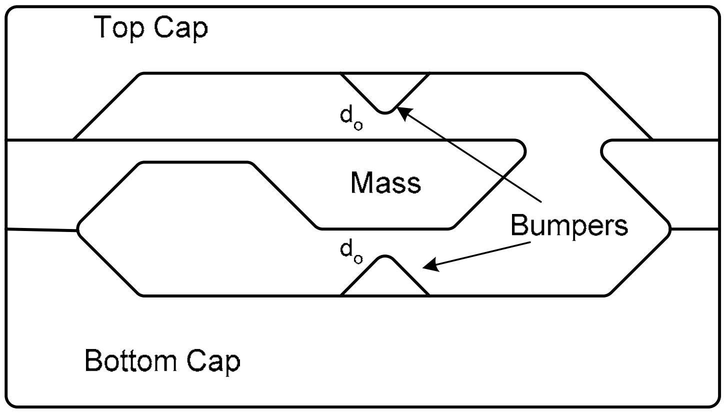

Figure 1.5 Structure of a piezoresistive accelerometer having over range protection capability. Two bumpers at the top and bottom of the seismic mass, limits the deflection of the seismic mass [17].

However, the disadvantages of piezoresistive accelerometers make them not suitable for high performance applications. First of all, output voltages of the piezoresistive accelerometers are not very high, typical voltage sensitivities of piezoresistive accelerometers are in the range of 1-3 mV/g [18]. Secondly, the piezoresistive coefficients are temperature dependent which causes drift in sensitivity. Finally, thermal noise is generated in the resistors. These facts restrict the use of piezoresistive accelerometers for high performance applications.

1.2.2 Capacitive Accelerometers

Capacitive accelerometers convert the acceleration into a capacitance change. When an acceleration is applied to the accelerometer, the seismic mass deflects from its rest position and changes the capacitance between the mass and the conductive stationary electrodes by a narrow gap. An electronic circuitry can easily measure this capacitance change.

Capacitive accelerometers have several advantages, which make them very attractive for numerous applications. They have a low temperature dependency unlike piezoresistive accelerometers. Moreover, they have very good DC response, high voltage sensitivity, low noise floor, and low drift. Another important property of the capacitive accelerometers is their low power dissipation, as well as their simple structure. However, one drawback of the capacitive accelerometers is their sensitivity to electromagnetic interference, as their sense nodes are high impedance, addressing the necessity of high-quality packaging and shielding of both the sensor and the readout circuit [18].

Figure 1.6 and 1.7 show most widely used capacitive accelerometer structures. The first one is a vertical accelerometer structure. The mass and the conductive electrode under the mass form a parallel plate capacitor. Many vertical capacitive accelerometers utilize this principle for forming parallel plate capacitors [19-22]. Acceleration through z-axis deflects the mass resulting in a change in the gap between the mass and the conductive electrode. So, the capacitance of the structure either decreases or increases regarding to the direction of the applied acceleration. There are also accelerometer structures consist of thick silicon proof mass and two electrodes under and top of the mass forming a differential capacitance structure [21]. The accelerometer operates between ±1.2 g having an equivalent acceleration resolution of $20\,\mu\mathrm{g}/\sqrt{\mathrm{Hz}}$. Another vertical accelerometer structure composed of interdigitated sense fingers operates in ± 27g range [23]. Three metal layers of a conventional CMOS process are placed inside the sense fingers such that vertical deflection of the mass changes the overlap area of these metal layers. This device has a voltage sensitivity of 0.5 mV/g/V with cross axis sensitivity lower than -40 dB and noise floor of $6\,\mathrm{mg}/\sqrt{\mathrm{Hz}}$.

Figure 1.7 shows the basic lateral accelerometer structure [24-29]. In this structure, the overlap area of the fingers connected to the mass, and fingers connected to the stationary anchors form the sense capacitance. When the mass of the accelerometer deflects, so the fingers connected to the mass, gap between movable fingers and stationary fingers increases on one side and decreases on other side. Hence, capacitance of the one side increases and capacitance of the other side decreases. Consequently, these types of accelerometers are sensitive to acceleration in the substrate plane.

Another conventional name of the stated devices is the varying gap accelerometers, since the capacitance variation due to acceleration is based on the changing gap between the mass and electrode as in Figure 1.6, or the changing gap between the stationary and movable fingers. However, for the varying gap accelerometers, crashing problem between the electrodes is possible [30]. Because of this problem, there are also varying area type accelerometers in the literature. Most of these are based on the overlap length change of the stationary and movable fingers [31, 32].

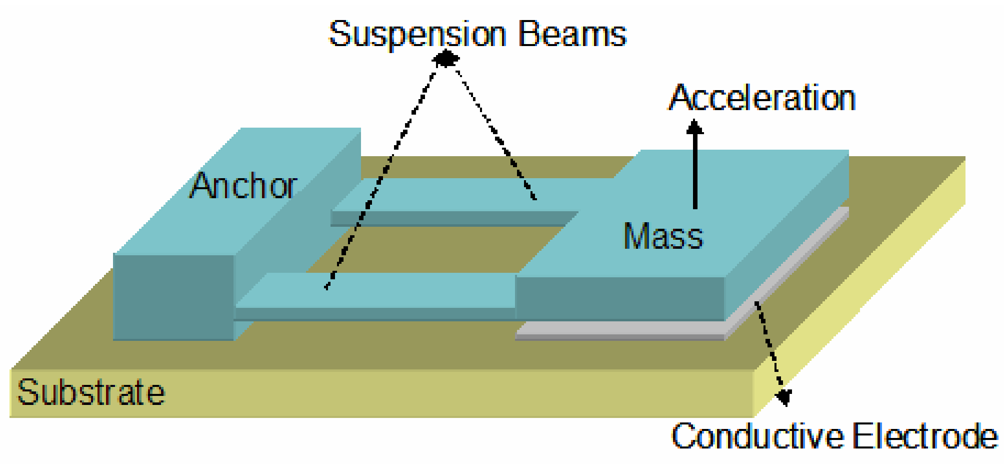

Figure 1.6 The vertical capacitive accelerometer structure. Mass and conductive electrode under the mass form the sense capacitance. Sensitive axis is perpendicular to the substrate plane.

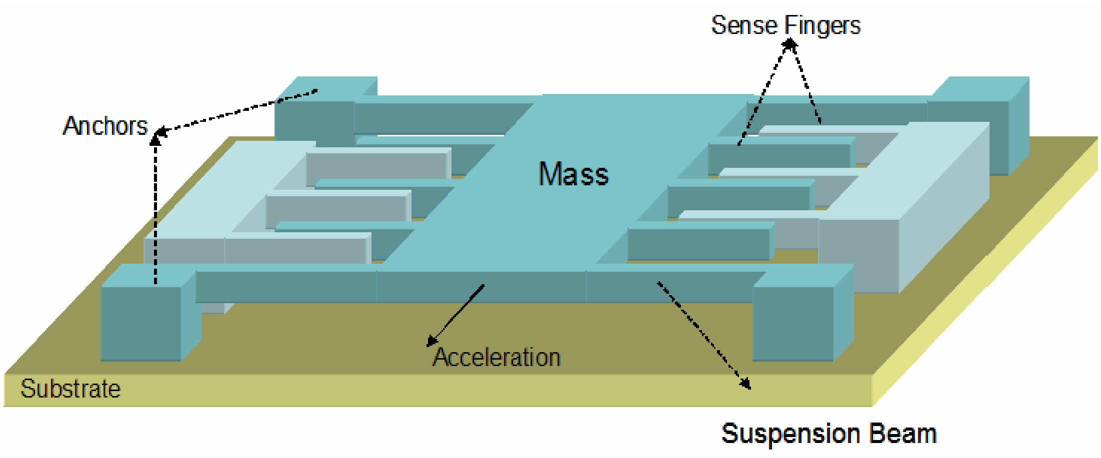

Figure 1.7 The lateral capacitive accelerometer structure. Fingers connected to the mass and fingers connected to the anchors form the sense capacitance. When mass deflects capacitance between the movable and stationary fingers increases on one side and decreases on the other side. The sensitive axis is in the substrate plane

Some other accelerometer designs use torsional springs and parallel plate capacitors for acceleration sensing in vertical direction [27, 33]. One side of the mass is heavier than the other side so, the proof mass moves along the out of plane direction under acceleration along z-axis. Advantage of this structure on conventional z-axis accelerometers is the built in over-range protection [18].

There are two basic methods for the fabrication of the capacitive accelerometers. One is the surface micromachining where the sensor is fabricated on the top of a substrate and the other is the bulk micromachining in which bulk Si substrate is etched with wet or dry etching. Surface micromachined accelerometers [23, 28, 30] are finding widespread commercial use in automotive and industrial applications. Analog Devices' ADXL series accelerometers are available commercially with different resolutions and ranges. Figure 1.8 shows the structure of a lateral capacitive accelerometer. The sensor is fabricated with surface micromachining using polysilicon as the structural layer [25], and it operates between ±5g with a resolution of 2 mg and a bandwidth of 10 kHz [34]. Although the surface micromachinining technology is IC compatible, low cost, and small size, they have high noise due to the small mass, poor stability, and lack of flexibility. On the other hand, bulk micromachining, provides of low noise, good stability, and flexible design, with the drawbacks of higher cost, bulky size, and complex fabrication.

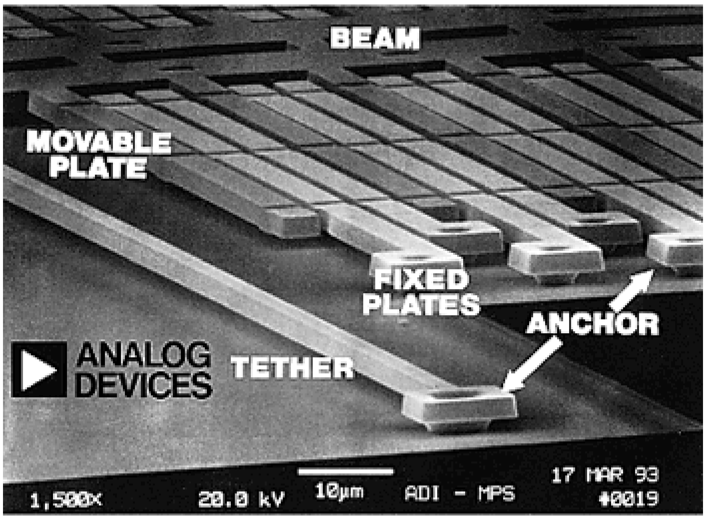

Figure 1.8 Structure of ADXL 05 accelerometer, fabricated with surface micromachining. Polysilicon is used as the structural layer.

The open loop sensitivity of capacitive accelerometers are proportional to the seismic mass size and sense capacitance overlap area, and inversely proportional with the spring constant and square of the gap forming the sense capacitances. Therefore, the most important parameters for a high performance accelerometer are the seismic mass size and the gap forming the sense capacitances. A large seismic mass is either achieved with the LIGA process and electroplating [27, 31] or bulk micromachining [20, 35, 36], where full wafer thick seismic masses can be obtained. On the other hand, the DRIE (Deep Reactive Ion Etching) technology enables the fabrication of high aspect ratio and small gap devices [29, 32, 36, 37, 38].

New accelerometer fabrication techniques utilize the advantages of both surface and bulk micromachining in order to overcome the drawbacks of both designs. There are two such accelerometers reported in the literature, where one of them has z-axis sensitivity [21] and the other has lateral axis sensitivity [39].

Voltage sensitivity of the lateral accelerometer is 0.49 V/g and the total noise floor of the accelerometer and the readout circuit is $1.6\,\mu g/\sqrt{Hz}$ [39].

In conclusion, most of the research on the accelerometers is based on the capacitive accelerometers, as they provide high sensitivity, low noise floor, and low temperature dependence, making them attractive for the areas where high performance is necessary.

1.2.3 Tunneling Current Accelerometers

Tunneling accelerometers convert acceleration to a tunneling current. There is always a possibility of electron tunneling between two conductive electrodes, if these electrodes are close enough to each other. The tunneling current is observable when the gap between the two conductive materials is about 10 Å. As the gap between the conductive materials decreases, the tunneling current increases. Two facts determining the tunneling current between two electrodes are the gap between the electrodes and the sharpness of the tip of the conductive material. As the tip of the conductive material is sharper, the probability of the electron tunneling increases [40].

Since the gap between the two electrodes is in the order of few angstroms, close loop operation is necessary for these accelerometers. Figure 1.9 shows the structure and the operation principle of a close-loop tunneling accelerometer [41]. Once the tip of the electrode is brought sufficiently close to the tunneling counter-electrode by applying proper voltage, V_o, to the bottom deflection electrode, a constant tunneling current, I_{tun}, is established. This tunneling current is constant, if the proof mass is stationary and the tunneling voltage (V_{tun}) is constant. Under acceleration, the proof mass deflects from its rest position resulting in a change in the tunneling current. The readout circuit senses this change and adjusts the voltage, V_o, for nulling the proof mass displacement. With this feedback mechanism, the tunneling current remains constant and acceleration can be measured from the change in the voltage, V_o. The top deflection electrode is used for self-test purposes.

Test results of the fabricated device together with its readout circuitry are presented in [42]. The device occupies an area of 400 µm x 400 µm, and a voltage sensitivity of 125 mV/g is achieved over -20g to 10g, where the minimum detectable acceleration is 8 mg.

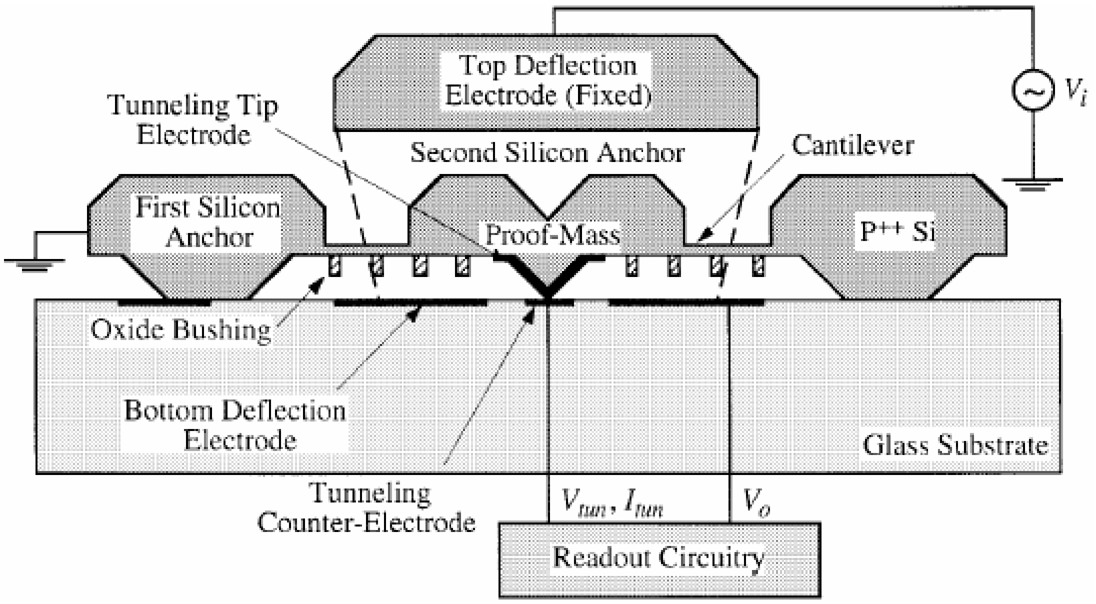

Figure 1.9 Structure of the tunneling current accelerometer proposed by [41]. V_o controls the gap between the tunneling-tip electrode and tunneling counter-electrode. Under constant tunneling voltage (V_{tun}) and no acceleration, the tunneling current, I_{tun}, is constant. When an acceleration is applied, the gap between the electrodes change so the tunneling current, I_{tun}. Readout circuitry senses this change and adjusts the voltage V_o to achieve the initial tunneling current, I_{tun}.

A high performance tunneling accelerometer is proposed by [43], where the sensor is fabricated with bulk silicon micromachining. The device consists of a substrate having tunneling tip, a proof mass, and a cap. All these parts are fabricated separately and then bonded together. Dimensions of the proof mass are 7mm x 7.8 mm x 0.2 mm suspended by a pair of 33.2 µm thick hinges. This device has a noise floor of 20 $ng/\sqrt{Hz}$ and a bandwidth of 1.5 kHz.

Tunneling accelerometers have high sensitivity since tunneling current is highly sensitive to displacement. These devices have small size, wide bandwidth, and high sensitivity, however, they suffer from drift and also 1/f noise [43]. In addition, fabrication is not easy. Therefore, they are not widely used in industrial applications

1.2.4 Piezoelectric Accelerometers

Acceleration detection principle of piezoelectric accelerometers is based on applying stress on the piezoelectric material in order to generate charge, proportional to the applied acceleration. Piezoelectric materials, such as zinc oxide (ZnO), aluminum nitride (AlN), and lead zirconate-titanate (PZT), lack inversion symmetry and therefore they create internal polarization in response to stress.

It is possible to implement accelerometers using piezoelectric materials and micromachining technologies. Unlike piezoresistive accelerometers, piezoelectric accelerometers are active devices, since they generate their own power, and theoretically they do not need to be powered.

Figure 1.10 shows a piezoelectric accelerometer, which uses a thin film piezoelectric material (PZT) deposited between the seismic mass and bottom electrode [44]. The seismic mass exerts force on the piezoelectric material under acceleration in the polarization direction of the piezoelectric material. This force on the piezoelectric material results in generation of a charge due to the piezoelectric effect. A charge-sensitive preamplifier can directly sense this charge generated by the piezoelectric film. The readout circuit of the accelerometer consists of a charge sensitive preamplifier, where feedback capacitance is 2 pF. The voltage sensitivity of the device is 300 mV/g, upper cut-off frequency is 200 kHz, and lower cut off frequency of the device is 1 Hz.

Figure 1.11 shows a cantilever type piezoelectric accelerometer [45]. The cantilever beam serves both as the seismic mass and the sensing element.

Acceleration through the sensitive axis of the accelerometer causes the cantilever beam to bend, resulting in a stress of the ZnO piezoelectric material. Then, a charge amplifier senses the charge created by the ZnO. The mechanical structure is fabricated from phosphorus-doped polysilicon, which also acts as the lower electrode. Then, a Si_3N_4 layer is deposited on top of the polysilicon, acting as a stress compensator for the ZnO layer, which has high compressive stress. Following the deposition of the ZnO, a thin Pt layer is deposited for the upper contact layer. The measured sensitivity of the device is 0.21 fC/g, and the device exhibits nonlinearity less than 2 % over the full-scale range of 25 g [45].

Although piezoelectric accelerometers are low power accelerometers and have the advantage of monolithic integration with readout circuitry, they do not have DC response since the charge generated on the piezoelectric element leaks away under a constant force. Therefore, low frequency operation with piezoelectric accelerometers is not possible. Moreover, piezoelectric coefficients of the materials, which determine the sensitivity, are also temperature dependent. Therefore, temperature compensation is needed for the piezoelectric accelerometers [44].

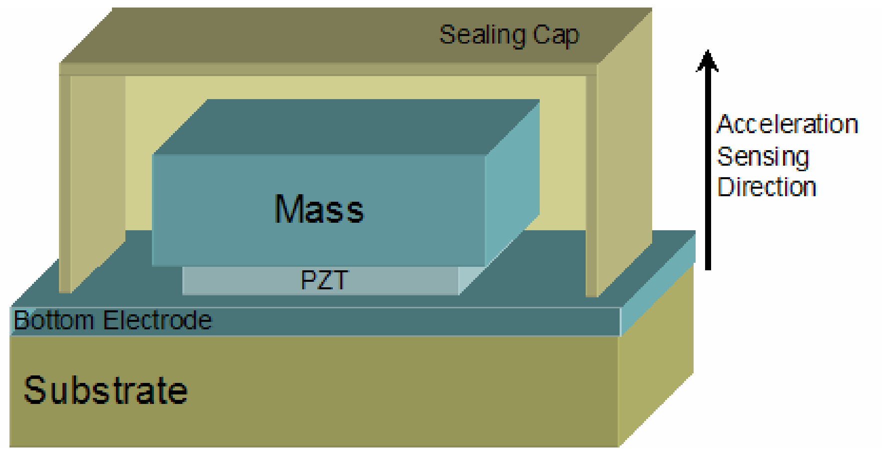

Figure 1.10 Structure of a piezoelectric accelerometer. Piezoelectric material (PZT) converts the exerted force by the seismic mass to charge [44].

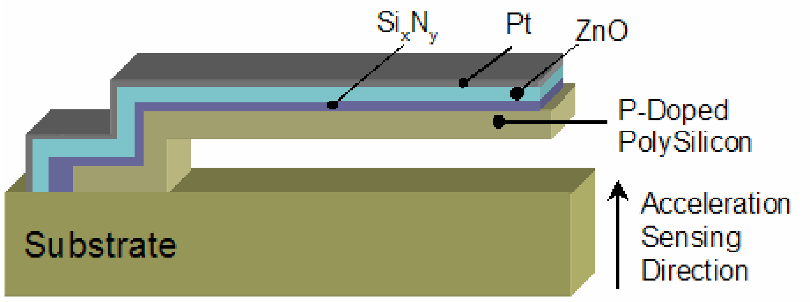

Figure 1.11 Piezoelectric accelerometer consisting of a piezoelectric film (ZnO) deposited on a cantilever beam [45]. Bending of the cantilever through acceleration exerts stress on the piezoelectric material, where it generates charge proportional with the applied acceleration.

1.2.5 Optical Accelerometers

There are two basic sensing mechanisms for optical accelerometers: the first one is by measuring the intensity of light coupling to the output fiber optic cable [46-48], and the second one is by measuring the change of wavelength of the light, reflected from a surface [49].

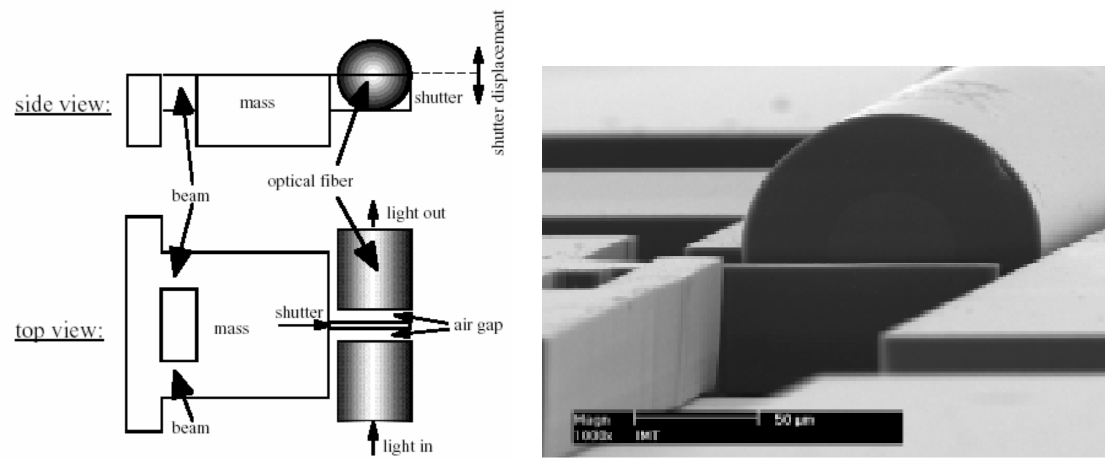

(a) (b)

Figure 1.12 (a) Structure of the fiber-optic accelerometer [48]. Shutter between the two fiber-optic cables controls the light coupling from the input to the output fiber-optic cable. Under acceleration shutter moves downwards or upwards (in and out of plane) controlling the coupling amount, (b) SEM picture of the fabricated device [48].

Figure 1.12 shows the structure and SEM picture of the fiber-optic accelerometer by Guldimann et. al. [48]. Operation of the device depends on measuring the light intensity coupling to the output fiber-optic cable. The accelerometer consists of two fiber-optic cables, a shutter connected to a mass, and a beam used for suspending the mass. All the parts of the accelerometer are fabricated on SOI wafer at a single step, and the structure is suspended by backside etching [48]. In order to increases the shutter quality, it is coated with gold by e-beam evaporation, and fiber cables are inserted and bonded with UV-sensitive glue. Under acceleration, shutter moves upward or downward as shown in Figure 1.12(a), decreasing or increasing the intensity of the light coupling to the output fiber. The structure shows a linear response between ± 5g, and the noise equivalent acceleration is measured as $90\,\mu g/\sqrt{Hz}$.

There are two important advantages of the fiber-optic accelerometers: (i) they are immune to electromagnetic interface, and (ii) they have the ability to operate at high temperatures. However, integration of LEDs (Light Emitting Diodes) and detectors with MEMS components for optical generation and sensing is not easy. Therefore, they are not widely used.

1.2.6 Thermal Accelerometers

Thermal transduction mechanisms can also be used for accelerometers. There are two basic types of thermal accelerometers: moving heat sink [50, 51] and moving heat bubble [52]. Operation principle of the first type of accelerometer depends on the principle that the temperature flux from the heat source to the heat sink is inversely proportional with the gap between them. This device uses a seismic mass positioned above a heat source. Due to the heat difference between the heat source and the seismic mass, heat flows from the heat source to the seismic mass. If the gap between the heat source and heat sink is large, there is not much heat flow between the source and the sink, so the heat source remains at the same temperature. However, if the seismic mass comes closer to the heat source due to acceleration, a considerable heat flow starts from the source to the sink, which results in a decrease in the temperature of the heat source. Temperature of the heat source is measured by thermopiles, giving a measure of acceleration [50, 51]. The fabricated accelerometer has a voltage sensitivity of 50 mV/g without electronic amplification [51].

Other type of thermal accelerometer does not have any moving mechanical parts. Instead, it uses a convective gas flow as a seismic mass generated due to the temperature difference between the heater and surrounding as a seismic mass [52]. Figure 1.13 shows the SEM picture of the fabricated device, implemented in a standard CMOS process. A thermally isolated heater forms a hot air bubble. The heat distribution of this bubble changes with the acceleration and becomes asymmetric according to the heater. This asymmetry in the heat distribution is sensed using thermocouples located at the sides of the heater. Fabricated device has a voltage sensitivity of 136 µV/g and nonlinearity less than 0.5 % in ±1 g range.

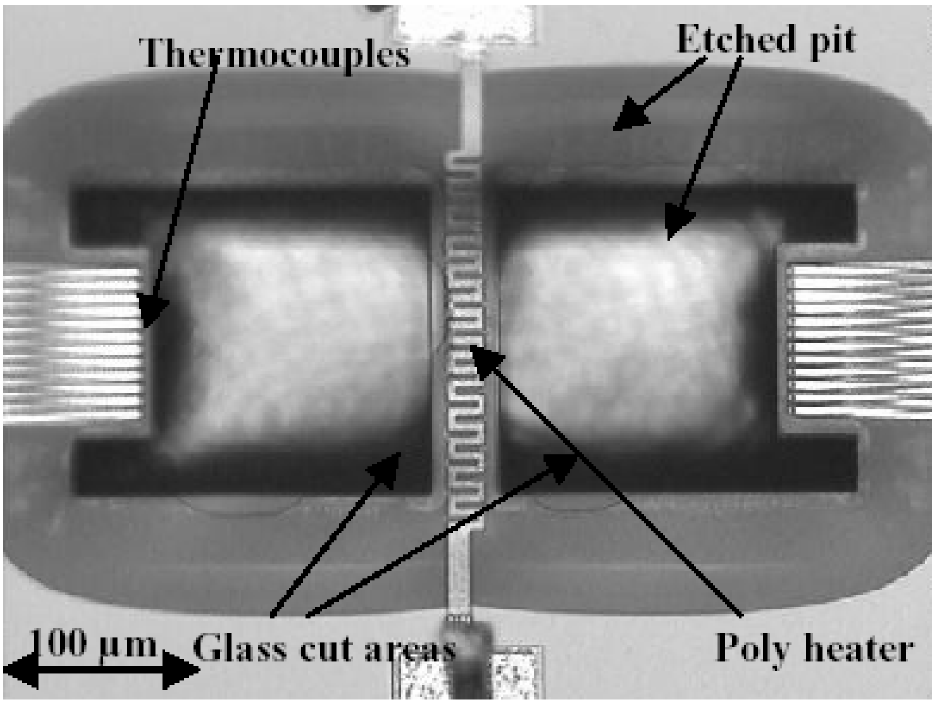

Figure 1.13 SEM picture of a thermal accelerometer based on convective gas flow [52]. A thermally isolated poly heater forms a hot air bubble. Under acceleration, this bubble deflects one side. The deflection of the hot air bubble is sensed by thermocouples at the sides of the poly heater.

1.2.7 Resonant Accelerometers

Resonant accelerometers are force-sensing accelerometers, which directly detect the force applied on the mass [53]. The main difference of the resonant accelerometers from the other types of accelerometers is that they have a continuously resonating mass at its natural frequency under zero acceleration; whereas, the previous types of accelerometers have stationary seismic masses. Detection principle of the resonant accelerometers depends on sensing the change of natural frequency of the vibrating member. Under acceleration, an inertial force acts on the seismic mass of the accelerometer, and this causes a strain in the resonating member of the accelerometer. This strain shifts the resonant frequency of the resonating member according to the sign of the applied stress by the seismic mass.

Driving and sensing mechanisms of the resonant accelerometers vary. Some of the most common types of driving and sensing mechanisms are thermal drive-piezoresistive sensing [54, 55], capacitive drive–piezoresistive sensing [56], and capacitive drive–capacitive sensing [53, 57]. Figure 1.14 shows the structure of a thermal drive–piezoresistive sense type resonant accelerometer [55]. One side of the doubly clamped resonator is attached to the cantilever support of the laterally movable seismic mass. Acceleration deflecting the mass exerts tensile or compressive stress to the resonating beam. This stress on the resonating beam shifts the resonant frequency of the beam. An implanted resistor excites resonating beam thermally, and vibration of the beam is sensed by a piezoresistor. First mode frequency of the resonating beam is at 400 kHz. The fabricated device achieves a sensitivity of 45 Hz/g and 0.1 g resolution in 10 kHz bandwidth.

Another resonant accelerometer based on electrostatic stiffness changing effect is presented in [57]. Device utilizes torsional springs for achieving higher Q factors at lower vacuum levels. The structural layer consists of a 40 µm-thick polysilicon, and the device achieves 73 Hz/g sensitivity.

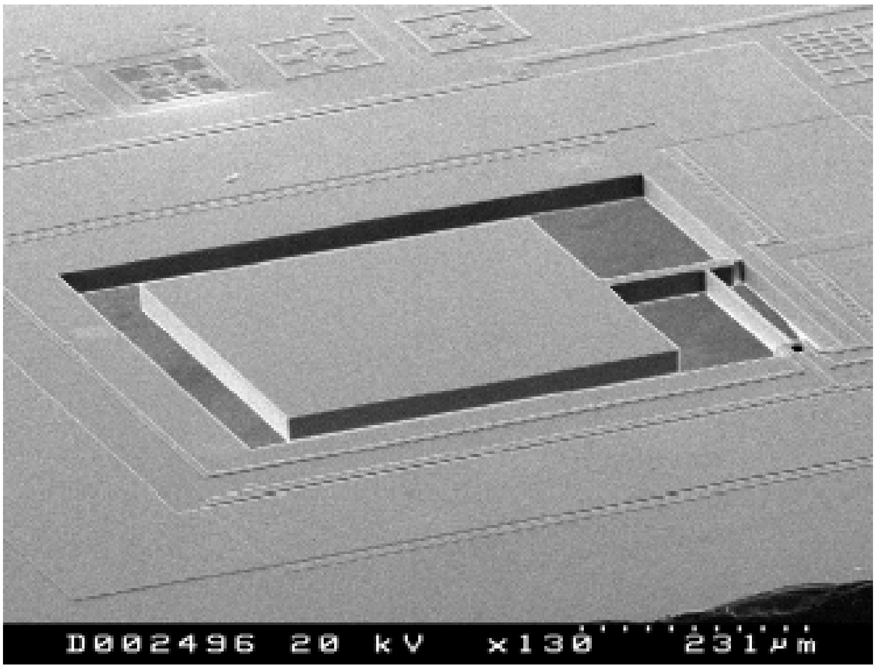

Figure 1.14 SEM picture of resonant accelerometer with thermal excitation and piezoresistive sensing. Doubly clamped beam is excited thermally and resonant of the beam is sensed by a diffused piezoresistor [55]. Acceleration deflecting the mass causes stress on the doubly clamped beam. This stress on the beam results in a shift of the resonant frequency.

A high performance resonant accelerometer is proposed by Burns et. al. [56], which uses electrostatic drive and piezoresistive sensing utilizing 700 Hz/g sensitivity with a base frequency between 500-700 kHz. Moreover, the device shows good stability, less than 2 ppm of the base frequency over seven-day stability test.

Most important advantage of the resonant accelerometers is their direct digital output, which eliminates the need for ADC. Moreover, since the output of the transducer is frequency, it is less sensitive to parasitic capacitances. Most important disadvantage of the resonant accelerometers is their low bandwidth. In addition, they need vacuum packaging in order to achieve high performance values.

1.2.8 Other Types of Accelerometers

Accelerometers in the literature are not restricted with the presented seven categories. There are also novel accelerometer structures based on different non-standard fabrication technologies and different operation principles.

One accelerometer type uses threshold switches to obtain a quasi-analog output for an input acceleration [57, 58]. This structure consists of several cantilever beams with different resonant frequencies. Under acceleration, the cantilever beam deflects and closes a contact. Knowing the bandwidth of the acceleration, threshold, and resonant frequencies of the microswitch, the array can be designed for various applications. Since the operation principle of these quasi-analog accelerometers depends on closing a contact, there is no need for a complex readout circuitry, and they are immune to EMI.

Another novel accelerometer type is based on electrostatically levitated structures. These structures have no suspension beams and suspended by electrostatic forces. Because of that, these structures are not suffer from mechanical damping, but they require complex feedback. Analysis, design, and simulation results for an electrostatically levitated disk are presented by references [60, 61]. In this accelerometer structure, suspension of the disk is performed electrostatically, and sensing of the displacement is achieved by sensing the capacitance change between the disk and the electrodes. R. Toda et. al. [62] has proposed a similar type 3-axis accelerometer where the levitated mass is in spherical form fabricated by the ball semiconductor technology [63].

Figure 1.15 shows the structure of the accelerometer consists of a spherical seismic mass enclosed in a shell, which can freely move with the gap between the outer shell, and metal surrounding the seismic mass. There are neither electrical nor mechanical connections to the seismic mass. The metal electrodes at the inner surface of the outer shell and the metal layer surrounding the seismic mass form the sense and drive capacitances. Electrical connection to these electrodes is achieved through the bumps underneath the spherical outer shell. Six semicircular electrodes at the top and bottom part of the outer shell are used for excitation and force feedback, whereas remaining two electrodes are used as detection electrodes. After the capacitance formed between the upper and lower electrodes are sensed by excitation with two out of phase sinusoidal signals, the seismic mass is brought back to its neutral position. For detection of the three orthogonal directions, three different modulation frequencies are used. Test results show that the noise floor of the fabricated structure is 40 $\mu g/\sqrt{Hz}$ [62].

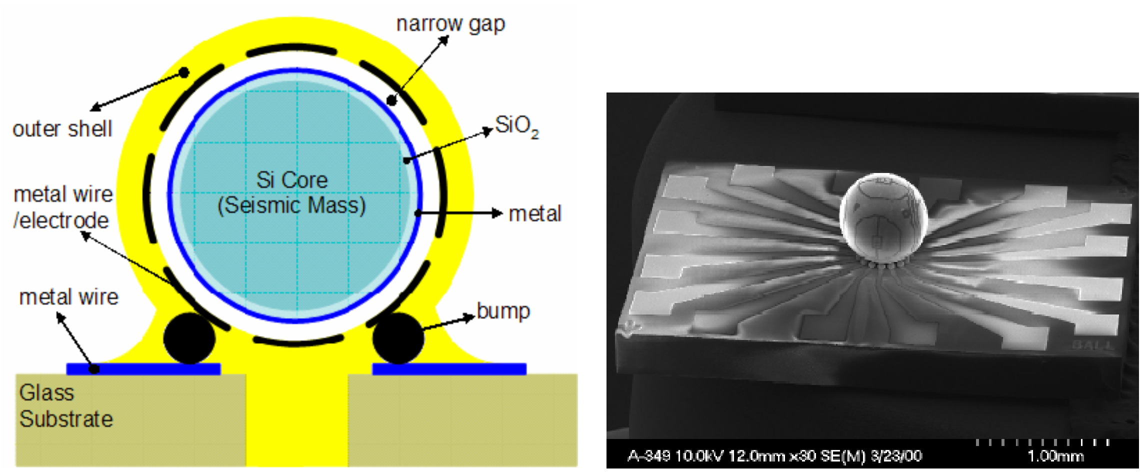

(a) (b)

Figure 1.15 (a) Structure of the electrostatically levitated spherical accelerometer. Spherical seismic mass enclosed in a shell is free to move within the gap between the metal surrounding the seismic mass and outer shell. Levitation of the spherical mass is through the six pairs of semi-circular electrodes located at the top and bottom side. Lateral electrodes used as detection electrodes, (b) SEM picture of the fabricated device [62].

1.3 Accelerometers Designed and Fabricated in This Study

Table 1.2 gives the summary of the advantages and the disadvantages of the major accelerometer classes excluding the thermal accelerometers due to its small amount of application areas, good packaging need, and temperature dependency. Capacitive accelerometers are the most promising class for the high performance applications due to their various advantages shown in Table 1.2. Therefore, capacitive type accelerometers are selected for the implementation of accelerometers in this study.

Table 1.2 Comparison of the advantages and the disadvantages of the major accelerometer classes.

	Piezoresistive	**Capacitive**	**Tunneling**	**Piezoelectric**	**Optical**	**Resonant**
Sensitivity		✓	✓		✓	✓
Ease of Readout	✓	✓		✓		✓
Temperature Independency		✓	✓		✓	
Ease of Fabrication	✓	✓		✓		✓
DC response	✓	✓	✓		✓	✓
EMI Sensitivity					✓	✓
Noise Floor		✓	✓		✓	
Comments			Close-loop operation is needed		Hard to implement optics with MEMS	Very-low bandwidth, Vacuum packaging needed

There are 8 different capacitive accelerometer prototypes designed in this study. These designs include the usage of different spring topologies and also different sense capacitances. Six of these prototypes are lateral accelerometers, where as two of them are z-axis accelerometers. Each accelerometer prototype has different versions with different dimensions and gaps, in order to fabricate the highest performance accelerometer after the optimization of the fabrication process. Therefore, there are a total of 65 accelerometer structures designed in this study. Resonant frequencies of these structures are changing between 740 Hz and 5.27 kHz.

Calculated sensitivities of the accelerometers based on the simulated resonant frequencies are ranging from 1 fF/g to 69 fF/g.

Figure 1.16 shows the structure of the one of the prototypes. The accelerometer consists of a seismic mass that converts the acceleration into motion and comb fingers that converts the seismic motion into capacitance change. When the accelerometer undergoes an acceleration along its sensitive axis, the seismic mass deflects relative to the substrate in opposite direction with the applied acceleration. This deflection increases the capacitance between the comb fingers on one side and decreases the capacitance between the comb fingers on the other side. This capacitance mismatch between the sense capacitances can be detected with a readout circuit, whose output voltage gives the measure of the applied acceleration.

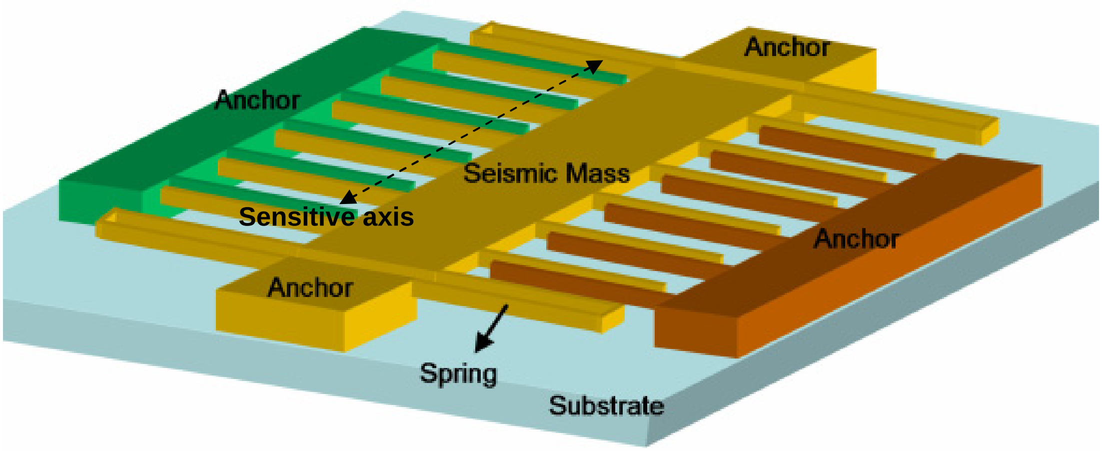

Figure 1.16 Structure of the one of the accelerometer prototype developed in this study. When the accelerometer undergoes an acceleration through its sensitive axis, the seismic mass deflects relative to the substrate in opposite direction with the applied acceleration. This deflection of the seismic mass results in capacitance mismatch between the comb fingers on the two sides of the accelerometer.

All the accelerometer prototypes are fabricated with a 3-mask surface micromachining process, where the electroplated nickel is used as the structural layer. The fabrication steps only include lithography, electroplating, and wet etching, which are very low cost processes and are suitable for the low-cost accelerometer fabrication. Following section presents the objectives of this study and thesis organization.

1.4 Objectives of the Study and Thesis Organization

Goal of this thesis is to design and fabricate an accelerometer system having a nonlinearity less than %1, a noise floor smaller than $1.5\,\mathrm{mg}/\sqrt{\mathrm{Hz}}$, a bias instability less than 20 mg, and cross-axis sensitivity less than 5%, which is suitable for automotive applications. The specific objectives of this study can be summarized as follows:

- To gain experience on the design and the simulation of micromachined accelerometers. For this purpose, eight different accelerometer prototypes are designed based on the accelerometer types in the literature. Optimization of these prototypes is performed with the help of COVENTORWARE and MATLAB simulations.

- To optimize the fabrication process of the accelerometers, especially the optimization of the structural photoresist. Accelerometer prototypes are fabricated with a 3-mask surface micromachining process, where electroplated nickel is used as the structural layer. The fabrication procedure is simple and very low cost, which is ideal for mass production of the accelerometers. Process steps include only lithography, electroplating, and wet etching. SJR 5740 and SU-8 photoresists are optimized for the fabrication of the structural mold. The thickness of the SJR 5740 photoresist is 16 µm, and the thickness of the SU-8 is around 42 µm. Aspect ratios around 5.3 and 10.5 are achieved for these two photoresists respectively.

- To design readout circuits for the micromachined capacitive accelerometers. Designed accelerometer prototypes convert their seismic mass displacement to capacitance change. In order to detect this capacitance change a readout circuit that can operate both in open and close loop is designed and fabricated in AMS 0.8 μm n-well CMOS process. This readout circuit has the advantage of force-feedback operation and digital output in close loop form. Moreover, for the future developments of the micromachined accelerometers, a high performance readout circuit is designed and fabricated. This design has the advantage of fully-differential operation in order to reduce common mode errors, also have force-feedback and digital output in close loop form.

- To built a hybrid micromachined accelerometer system. A micromachined accelerometer is hybrid connected to the single-ended readout circuit in open-loop. All the necessary tests are performed on the open-loop system, including linearity, noise floor, and bias instability.

- To design circuit block for an Inertial Measurement Unit (IMU). Such systems are formed with 3 accelerometers and 3 gyroscopes. The gyroscopes are being developed in the framework of another research, however, a unity-gain buffer that will be used as a capacitive interface between a micromachined gyroscope and the control circuit of the micromachined gyroscope is designed in this work. An improved buffer circuit having very high input impedance is designed and fabricated with AMS 0.8 μm n-well CMOS process. This circuit is hybrid connected to a gyroscope sample and tested.

This thesis reports the development of a micromachined accelerometer system together with its readout circuitry. Works that are done in this thesis can be divided into four main groups;

- Design and fabrication of the accelerometer prototypes
- Design of two different readout circuit for accelerometer prototypes
- Hybrid connection of the accelerometer and readout circuit and testing of the system
- Design of a capacitive interface circuit for micromachined gyroscopes.

Chapter 2 describes the theoretical background necessary for designing micromachined accelerometers. It presents all the mechanical and electrical background for designing accelerometers.

Chapter 3 describes the fabrication steps of the micromachined accelerometers. It gives the details about the fabrication process and the designed masks for the fabrication of the accelerometers. It also gives the optimized parameters for the fabrication of the accelerometers.

Chapter 4 describes the designed surface micromachined accelerometer prototypes, starting with the general design challenges about accelerometers, and then giving the structures of the designed prototypes. Comparison of simulation and calculations are supplied for each prototype.

Chapter 5 discusses the capacitive readout circuits and the capacitive interface circuit designs. It describes all the analog and digital building blocks of these circuits. Moreover, it explains the operation of these building blocks and also the overall circuits. Simulation results of each block and overall circuits are supplied. It compares the proposed circuit with the circuit proposed by [100] for the improved buffer capacitive interface circuit.

Chapter 6 gives the fabrication and test results of the designed accelerometers, readout circuits, and improved buffer interface circuit. Chapter starts with giving the fabrication results of the accelerometer prototypes. It discusses on the possible problems that is faced during the fabrication of the accelerometer prototypes. It also gives the test results for each accelerometer prototype and building blocks of the readout and interface circuits. Finally, the chapter presents the results of the two hybrid systems, gyroscope connected to the interface circuit, and single-ended readout circuit connected to an accelerometer prototype operating in open loop.

Finally, Chapter 7 gives the conclusion of this work and suggestions about the future work on micromachined accelerometers.

CHAPTER 2

THEORETICAL BACKGROUND

This chapter presents the theoretical background on the design of capacitive MEMS accelerometers. Section 2.1 gives the details and definitions of some mechanical terms related with the accelerometer design. Section 2.2 shows the derivations of the necessary formulas for the spring constants. Section 2.3 discusses the governing equations related with the basic accelerometer model and also gives the definition of damping coefficient which is necessary to understand the dynamic behavior of an accelerometer. Section 2.4 discusses the different types of capacitances used for sensing the motion of the seismic mass. Finally, Section 2.5 gives the summary of the whole chapter.

2.1 Definition of Mechanical Terms

The accelerometer is the transducer that converts acceleration into electrical signal by means of mechanical and electrical elements. Therefore, an accelerometer design requires both mechanical and electrical background. The mechanical design plays an important and vital role on the performance of the accelerometer. Familiarity with moment, force, stress, and strain calculations allows the designer to understand the mechanical formulas related with deriving necessary equations for sensitivity and frequency response of the accelerometer. Moreover, these mechanical terms are also necessary to explain some of the problems occurring during the fabrication process, like residual stress of the deposited layers and affects of these problems on the performance of the accelerometer. Therefore, following sections provide a review of the mathematical terms used in the design of accelerometers.

2.1.1 Definition of Internal Forces and Stress

A basic mechanical definition to start with is the equilibrium of a two-force member. If a two-force member is in equilibrium, then two forces acting on the member should have same magnitude, same line of action and opposite directions as shown in Figure 2.1(a). Therefore, the following equation must hold for a two-force member to be in equilibrium;

$$\sum F_x = 0; \quad \sum F_y = 0; \quad \sum M = 0 \tag{2.1}$$

Equation 2.1 states that x and y components of the all forces acting on the member and the total moment exerted on the member according to any point in space must sum up to zero. Example of a two-force member can be generalized to the equilibrium of an object under the action of external forces. This means that, for an object to be in equilibrium, vector summation of the forces acting on the object must be zero and the moment of these forces according to any point must sum up to zero [64].

Apart from the external forces there are also internal forces existing in a rigid body. These forces are defined as the forces holding the components of a rigid body together [64]. Figure 2.1(b) shows the section KL of the member KLMN. There should exist some internal force at section L that balances the force and moment exerted on the section KL, which is in equilibrium due to the applied external force P.

The force, F balances the x-component, the force V balances the y-component, and the moment M balances the moment of the externally applied force P. The internal force, F, which is normal to the cross-section of the member KLMN at point L, is called the *normal force,* and creates the *normal stress* (σ) in the member. The force V which is parallel to the cross-section of the member KLMN at point L, is called the *shear force*, and creates the *shear stress* (τ) in the member. Stresses that are created due to the applied forces in the member can be defined as follows;

$$\sigma = \frac{F}{A} \tag{2.2}$$

$$\tau = \frac{V}{A} \tag{2.3}$$

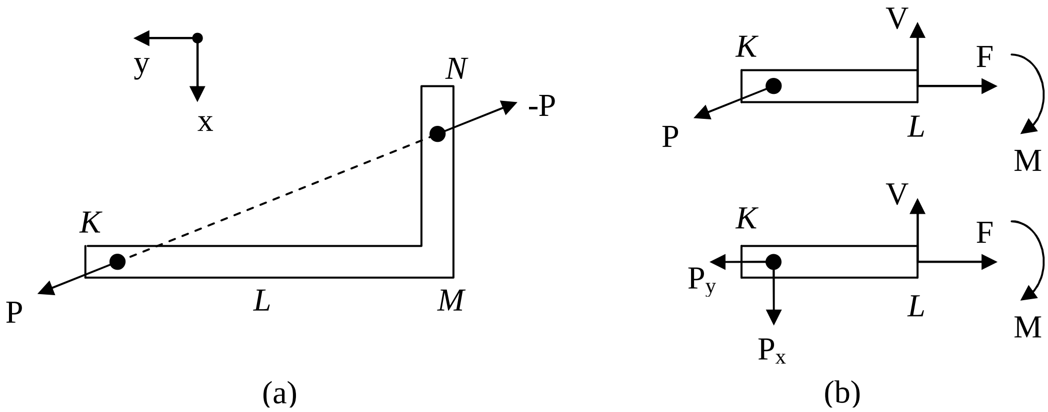

Figure 2.1 (a) Two force member in equilibrium. Two forces acting on a member having same line of action, same magnitude and opposite direction. (b) Internal forces existing at section L of the member KLMN for equilibrium.

By definition, if the force F tries to elongate the member KL, the normal stress is said to be positive and named as tensile stress. If it tries to compress the member KL, it is said to be negative and named as compressive stress [65].

2.1.2 Definition of Strain

Another important mechanical term is related with the deformation of the bodies under force. Figure 2.2 shows a rod, AB, axially loaded with a tensile force, F, at its free end. This force tries to elongate the rod through the direction of the applied force. *Normal strain* can be defined as “deformation of the rod per unit length" and denoted by letter, ε, [65]. Hence, for a rod having uniform cross-section area, *normal strain*, can be calculated from equation;

$$\varepsilon = \frac{\delta}{L} \tag{2.4}$$

where δ is the amount of elongation, and L is the length of the rod. The same formula is also valid for a compressive force, which is trying to shorten the rod.

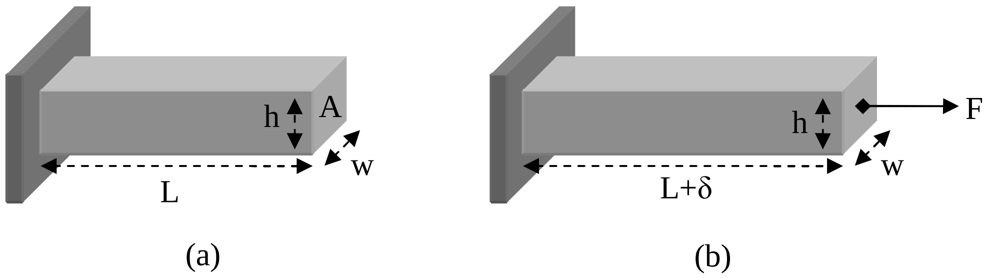

Figure 2.2 (a) Rod with length, L, and area, A. (b) Rod is elongated by an amount of, δ, by an axial tensile load F. Strain is defined as "deformation of the rod per unit length" [65].

Load, F, creates a stress in the rod, while trying to elongate it. Relation between stress and strain is an important property to characterize the behavior of material under an axial load. Behavior of a member under axial load can be understood from stress-strain graphics. Figure 2.3 shows the typical relation between stress and strain for a ductile material. There exist four regions in the graph. Region I is called the proportional region or elastic region, region II is called the yielding region, region III is called the strain hardening region, and region IV is called the necking region. Boundary of the elastic region is denoted with σ_y, which is called the yield limit, representing the maximum achievable stress in the elastic region. If the elastic region is considered then strain of the material is directly proportional to stress. This proportionality can be expressed with the famous Hooke's law as written is Equation 2.5;

$$\sigma = E\varepsilon \tag{2.5}$$

where E is called the Young's modulus, ε is the strain, and σ is the normal stress [65].

If the equations governing the normal stress (2.2) and strain (2.4) are inserted in Equation 2.5, axial deformation of a member under axial loading can be expressed in terms of externally applied load and mechanical properties of the member with Equation 2.6;

$$\delta = \frac{F \times L}{E \times A} \tag{2.6}$$

where F is the axial load, L is the length of the member, E is the Young's modulus and A is the cross-section area of the member

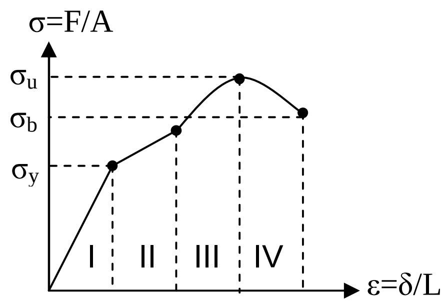

Figure 2.3 Stress vs. Strain graphic of a ductile material. Region I is the proportional region, where relation between the stress and strain can be expressed with the Hooke's law. Region II is the yielding region, region III is the strain hardening, and region IV is the necking region. σ_y is the stress limit for the elastic region. σ_b is called the breaking stress corresponding to the rupture point of the material, and σ_u is the maximum achievable stress [65].

The second type of strain is called the *shearing strain*, and denoted by γ. If a structure is loaded with two equal, opposite direction and unaxial forces as shown in Figure 2.4, member ABCD will deform and point K and K' makes an angle (γ) with respect to M. This angle (γ), measured in radians, is called *shearing strain* [65].

Relation between the shearing stress (τ) and shearing strain (γ) can be expressed with the Hooke's law as written in Equation 2.7, if the elastic region is considered. The proportionality constant G is called the *modulus of rigidity* or the *shear modulus*.

$$\tau = G\gamma \tag{2.7}$$

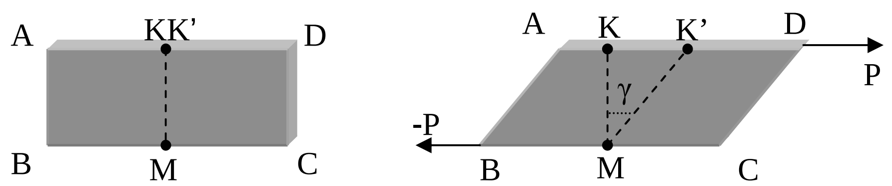

Figure 2.4 Unaxial forces, P and –P, applied to member ABCD deform the structure and result in a shear strain [65].

2.1.3 Definition of Poisson's Ratio

In the previous section, only one-dimensional deformation of the member under loading is considered but actually this is not the case. If an axial load is applied to a member, elongation in one direction results in contraction in the other direction as expected or vice versa. Figure 2.5 illustrates this phenomenon. The axial tensile force elongates the member in axial direction and this elongation results in a contraction in the transverse direction. The Poisson's ratio, υ, is defined as the ratio between the lateral strain, which is the strain in transverse directions, and axial strain. Poisson's ratio can be expressed with the following equation [65];

$$\upsilon = \frac{|Lateral\ Strain|}{|Axial\ Strain|} = \frac{|\delta_y / h|}{|\delta_x / L|} = \frac{|\delta_z / w|}{|\delta_x / L|} \tag{2.8}$$

where definitions of the terms are given in Figure 2.5.

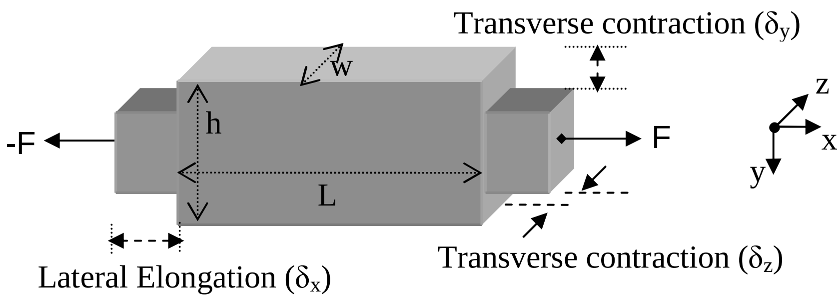

Figure 2.5 Picture illustrating the elongation in axial direction due to tensile load F and contraction in transverse directions accompanied by this axial elongation.

2.1.4 Definition of Moment of Inertia

Moment of inertia of areas with respect to an axis can be calculated by multiplying the infinitesimal area element, dA, with the square of the distance of this infinitesimal element to axis and summing up the results. This axis lies in the plane where area of interest resides. Figure 2.6 illustrates the moment of inertia calculations of an area according to x and y axis. The moment of inertia of an area is written as [64];

$$I_x = \int y^2 dA \qquad I_y = \int x^2 dA \tag{2.9}$$

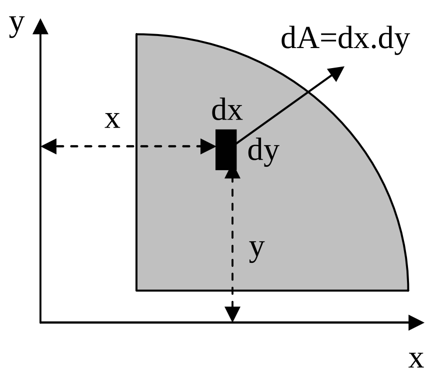

Figure 2.6 Picture showing the infinitesimal element used for moment of inertia calculation for an area.

Similarly, moment of inertial of a mass can be calculated by taking an infinitesimal mass element, dm, and multiplying it with the distance of this element to the axis of interest and summing up the results. So moment of inertia of a mass can be calculated from the following integral;

$$I = \int r^2 dm \tag{2.10}$$

where r is the distance of the infinitesimal mass element to the axis of interest [64]. If a moment of inertia according to a point is to be calculated then radial distance of the infinitesimal element should be considered. This is called the *polar moment of inertia* [64]. Moment of inertia of areas and moment of inertia of masses for different areas and masses can be found in reference [64].

2.2 Spring Constant Calculation

Springs are the most important mechanical elements of the accelerometers that affect the performance of the accelerometer considerably. Therefore, their simulation, design, and fabrication should be made carefully knowing details of springs. This section describes all the necessary details for understanding the basics behind springs.

2.2.1 Deflection of Beams

Figure 2.6 shows a deflected cantilever type beam, that is free to move at one end and other end is fixed. Beam is represented with its neutral line, which is the center line of the cantilever. Deflection amount of the beam according to position is represented by variable w(x).

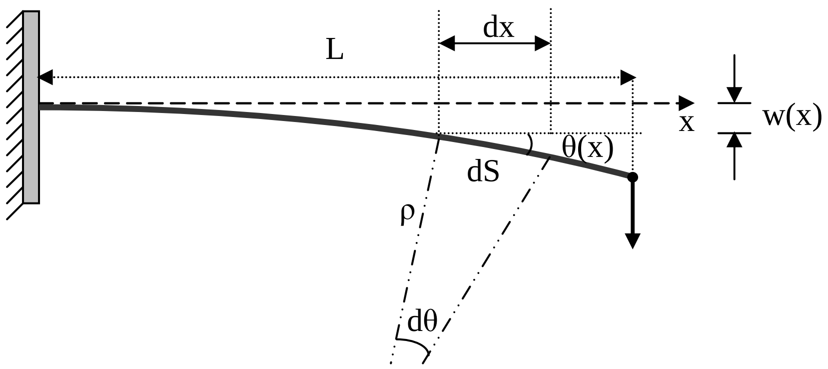

Figure 2.7 A deflected cantilever beam. Deflection amount according to position is represented by w(x) [66].

An infinitesimal beam element, dS, is chosen which makes an angle of θ(x) with the x-axis. From the right triangle approximation dx can be written in terms of dS and θ as;

$$dx = dS\cos(\theta) \tag{2.11}$$

and the slope of the beam at any point, x, can be written as;

$$\frac{dw}{dx} = \tan(\theta) \tag{2.12}$$

As a next step, dS can be written in terms of radius of curvature of the beam, ρ, and dθ, from the arc length formula of a circle;

$$dS = \rho\, d\theta \tag{2.13}$$

If the angle θ(x) is very small, then cos(θ) is very close to 1, so we can conclude from Equation 2.11 that length of the infinitesimal element, dS, is equal to dx. So by replacing dS in Equation 2.13 with dx, following equation can be written easily;

$$\frac{d\theta}{dx} = \frac{1}{\rho} \tag{2.14}$$

From the small angle approximation, θ in Equation 2.14 can be replaced with the right hand-side of Equation 2.12 and written as;

$$\frac{d^2 w}{dx^2} = \frac{1}{\rho} \tag{2.15}$$

Radius of curvature of the beam can be written in terms of, internal bending moment M, young's modulus E, and moment of inertia I [66]. Combining this knowledge with Equation 2.15, the differential equation for beam bending can be obtained as;

$$\frac{d^2 w}{dx^2} = -\frac{M}{EI} \tag{2.16}$$

Equation 2.16 is a useful equation for calculating the spring constant of various types of beams under various types of loading. In order to calculate the deflection of the beam for an applied load, only unknown in the Equation 2.16 is the internal bending moment, M.

2.2.2 Spring Constant Calculation for a Cantilever Beam

Derivation of the spring constant of an axially loaded beam is quite simple. Considering the axially loaded beam in Figure 2.2, normal stress in the beam due to the force F can be expressed by Equation 2.2. If Equation 2.2 is inserted in Equation 2.5, we can express the strain, ε, of the material in terms of force, F, Young's modulus, E, and cross-section area of the beam;

$$\varepsilon = \frac{F}{E\,w\,h} \tag{2.17}$$

If the definition of strain in Equation 2.4 is inserted in Equation 2.17, spring constant, k, of the cantilever beam can be written as;

$$k = \frac{F}{\delta} = \frac{E\,w\,h}{l} \tag{2.18}$$

where δ is the amount of elongation or contraction of the tip point of the cantilever beam.

Spring constant of the cantilever beam due to transverse loading can be calculated from the Equation 2.16, which relates the deflection amount of the beam to the internal bending moment of the beam. Equation 2.19 gives the internal bending moment of the beam at any point, x, for the cantilever beam of Figure (2.7), deflected due to transversely applied force F [66]. If Equation 2.19 is inserted in Equation 2.15, the differential equation relating the transverse force F to the deflection of the beam can be written as in Equation 2.20, where w is the deflection of the beam, E is the young's modulus, and I is the moment of inertia.

$$M = -F\left(L - x\right) \tag{2.19}$$

$$\frac{d^2 w}{dx^2} = \frac{F\left(L - x\right)}{E\,I} \tag{2.20}$$

In order to solve this differential equation, first, the boundary conditions must be defined. Analyzing Figure 2.7, amount of the deflection and the first derivative of the deflection of the beam at the support end is zero, so the boundary conditions can be written as;

$$w(0) = 0 \quad \& \quad \frac{dw}{dx}\Big|_{x=0} = 0 \tag{2.21}$$

By solving the differential Equation 2.20 with the boundary conditions, deflection of the beam according to the position x can be written as [66];

$$w(x) = \frac{FL}{2EI} x^2 \left(1 - \frac{x}{3L}\right) \tag{2.22}$$

Maximum deflection of the beam occurs at the tip point, so by replacing x with length of the beam, L, transverse spring constant of the cantilever beam can be written as;

$$k = \frac{F}{w} = \frac{3EI}{L^3} \tag{2.23}$$

and substituting the moment of inertia, I, in the Equation 2.23 yields the spring constant of a transversely loaded cantilever beam [66];

$$I = \frac{1}{12} wh^3 \tag{2.24}$$

$$k = \frac{Ewh^3}{4L^3} \tag{2.25}$$

2.2.3 Spring Constant Calculation for a Beam with Fixed-Guided End Conditions

When one end of the beam is connected to the support and the movable end is attached to the mass, and if the mass is restricted to move along a linear path then the spring constant of the beam differs from the one given in Equation 2.21, due to the extra bending moment appearing at the mass side. Figure 2.8 illustrates the mass-spring-support system and deflection of the beams under loading with a force F. As can be seen from Figure 2.8(b), curvature of the beams differs from the curvature of the beam of Figure 2.7. Cross-sections of the beams at the support and mass boundaries remain parallel all the time.

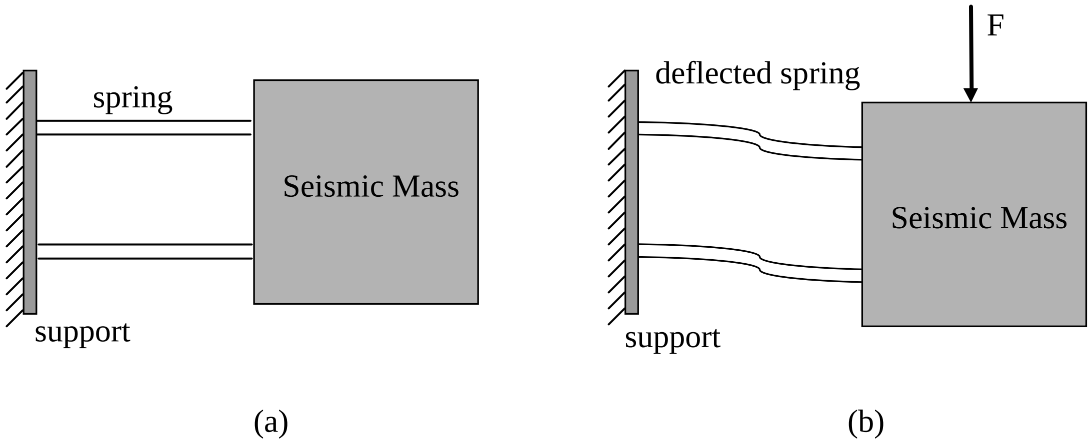

Figure 2.8 (a) Picture of a fixed guided-end spring-mass system. (b) The deflections of the spring beams when connected to a rigid seismic mass.

Figure 2.9 shows the deflection of the neutral line of the beam, which is connected to the seismic mass as shown in Figure 2.8. Different from the free end cantilever beam, there exists a bending moment at the mass side of the beam as shown in Figure 2.9. So internal bending moment at any location can be written as;

$$M = -F(L-x) + M_0 \tag{2.26}$$

where M_0 is the bending moment exerted on the beam by the seismic mass. Then inserting the total internal bending moment expression in Equation 2.16 and giving the boundary conditions as;

$$w(0) = 0 \quad \frac{dw}{dx}\Big|_{x=0} = 0 \quad \& \quad \frac{dw}{dx}\Big|_{x=L} = 0 \tag{2.27}$$

deflection of the beam can be calculated as;

$$w(x) = \frac{-F}{6EI}x^3 + \frac{FL}{4EI}x^2 \tag{2.28}$$

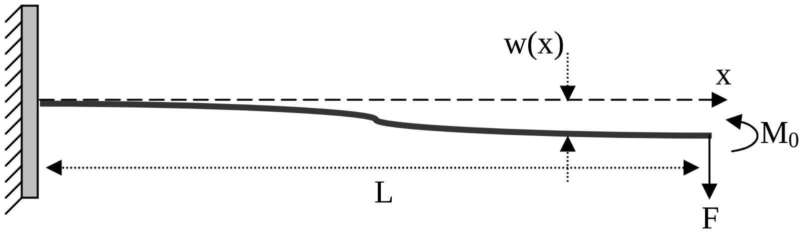

Figure 2.9 Neutral line of a beam deflected by a rigid mass.

For the calculation of the spring constant of the beam, position variable, x, in Equation 2.28 is replaced with beam length, L, and moment of inertia, I, expression is inserted, which yield the equation;

$$k = \frac{Ewh^3}{l^3} \tag{2.29}$$

2.2.4 Effect of Residual Stress on Spring Constant and Folded Springs

Formulas in subsections 2.2.2 and 2.2.3 are derived assuming that materials of the beams have no residual stress. However, this is not the case in practice. Residual stress can be defined as a tension or compression, which exists in a bulk of a material without application of an external load.

If a material has a compressive residual stress, it means that material has a built in force trying to elongate the structure. If material is released or no external force is applied to the structure, material will elongate or expand in order to release the compressive residual stress. Similarly, if a material has a tensile residual stress, it means that it has an internal force trying to contract the material, and if the material is released then structure will contract in order to release the tensile residual stress.

Hence, from these definitions, it can be concluded that a structure having tensile residual stress becomes stiffer, where as structures having compressive stress becomes less stiff. This effect can be used for designing springs with different spring constants than its theoretical stress-free spring constant values. If a spring consists of a material having compressive residual stress, its spring constant decreases and conversely if material has a tensile residual stress, its spring constant increases.

Theoretical calculation for the effect of the residual stress on the spring constant can be found in [67]. During the design of the accelerometers FEM simulators are used for effectively simulating the residual stress effect, instead of calculating the effect of residual stress on the spring constant.

2.3 Accelerometer Model

An accelerometer can be modeled as a mass-spring-damper system where acceleration deflects the mass from its rest position. This deflection is measured by means of transduction mechanisms from mechanical to electrical domain. In this section, equations of motion are presented for a mass-spring-damper system, and the dynamic behavior of an accelerometer system is analyzed.

2.3.1 Mass-Spring-Damper System

Accelerometers generally consist of a seismic mass, a suspension element or spring, and a damper. Figure 2.10 shows the general dynamic model of an accelerometer, where a seismic mass is connected to a supporting base via a spring; there also exists a damper for energy loss, where k is the spring constant and b is the damping coefficient.

In order to have a system in equilibrium total forces acting on the seismic mass should sum up to zero as written in Equation 2.1. Based on this principle, the equation of motion for the accelerometer model can be written as;

$$m\,\ddot{z}(t) + b\,\dot{z}(t) + k\,z(t) = -m\,a(t) \tag{2.30}$$

where

$$z(t) = x(t) - y(t) \tag{2.31}$$

and

$$a(t) = \ddot{y}(t) \tag{2.32}$$

where k is the spring constant, b is the damping coefficient, m is the mass, and a(t) is the acceleration [68]. As shown in Equation 2.30 there is a minus sign in front of the term representing force applied by the external acceleration. This indicates that the displacement of the seismic mass is in the opposite direction with the applied acceleration.

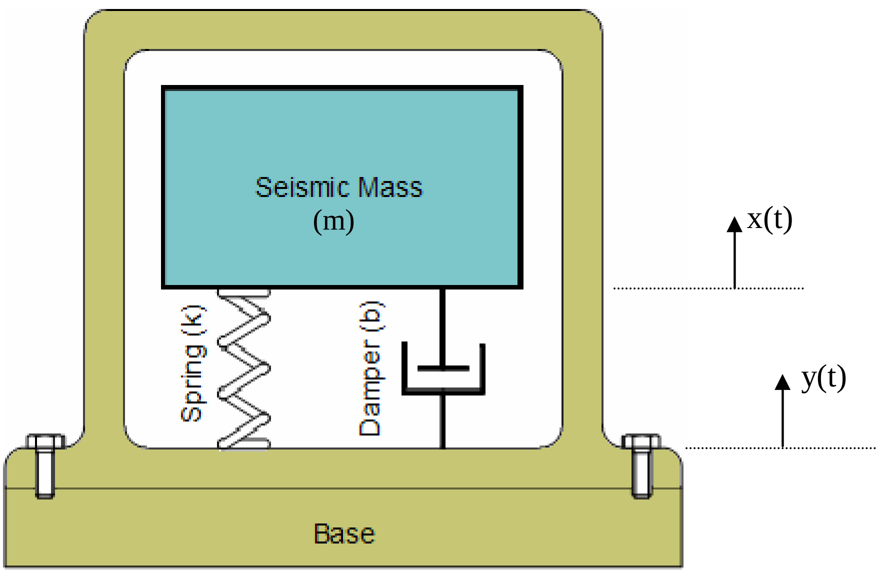

Figure 2.10 Dynamic model of an accelerometer [30].

2.3.2 Steady State Response

If the acceleration applied to the system is not changing, or equivalently, if the applied acceleration is DC, then Equation 2.30 reduces to;

$$\frac{z(t)}{a(t)} = -\frac{m}{k} \tag{2.33}$$

which also represents the sensitivity of the device. This equation shows that sensitivity of the device is directly proportional to the seismic mass size and inversely proportional to the spring constant of the system. Therefore, the sensitivity of the device can be increased by increasing the seismic mass and decreasing the spring constant of the system. Another important result appearing from the steady state acceleration sensitivity formula is that the damping coefficient has no effect to the performance of the accelerometer.

2.3.3 Frequency Response

With a slight modification Equation 2.30 can be rewritten as [68];

$$\ddot{z}(t) + 2\xi\, w_n\, \dot{z}(t) + w_n^{\,2} z(t) = -\ddot{y}(t) = -a(t) \tag{2.34}$$

where w_n is called the resonant frequency of the system and can be expressed with Equation 2.35, ξ, is called the damping factor and can be expressed with Equation 2.36.

$$w_n = \sqrt{\frac{k}{m}} \tag{2.35}$$

$$\xi = \frac{b}{2\, m\, w_n} \tag{2.36}$$

If we assume that a sinusoidal motion is applied to the systems then displacement of the base, shown in Figure 2.10, can be expressed as;

$$y(t) = Y \sin(wt) \tag{2.37}$$

where w is the frequency of the motion and Y is the amplitude of motion. If this motion equation of the base is inserted into the Equation 2.34 we can get;

$$\ddot{z}(t) + 2\xi w_n \dot{z}(t) + w_n{}^2 z(t) = Y w^2 \sin(wt) \tag{2.38}$$

Steady state solution of this equation can be found by inspection as;

$$z(t) = Z \sin(wt - \phi) \tag{2.39}$$

where

$$Z = \frac{Y\left(\frac{w}{w_n}\right)^2}{\sqrt{\left[1-\left(\frac{w}{w_n}\right)^2\right]^2 + \left[2\xi\frac{w}{w_n}\right]^2}} \tag{2.40}$$

and

$$\tan(\phi) = \frac{2\xi\left(\frac{w}{w_n}\right)}{1-\left(\frac{w}{w_n}\right)^2} \tag{2.41}$$

Figure 2.11 shows the plot of Z/Y, ratio of relative displacement of the seismic mass to the base movement, versus frequency ratio, the ratio of acceleration frequency to the resonance frequency of the system, for different values of damping factor, ξ . Figure 2.11 also shows the frequency ratio range where mass-spring-damper system measures acceleration or act like an accelerometer. For the system to act like a accelerometer Z/Y ratio should track the $(w/w_n)^2$ ratio with minimum error, which is valid for low operation frequencies where operation frequency, w, is much smaller than the resonance frequency of the system, w_n.

If the frequency of the external acceleration assumed to be much smaller than the resonance frequency of the system then Equation 2.40 can be reduced to

$$Z = Y\left(\frac{w}{w_n}\right)^2 = \left|\frac{\ddot{y}(t)}{w_n^{\ 2}}\right| = \frac{|acceleration|}{w_n^{\ 2}} \tag{2.42}$$

which means that relative displacement of the seismic mass to the base is directly proportional to the input acceleration and inversely proportional with the square of the resonance frequency of the system. Therefore, in order to increase the sensitivity of an accelerometer, its resonant frequency should be as low as possible, which can be achieved by increasing the seismic mass size and lowering the spring constant.

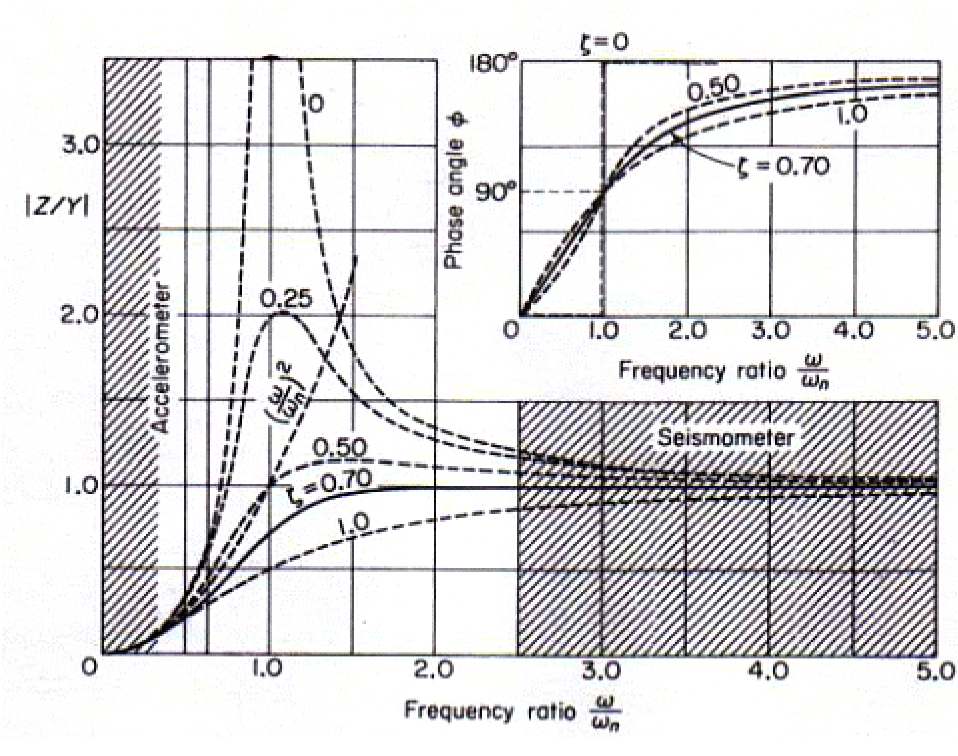

Figure 2.11 Response of a vibration-measuring instrument [68].

Bandwidth of the accelerometer is another important issue, which can be found by calculating the error introduced to the Equation 2.42 by the divisor of the Equation 2.40. Figure 2.12 shows the acceleration error sensed by the accelerometer for different damping factors. It shows that maximum bandwidth of the accelerometer can be achieved with damping factor of 0.7 where the useful frequency range is $0 \leq w/w_n \leq 0.2$ with a maximum error less than 0.01 %.

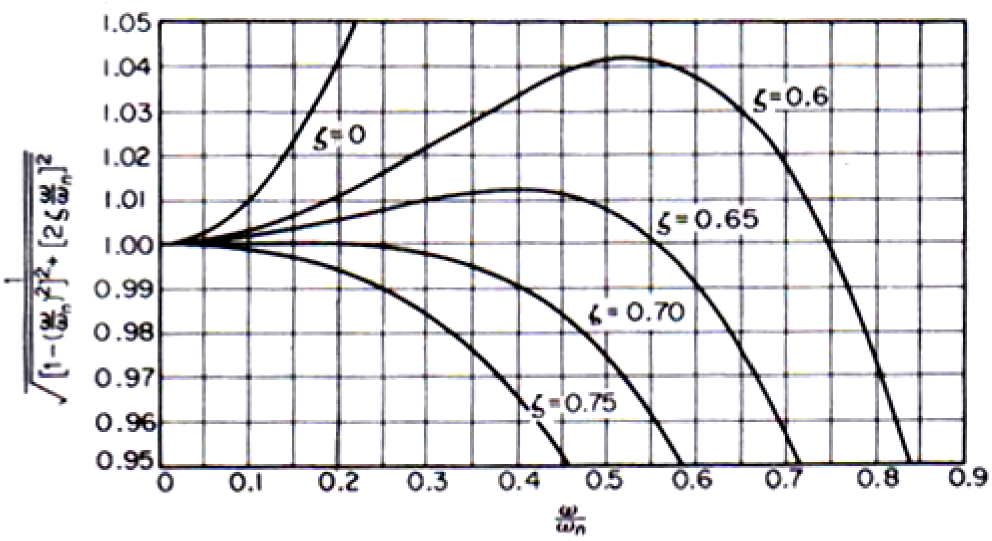

Figure 2.12 Acceleration error vs. frequency ratio (w/w_n) for different values of damping factors (ξ) [68].

2.3.4 Damping and Quality Factor

The damping and quality factors are very important parameters on the performance of the accelerometer. Therefore, types of damping mechanisms should be well understood for a good accelerometer design. Basically, there are two types of damping mechanisms: the structural damping and the viscous air damping. At atmospheric pressure levels, the viscous air damping is the dominant mechanism. Since accelerometers generally work at atmospheric pressure levels, the structural damping, which is due to energy loss in the structural material, can be neglected.

One of the components of the viscous air damping is the squeeze-film damping. Figure 2.13 illustrates this damping mechanism. When the movable plate moves in positive x direction, pressure of the air between the two plates is increased, and the gas moves out from the edges of the plate. If it moves in negative x direction, situation reverses. During the motion of the air, a dissipative force created by the moving air molecules opposing the motion of the plate. This force is called *squeeze-film damping*. Detailed analysis of the squeeze-film damping can be found in [69].

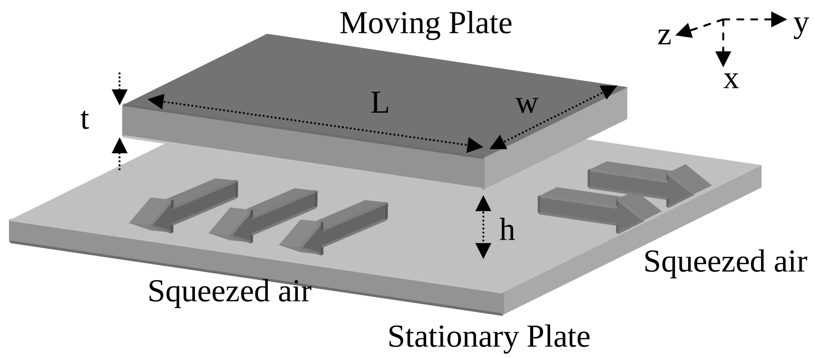

Figure 2.13 Picture illustrates the basic idea behind the squeeze-film damping. Plate moves in positive x direction, increasing the pressure of gas between the two plates, and gas moves out from the edges of the plate.

Another squeeze-film damping effect exists between the comb-fingers. This squeeze-film effect differs from the one existing between the large parallel plates where the gap, h, between the parallel plates is much smaller than the parallel plate dimensions. Assuming Hagen-Poiseuille flow [70], squeeze-film damping coefficient between comb fingers can be written as;

$$b = 7.2\,\mu_{eff}\, l \left(\frac{t}{h}\right)^3 \tag{2.43}$$

where l is the overlap length of the fingers, t is the thickness of the fingers, h is the finger gap, and μ_{eff} is the effective viscosity. μ_{eff} can be calculated as [71];

$$\mu_{eff} = \frac{\mu_{air}}{1 + 9.638 K_n^{1.159}} \tag{2.44}$$

where μ_{air} is the viscosity of the free air, and K_n is the Knudsen number determined by equation;

$$K_n = \frac{\lambda}{h} \tag{2.45}$$

In this equation $\lambda = 0.069/P_a$ (µm) is the mean free path of the air molecules, h is the air gap between the comb fingers and P_a is the ambient pressure.

Other viscous air damping mechanism is called *Couette-flow damping*. This damping is a slide-film damping mechanism occurring between two parallel plates, moving parallel to each other as illustrated in Figure 2.14.

Figure 2. 14 Picture illustrates the basic idea behind Couette flow.

Damping coefficient of Couette flow can be calculated as [72];

$$b = \frac{\mu_{eff} A}{h} \tag{2.46}$$

where μ_{eff} is the effective viscosity of the air and can be calculated from Equation 2.44, A is the overlap area of the moving and stationary plate, and h is the gap between the two plates. An example of Couette-flow in accelerometers occurs between the mass and substrate of the lateral accelerometers. This damping mechanism must be taken into account during the design, if the separation between the mass and the substrate is not so large.

As a result, damping coefficient mostly depends on the pressure of air in the sensor environment. Decreasing or increasing the air pressure in the environment effectively decreases or increases the damping coefficient of the accelerometer system. Another method for decreasing the squeeze-film damping for z-axis accelerometers is to use damping holes in the proof mass. Modeling of squeeze-film damping in microstructures having damping holes can be found in [73].

In order to calculate the total damping coefficient of an accelerometer, damping coefficients of each mechanism are calculated separately, and then added. After calculating the total damping coefficient of the system, quality factor, Q, of the accelerometer can be calculated as;

$$Q = \frac{w_n\, m}{b} \tag{2.47}$$

where w_n is the resonant frequency of the mass-spring-damper system, given in Equation 2.35, b is the total damping coefficient, and m is the mass of the sensing element.

2.4 Sensing Capacitors

Capacitive accelerometers utilize different types of capacitive sensing structures in order to sense the displacement of the seismic mass. There exist three main capacitive detection techniques used in capacitive accelerometers: parallel plate movement detection, transverse comb finger sensing, and lateral comb finger sensing. This section introduces all these types of capacitive sensing topologies, after giving the basics of capacitors in the next section.

2.4.1 Basics of Capacitors

Capacitance, C, formed between a two large conductive plates separated by a gap, z_0, and an overlap area of A is;

$$C = \varepsilon \frac{A}{z_0} \tag{2.48}$$

where ε is the permittivity of the material between the plates. Usually material between the conductors forming the capacitor is air, and its permittivity approximately equal to the permittivity of free space, ε_0 =8.85x10^{-12} F/m.

If energy stored between two charged conductors is denoted by E, then;

$$E = \frac{1}{2} C V^2 \tag{2.48}$$

where C is the capacitance between the two charged conductors and V is the potential applied between conductors. Since these two charged conductors have different polarities, they exert force to each other. This force can be calculated from the ratio of the change in the stored energy to change in the gap between two conductors in the movement direction. Hence, electrical force, F_e, between the two charged conductors is;

$$F_e = \frac{\partial E}{\partial x} = \frac{1}{2} \frac{\partial C}{\partial x} V^2 \tag{2.49}$$

2.4.2 Varying-Gap Sensing

Varying-gap capacitance detection method uses change of capacitance between two conductors as the gap between them changes. There are basically two type of structures to obtain varying gap capacitances in accelerometers. First one is parallel plate capacitances formed by two parallel plates and other one is comb finger type varying gap capacitance. The detailed descriptions of these two structures are given below.

2.4.2.1 Parallel Plate Varying Gap Capacitance Sensing

Figure 2.15 shows the structure of a varying gap parallel plate capacitance, formed by a top electrode and a bottom electrode. Motion of the top electrode is restricted in z direction and bottom electrode is fixed. If fringing fields are neglected, then the capacitance formed between the top and bottom electrode can be written as;

$$C = \frac{\varepsilon_0 W x}{z} \tag{2.50}$$

where ε_0 it the permittivity of air, W is the width, x is the length of the top electrode, and z is the gap between the top and bottom electrode. From Equation 2.49 force exerted on the seismic mass in z direction can be calculated as;

$$F_{e,z} = -\frac{\varepsilon_0}{2}\frac{W x}{z^2}V^2 \tag{2.51}$$

where the minus sign indicates that the force in the z-direction is trying to decrease the gap between the conductors. Therefore, this electrostatic force is trying to increase the capacitance between the two electrodes.

Capacitance sensitivity of the varying-gap capacitance is defined as the capacitance change per unit change in the gap, and it can be expressed with the following equation;

$$\frac{\partial C}{\partial z} = -\varepsilon_0 \frac{A}{z^2} \tag{2.52}$$

where z is the gap, and A is the overlap area. Equation 2.52 indicates that the change of the capacitance with changing gap is not linear. Therefore, for the accelerometers utilizing varying gap capacitances, differential configuration must be used, i.e., when capacitance of one parallel plate increases, capacitance of another parallel plate must decrease. However, forming differential parallel plate sense capacitance is not easy with classical fabrication techniques,.

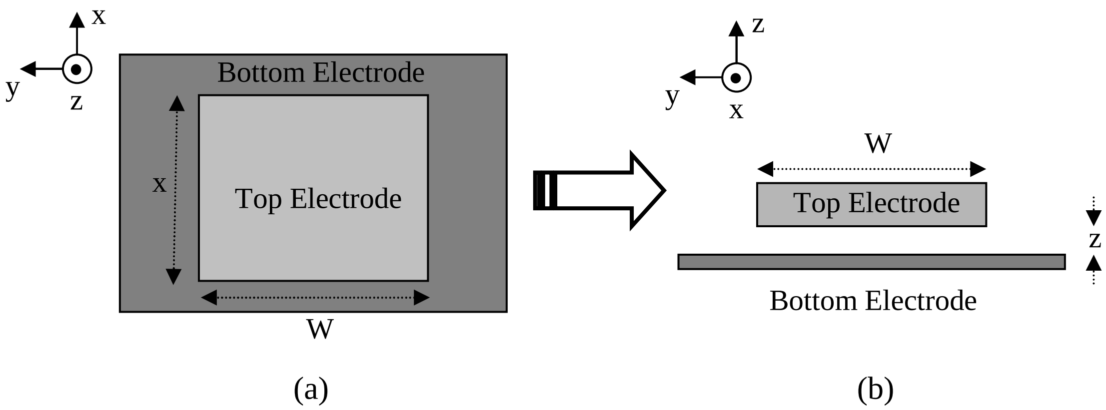

Figure 2.15 Parallel plate varying gap capacitance formed by two electrodes. Motion of the seismic mass is restricted z-direction. (a) Top view. (b) Side view

If a spring is attached in between the top and bottom electrode, the structure shown in Figure 2.15 can be used as an accelerometer. If the mechanical spring constant of the spring, k_{mech}, is smaller than the electrostatic spring constant, then a problem may occurs due to the electrostatic force in the –z direction, which is called pull-in problem. When the electrostatic force is larger than the mechanical force, the top moving plate collapses to the bottom electrode. The voltage that causes this force is called the pull-in force voltage. Defining z as the gap between the seismic mass and the bottom electrode under zero voltage, which is applied between the seismic mass and bottom electrode, *pull-in* phenomenon can be described as follows. If the voltage, V, applied between the electrodes increases, the mass will deflect in the -z direction an amount of Δz due to the electrostatic force between the mass and the bottom electrode. Then, an equilibrium point will be achieved between the electrostatic force and mechanical force which are defined as;

$$F_{el} = -\frac{\varepsilon_0}{2} \frac{W\, x}{(z-\Delta z)^2} V^2 = -\frac{1}{2} \frac{CV^2}{(z-\Delta z)} \tag{2.53}$$

$$F_{mech} = k_{mech} \Delta z \tag{2.54}$$

where F_{el} is the electrostatic force defined by Equation 2.49, and F_{mech} is the mechanical force exerted by the spring on the seismic mass. We can conclude from Equation 2.54 that electrostatic force is always increasing as the mass deflects in –z direction. For static equilibrium of the system, summation of these two forces must be zero. Therefore, electrical spring constant, k_{el}, of the system can be calculated as,

$$-F_{el} = F_{mech} \tag{2.55}$$

$$k_{el} = \frac{dF_{el}}{dz} = \frac{CV^2}{(z-\Delta z)^2} \tag{2.56}$$

$$k_{el} = k_{mech} \frac{2\Delta z}{z-\Delta z} \tag{2.57}$$

If Equation 2.57 is further analyzed we see that when the displacement due to the applied voltage, Δz, of the seismic mass is 1/3 of the total gap, z, then electrical spring constant of the system exceeds mechanical spring constant of the system. Then, the seismic mass will move suddenly along –z direction and will stick to the bottom electrode, which is called *pull-in*. The *pull-in voltage* of a parallel plate capacitor is given by;

$$V_{pull-in} = \sqrt{\frac{8z^3 k_{mech}}{27\varepsilon_0 A}} \tag{2.58}$$

where A is the overlap area of the parallel plate conductors. This drawback of the parallel plate capacitors sets a limit to the applied voltage to the parallel-plate capacitor accelerometers, which is important for sensing the capacitance change of the accelerometer.

2.4.2.2 Varying Gap Comb Finger Capacitance Sensing

The varying gap comb finger topology solves the nonlinearity problem of the parallel plate varying gap capacitors by using a differential sensing topology. Figure 2.16 illustrates the varying gap comb finger structure together with the differential sensing topology. Figure 2.16(a) shows the capacitances formed between the sidewalls of the rotor and stator fingers. Figure 2.16(b) shows the change of capacitances when the rotor moves, where C2 increases and C1 decreases. Capacitance change of the structure to the total rest capacitance of the structure (Figure 2.16 (b)) is;

$$\frac{C2 - C1}{C2 + C1} = \frac{\Delta z}{z} \tag{2.59}$$

where Δz is the deflection of the rotor and z is the gap between the rotor and stator fingers. Equation 2.59 shows that capacitance change is totally linear with the displacement of the rotor.

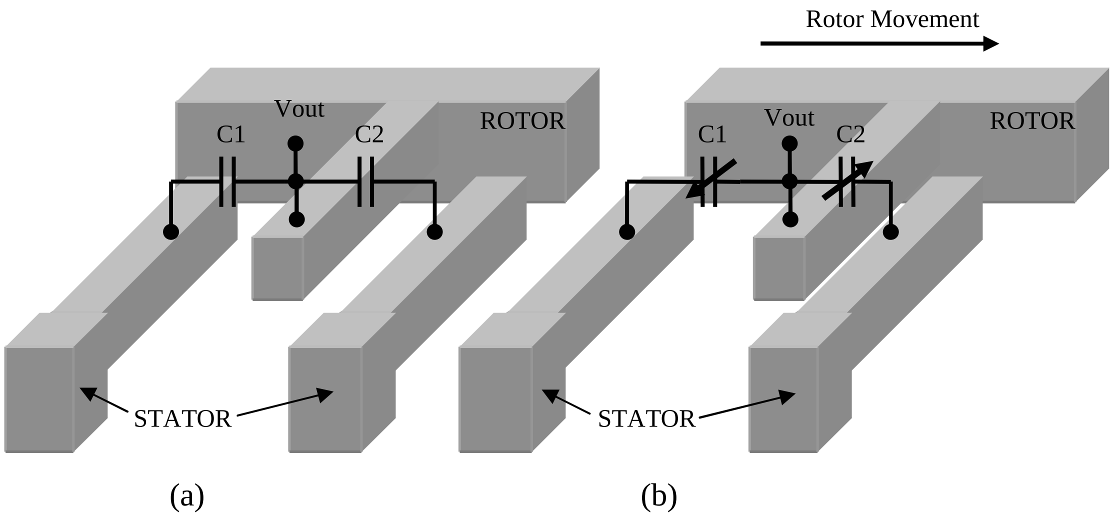

Figure 2.16 Picture of varying-gap comb-finger topology, (a) Capacitances C1 and C2 formed between the sidewalls of the comb fingers, (b) change of capacitances when the rotor moves.

In order to sense the change of the capacitance, differentially connected capacitances are biased with out-of-phase signals from the stator fingers, and the output voltage is sensed from the rotor as shown in Figure 2.16. However, this biasing scheme affects the resonance frequency of the system due to the electrostatic forces occurring between the stator and rotor fingers. This is illustrated in Figure 2.17, where two out of phase sinusoidal waves with amplitude, V, and frequency, w, are applied to the stator finger. Assuming that rotor finger is at analog ground, we can write;

$$V1^2 = V2^2 = \frac{V^2}{2} - \frac{V^2}{2}\sin(2wt) \tag{2.60}$$

and electrostatic force appearing between the rotor and stator fingers can be written from Equation 2.49. Equivalent electrostatic force acting on the rotor finger is the difference between the two electrostatic forces, F_{el1} and F_{el2}. Difference between the these electrostatic forces has two components: one is static due to the first term in Equation 2.60, and other one is altering due to the second term in Equation 2.60. Alternating component of the resultant electrostatic force can easily be suppressed by the low-pass mechanical characteristics of the accelerometer system. Therefore, the static component of this force can be expressed as;

$$F_{el,static} = F_{el1} - F_{el2} = \frac{\varepsilon_0 A V^2}{4}\left[\frac{1}{(z-\Delta z)^2} - \frac{1}{(z+\Delta z)^2}\right] \tag{2.61}$$

where A is the overlap area of the rotor and stator fingers and ε_0 is the permittivity of air. This static component can also lead to pull-in as described in Section 2.4.2.1. Moreover, this component can also be modeled as an electrostatic spring assuming small deflection of the rotor finger where

$$k_{el} = -\frac{d}{dz}(F_{el1} - F_{el2}) = -\frac{\varepsilon_0 A V^2}{z^3} \tag{2.62}$$

This electrostatic spring affects the overall spring constant of the accelerometer system. Hence, it should be taken in to account while calculating the resonance frequency of the system. Considering the electrostatic spring effect, the resonance frequency of the system can be calculated from Equation 2.35.

$$w_r = \sqrt{\frac{k}{m}} = \sqrt{\frac{k_{mech} + k_{el}}{m}} = w_n \sqrt{1 + \frac{k_{el}}{k_{mech}}} \tag{2.63}$$

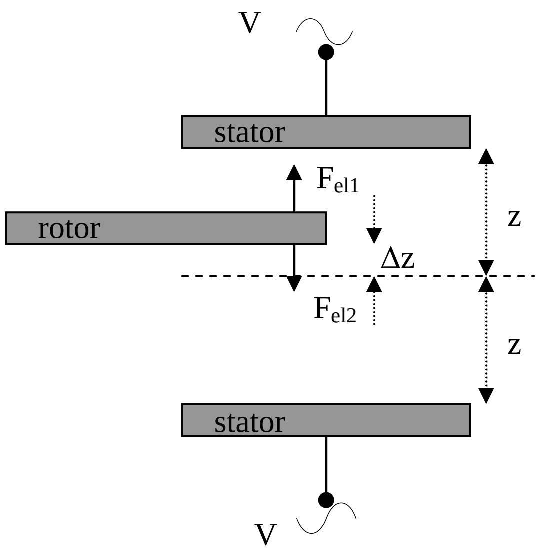

Figure 2.17 Picture illustrating the electrostatic forces on the rotor finger due to the out of phase bias signal to the stator fingers

where w_r is the resonance frequency of the system including the electrostatic spring effect, m is the mass, and w_n is the resonance frequency of the system only due to the mechanical spring constant, k_{mech}.

Since the sign of the electrostatic spring is negative, it decreases the spring constant of the system. This finds application in order to increase the capacitance sensitivity of inertial sensors since decrease in effective spring constant increases the capacitance sensitivity of the sensor as shown in Equation 2.42.

2.4.3 Varying-Area Sensing

Varying area devices sense the movement of the mass by measuring the capacitance change due to the change in the area term in the capacitance Equation 2.50. Most important advantage of the varying-area capacitors on the varying gap capacitors is the linearity of the capacitance change. Figure 2.18 shows the operation principle of a varying area comb finger type capacitors. Sidewalls of the comb fingers form the capacitance between the rotor and stator (C1+C2). When the rotor moves in the indicated direction, the overlap length of the comb fingers changes resulting in an increase in the capacitance between the rotor and stator.

Based on the Figure 2.18 capacitance sensitivity of the varying area capacitor can be calculated as;

$$\frac{\partial C}{\partial L} = \frac{2\varepsilon_0 t}{z} \tag{2.64}$$

where t is the thickness of the comb fingers, ε_0 is the permittivity of air, and z is the gap between the comb fingers. As Equation 2.64 demonstrates, the change of the capacitance with changing overlap length is linearly proportional. Therefore, varying area comb finger capacitances show higher linearity than the varying gap capacitances. However, if we compare the capacitance sensitivity Equations 2.52 and 2.64 for varying gap and varying area capacitances, varying gap capacitances have a higher sensitivity. Moreover Equations 2.52 and 2.64 describe the electrostatic forces occurring between the varying gap and varying area capacitances, where varying gap devices exert more force on the rotor fingers, which is an important property for feedback operation.

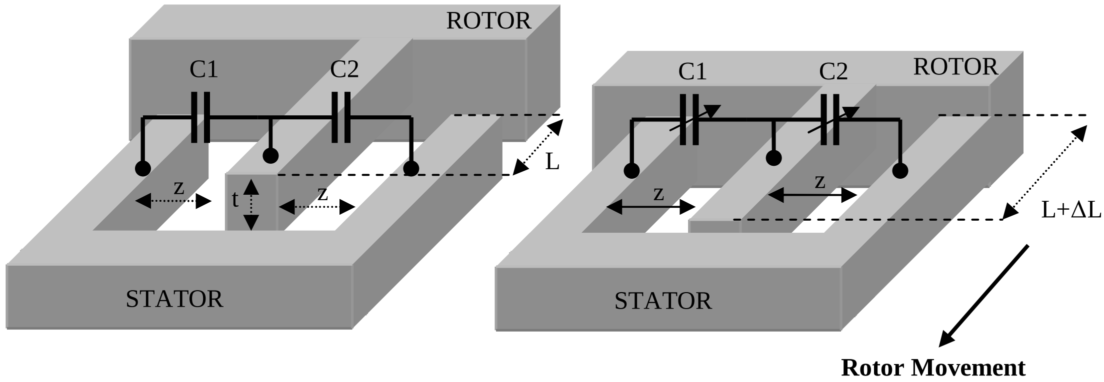

(a) (b)

Figure 2.18 Picture of varying-area comb-finger topology. (a) Capacitance formed between the sidewalls of the rotor and stator fingers, (b) Capacitance change due to the movement of the rotor.

2.5 Summary

This chapter presented the details of multidisciplinary background of the micromachined accelerometers, which consists of both mechanics and electronics. From mechanics point of view, an accelerometer is a mass-spring-damper system where an external acceleration deflects the mass of the system. For the mechanical characterization of the accelerometer, basic mechanical terms like stress, strain, Young's modulus, and Poisson's ratio are defined and also transfer function of the mechanical system is derived. Behaviors of this mechanical system under static and dynamic accelerations are investigated. From the electronics point of view, capacitive sensing mechanisms to sense the deflection of the mass are investigated. Capacitance sensitivity equations for different types of capacitance detection schemes are presented. Moreover pull-in and electrostatic spring constant effects related to the capacitance detection schemes are discussed.

CHAPTER 3

SURFACE MICROMACHINED ACCELEROMETER FABRICATION

This chapter gives the details of the fabrication process of the micromachined accelerometers and masks used during the fabrication process. Section 3.1 introduces the basic fabrication processes. Section 3.2 describes the fabrication steps of the micromachined accelerometers. Section 3.3 describes the designed masks for the fabrication of the micromachined accelerometers. Section 3.4 describes the fabrication of the SU-8 photoresist for fabricating thicker micro-devices. As a last section, Section 3.5 provides a summary of this chapter.

3.1 Introduction to Micromachining

The term micromachining refers to the fabrication of micromechanical structures with the aid of etching techniques to remove part of the substrate or deposited thin film [75]. Basically, two main micromachining techniques exist: surface and bulk micromachining.

Bulk micromachining can be considered as etching deeply into the silicon wafer to fabricate the microstructures. There are several methods to etch the silicon. One of them and the most basic one is wet etching. Wet etching of the silicon can be considered in two categories: isotropic etching and anisotropic etching. Figure 3.1 briefly describes the difference between the two wet etching techniques. Isotropic etching is not directional, that is, the etch rates of isotropic silicon etchants are same for all directions in silicon. However, anisotropic etchants are direction sensitive and their etch rates depend on the crystal orientation. While their etch rate is very small for a particular direction, they can etch very fast in another direction. As illustrated in Figure 3.1(a), circular or cylindrical cavities can be obtained by isotropic wet etching; whereas with anisotropic etching, V-grooves can be obtained due to the directionality of etching behavior. In addition to wet etching, there are also dry etching techniques for bulk micromachining. These techniques are vapor-phase etching and plasma-phase etching (RIE etching) [76].

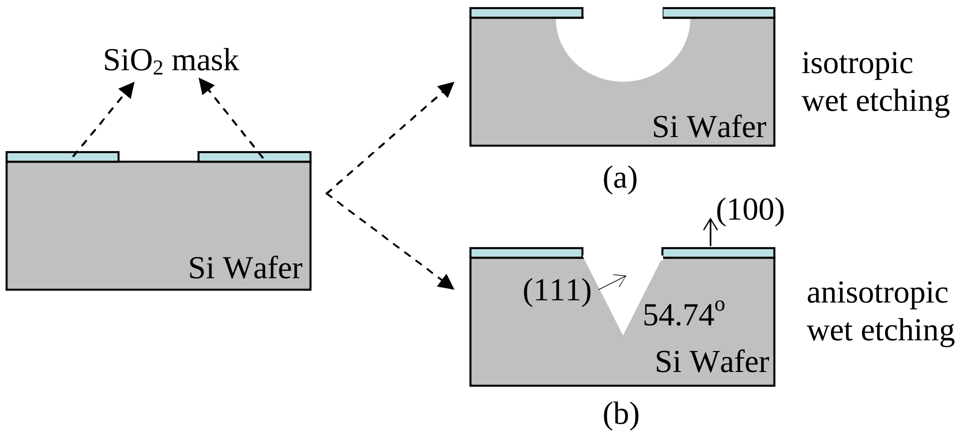

Figure 3.1 Difference between anisotropic wet etching (a), and isotropic wet etching (b) of silicon

Most important advantage of bulk micromachined devices is the utilization of thick structures since device height only depends on the wafer thickness, which is several hundred microns. This property of the bulk micromachinining is very attractive for accelerometers since high seismic masses can be achieved by utilizing full wafer thickness. On the other hand, the most important disadvantage of the bulk micromachining is the complexity of the process. Moreover, the bulk micromachining process is not fully compatible with the clean room since some wet etchants are considered as dangerous for clean room processes (like KOH). This disadvantage can be overcome, if the etching is performed as the final step of the process. Another disadvantage of the conventional bulk micromachined accelerometers is the size. Together with high thicknesses achieved with bulk micromachining, devices have large feature dimensions due to isotropic wet etching. Fortunately, with the new dry etching techniques bulk micromachined accelerometers having small lateral dimensions can be fabricated. Many different types of capacitive bulk micromachined accelerometers are fabricated successfully with wet [35, 77, 78] and dry etching [29, 36] or combination of both [79].

Surface micromachining uses thin films to form the mechanical structures on the top of a substrate. Figure 3.2 briefly describes the basics of surface micromachining. Process starts with depositing sacrificial layer on the substrate. Deposited sacrificial layer is then patterned (Figure 3.2 (b)). Then structural layer is deposited on the top of sacrificial layer and patterned (Figure 3.3 (c)). Finally, sacrificial layer is etched in order to release the structure (Figure 3.3 (d)).

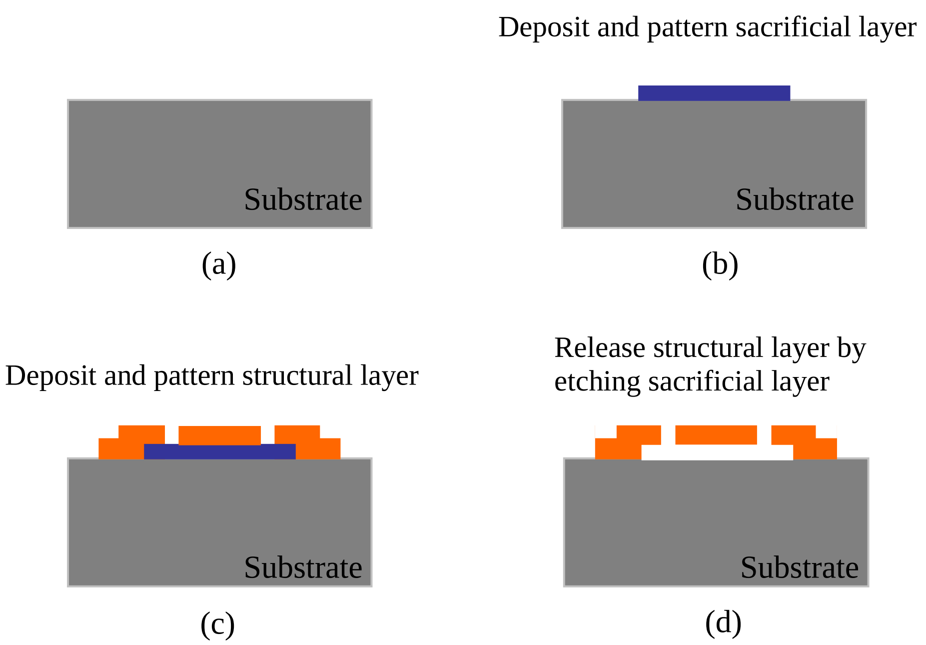

Figure 3.2 Description of surface micromachining. (a) Start with bare substrate, (b) deposit and pattern sacrificial layer, (c) Deposit and pattern structural layer, (d) Etch the sacrificial layer and release the structure

Most important advantage of the surface micromachining technology is its compatibility with the standard IC process. Since materials like polysilicon and aluminum are readily used in standard IC technology, it is easy to form mechanical structures from polysilicon and aluminum. This property of surface micromachining decreases the chip size considerably, eliminating the need for extra package for the readout circuitry. Moreover high vertical walls can be achieved easily by pattering thin films which makes the formation of sidewall capacitances very easy. On the other hand, with standard surface micromachining technology it is not easy to form thick mechanical layers. In addition, residual stress and stress gradient in the polysilicon layers result in some problems for the mechanical structures. More importantly, the stiction problem makes the release of the mechanical structures difficult due to the liquid capillary-forces acting on the structures during releasing [75].

Mechanical structures fabricated in surface micromachining technology include deposited thin films of polysilicon, aluminum, and silicon nitride [80]. Other non-standard methods for surface micromachining are dry-release process for tunneling-tip microstructures, buried-cavity dry-release technology, high-aspect ratio silicon-on-insulator technology [81], and electroplating process through resist molds [27, 31, 82, 83].

Electroplating is a promising technique for the fabrication of microstructures. Surface micromachined accelerometers using electroplating process are demonstrated in the literature [27, 31, 83]. Advantages of utilizing electroplating process for the fabrication of microstructures are;

- Low temperature process, compatible with IC fabrication, and reduced thermal stress.
- Low cost equipment, easy deposition.
- High rate of deposition.
- Conformal deposition or deposition through resist masks.

- High aspect ration structures can be obtained with well defined resist masks
- Great reliability for high aspect ratio structures.
- Well understood behavior, and actively used in industry for a long time.

In addition to these properties many different metals can be deposited with electroplating process, like copper, nickel and gold. Nickel, which is one of the common material for electroplated microstructures, provides attractive mechanical properties such as Young's modulus, yield strength [84] and hardness with zero residual stress deposition [31]. Moreover copper and gold are suitable for interconnect layers due to their high conductivity [85].

Due to these superior properties of electroplating process and good mechanical properties of nickel, electroplating process is used for fabrication of micromachined accelerometers, where electroplated nickel is used as the structural layer, and electroplated copper is used as the sacrificial layer.

3.2 Surface Micromachined Accelerometer Fabrication

Fabrication of the micromachined capacitive accelerometers described in this section is the improved version of the process steps described in [86]. Details of fabrication procedure for the micromachined accelerometers are shown in Figure 3.3. In this process, which is established at METU Electrical-Electronics Engineering Department, nickel is used as the structural layer and glass is used as the insulating substrate. Insulating glass substrate prevents the levitation effect, which is due to the asymmetric field distribution between the stationary comb finger electrodes and movable comb finger electrodes [87].

The fabrication procedure is simple and very low cost, which is ideal for mass production of the accelerometers. Process steps include only lithography, electroplating, and wet etching. The process starts with the formation of the metallization layer on the top of glass substrate (Figure 3.3 (a)-(c)). Then the sacrificial layer is formed by electroplating where a negative photoresist is used as the mold (Figure 3.3 (d)-(j)). On the top of the sacrificial layer, the structural mold layer is formed with SJR 5740 photoresist. Inside the mold nickel is electroplated as the structural layer (Figure 3.3 (k)-(m)). Following this step, the wafer is diced, and accelerometers are released by etching the sacrificial copper layer (Figure 3.3 (n), (o)). During these fabrication steps only 3 masks are used; the metallization mask, the anchor mask, and the structural layer mask. Details of the process steps are given in the Sections 3.2.1, 3.2.2, and 3.2.3

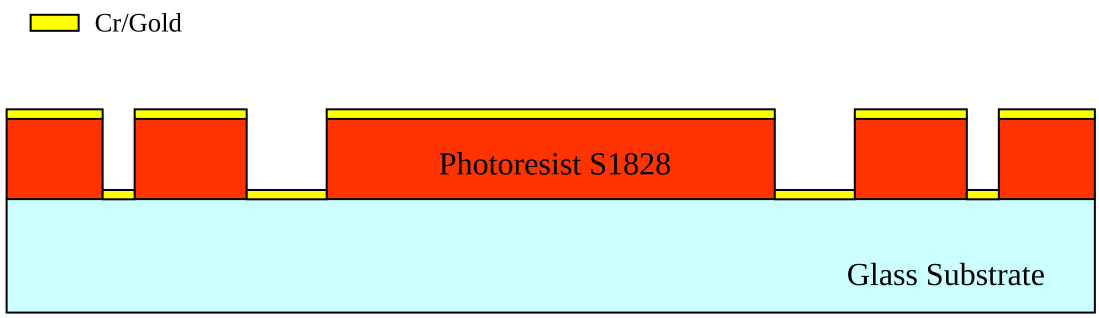

(a)

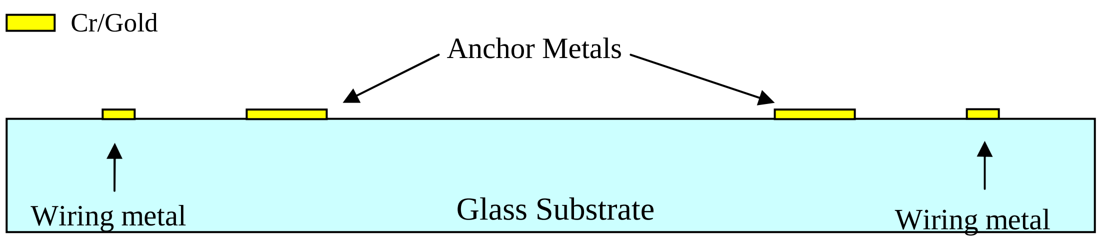

(b)

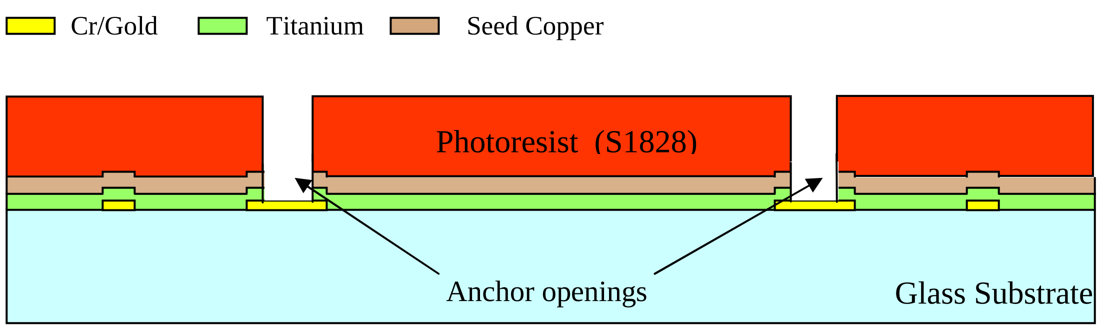

(c)

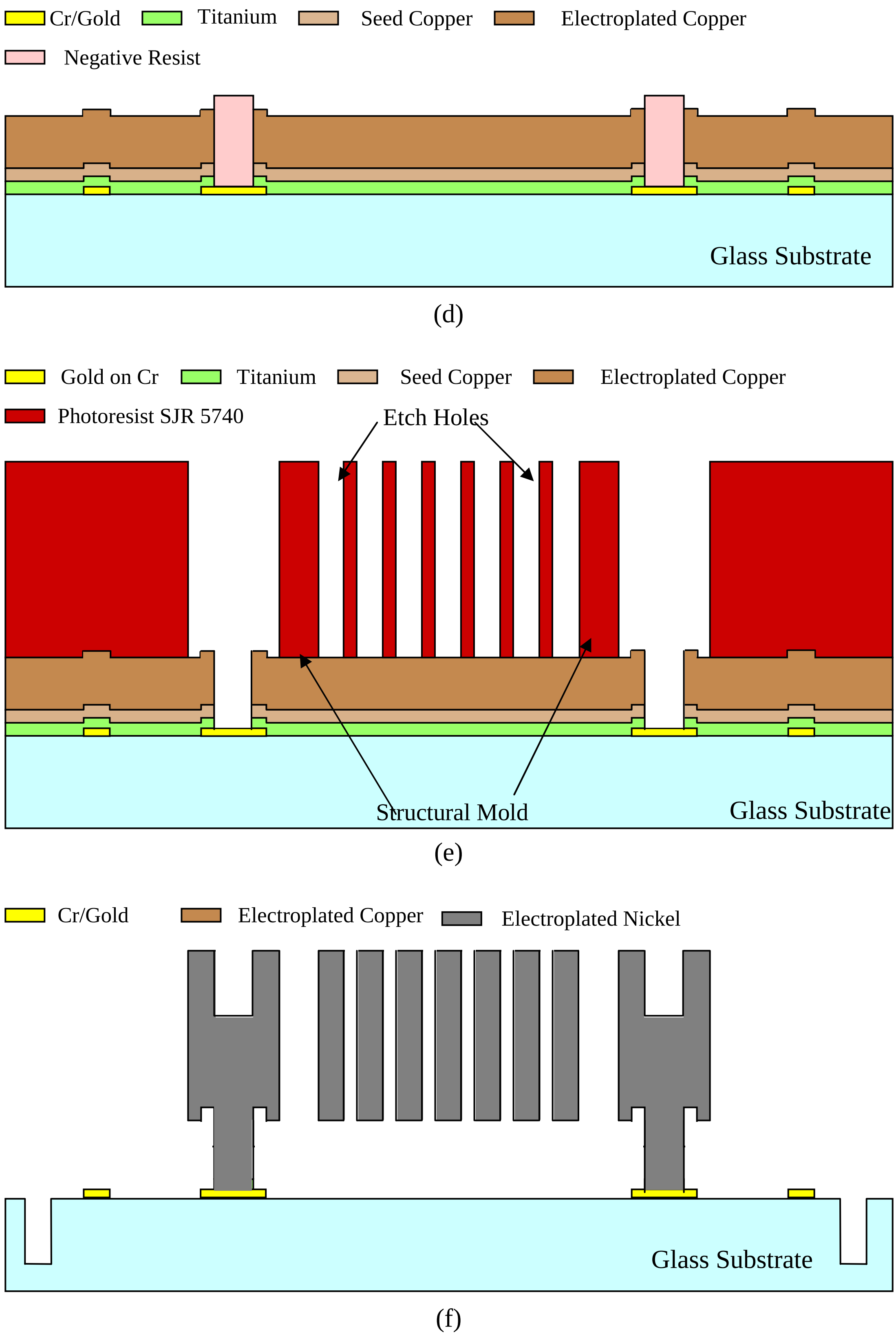

Figure 3.3 Fabrication steps of the capacitive surface micromachined accelerometer structures.

3.2.1 Fabrication of the Metallization Layer

The metallization layer is used both for routing the signals and for the adhesion of the nickel structural layer to the glass substrate. In this process, gold is used as the main metallization layer, and chromium is used to improve the adhesion of gold to glass. The fabrication technique used for the formation of the metallization layer is lift-off. Process details are given below.

The metallization process starts by coating Shipley's S1828 photoresist on the glass wafer using a spinner operating at 3000 rpm to achieve a thickness around 4 μm, which makes the lift-off process easy. Then, photoresist is soft baked at 115^o C for 1 min, and exposed for 9.5 seconds (~170 mJ/cm^2) at vacuum-contact mode with EVG 620 mask aligner through the metallization mask. Development of the exposed the photoresist is performed with NaOH:DI (17.8gr:1600 ml) solution for 1.5 min. Then wafer is dipped into Buffered-HF (BHF, 5:1 NH_4: HF) for 30 seconds, where photoresist layer is used as the etching mask. Buffered-HF etches the glass and makes the surface rough to increase the adhesion of the Chromium layer to the glass substrate. After this step, chromium (500 Å) and gold (1500 Å) is evaporated on the wafer (Figure 3.3 (a)). Since adhesion of gold to glass is poor, chromium is used as the intermediate layer between the glass and gold, which has a very good adhesion to both.

Evaporation does not have good step coverage, therefore, gold and chromium residing on the top of the photoresist can be easily lifted-off with acetone with the help of a buzzer, resulting in metallization layers residing on the glass wafer (Figure 3.3 (b)). With metallization layer, pads and routing layers are fabricated. Moreover, the metallization layer is also used as the intermediate layer between the structural nickel and glass substrate, in order to improve the adhesion of nickel to substrate at anchor points.

3.2.2 Fabrication of Sacrificial Layer

The sacrificial layer is used to suspend the movable parts of the micromachined structures. Thick sacrificial layers are advantageous in terms of preventing stiction problem, and also lowering the air damping. Copper is selected as the sacrificial material since it can be selectively etched without damaging the structural nickel.

Formation of the sacrificial layer starts with the deposition of a thin titanium layer. The titanium layer serves as an adhesion layer between copper seed layer and glass substrate. For this purpose, 75 Å of Titanium layer is sputtered on the top of the metallization layer with a long pre-sputtering period at room temperature. On the top of the titanium, 2500 Å thick Copper is sputtered at room temperature, which serves as a seed layer during the electroplating process.

After formation of the seed layer, the photoresist S1828 is coated on the wafer again to act as the etching mask for anchor opening, which is necessary for gold-nickel contact. S1828 is coated with the same conditions as in metallization formation process and exposed with anchor mask. Development is performed again with the NaOH:DI solution. First electroplated Copper is etched through the openings of the photoresist layer with CH_3COOH:H_2O_2:DI (1:1:18) solution for 90 seconds. No undercut is observed during the etching of the copper, which is important for achieving electrical contact to gold layer. Then sputtered titanium layer is etched through photoresist openings with HF:H_2O_2:DI (1:1:640) for 3 min. (Figure 3.3 (c)). After etching is completed, the mask photoresist is removed.

After these steps, the wafer is ready for the formation of the sacrificial photoresist mold for the copper electroplating process. Negative photoresist MaN-332s is coated on the wafer with a thickness around 5-6 μm and soft baked at 95^o C for 6.5 min. Exposure of the negative photoresist is performed through the same anchor mask for 90 seconds at vacuum contact mode with the EVG 620 mask aligner, and development is performed with the maD-332s for 1 min. Electroplating of copper is performed through the negative photoresist mold with a thickness around 4-5 µm (Figure 3.3 (d)). After the electroplating of the copper the sacrificial layer, the negative photoresist mold removed. Then the wafer is ready for the preparation of the structural mold photoresist and electroplating of structural nickel.

3.2.3 Fabrication of Structural Layer

The structural layer formation is the final process step and it is achieved in two steps: first one is the preparation of the structural mold photoresist and other one is the nickel electroplating process performed through the photoresist mold.

The structural mold formation is the most critical process step in the accelerometer fabrication, as it defines the aspect ratio of the structural layer, i.e., ratio of the thickness of the structural layer to the minimum achieved dimension. A higher aspect ratio allows implementing narrow and tall finger structures that provide larger sensing capacitances.

For the fabrication of the structural mold, Microposit's SJR 5740 photoresist is selected for its attractive lithographic capabilities [88]. Reference [89] reports an aspect ratio of 6.8 with a photoresist thickness of 17.6 µm using SJR 5740. First SJR 5740 is coated on the top of the sacrificial layer with a thickness around 18 µm. After the coating of photoresist, a relaxation period of 5 min. is needed, which reduces the film stress and improves the uniformity. Then, soft bake of the photoresist is performed at 105^{o} C by putting the wafer for 10 min. onto a hot plate. After that a relaxation period more than 10 h. at a humidity environment around % 50 is needed. This relaxation period is necessary for the formation of developer-soluble acids in the photoresist and improves the resolution of the photoresist. Photoresist is exposed for 27.5 sec. (~495 mJ) at vacuum contact mode with EVG 620 mask aligner. After another relaxation period of more than 10 h., photoresist is developed with Microposits 2401 solution diluted with DI water (1:4) (Figure 3.3 (e)).

After the mold is prepared, the next step is the electroplating of the structural nickel on the mold photoresist. Sulfur activated nickel anodes and the glass wafer are dipped into Nickel Sulfamate solution. By applying proper current (~4 A) through the solution, wafer is coated with nickel to a thickness around 16 μm. It should be noted that deposition rate of the electroplated nickel affects the mechanical properties of the material. Main effect of the deposition rate on the structural nickel is the changing residual stress. As the deposition rate increases, tensile stress of the electroplated nickel increases (compressive stress decreases).

The wafer is diced before releasing the structures. After that, accelerometers are released sample by sample. First, the photoresist mold is removed. Then, sacrificial Copper is etched with $CH_3COOH:H_2O_2$:DI (1:1:18) solution for 2 hours. In order to fasten the etch time of sacrificial copper, etch holes are replaced on the seismic masses of the accelerometers. Then, Titanium is etched with $HF:H_2O_2$:DI (1:1:640) solution. After rinsing the samples in DI, they are quickly dipped into IPA solution for 3 min., and DI is changed with IPA. Then samples are dipped into Methanol for 3 min., and Methanol is evaporated on the hotplate with plate temperature of 90^o C. With this technique no stiction problem observed. Figure 3.3 (f) shows the cross-section of the accelerometers at the end of fabrication step.

3.3 Mask Design for Accelerometer Fabrication

As stated in the previous section, three masks are used for the fabrication of the surface micromachined capacitive accelerometers. Although device layouts are presented in the next section, this section gives some common layout features for all the designed micromachined accelerometers. In all the figures given in this section, red color corresponds to the structural layer layout on the structural mask, blue color corresponds to metallization layer layout on the metallization mask, and green color corresponds to the anchor layout on the anchor mask. Figure 3.4 shows a sample layout drawn for an accelerometer design.

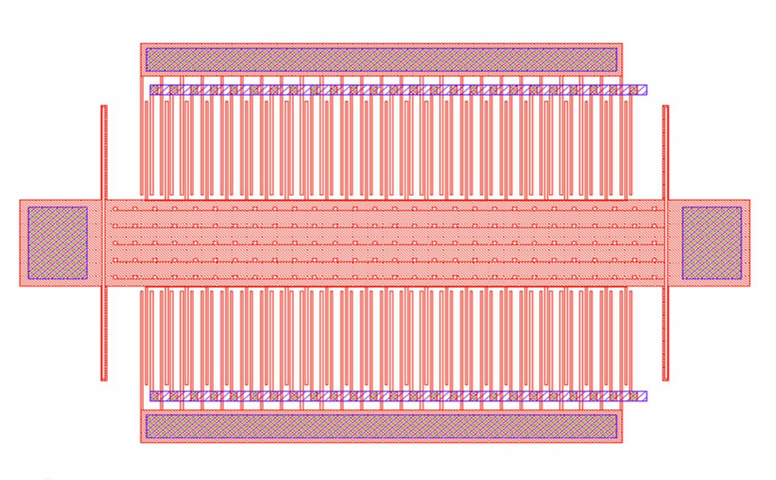

Figure 3.4 The layout of a designed accelerometer, showing the mask layers. Red corresponds to the structural layer, blue corresponds to the metallization layer, and yellow corresponds to the anchor layer.

There are two important features on the drawn layouts, first one is the structure of the anchor layer and second one is the structure of the comb fingers. Figure 3.5 shows the layout of an anchor. Anchor of an accelerometer is composed of combination of all three layers; structural, metallization, and anchor layers. The important point in the layout is the sizes of anchor and metallization layers.

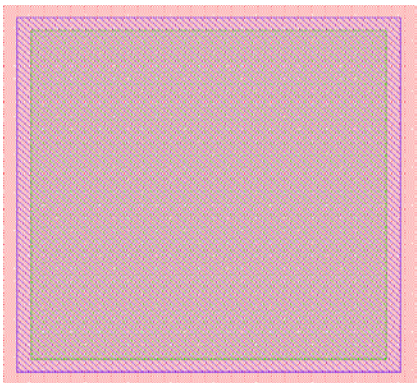

Figure 3.5 Picture showing the layout of anchor layers. Metallization layer should overlap the anchor layer for guaranteeing the electroplating of the structural layer on the top of the anchor metal.

Another common layout structure for the accelerometers is the comb fingers. There are two types of comb fingers in the designed accelerometers. One is the conventional comb fingers, and other one is the cross over comb fingers. Figure 3.6 shows the structures of these two comb finger topologies. Difference between the two comb fingers is that the cross-over combs include the small-size anchors. Fingers given in Figure 3.6 are for varying gap type comb fingers. The structure of the varying area type comb fingers are similar to conventional comb fingers shown in Figure 3.6(a).

Figure 3.7 shows the overall layout of the masks, designed for the fabrication of the accelerometers. Instead of showing each mask separately, this figure shows all the masks at the same time. Empty areas are reserved for another MEMS design that would be fabricated with the same process. A 0.5 cm region from the wafer edge is left empty for edge bead removal. Alignment marks are placed at the sides of the layout to decrease the alignment error.

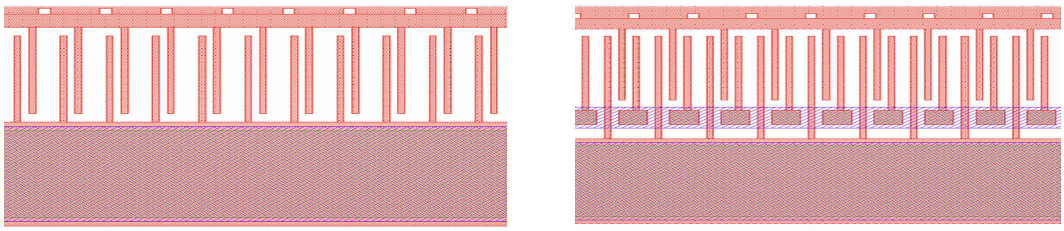

(a) (b)

Figure 3.6 Examples of comb finger designs, (a) conventional comb finger structure, (b) cross over comb finger structure.

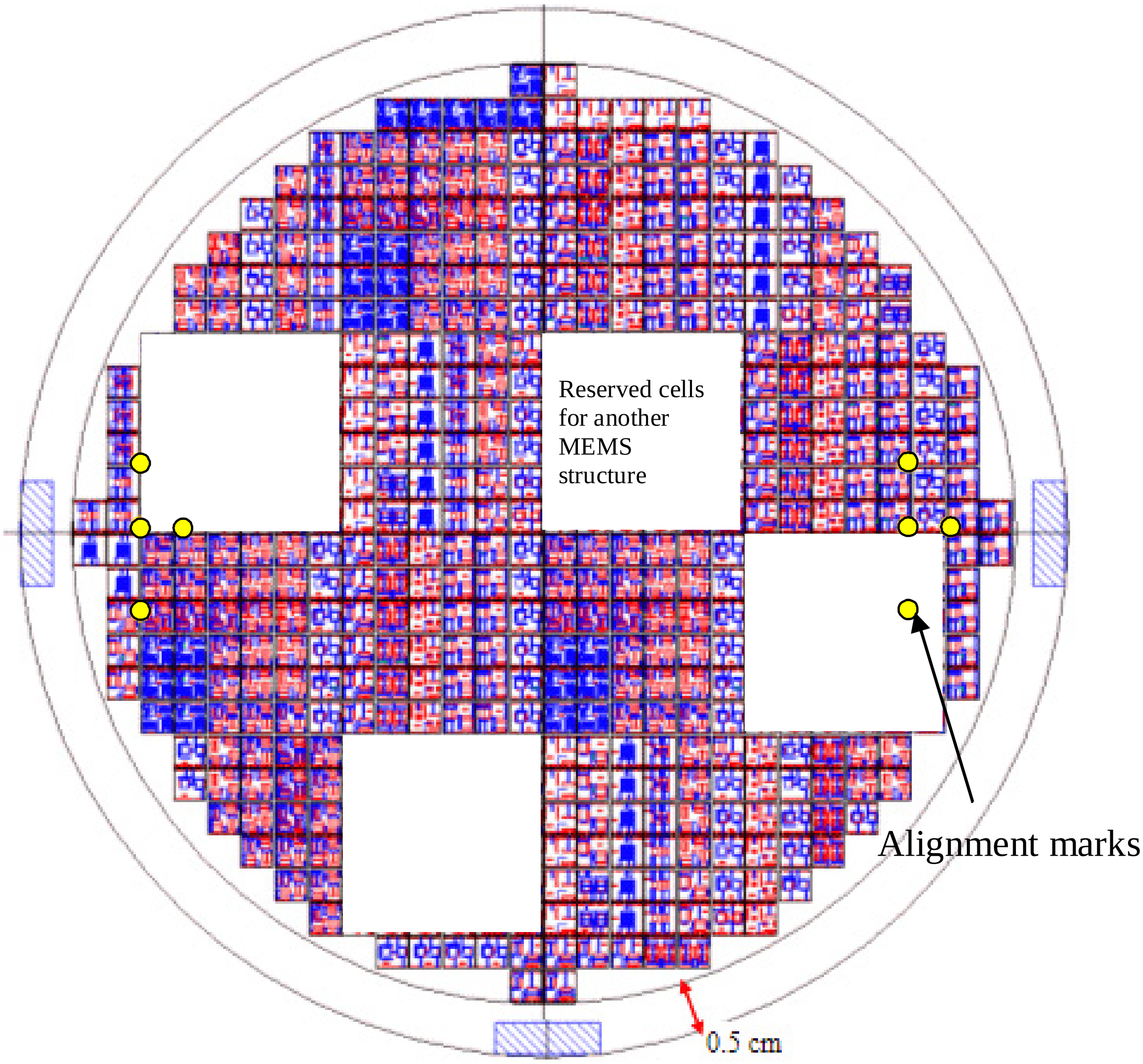

Figure 3.7 Layout of the masks. Empty cells are reserved for another MEMS design that would be fabricated with same process.

3.4 SU-8 Optimization

As mentioned in the previous section, the structural mold layer is the most critical step in the fabrication of the electroplated accelerometers. Thick and high aspect ratio molds are required to achieve tall and narrow structures, which provide higher sense capacitance and lower Brownian noise. In section 3.2, it is mentioned that SJR 5740 is selected as the structural mold layer, which provides an aspect ratio up to 7 with a thickness about 17 µm. It is possible to obtain much higher thicknesses (up to 200 µm) with an aspect ratio around 10 using SU-8 as the structural mold. In the framework of this research optimization studies have been performed for SU-8 structural mold, as explained below.

SU-8 is a negative-tone, epoxy based photoresist developed for MEMS micromachining processes, where a thick, chemically and thermally stable photoresist is desired [90]. For fabricating thicker structural layers, SU-8 50 can be used, where it is possible to fabricate more than 50 µm thick structural photoresist mold in a single coating. Formation of SU-8 photoresist mold consists of 5 main steps; coating, soft bake, exposure, post exposure bake, and development. Optimized process conditions can be described below;

First, the wafer was prepared where a 2500 Å thick copper was sputtered on the top of the wafer. Coating of the photoresist is performed 3500 rpm for 30 second with a dispense speed of 500 rpm for 10 sec. This spin speed results in a 40-50 µm photoresist thickness. There is relaxation period of 15 min, before continuing with the soft bake of the photoresist. This increases the uniformity of the photoresist throughout the wafer.

Soft bake of the SU-8 photoresist is important in order to reduce the film stress of the photoresist. A three step soft bake procedure is applied to the coated photoresist. Figure 3.8 shows the temperature versus time diagram of the soft bake procedure of the photoresist. First photoresist is soft baked at 50^{o} C for to 2 minutes. This improves the uniformity of the photoresist and also helps reducing the edge bead of the photoresist. Then, temperature of the hot plate is slowly increased to 65° C. Since our hot plate does not have any temperature rate control, this is achieved by increasing the hot plate temperature with 5° C steps. These two low initial bake temperatures allow the solvent in the photoresist to evaporate out of the film at a more controlled rate, which results in better coating fidelity, reduces edge beads, and provides better photoresist to substrate adhesion [90].

Exposure of the photoresist is also important in terms of defining the resolution and sidewall angle of the photoresist. However it has been observed that photoresist stress depends on the exposure time. Higher exposure times results in higher stress in the photoresist film. Therefore, exposure energy of the photoresist was optimized as 270 mJ in the vacuum-contact mode. The relaxation period between the soft bake and exposure is around 12 hours. Also note that edge bead of the photoresist should be removed before the exposure of the photoresist.

Post exposure bake is also important to define the resolution and sidewall angle of the photoresist. Higher post exposure bakes results in vertical sidewalls and higher resolution. However, stress of the film increases so much that, deformation and cracks on the photoresist layer can be observed. Optimized post exposure bake procedure of the photoresist is same with the soft bake procedure as shown in Figure 3.8.

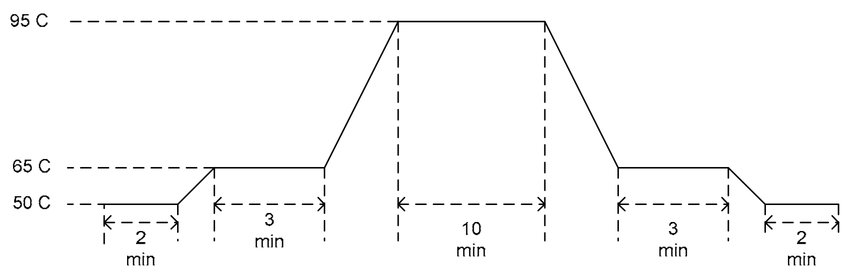

Figure 3.8 Soft bake and post exposure diagram of the SU-8 photoresist.

After the post exposure bake, a relaxation time of 12 hours is also necessary for letting the photoresist release some of its stress. Development of the photoresist was performed with the SU-8 developer supplied by the MicroChem. Continuous agitation is necessary during development, however it should not be so strong because this could result in a deformation of the film.

Figures 3.9 and 3.10 show the results of the optimized fabrication process. Thickness of the photoresist is approximately 42 µm. Figure 3.9 shows the part of a seismic mass of the device, where the SU-8 mold shows the etch holes on the seismic mass. As can be seen from the figure sidewalls are nearly vertical. Figure 3.10 shows the SU-8 mold taken from a part of the accelerometer, showing the etch holes on the seismic mass and comb fingers. Note that comb finger widths on the mask is 4 µm, resulting in an aspect ratio higher than 10.5.

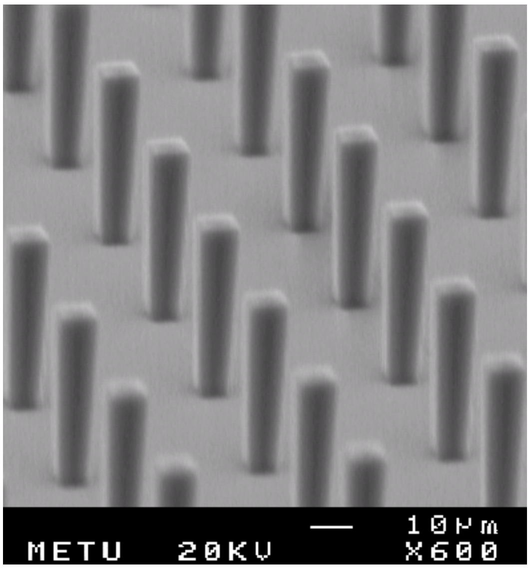

Figure 3.9 Part of the SU-8 mold of the seismic mass, where SU-8 mold represents the etch holes on the seismic mass. Thickness of the photoresist is around 42 µm.

It should be noted that there is an adhesion problem between the photoresist and the substrate, especially around the anchors of the devices. Since photoresist mold is not touching the substrate around the anchors, electroplating occurs in these regions resulting in short circuit between the anchors of the seismic mass and the anchors of the comb fingers. This adhesion problem can be solved with SU-8 2000 series of MicroChem, which has improved adhesion properties, as well as, improved uniformity [91]. Moreover, since most of the springs of the devices are 3 μm, mold of these springs are touching to each other at the top of the photoresist. This problem can also be solved with SU-8 2000 photoresist. After solving these problems and using SU-8 photoresist as the structural mold layer, it is possible to obtain higher performance accelerometers with the current mask set.

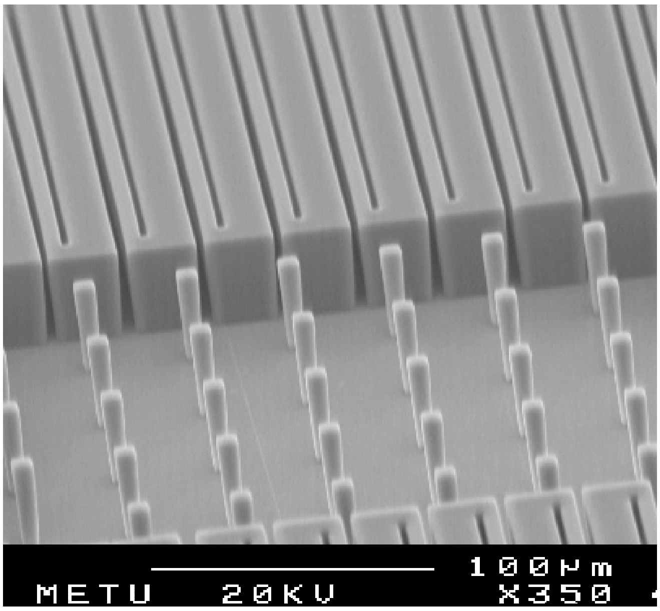

Figure 3.10 SU-8 mold of the part of an accelerometer. Comb finger widths are 4 μm on the designed mask, resulting in an aspect ratio higher than 10.5.

3.5 Summary

This chapter presents the fabrication steps of the surface micromachined capacitive accelerometers. For the fabrication of the surface micromachined accelerometers three dark-field masks are used; metallization, anchor, and structural. Fabrication of the accelerometers does not involve any complex steps, instead lithography, etching, and electroplating are used for the fabrication of surface micromachined accelerometers. The electroplating technique is used for the fabrication of the sacrificial layer and also for fabrication of the structural layer. The sacrificial layer is fabricated from copper electroplating through a negative resist mold. Similarly, structural layer is fabricated by nickel electroplating through a thick resist mold, which is patterned by standard UV lithography. Finally, structures are released by etching the sacrificial layer. Moreover this chapter includes the optimization of SU-8 negative tone resist that can be used to fabricate thicker and higher performance accelerometers in the future.

CHAPTER 4

SURFACE MICROMACHINED ACCELEROMETER DESIGN

This chapter gives the details of the surface micromachined accelerometer designs. Section 4.1 describes the important parameters of the accelerometers and challenges affecting these parameters. Section 4.2 describes the reasons behind designing variety of accelerometers based on the same prototype. Section 4.3 gives the details of the designed accelerometers, their performance values, and also calculated capacitance sensitivity parameters. Finally, Section 4.4 gives the summary of this chapter.

4.1 Design Challenges for Surface Micromachined Accelerometers

Main considerations for the evaluation of the micromachined accelerometers are the resolution, voltage sensitivity (scale-factor), nonlinearity (scale-factor nonlinearity), bias instability, and cross-axis sensitivity. Resolution is the minimum resolvable acceleration by the accelerometer and is the most important criteria for the evaluation of accelerometers. Voltage sensitivity is the change in the output voltage to 1g acceleration input. Nonlinearity is the deviation of the output of the accelerometer from the linear input-output curve plotted according to the sensitivity of the accelerometer, which is necessary for extracting the acceleration information from the output of the accelerometer system. Bias instability is the change of the accelerometer output to the same variable change, which is an important property for inertial navigation applications. Cross-axis sensitivity is sensitivity of the accelerometer to the off-axis accelerations. An accelerometer has to be evaluated in all areas stated above to be considered as high performance. Further explanation of the performance specifications are given in Appendix A.

Design of a high performance accelerometer consists of selecting process technology, designing the readout circuit, and choosing packaging facilities. From this trio, basic and the most important one is the process technology, which directly affects the structure and performance of the accelerometer. Therefore, the process technology must be considered primarily for an accelerometer system.

Resolution of the accelerometer is determined by the noise floor of the accelerometer system and bandwidth of operation. There are two different noise sources in an accelerometer: electronic noise which is due to the readout circuit of the accelerometer and mechanical noise, which is due to the Brownian noise [92] and can be expressed in terms of mass size and total damping [21, 93].

Mass size of the accelerometer is totally process dependent. For example, if polysilicon is used as the structural layer, which can be deposited only few μm's, devices will have small seismic masses [22, 25]. Alternatively, electroplating process can be used to from thick seismic masses, by the help of thick molds prepared by LIGA [27]. Another example to achieve large seismic masses is to utilize full wafer thick masses with DRIE Si etching [36, 94].

Damping of the accelerometer can be reduced by vacuum packaging, which decreases the effective viscosity of air surrounding the accelerometer as given in Section 2.3.4. Vacuum packaging is reported for the resonant accelerometers to achieve high quality factor [53, 57]. On the other hand, reduced damping decreases the bandwidth of the accelerometer having static seismic masses as shown in Section 2.3.3. Another drawback of high quality factor for this type of accelerometers is the vibration of seismic mass at resonance frequency under static accelerations. Hence, accelerometers having the high quality factor and the static seismic masses should be operated under force balanced operation to prevent oscillation at resonance frequency.

Voltage sensitivity of an accelerometer is related with the resonance frequency, sense capacitance, and readout circuit of the accelerometer, where first two are process dependent design considerations. Resonance frequency of the accelerometer can be reduced with high seismic mass size and low spring constant. However, small sense capacitance values is a big problem for sensing the mass displacement of the accelerometer, since parasitic capacitances degrades the output of the accelerometer. There are two solutions to this problem. Either the accelerometer can be monolithically integrated with its readout circuitry in order to decrease the parasitic capacitances [22-25, 28] or the accelerometer should have high sense capacitance values, where effect of the parasitic capacitances can be reduced. However, achieving high sense capacitances is directly related with the process technology. For high sense capacitances, high overlap area and small gap are needed, which addresses the need for high aspect ratio process technology. Unfortunately, achieving high aspect ratio microstructure with conventional surface micromachining technology is not possible. Voltage sensitivity and noise floor of the accelerometer defines the SNR (Signal-to-Noise Ratio) of the accelerometer, which is the main design consideration.

Nonlinearity is a geometry dependent parameter. Structure of the sense capacitances can introduce nonlinearity to the output of the accelerometer. Especially for the varying-gap type sense capacitances, a differential sensing scheme is necessary for linearity. Process variations while forming the differential sense capacitances can introduce a mismatch to the varying-gap sense capacitances, which results in nonlinearity. Therefore, the process has an important effect on the linearity of the accelerometer. Fortunately, this mismatch between the sense capacitances can be eliminated with force feedback operation.

Bias instability shows the sensitivity of the accelerometer to the changing conditions and aging. For example, changing the ambient temperature can change the resonance frequency of the accelerometer, especially if the structural material of the accelerometer is sensitive to the temperature changes. This change can affect the sensitivity of the accelerometer. Moreover, due to the temperature change, sense capacitance value of the accelerometer can change, again resulting in a different capacitance sensitivity. As a result, accelerometer output loses its repeatability. This temperature change affects the performance of the accelerometer, and this problem can be solved with good packaging where it isolates the accelerometer from the changing environmental conditions. Another cause for the low bias instability is aging. Due to long operation times of the accelerometer, mechanical properties of the structural layer can change, resulting in a change at the output of the accelerometer. Aging is especially important for the resonant accelerometers, where mass of the accelerometer is continuously vibrating.

As a result, main consideration for an accelerometer is the selection of the process technology. The process technology plays an important role on all the critical performance considerations for an accelerometer ranging from selection of the structural material to the sensitivity of the accelerometer. Next important design consideration is the readout circuitry, where it plays an important role on the resolution of the accelerometer. Also, some of the drawbacks of the design can be eliminated with a force balance operation implemented together with readout circuitry. Finally, packaging is a must for stable and reliable operation of the accelerometer, which also increases the operation lifetime of the accelerometer.

4.2 Surface Micromachined Capacitive Accelerometer Design

As described in the previous section, the most important property of the accelerometer is the resolution. In order to increase the resolution of the accelerometer, its natural resonant frequency must be lowered, and also, the sense capacitance must be increased as much as possible. However, both of these design considerations depend on the fabrication process.

Moreover, since accelerometer designs are made before the optimization of the fabrication process, there are many different accelerometer layouts based on the same accelerometer structure. An example can be given for the spring designs, for achieving the maximum resolution, spring constant of the accelerometer should be as low as possible. However, minimum achievable spring constant in our process depends on the size of the springs and seismic mass size. Resolution of the lithography process defines the minimum width of the springs. On the other hand, material properties of the electroplated nickel define the maximum length of the springs. Therefore, some devices have 3 different spring lengths and widths.

Same considerations are also valid for the length and width of the comb fingers. In order to increase the sensitivity of the accelerometer, maximum sense capacitance value should be achieved. Therefore, for the comb finger type sense capacitances, overlap area of the rotor and stator fingers must be increased. Again, thickness of the structural nickel layer defines the height of the comb fingers, and overlap length is defined by the length of the comb fingers. If the length of the comb fingers is too long, and stress gradient of the structural nickel is high, comb fingers can buckle upwards resulting in a lower sense capacitance value. For this purpose, most of the devices utilizing comb finger sense capacitances have three different types of finger length. Another method to increase the sense capacitance value is to decrease the gap between the comb fingers. However, this depends on the resolution of the lithography process. For this purpose there are 3 different sense finger gaps; 3μm, 4μm, and 5μm for most of the accelerometer designs.

In conclusion, there are different designs of the same accelerometer topology. This provides to fabricate the best performance accelerometer, after the optimization of the fabrication process.

4.3 Surface Micromachined Capacitive Accelerometer Prototypes

This section describes the designed accelerometer prototypes for fabrication with surface micromachining process, which is described in Chapter 3, and it provides their critical dimensions, calculated and simulated resonant frequencies, and sense capacitance values. Moreover, it presents the figures showing fundamental and secondary resonant modes of the accelerometer designs.

We have designed 8 prototypes. These designs include the usage of different spring topologies and also different sense capacitances. There are several versions for each prototype. These versions have different spring lengths and widths, and also different comb finger gaps. There are a total of 65 different accelerometer designs. This provides the fabrication of the best performance accelerometer, after the optimization of the fabrication process. Resonant frequencies of the accelerometers are changing between 740 Hz and 5.27 kHz. Calculated sensitivities of the accelerometers based on the simulated resonant frequencies are ranging from 1 fF/g to 69 fF/g.

Resonant frequency simulations of the accelerometers are performed with a finite-element-simulator (FEM) called COVENTORWARE, a program specifically designed for MEMS applications. During the resonant frequency simulation of the accelerometer prototypes, fingers of the lateral accelerometers are neglected. This will introduce only a small error to the resonant frequency simulations, since contribution of these comb fingers to the total mass of the seismic mass is negligible. Table 4.1 shows the material properties of the structural nickel for the simulation and the calculation purposes.

Table 4.1 Material properties of electroplated nickel used in the simulations and calculations

Density (kg/m^3)	8908
Young's Modulus (GPa)	100
Poisson's ratio	0.3
Residual Stress (MPa)	0

4.3.1 Prototype-1

This prototype is a lateral accelerometer. It is based on the accelerometer structure in Figure 1.5, where folded spring structure is used instead of the clamped springs. Figure 4.1 shows the simplified diagram of the accelerometer structure and common dimensions for each version are indicated on the figure. Etch holes and comb fingers are not shown for the simplicity of the diagram. There are 3 different versions of the same structure having 3 different spring lengths. Each version can also be divided into two groups as, having conventional comb fingers and cross-over comb fingers. Each comb finger type has 2 different overlap lengths. For the optimization of the comb finger spacing in the process, 3 different comb finger gaps are used in the designs. Therefore, there are a total of 30 different accelerometers based on prototype-1 design.

Figure 4.2 and 4.3 shows the cross-over and conventional comb finger sensing schemes of lateral accelerometers. Other versions also have the same structures having different spring lengths. Thicknesses of all the devices are same and 16 µm. Moreover, anchor width and seismic mass width are same for all devices and denoted with the same letter. Table 4.2 gives the dimensions specific to each accelerometer. In the same table, calculated and simulated resonant frequencies of each version are also presented. During the calculation of the resonant frequencies, etch holes and fingers are not taken into account. Resonant frequency of this accelerometer can be found by calculating the total spring constant and inserting it into the Equation 2.35. Spring constant of the folded spring, equals to the half of the spring constant of a beam with same length. Total spring constant of the accelerometer can be calculated as;

$$k_{total} = 2\frac{E\,h\left(SW\right)^3}{\left(SL\right)^3} \tag{4.1}$$

where E is the Young's modulus, h is the thickness of the spring, SW is the width of the spring, and SL is the length of the spring. Based on the simulated resonant frequencies, capacitance sensitivity of the each version are also calculated and shown in Table 4.2.

Figure 4.4 shows the deflections of the accelerometer prototype in its fundamental and secondary resonant modes, and Table 4.3 compares the fundamental and secondary mode resonant frequencies. This is important to evaluate the cross-axis sensitivity of the accelerometer. It can be concluded from the Table 4.3 that mechanical cross-axis sensitivity of the structure is around 5 %. However, secondary resonant mode is along z-direction. Therefore, seismic mass motion in this direction does affect the sense capacitance mismatch of the accelerometer. Thus, cross-axis sensitivity of the accelerometer is expected to be much lower than 5 %.

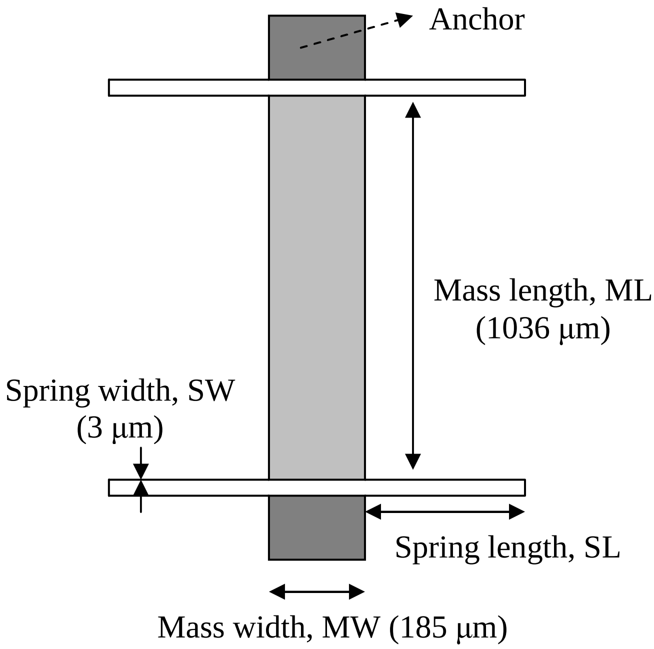

Figure 4.1 Simplified structure of the prototype-1. Comb fingers and etch holes are not shown.

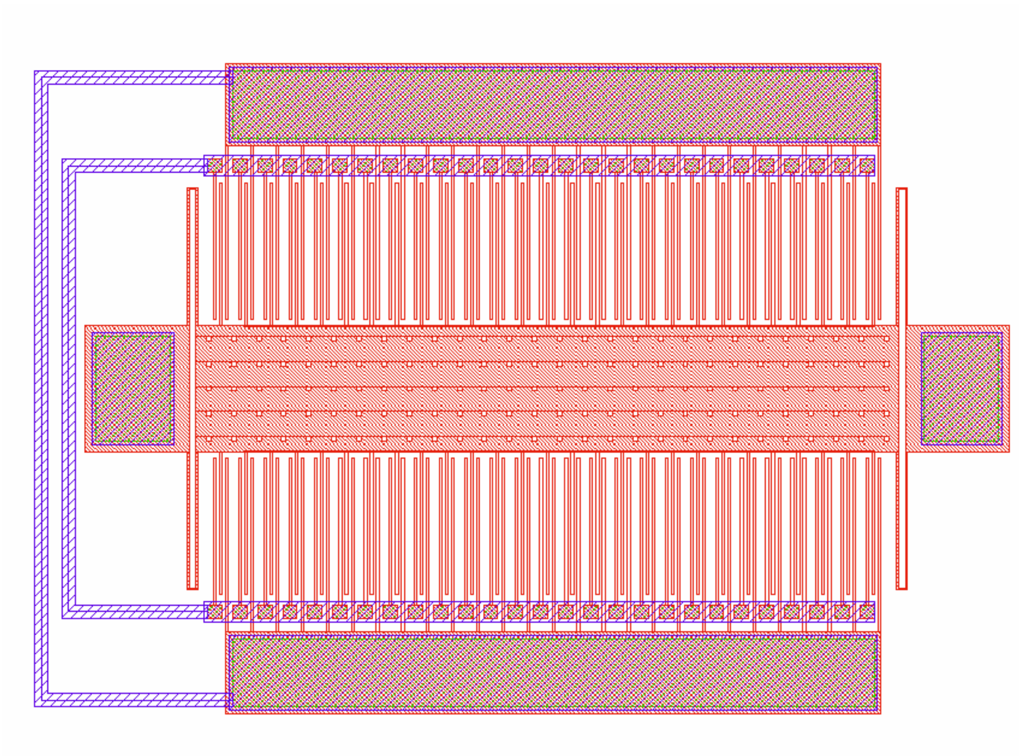

Figure 4.2 Layout of prototype-1 having cross-over comb finger sensing scheme.

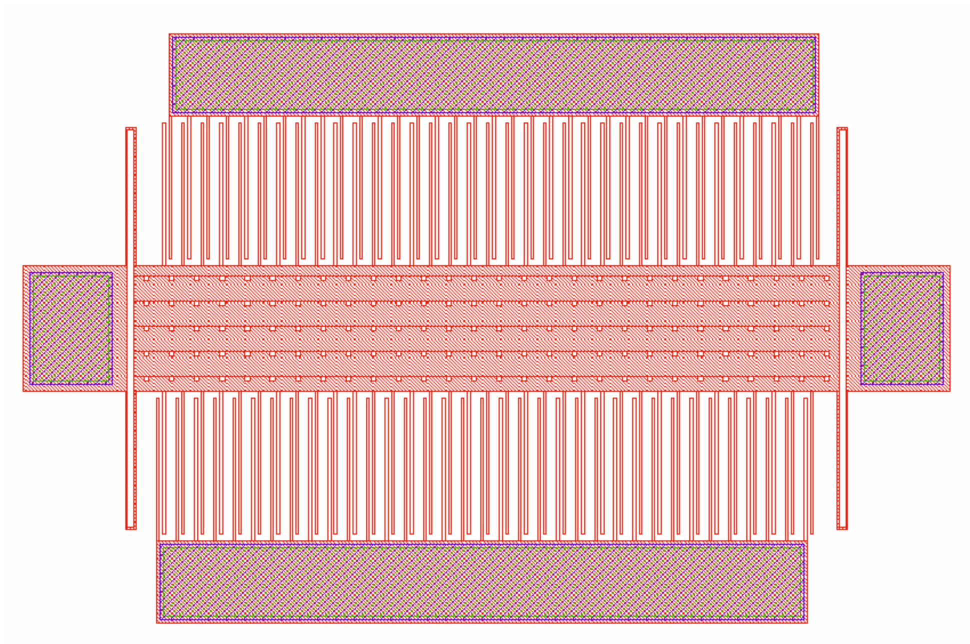

Figure 4.3 Layout of prototype-1 having conventional comb finger sensing scheme.

Table 4.2 Dimensions and performance values of the each version of prototype-1. “FOL” refers to the overlap length of the comb fingers, “FS” refers to the spacing between the rotor and stator fingers, “SC” refers to the sense capacitance value. Capacitance sensitivity calculation is based on the simulated resonant frequency. Finger type 1 corresponds to conventional comb finger structure and type 2 corresponds to the crossover comb finger structure.

	Resonant Frequency (kHz)		**Finger Type**	**FOL (µm)**	**FS (µm)**	**Total SC (fF)**	**Capacitance Sensitivity (fF/g)**
	Calc.	**Sim.**					
Ver.1 SL=200µm	3.165	3.118	1	90	4	223	1.42
					5	178.4	0.91
				200	4	495.6	3.16
					5	396.4	2.02
			2	90	3	509.8	4.34
					4	382.4	2.44
					5	305.8	1.56
				200	3	1019.6	8.67
					4	764.6	4.88
					5	611.6	3.12
Ver.2 SL=300µm	1.722	1.708	1	90	4	223	4.74
					5	178.4	3.03
				200	4	495.6	10.54
					5	396.4	6.74
			2	90	3	509.8	14.4
					4	382.4	8.13
					5	305.8	5.20
				200	3	1019.6	28.92
					4	764.6	16.27
					5	611.6	10.41
Ver.3 SL=400µm	1.118	1.102	1	90	4	223	11.40
					5	178.4	7.29
				200	4	495.6	25.32
					5	396.4	16.20
			2	90	3	509.8	34.73
					4	382.4	19.54
					5	305.8	12.50
				200	3	1019.6	69.47
					4	764.6	39.07
					5	611.6	25.00

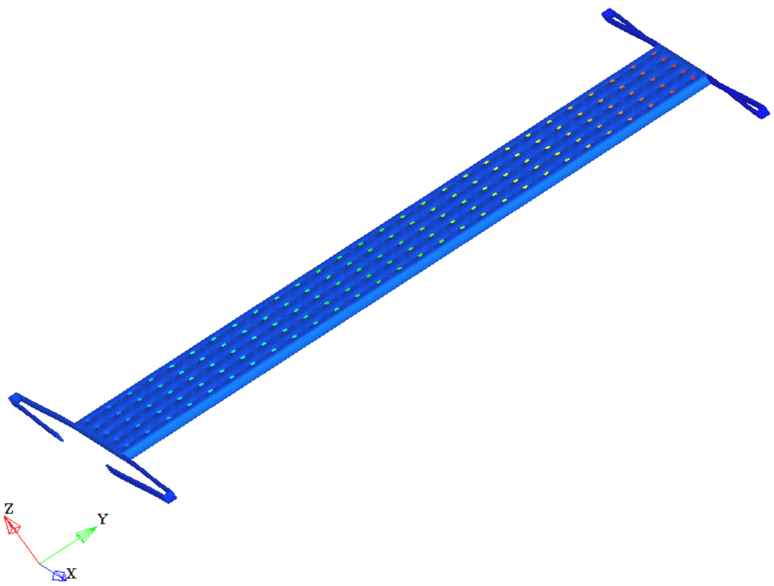

(a)

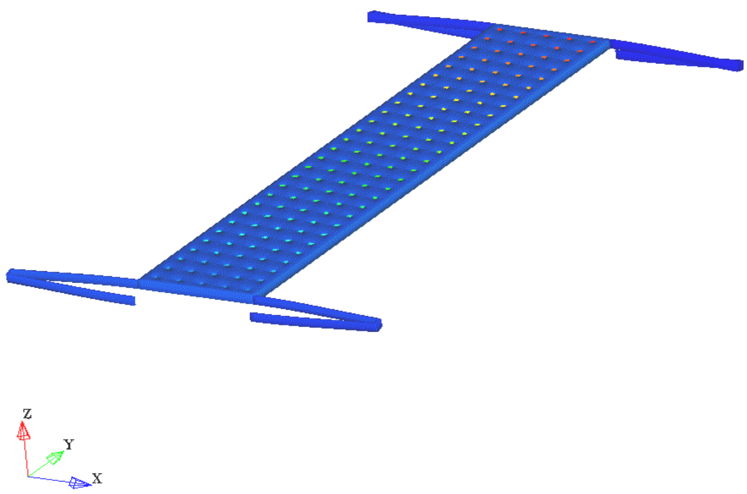

(b)

Figure 4.4 Two resonant modes of the prototype-1, (a) fundamental resonant mode (in y-direction), (b) secondary resonant mode (in z-direction).

Table 4.3 Fundamental mode and secondary mode resonant frequencies of different versions of prototype-1.

	Fundamental Mode Frequency (kHz)	Secondary Mode Frequency (kHz)	Ratio of Spring Constants.
Version 1	3.118	11.752	0.0703
Version 2	1.708	7.070	0.0584
Version 3	1.102	4.817	0.0523

4.3.2 Prototype-2

This prototype is a lateral accelerometer structure having varying-area type comb fingers. Figure 4.4 shows the simplified diagram of the accelerometer structure. This structure also utilizes folded type springs. There are 2 different versions of the same structure with different finger lengths and different overlap lengths. For each version 3 different finger gaps are used to fabricate the highest performance device after the optimization of the fabrication process. All versions have the same dimensions, except the finger length and finger overlap length. There are a total of 6 accelerometer based on prototype-2.

Figure 4.6 shows the layout of the prototype-2 for a specific device version. Other versions of prototype-2 group also have the same layout with different comb finger overlap lengths and gaps. Table 4.4 gives the calculated and simulated fundamental mode resonant frequency of prototype-2 and based on the simulated resonant frequency, capacitance sensitivity of each device is calculated. Equation 4.2 that gives the spring constant formula is used for the calculation of the resonant frequency, where E is the Young's modulus, h is the thickness of the device (for the definitions of other variables refer to Figure 4.5). Finally, for the evaluation of cross-axis sensitivity, Table 4.5 gives the resonant frequencies of fundamental and secondary mode of prototype-2, where Figure 4.7 (a) and (b) show deflection of the seismic mass in these modes.

$$k_{total} = 4\frac{E\,h\,SW^{3}}{\left(SL_1^{\;3} + SL_2^{\;3}\right)} \tag{4.2}$$

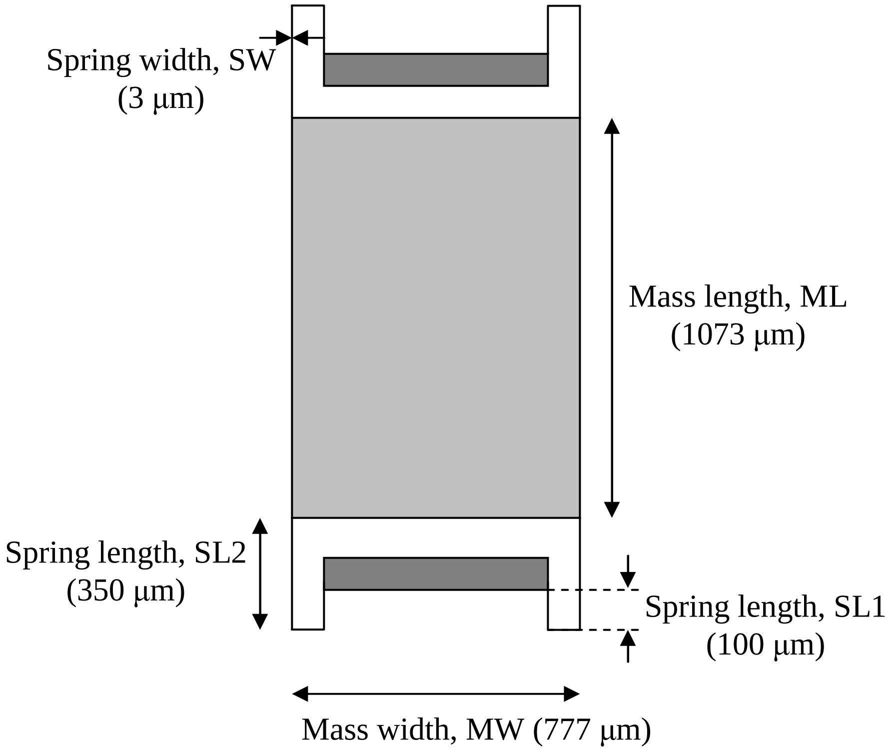

Figure 4.5 Simplified diagram of the prototype-2. Comb fingers and etch holes are not shown.

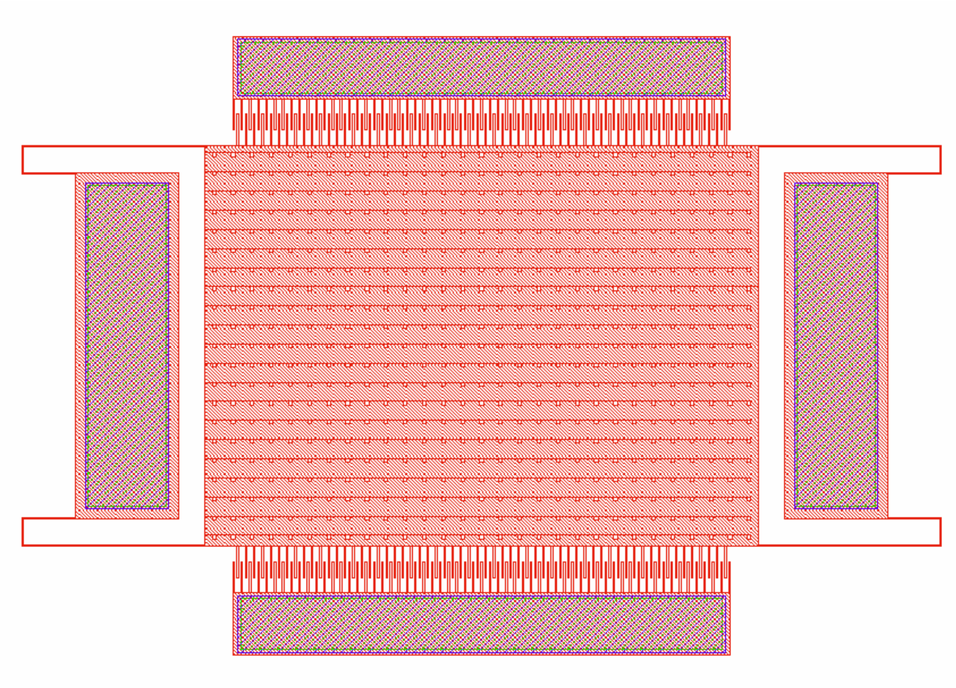

Figure 4.6 Layout of prototype-2 for a specific device version. Other versions of prototype-2 group have different finger lengths and finger overlap lengths.

Table 4.4 Dimensions and performance values of the each version of prototype-2. “FL” refers to the finger length, “FOL” refers to the overlap length of the comb fingers, and “FN” corresponds to the finger number on the seismic mass. “FS” refers to the spacing between the rotor and stator fingers, and “SC” refers to the sense capacitance value. Capacitance sensitivity calculation is based on the simulated resonant frequency.

	Resonant Frequency (Hz)		FL (µm)	FOL (µm)	FN	FS (µm)	Total SC (fF)	Capacitance Sensitivity (fF/g)
	Calc.	Sim.						
Ver.1	916.3	866.7	30	10	160	3	151	4.99
				10	138	4	97.7	3.23
				10	120	5	68	2.25
Ver.2	916.3	866.7	60	30	160	3	453	4.99
				30	138	4	293	3.23
				30	120	5	204	2.25

Table 4.5 Fundamental and secondary mode resonant frequencies of prototype-2.

	Fundamental Mode Frequency (Hz)	Secondary Mode Frequency (kHz)	Ratio of Spring Constants.
Prototype-2	866.7	2326	0.1388

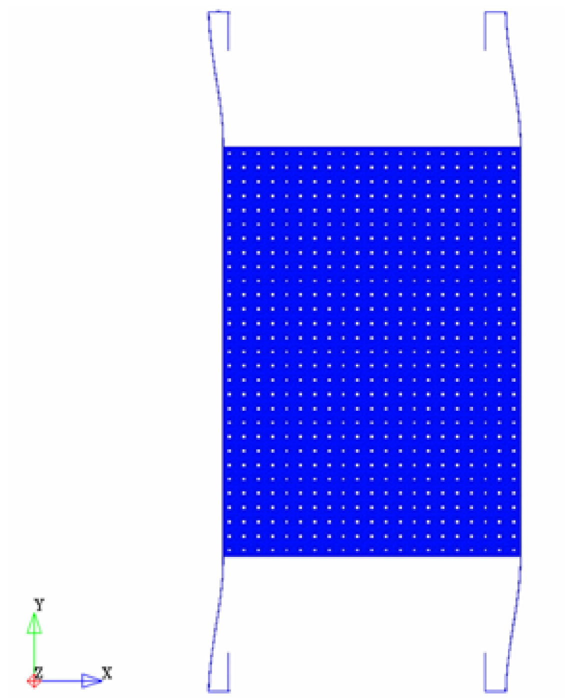

(a)

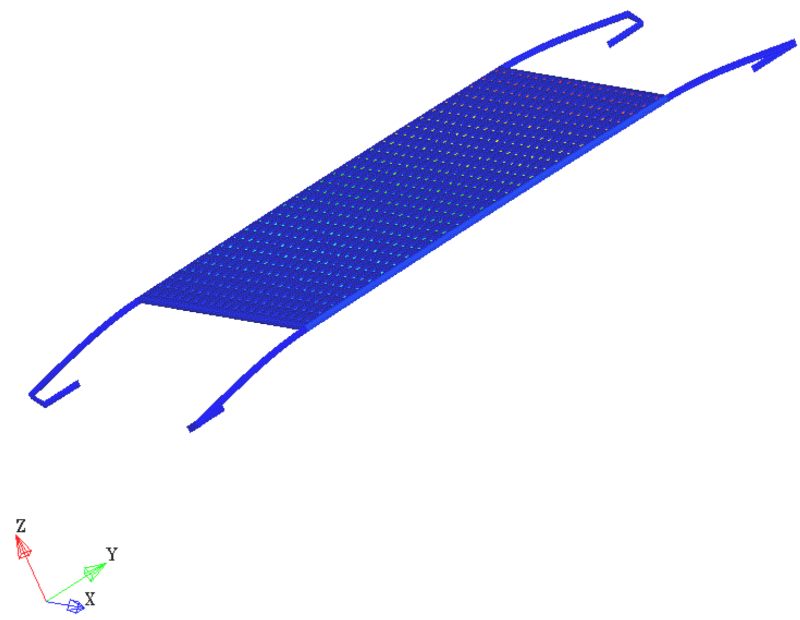

(b)

Figure 4.7 Two resonant modes of prototype-2, (a) fundamental mode in x direction, (b) secondary mode in z-direction.

4.3.3 Prototype-3

This structure is a lateral accelerometer having varying area type comb fingers. Figure 4.8 shows the simplified diagram of the prototype-3, where etch holes and fingers are not shown. This prototype utilizes clamped type springs. Moreover, seismic mass of this prototype is large in order to decrease the Brownian noise floor. This accelerometer structure has 2 different versions having different finger length and finger overlap lengths. Similar to the other prototypes, this prototype has also 3 different finger gaps for each version. There are six versions of this prototype group.

Figure 4.9 shows the layout of protype-3 for a specific version. Table 4.6 gives the calculated and the simulated fundamental mode resonant frequencies of each version. Capacitance sensitivity of the different versions are calculated based on the simulated resonant frequencies. Equation 4.3 is used for the calculation of the total spring constant. Moreover, Table 4.7 is provided for the comparison of the cross-axis sensitivity. Figure 4.10 (a) and (b) shows the displacement of the seismic mass in fundamental and secondary modes.

$$k_{total} = 4\frac{E\,h\,SW^3}{SL^3} \tag{4.3}$$

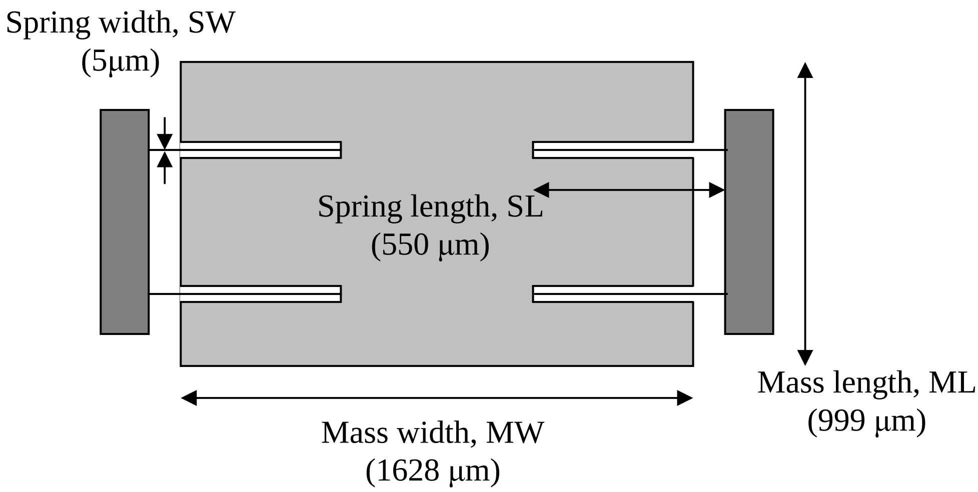

Figure 4.8 Simplified diagram of prototype-3. Etch holes and fingers are not shown.

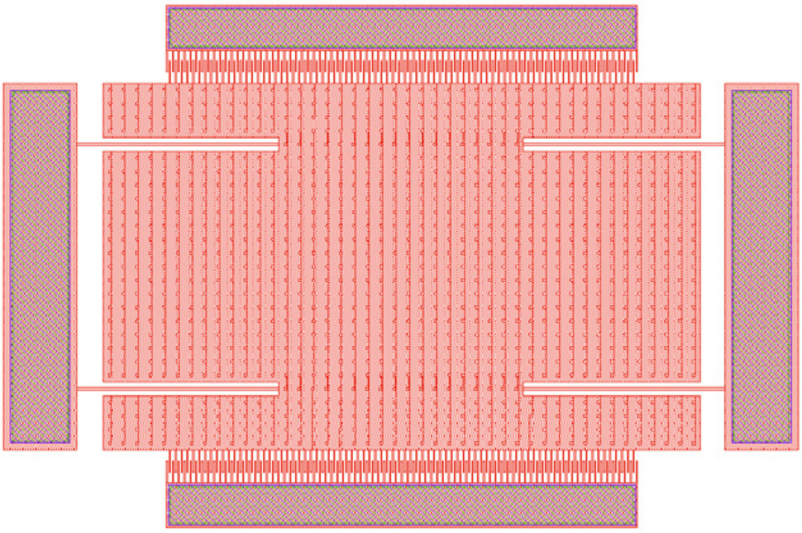

Figure 4.9 Layout of prototype-3 for a specific device version.

Table 4.6 Dimensions and performance values of the each version of prototype-3. "FL" refers to the finger length, "FOL" refers to the overlap length of the comb fingers, "FN" refers to the finger number on the seismic mass, "FS" refers to the spacing between the rotor and stator fingers, and "SC" refers to the sense capacitance value. Capacitance sensitivity calculation is based on the simulated resonant frequency.

	Resonant Frequency (Hz)		FL (µm)	FOL (µm)	FN	FS (µm)	Total SC (fF)	Capacitance Sensitivity (fF/g)
	Calc.	Sim.						
Ver.1	740	743	30	10	214	3	202	9.08
				10	184	4	130	5.86
				10	162	5	91.7	4.13
Ver.2	740	743	60	50	214	3	1010	9.08
				50	184	4	651	5.86
				50	162	5	458	4.13

Table 4.7 Fundamental and secondary mode resonant frequencies of prototype-3.

	Fundamental Mode Frequency (Hz)	Secondary Mode Frequency (kHz)	Ratio of Spring Constants.
Prototype-2	743	2362	0.099

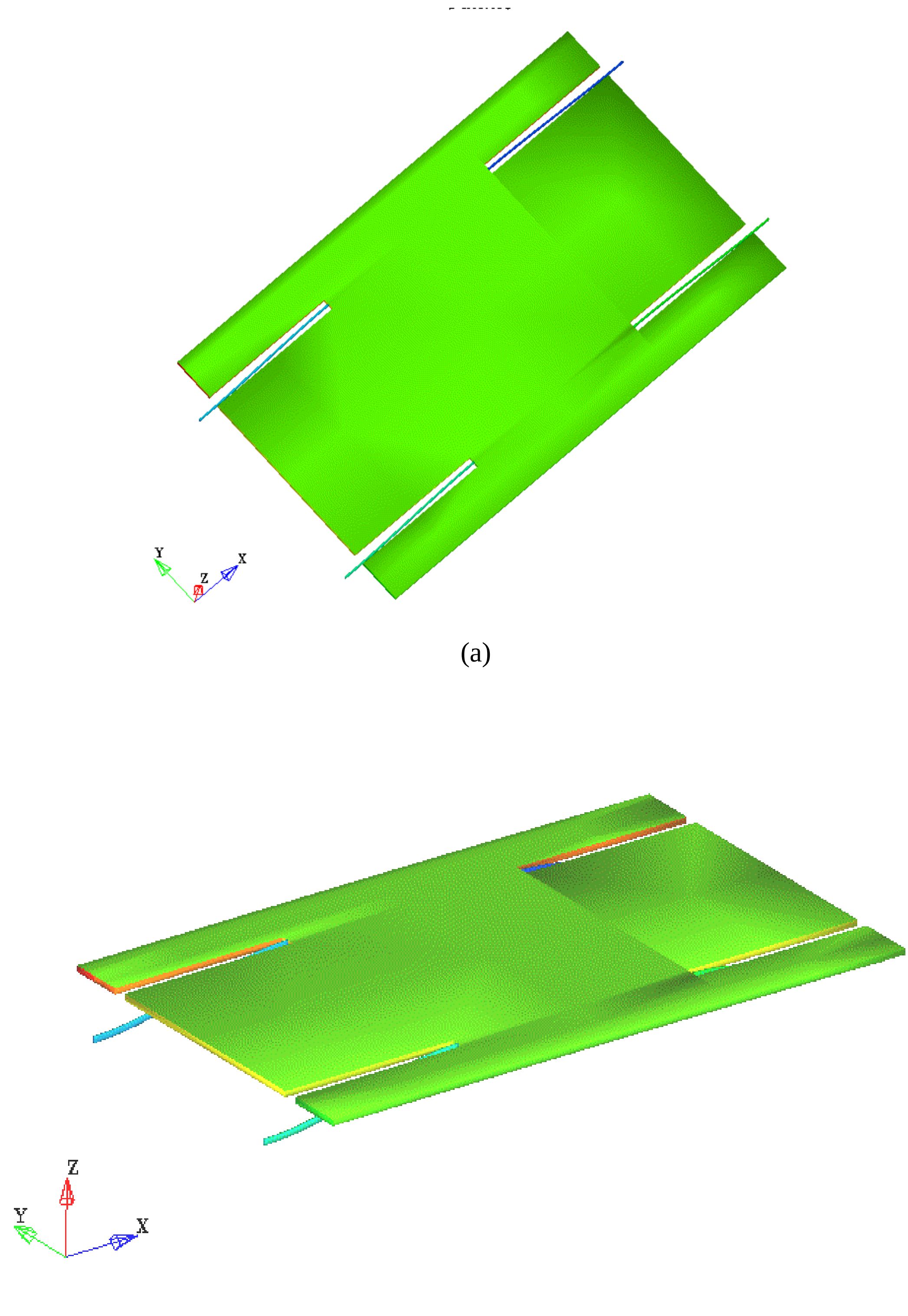

(a)

(b)

Figure 4.10 Two resonant modes of prototype-2, (a) fundamental mode in x-direction, (b) secondary mode in z-direction.

4.3.4 Prototype-4

Prototype-4 is a lateral accelerometer having varying-gap type comb fingers. Figure 4.11 shows the simplified structure of prototype-4. Prototype utilizes folded springs in order to prevent the effects of the residual stress on the resonant frequency. There are two different versions of the same prototype. Difference between the two versions is the structure of the comb fingers. Version 1 has conventional comb fingers and version 2 has cross-over type comb fingers. Cross-over comb fingers have three different gaps, where as conventional comb fingers have two different.

Figure 4.12 (a) and (b) shows the layout of the two different versions. Table 4.8 gives the details of the performance values of each prototype based on the simulated fundamental mode resonant. Resonant frequency of the structure can be calculated from Equation 4.1. Finally, Table 4.9 compares the simulated resonant frequencies of the fundamental and secondary modes, where Figure 4.13 (a) and (b) show these modes.

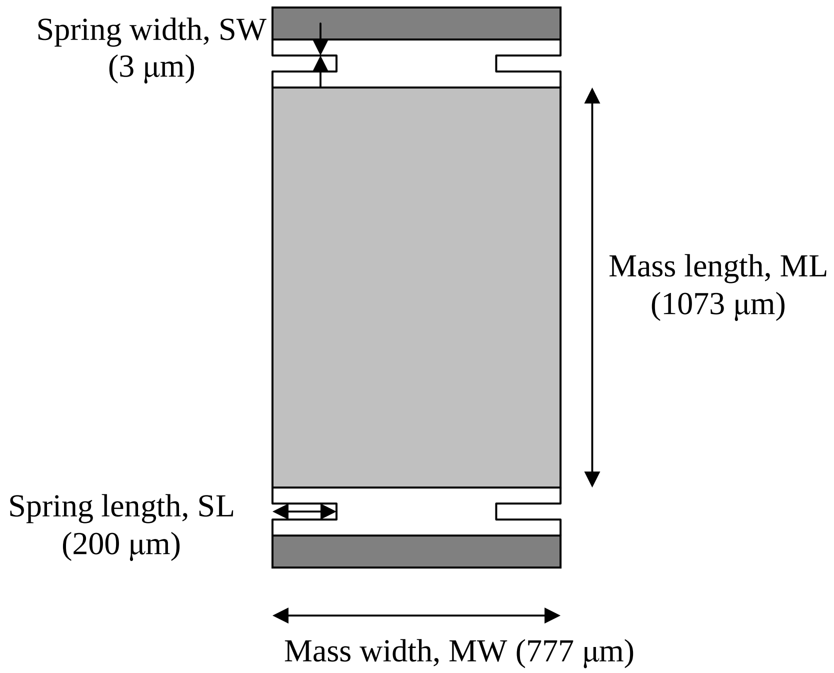

Figure 4.11 Simplified diagram of prototype-4. Etch holes and fingers are not shown.

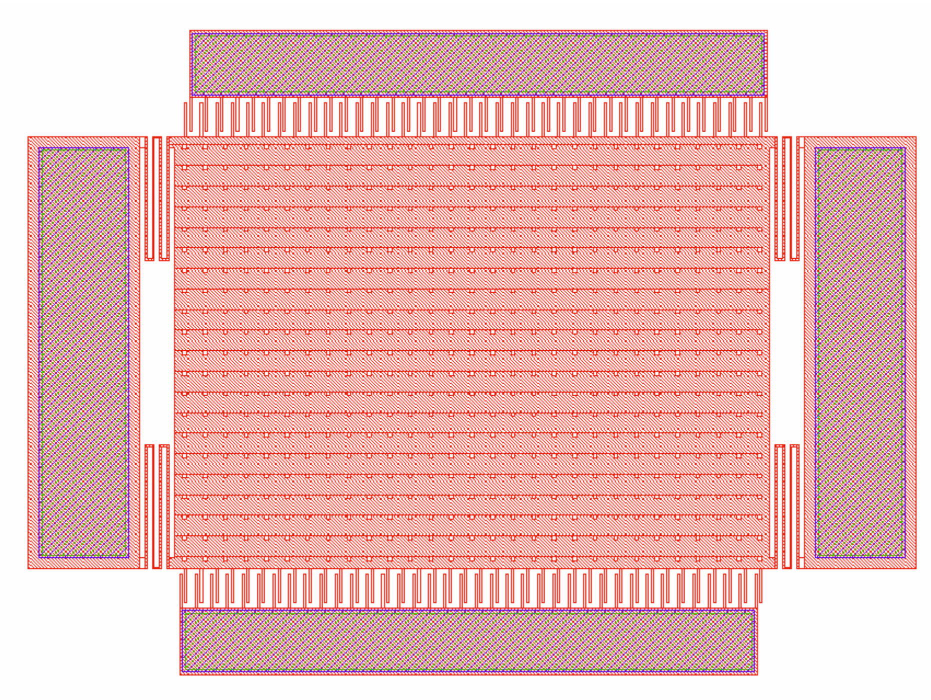

(a)

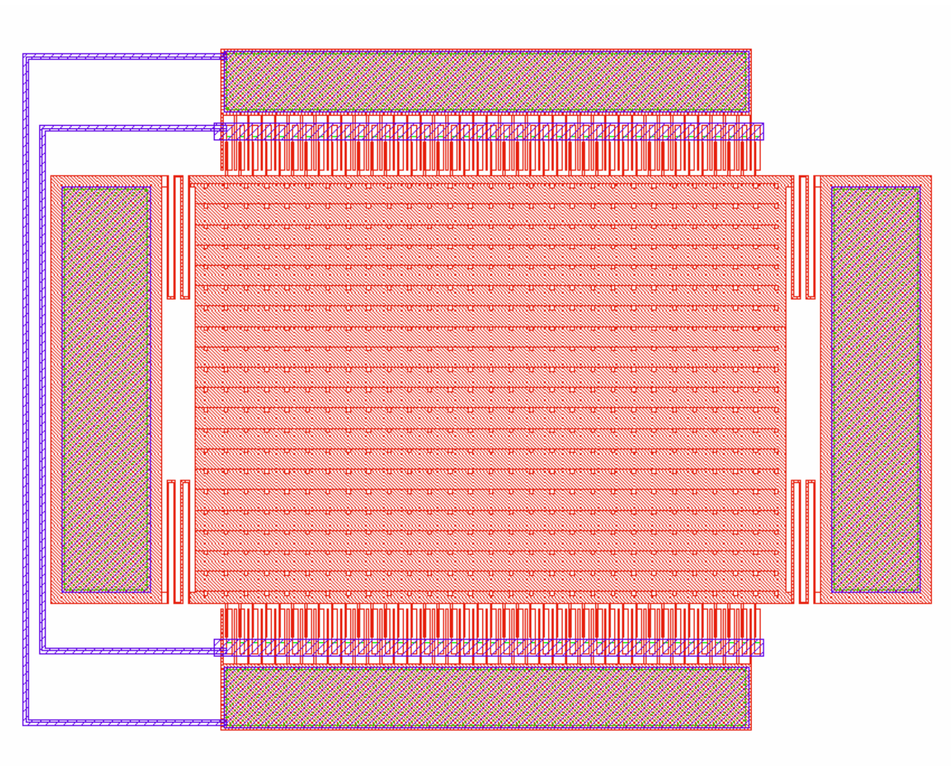

(b)

Figure 4.12 Layouts of two different versions of prototype-4, (a) structure utilizes conventional comb fingers (version 1), (b) structure utilizes cross over comb fingers (version 2).

Table 4.8 Dimensions and performance values of the each version of prototype-4. "FOL" refers to the overlap length of the comb fingers, "FN" refers to the finger number on the seismic mass, "FS" refers to the spacing between the rotor and stator fingers, and "SC" refers to the sense capacitance value. Capacitance sensitivity calculation is based on the simulated resonant frequency.

	Resonant Frequency (kHz)		FOL (µm)	FN	FS (µm)	Total SC (fF)	Capacitance Sensitivity (fF/g)
	Calc.	Sim.					
Ver.1	1.517	1.487	50	76	4	135	3.64
				76	5	107	2.31
Ver.2	1.517	1.487	50	82	3	194	6.97
				82	4	145	3.85
				82	5	116	2.46

Table 4.9 Fundamental and secondary mode resonant frequencies of prototype-4.

	Fundamental Mode Frequency (kHz)	Secondary Mode Frequency (kHz)	Ratio of Spring Constants.
Prototype-4	1.4870	5.2836	0.079

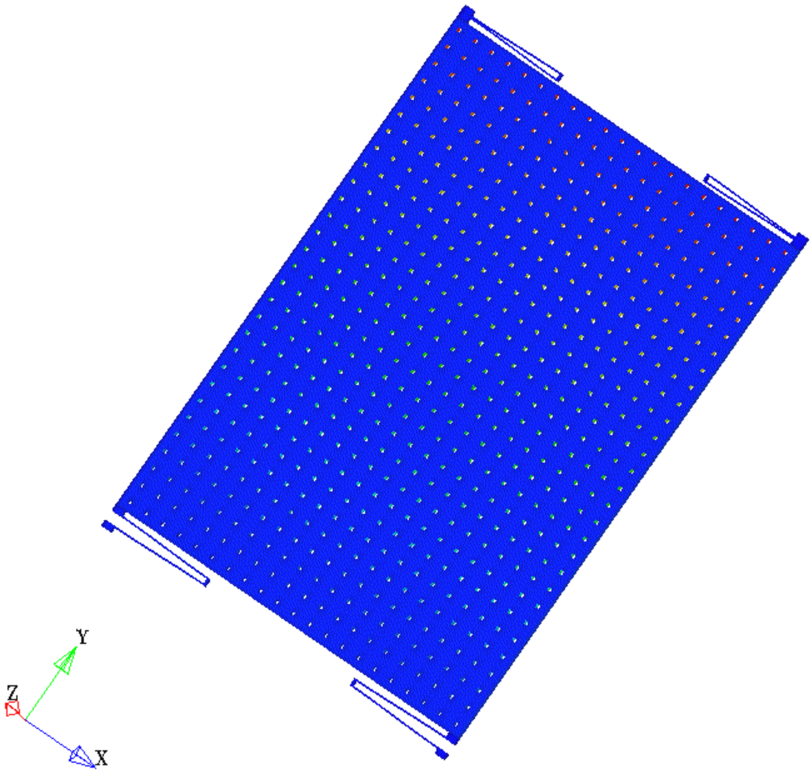

(a)

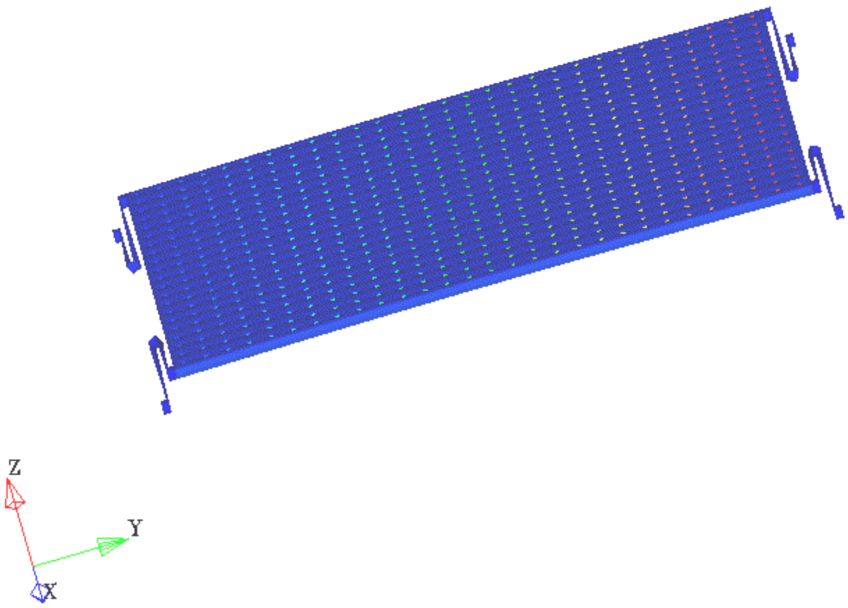

(b)

Figure 4.13 Deflection of the seismic mass of prototype-4 in, (a) fundamental mode in x-direction, (b) secondary mode in z-direction

4.3.5 Prototype-5

This prototype has similar structure with Prototype-4, but folded springs have more turns in order to lower the resonant frequency of the accelerometer. Again, there are two different versions of this prototype. Figure 4.15 shows the simplified schematic, and Figure 4.16 (a) and (b) shows the layouts of two different versions.

Table 4.10 compares the simulated and calculated resonant frequencies, and based on the simulated resonant frequencies, capacitance sensitivity of each version of prototype-5 is calculated. Spring constant of the device is 1/4 of the spring constant of prototype-2, which is expressed by Equation 4.2 (For the definitions of the variables refer to Figure 4.14). Table 4.11 gives the fundamental and secondary mode resonant frequencies of the prototype-4, where these modes are shown in Figure 4.17 (a) and (b).

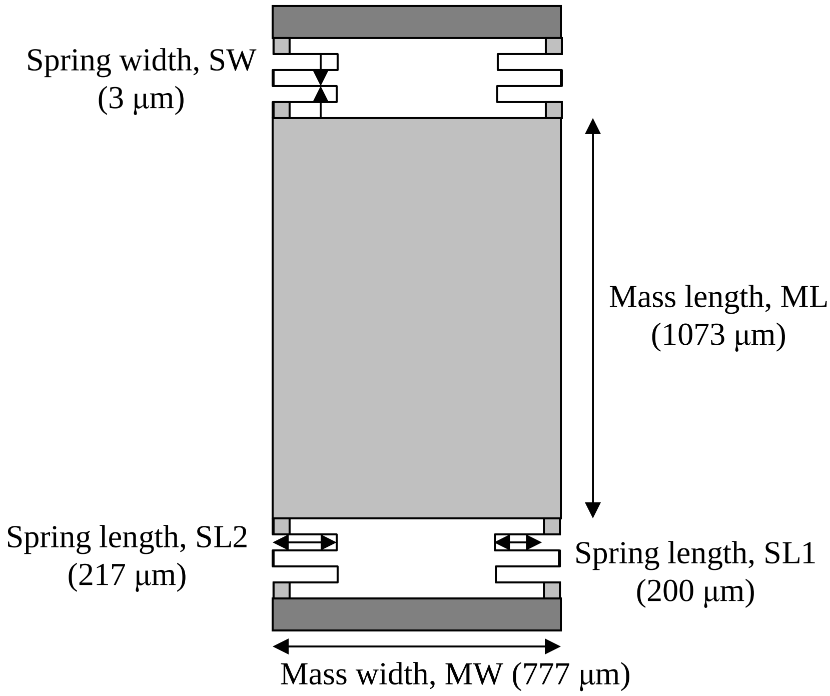

Figure 4.14 Simplified diagram of prototype-5. Etch holes and fingers are not shown.

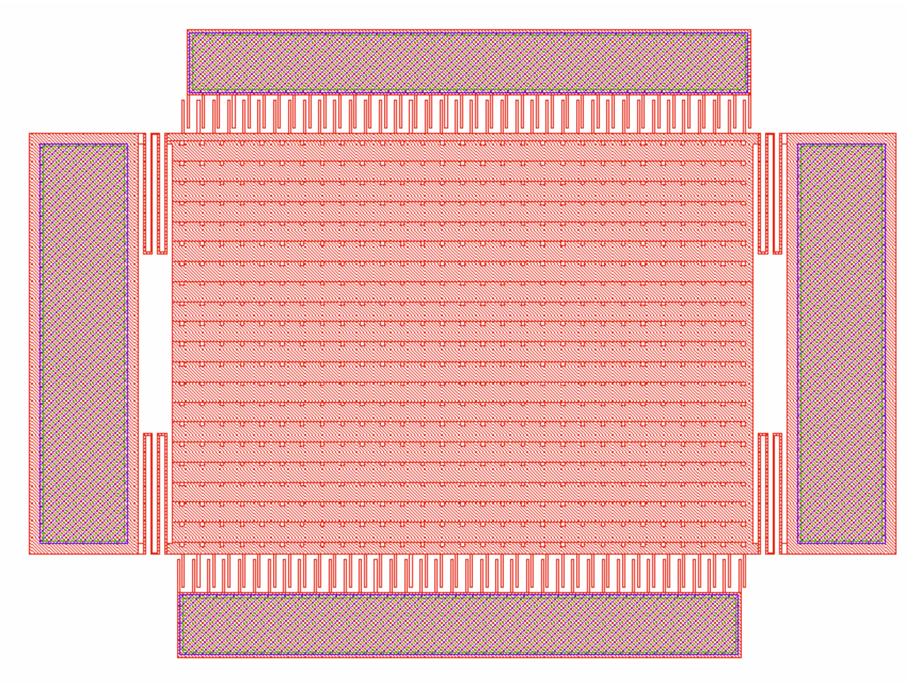

(a)

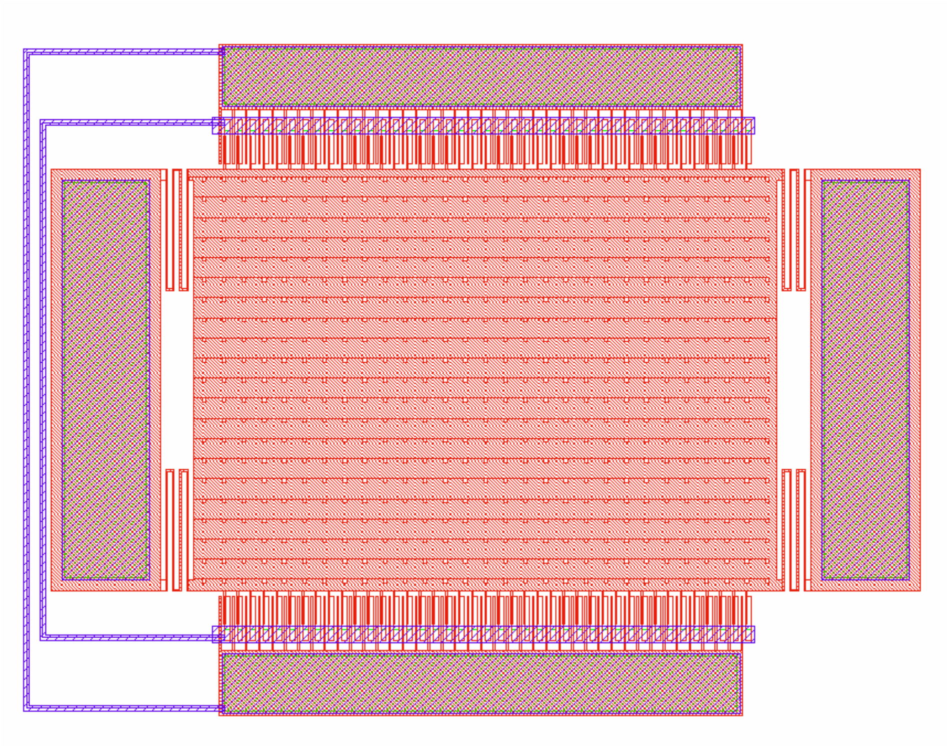

(b)

Figure 4.15 Layouts of two different versions of prototype-5, (a) conventional comb fingers (version 1), (b) cross over comb fingers (version 2).

Table 4.10 Dimensions and performance values of the each version of prototype-5. FOL" refers to the overlap length of the comb fingers, "FN" refers to the finger number on the seismic mass, "FS" refers to the spacing between the rotor and stator fingers, and "SC" refers to the sense capacitance value. Capacitance sensitivity calculation is based on the simulated resonant frequency.

	Resonant Frequency (kHz)		FOL (µm)	FN	FS (µm)	Total SC (fF)	Capacitance Sensitivity (fF/g)
	Calc.	Sim.					
Ver.1	1005	962.9	50	76	4	134	9.05
				76	5	108	5.28
Ver.2	1005	962.9	50	82	3	194	17.27
				82	4	145	9.71
				82	5	116	6.21

Table 4.11 Fundamental and secondary mode resonant frequencies of prototype-5.

	Fundamental Mode Frequency (Hz)	Secondary Mode Frequency (kHz)	Ratio of Spring Constants.
Prototype-5	962.9	2.7476	0.112

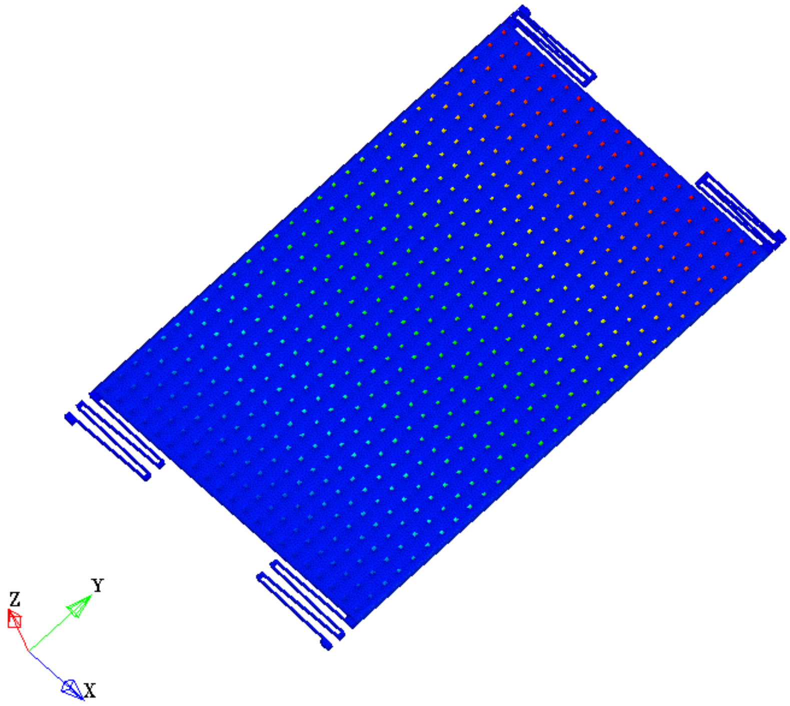

(a)

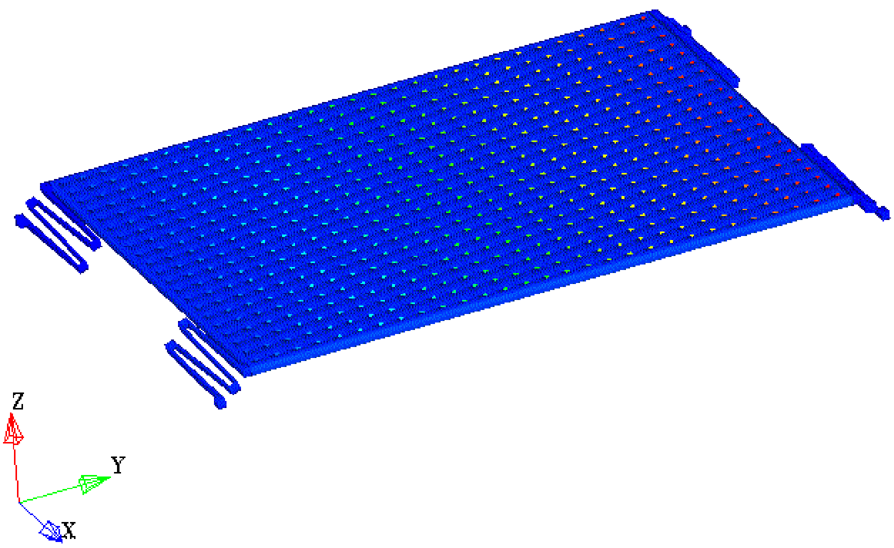

(a)

Figure 4.16 Deflection of seismic mass of prototype-5 in, (a) fundamental mode in y-direction, (b) secondary mode in z-direction.

4.3.6 Prototype-6

This prototype is a lateral accelerometer structure having folded-type springs. Figure 4.17 shows the simplified diagram of the prototype-6 and operation principle. This structure utilizes the gold metal-lines under the seismic mass for differential sensing. Sense capacitances are formed between the gold metal lines beneath the seismic mass and the lateral bars on the seismic mass. Varying-area comb fingers on the seismic mass can be used for force-feedback operation. This prototype has 3 versions, having 3 different spring width. Each version has 2 different bar width in order to fabricate highest possible sense capacitance. Figure 4.18 shows the layouts of two versions of prototype-6 having two different bar widths. Other versions differ in terms of spring widths. There are a total of six different accelerometers based on prototype-6 design.

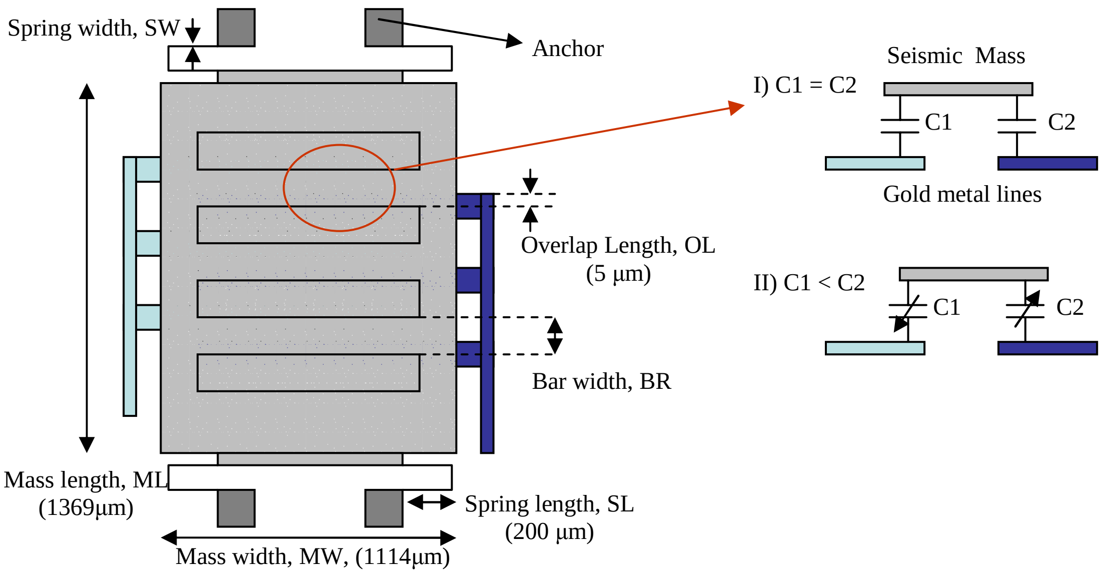

Figure 4.17 Simplified diagram of prototype-6, and capacitance change under acceleration.

Table 4.12 shows the simulated resonant frequencies of each prototype. It also gives the capacitance sensitivity of each device. Sacrificial layer thickness is assumed to be 4 µm for the calculation of total sense capacitance and capacitance sensitivity. Spring constants of the fundamental and secondary modes need to be compared for the determination of the cross-axis sensitivity, where Figure 4.19 (a) and (b) shows these modes. However, as can be seen from the simulations of the fundamental and secondary modes, effective masses of two modes are not equal. Therefore, for the calculation of the spring constants, simulated effective masses are considered. Table 4.13 shows the simulated resonant frequencies and effective masses in these two modes, and ratio of the spring constants.

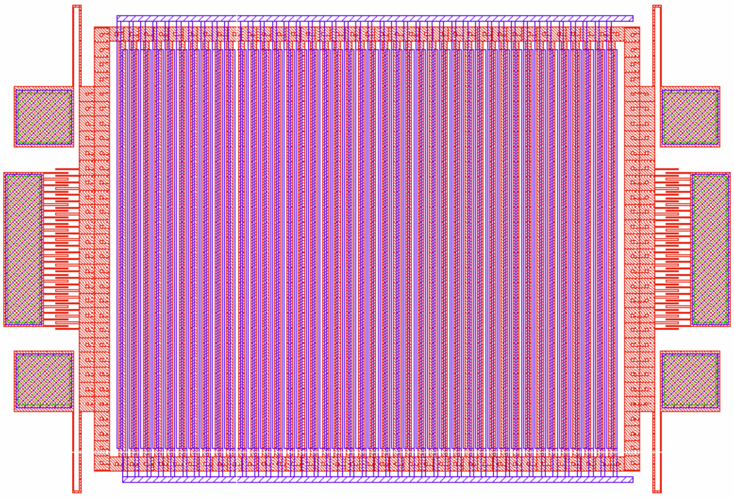

(a)

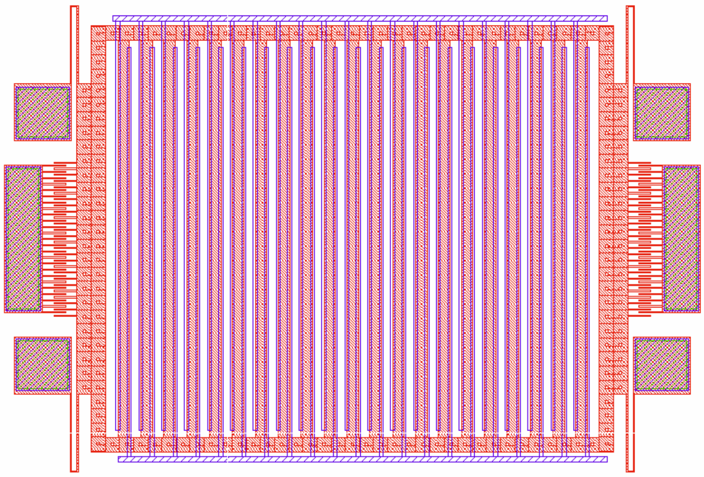

(b)

Figure 4.18 Layouts of two different structures of a version, (a) thin capacitance bars resulting in higher sense capacitance, (b) thick capacitance bars.

Table 4.12 Dimensions and performance values of the each version of prototype-6. "SW" refers to the spring width, "BW" refers to the bar width, and "SC" refers to the calculated capacitance sensitivity based on the simulated resonant frequencies.

	Resonant Frequency (kHz)	SW (μm)	BW (μm)	Metal Line #	Total SC (fF)	Capacitance Sensitivity (fF/g)
Ver.1	1.399	3	15	2x42	948	30.1
			30	2x21	474	15.0
Ver.2	2.139	4	15	2x42	948	12.9
			30	2x21	474	6.43
Ver.3	2.969	5	15	2x42	948	6.67
			30	2x21	474	3.34

Table 4.13 Ratio of spring constants of each version for determining of the cross-axis sensitivity. Spring constant calculations for each mode are based on the simulated effective masses.

	Resonant Frequency (kHz)	Effective Mass (kg)	Secondary Mode (kHz)	Effective Mass (kg)	Ratio of Spring Constants
Ver.1	1.399	1.278e-7	3.203	7.644e-8	0.31
Ver.2	2.139	1.278e-7	3.501	7.071e-8	0.67
Ver.3	2.969	1.278e-7	3.683	6.769e-8	1.22

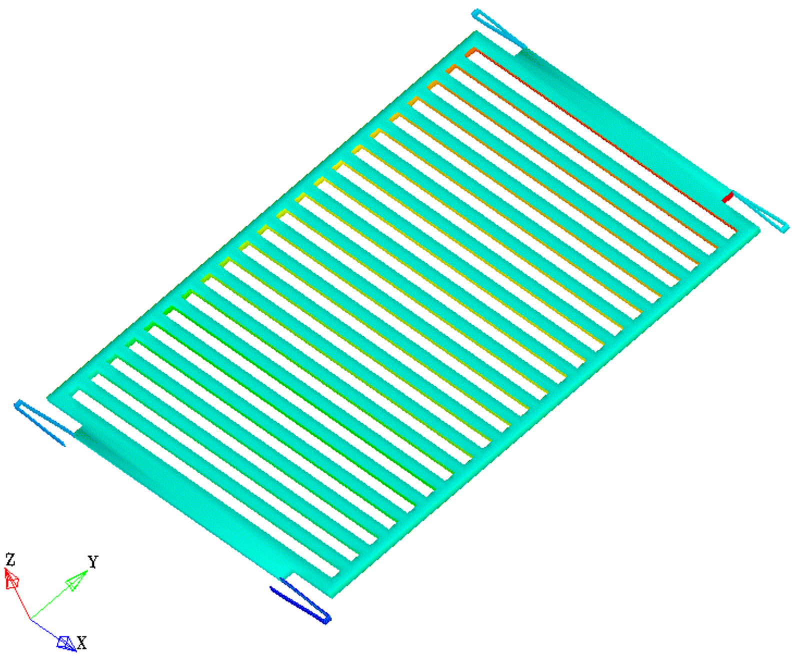

(a)

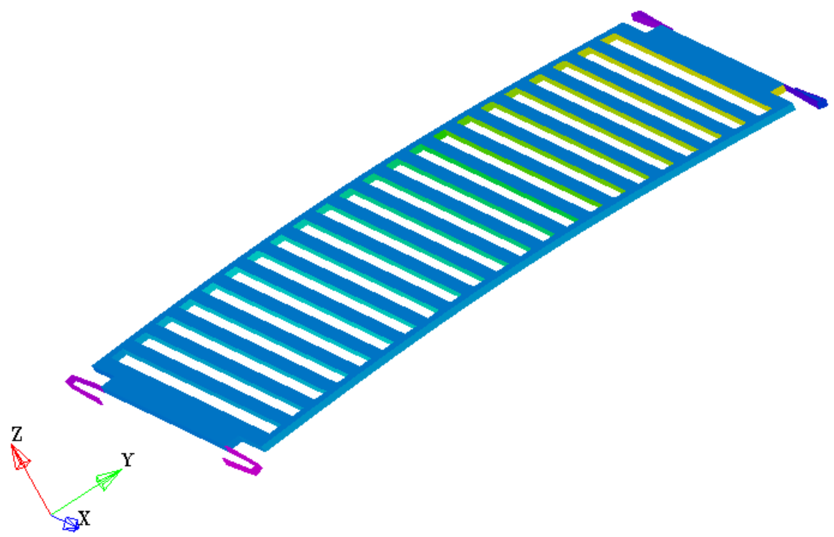

(b)

Figure 4.19 Two resonant modes of prototype-6, (a) fundamental mode y-direction, (b) secondary mode in z-direction.

4.3.7 Prototype-7

This prototype is z-axis (out-of-plane) accelerometer using clamped type springs. Figure 4.20 shows the simplified diagram of the accelerometer structure. Sense capacitance is formed between the seismic mass and the gold metal electrode beneath the seismic mass. A reference capacitor having the same capacitance with the sensor is formed between the seismic mass and metal electrode for reading the capacitance change. Since nickel layer of the reference capacitor is very stiff in the sense direction of the sensor, its capacitance does not change under acceleration. Therefore, change in the sense capacitance can be extracted by comparing the sensor capacitance and the reference capacitor. There are two versions of this prototype, having two different spring widths. Figure 4.21 shows the layout of prototype-7 for a specific version. Only difference between the versions is the width of the springs.

Table 4.14 summarizes the calculated and the simulated resonant frequencies of these two versions. Spring constant of the structure can be calculated using the following equation;

$$k_{total} = 4\frac{E\,SW\,h^3}{SL^3} \tag{4.4}$$

where E is the Young's modulus, SW is the spring width, SL is the spring length, and h is the thickness which is 16 μm. Capacitance sensitivity of each version is also given based on the simulated resonant frequencies. During the calculations sacrificial layer thickness is assumed to be 4 μm.

The cross-axis sensitivity of the device is minimized by suppressing the motion of the seismic mass in the lateral direction with the orthogonal alignment of the springs. Simulation results show that lateral motion of the seismic mass is not in the first three resonant modes. Table 4.15 shows the resonant frequencies of first three resonant modes, and Figure 4.22 (a)-(c) show the motion of the seismic mass in these modes. Note that deflection of the seismic mass in orthogonal direction is the secondary resonant mode.

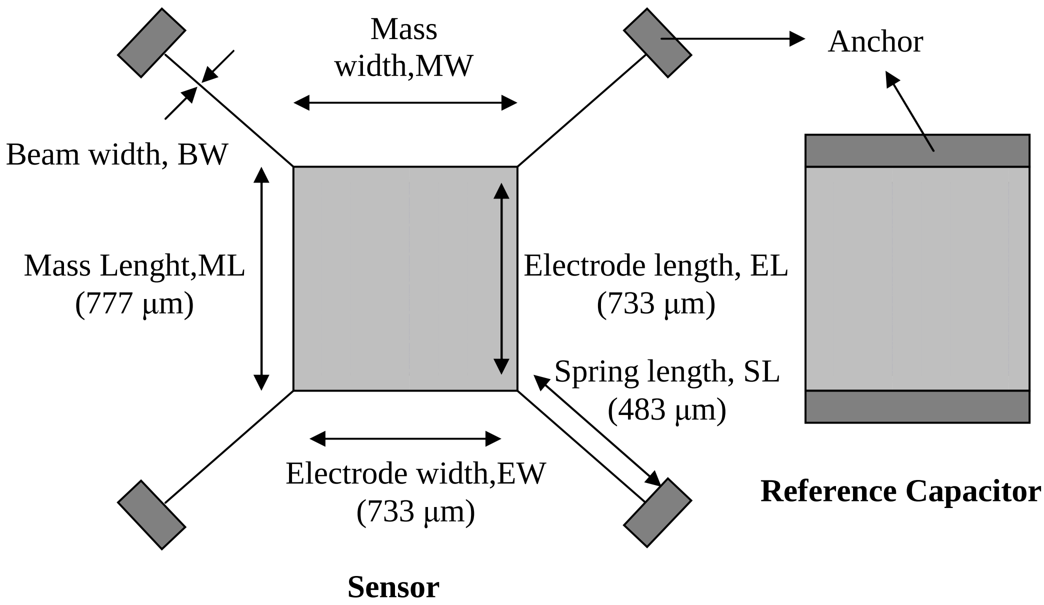

Figure 4.20 Simplified diagram of prototype-7, showing the sensor and the reference capacitor.

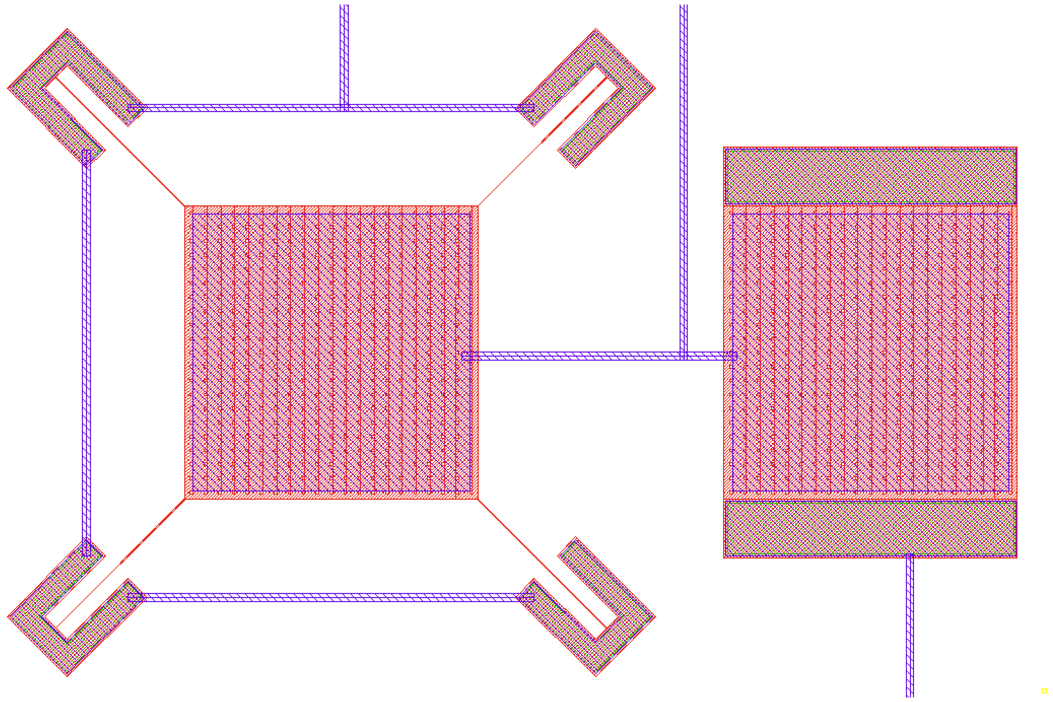

Figure 4.21 Layout of prototype-7, sensor having out-of-plane sensitive axis (left), reference capacitor (right).

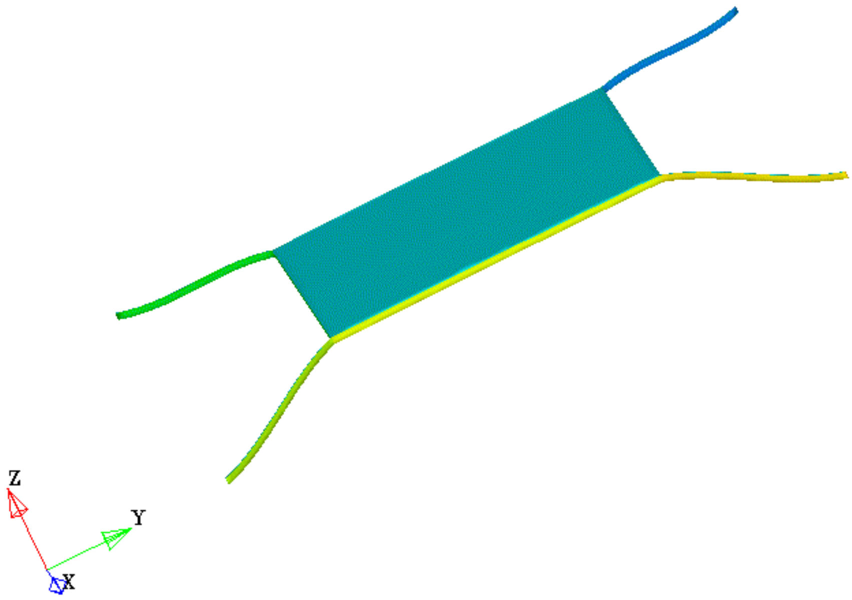

(a)

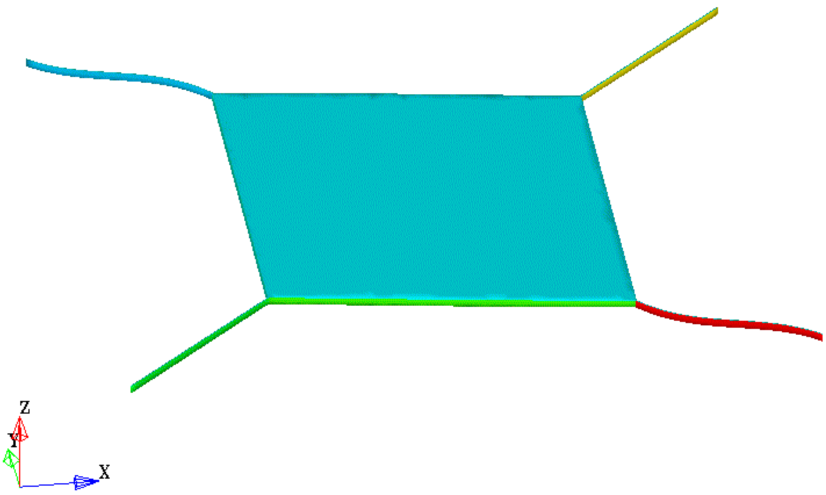

(b)

Figure 4.22 Two resonant modes of the prototype-7, (a) secondary resonant mode in z-direction, (b) third resonant mode (torsional).

Table 4.14 Simulated and calculated resonant frequencies of two versions of prototype-7. Capacitance sensitivity calculations are based on the simulated resonant frequencies. "SW" refers to spring width and "SC" refers to sense capacitance.

	Resonant Frequency (kHz)		SW (μm)	Total SC (pF)	Capacitance Sensitivity (fF/g)
	Calc.	Sim.			
Ver.1	3.48	3.352	2.83	1.335	6.56
Ver.2	4.26	4.007	4.24	1.335	5.17

Table 4.15 First three resonant mode frequencies of each version of prototype-7.

	Fundamental Resonant Mode (kHz)	Secondary Resonant Mode (kHz)	Third Resonant Mode (kHz)
Version 1	1.5893	3.3520	8.4614
Version 2	2.8793	4.007	10.111

4.3.8 Prototype-8

This prototype is a z-axis accelerometer having a similar operation principle with prototype-7. However, this device uses folded springs instead of clamped ones in order to releases the residual stress in the structural layer. There are 4 versions of this prototype having different spring lengths and widths. Figure 4.23 shows the simplified diagram of the structure and Figure 4.24 shows the layout of the prototype-8 for a specific version.

Table 4.16 gives the simulated resonant frequencies of each version. Capacitance sensitivity of each version is calculated based on the simulated resonant frequencies. Moreover, similar to prototype-7, secondary resonant mode corresponds to the out of plane motion of the seismic mass. Table 4.17 gives the simulated resonant frequencies of the structure corresponding to the first 3 resonant modes. Second and third resonant modes are shown in Figure 4.25.

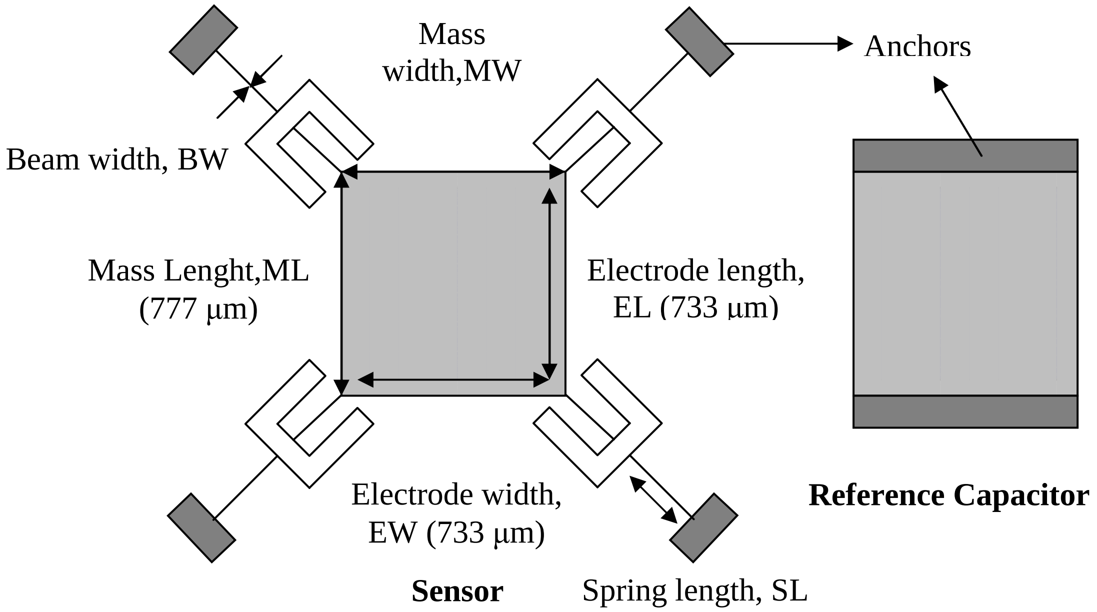

Figure 4.23 Simplified diagram of prototype-8, showing the sensor and the reference capacitor.

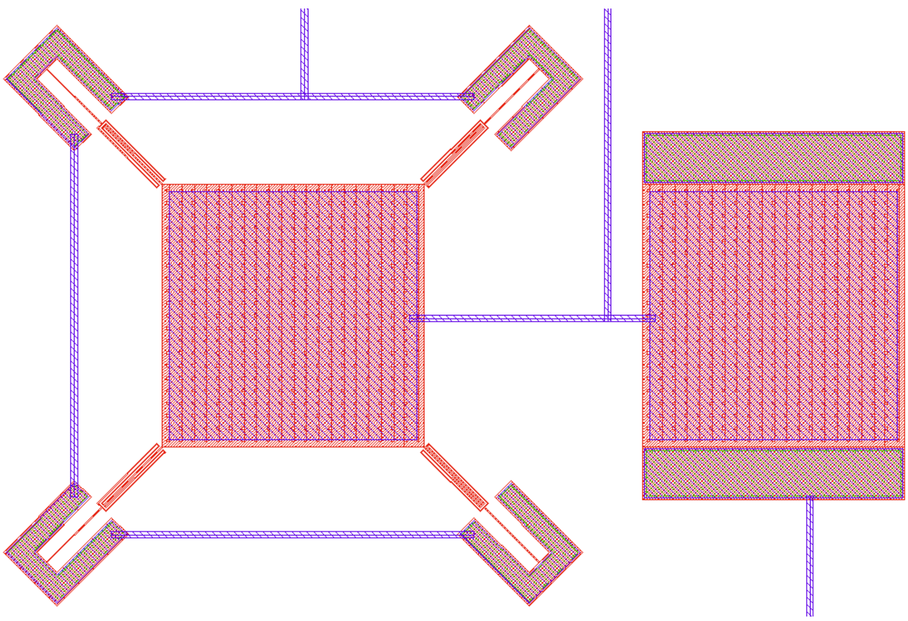

Figure 4.24 Layout of the prototype-8 for a version, for other versions only spring width and spring length changes.

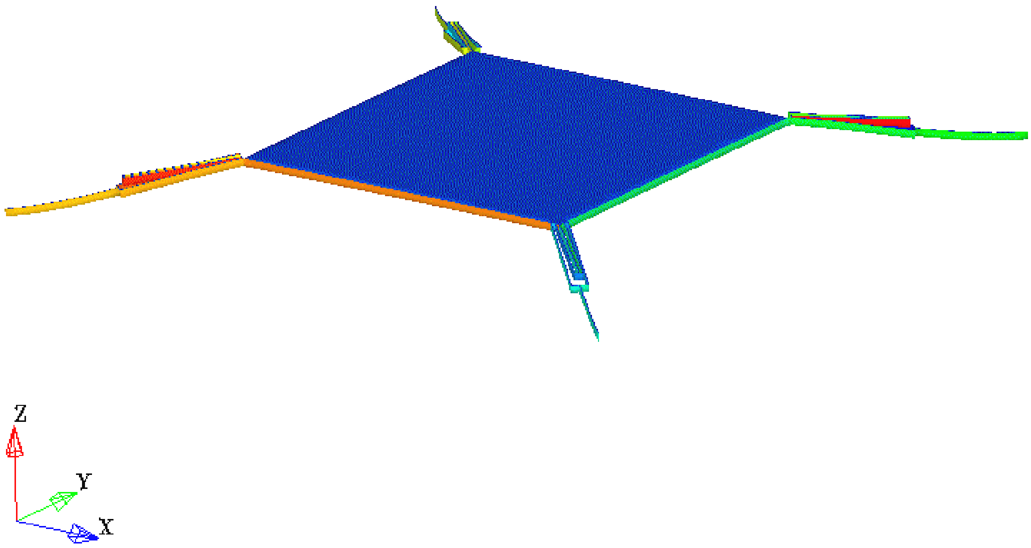

(a)

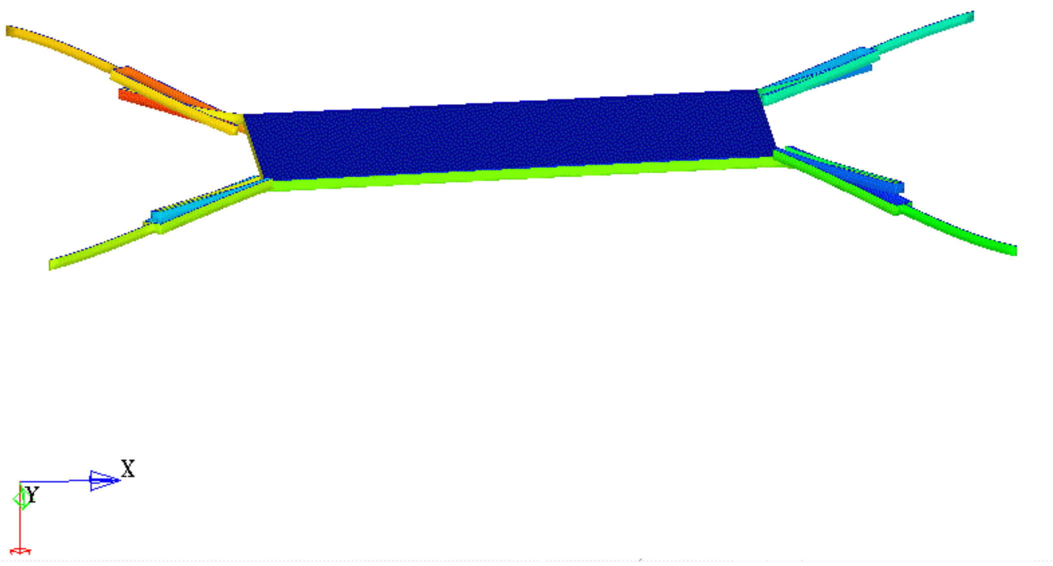

(b)

Figure 4.25 Resonant modes of prototype-8, (a) secondary resonant mode in z-direction, (b) third resonant mode (torsional).

Table 4.16 Simulated resonant frequencies and calculated sensitivities for each version of prototype-8. "SW" corresponds to spring width, "SL" corresponds to the spring length, and "SC" corresponds to sense capacitance.

	Resonant Frequency (kHz)	SW (μm)	SL (μm)	Total SC (pF)	Capacitance Sensitivity (fF/g)
Ver.1	2.8327	2.83	229	1.335	10.33
Ver.2	4.0810	2.83	106.7	1.335	4.97
Ver.3	3.7686	4.24	229	1.335	5.83
Ver.4	5.2765	4.24	106.7	1.335	2.98

Table 4.17 First three resonant mode frequencies of each version for prototype-8.

	Fundamental Resonant Mode (kHz)	Secondary Resonant Mode (kHz)	Third Resonant Mode (kHz)
Version 1	1.4266	2.8327	6.6363
Version 2	1.9357	4.0810	12.054
Version 3	3.5202	3.7686	8.6624
Version 4	4.9441	5.2765	16.645

4.4 Summary

Main considerations for the evaluation of an accelerometer are the resolution, voltage sensitivity, nonlinearity, bias instability, and cross-axis sensitivity. An accelerometer has to be evaluated in all of these areas to be considered as high performance.

Designing a high performance accelerometer involves careful consideration of the process technology, the readout circuit design, and packaging. Most important one from these three considerations is the process technology. Process technology sets the limits on the performance of the accelerometer, and also affects the performance of the readout circuit.

We have designed 8 prototypes. These designs include the usage of different spring topologies and also different sense capacitances. There are several versions for each prototype. These versions have different spring lengths and widths, and also different comb finger gaps. There are a total of 65 different accelerometer designs. This provides the fabrication of the best performance accelerometer, after the optimization of the fabrication process.

CHAPTER 5

CAPACITIVE READOUT CIRCUITS

Capacitive micromachined accelerometers are transducers that convert an acceleration to a capacitance change. Hence, performance of a micromachined accelerometer is limited by the minimum detectable capacitance change. In general, amount of the capacitance change for such sensors can be quite small, in the order of attofarads, due to the small feature size of MEMS accelerometers. Therefore, there is a need for a capacitive readout circuit capable of detecting capacitance changes in the order of attofarads for a high performance MEMS accelerometer. This chapter describes the design and implementation of the capacitive readout circuits capable of detecting such small capacitance changes, as well as performing force-to-rebalance operation in close loop operation for accelerometer prototypes described in Chapter 4. In addition to that, chapter describes a new capacitive interface circuit designed and implemented for capacitive MEMS gyroscopes. Described circuits are implemented with AMS 0.8 μm n-well process and simulation of the structures is performed with Cadence Design Environment, unless otherwise stated.

Section 5.1 explains different capacitive interfaces and their operations. Section 5.2 describes the design, implementation of a single-ended readout circuit. Section 5.3 introduces the fully-differential version of the readout circuit. Section 5.4 describes the on-chip testing of the fabricated single-ended and fully-differential readout circuits. Section 5.5 introduces a new interface circuit designed and implemented for micromachined capacitive gyroscopes. Section 5.6 shows the floor plan of the readout circuit chip. Finally, Section 5.7 gives the summary of the chapter.

5.1 Capacitive Interfaces

A micromachined accelerometer can be classified as a transducer which converts the mechanical acceleration to electrical signal by means of measuring the seismic mass displacement. In capacitive accelerometers, seismic mass displacement results in a capacitance change. This change is illustrated in Figure 5.1. Two sense capacitances are equal at equilibrium. When accelerometer undergoes an acceleration, seismic mass deflects resulting in a decrease in the gap between the top electrode and seismic mass, and an increase for the bottom gap. This results in an increase in the upper sense capacitance and decrease in the bottom sense capacitance.

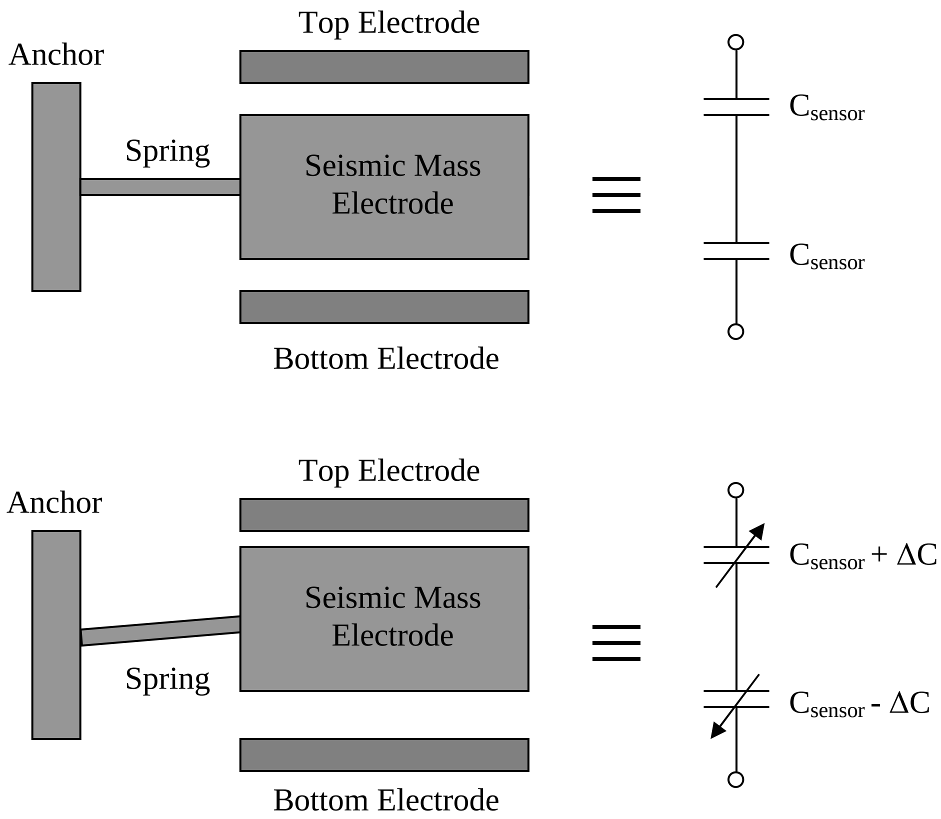

Figure 5.1 Picture illustrates the change of sense capacitances with movement of the seismic mass.

There are three different capacitive interfaces commonly used for capacitive accelerometers. These interfaces are called half-bridge capacitive interface, differential capacitive interface, and fully-differential capacitive interface. Figure 5.2 (a) shows the structure of the half-bridge capacitive interface. This structure is commonly used for surface micromachined z-axis capacitive accelerometers [95]. Structure consists of a variable sensor capacitance and a fixed reference capacitor. Change in the sensor capacitance can be detected by applying complementary square waves to the input nodes. Assuming square wave swinging between 0 and 5 V, output voltage at the middle node, V_{mid}, can be found from the voltage division as;

$$V_{mid} = 5 \times \frac{C + \Delta C}{2C + \Delta C} \tag{5.1}$$

However, linearity of this capacitive interface is not so high, as shown in Equation 5.1. This capacitive interface is not suitable, especially for varying gap sense capacitances, due to the additional nonlinearity. Higher linearity can be achieved with ratiometric operation with the differential capacitive interfaces. Figure 5.2 (b) shows the structure of the differential capacitive interface structure. This structure consists of two variable sensor capacitances, changing complementarily with the motion of the seismic mass. Assuming same bias signals with the half-bridge structure, output voltage at the middle node can be written as;

$$V_{mid} = 5 \times \frac{2\Delta C}{2C} \tag{5.2}$$

This structure shows higher linearity compared to the half-bridge structure, and suitable for varying-gap sense capacitances. However, two sensor capacitances constructing the differential-bridge must be equal for achieving highest possible linearity. Any mismatch between the two sensor capacitances affects the linearity of this capacitive interface. This effect can be reduced further by using a fully-differential capacitive interface shown in Figure 5.2(c). Most important property of this structure is that it enables the differential readout schemes, which are discussed later. Assuming identical sensor capacitances, the differential output voltage of this structure can be written as;

$$V_{mid} = 5 \times \frac{4\Delta C}{2C} \tag{5.3}$$

where the square wave signals are swinging between 0 and 5 V.

It should be mentioned again that typical displacement of seismic mass under acceleration is very small, in the order of sub-Angstroms, resulting in very small output electrical signals at the output of the capacitive interface [97]. This is valid especially for the surface micromachined accelerometers, where sense capacitances are small. Besides the small electrical signals, output node of the capacitive interfaces is a high impedance node, and it is not possible to read the voltages at this node via a simple measurement with probe or a multimeter. Moreover, capacitive interfaces are sensitive to parasitic capacitances at the input of the electronic interface [98]. Therefore, special attention must be paid to the readout circuit especially for hybrid systems, where the accelerometer and readout circuit are wire bonded to each other. As a result, capacitive accelerometers need a high performance readout circuit for detecting the signal coming from the capacitive interface.

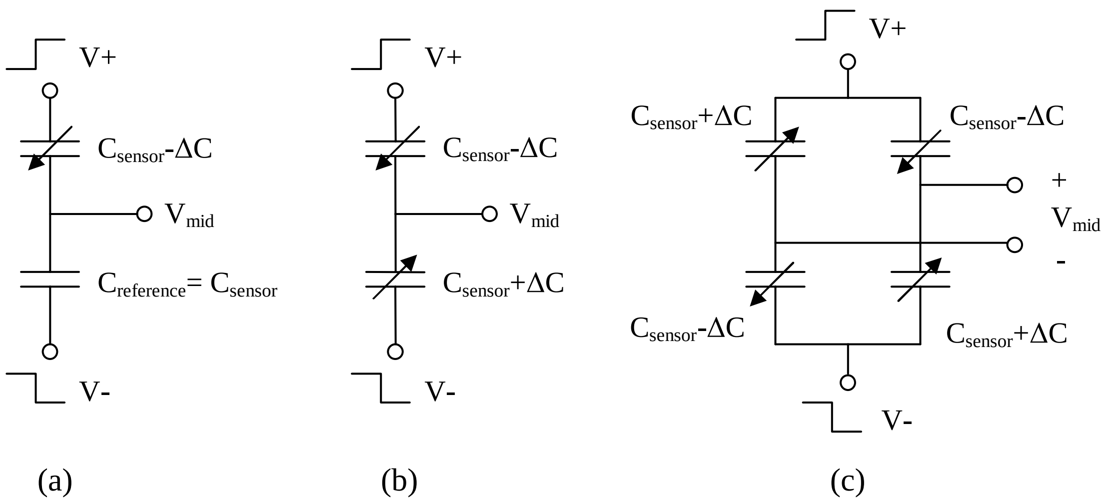

Figure 5.2 Three different types of capacitive interfaces, (a) The half-bridge capacitive interface [95], (b) The differential-bridge capacitive interface [96], and (c) The fully-differential bridge capacitive interface [24].

Several different types of capacitive readout circuits for capacitive interfaces are proposed in the literature. Front-end of these readout circuits are implemented with either a capacitance-to-frequency converter [99], or buffered capacitive ac-bridge [96, 100], or different types of switched-capacitor circuits.

Operation principle of the capacitance-to-frequency converter circuits depend on the charging and discharging time of a capacitor with a fixed current. Figure 5.3 shows the basic structure of the circuit proposed in [99]. Sensor capacitance is charged with a constant current, I. When the voltage on the sense capacitance exceeds a threshold value, switch is closed. This time sense capacitor is discharged with a constant current I until the voltage level falls below a threshold value. With this technique a triangular wave, whose frequency depends on the sense capacitance value, can be obtained.

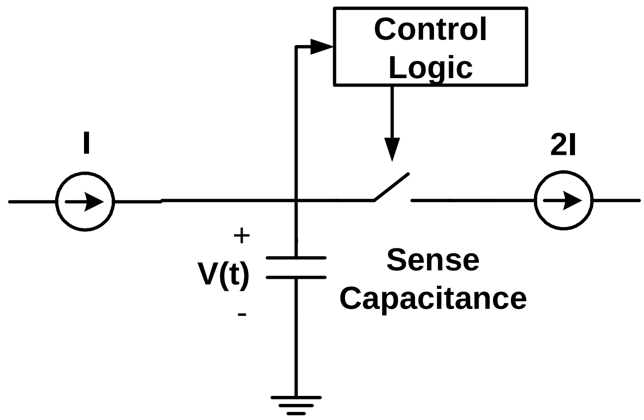

Figure 5.3 The basic structure of the capacitance-to-frequency converter circuit [99].

In buffered capacitive ac-bridge technique, capacitive interface is driven with two complementary signals. The output voltage generated at the middle node of the capacitive ac-bridge is sensed with a buffer circuit and demodulated. Advantage of this technique is built-in chopper stabilization, where capacitance change is modulated to high frequencies [96]. However, disadvantage of this circuit its sensitivity to the parasitic capacitances between the buffer circuit and the capacitive bridge. Therefore, the buffer circuit should have a small input capacitance, and parasitic capacitances at the input of the buffer must be reduced by means of special techniques, such as bootstrapping [100].

Switched-capacitor interface circuits can be designed to be parasitic insensitive [101] and can be monolithically implemented without any need for external circuit components. The sense capacitances are charged up with a constant voltage at the sense phase, and a packet of charge proportional to the sense capacitance mismatch is integrated with a charge-integrator [102]. Moreover, amplifier offset, kT/C noise and switch charge injection can be canceled together with reduction in flicker noise by correlated double sampling (CDS) [103]. In addition, switch capacitor front-end circuits have other advantages, as they can reduce power supply noise, EMI, switching-noise can be reduced [95].

Two different readout circuits are implemented in this work. First one is a capacitive readout circuit using switched-capacitor charge integrator as a front-end circuit [39, 87, 102, 104-106] that can operate in both open-loop and close-loop. Single-ended and fully-differential versions of this readout circuit are designed. Other one is an improved buffer circuit achieving very high input impedance by utilizing feedback and bootstrapping to minimize the input capacitance of the buffer circuit and the parasitic routing capacitances, respectively.

5.2 Single-Ended Readout Circuit

This readout circuit is basically an over-sampling converter and capable of working in both open and close-loop. System uses single bit quantization both for digital reading of the seismic mass displacement and also for the force-to-rebalance operation. Figure 5.4 shows the basic building blocks of the single-ended readout circuit [102]. Output of the circuit is in pulse density modulated form and can be low-pass filtered to obtain the analog reading of the acceleration information.

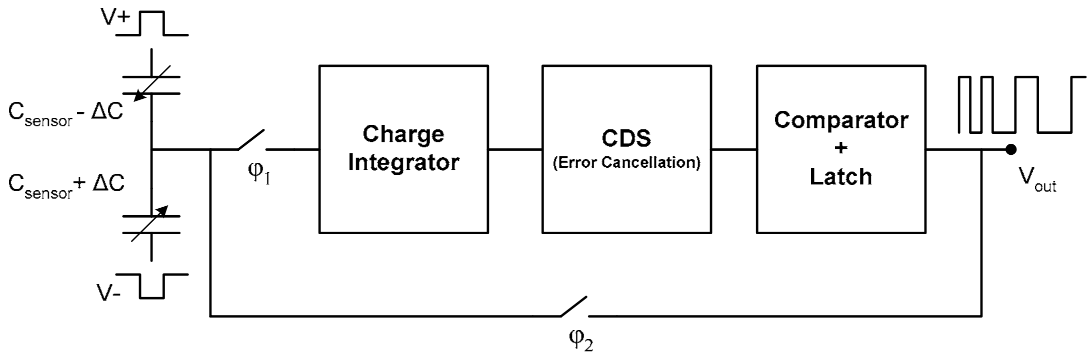

Figure 5.4 Basic structure of the single-ended readout circuit [102].

Operation principle of the circuit is simple and can be divided into two phases: the sense phase and the feedback phase. The sense phase starts with resetting the charge on the sense capacitance, when V+ is low. Then, the switch φ_1 is closed and middle node of the differential capacitance bridge is connected to the front-end charge integrator circuit. After bias signals V+ and V- change their states (V+ becomes high and V- becomes low), a charge imbalance occurs on the two sense capacitances proportional with the capacitance mismatch, ΔC. Charge integrator integrates this charge imbalance and shifts its output voltage from the analog ground level according to the amount of charge integrated. CDS cancels error sources like, charge integrator offset and switch charge injection to the first order. Then, the comparator circuit compares the output voltage of the CDS circuit and generates a 1-bit digital output voltage. Purpose of the latch circuit is to hold the output of the comparator and to synchronize it with the bias signals of the capacitance-bridge. In the feedback phase, switch φ_1 is opened and φ_2 is closed. Then, the output of the latch is connected to the middle node of the sense bridge. Output voltage of the comparator generates a force on the seismic mass counteracting the deflection of it and tries to null its position. Figure 5.5 illustrates the feedback operation. Note that the bias signals V+ and V- are still high and low respectively in this phase.

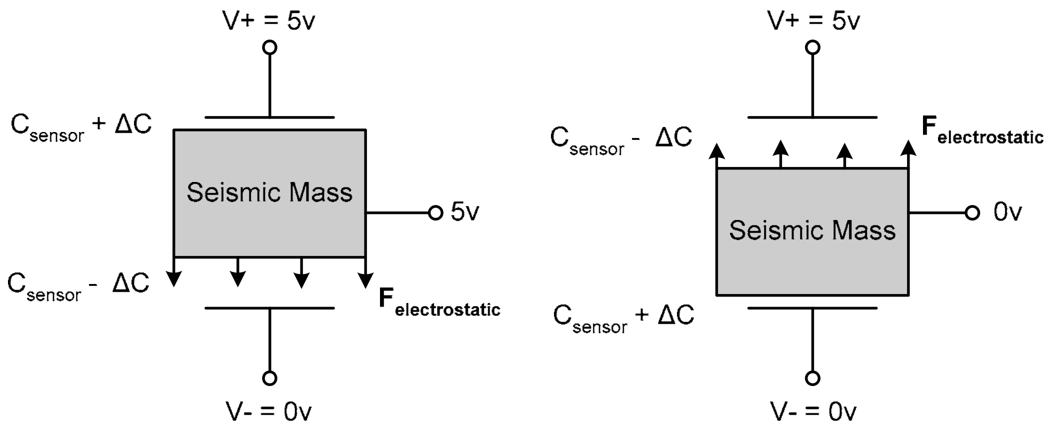

Figure 5.5 Force-feedback operation assuming V+ is 5V and V- is 0V. If seismic mass deflects upwards, feedback loop applies 5V to the seismic mass resulting in an electrostatic force trying to move the seismic mass to the bottom electrode. If mass deflects downwards, feedback loop applies 0V to the seismic mass and tries to pull the mass to upwards.

In the open-loop accelerometer, where a single charge integrator or a simple buffer circuit is used, overall linearity, bandwidth, and dynamic range of the accelerometer are determined by the sensor parameters. On the other hand, with closed-loop feedback operation, where the seismic mass is forced to stay in its null position, overall linearity, dynamic range, and bandwidth can be improved considerably [102]. Following sub-sections describe the building blocks of the single-ended readout circuit.

5.2.1 Single-Ended Folded-Cascode Operational Transconductance Amplifier

The Single-ended readout needs a wide bandwidth, low-noise, high-gain, and low-offset Operational Transconductance Amplifier (OTA) for implementing the front-end charge integrator.

An operational transconductance amplifier (OTA) can be considered as an OPAMP without an output stage. Therefore, output resistance of OTA is high compared to an OPAMP. As a result, OTAs can not drive small resistive loads but they are suitable for driving highly capacitive loads. Because of the stated reasons, a folded-cascode OTA is selected for the implementation of the front-end charge integrator. The main advantage of the folded-cascode topology is its, high bandwidth together with high phase margin, which are both achieved without a need for a compensation capacitance, because the load capacitance serves for that purpose [107]. Moreover, the folded-cascode topology can operate under a wide range of bias currents, which enables the designer to adjust the characteristics of the OTA for optimum performance.

Figure 5.6 gives the schematic of the folded-cascode OTA, which is designed for the implementation of the front-end charge integrator [107]. Table 5.1 gives the W/L ratios of the transistors. Length of the transistors is drawn 5 times larger than the minimum gate length to minimize the effect of process variations on the transistor parameters.

The low-frequency gain of the folded-cascode OTA is expressed by the transconductance of the input-stage multiplied by output resistance of the of the amplifier [107] as follows;

$$A_o = gm_1 (gm_4\, r_{d4}\, r_{d1} \,\|\, gm_6\, r_{d6}\, r_{d8}) \tag{5.4}$$

where gm is the transconductance and r_d is the output resistance of the transistors.

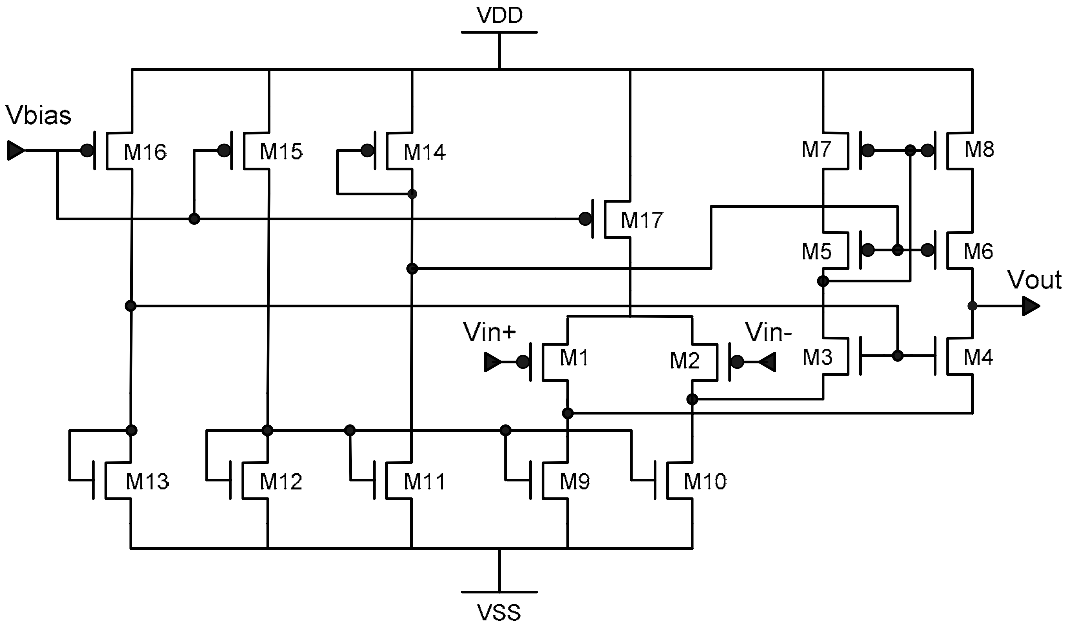

Figure 5.6 Schematic of the designed folded-cascode operational transconductance amplifier (OTA)

Table 5.1 The W/L ratios of the transistors of the folded-cascode OTA shown in Figure 5.6

M1, M2	400/4	**M12**	100/4
M3, M4	200/4	**M13**	17/4
M5, M6	150/4	**M14**	20/4
M7, M8	150/4	**M15**	100/4
M9, M10	200/4	**M16**	100/4
M11	100/4	**M17**	200/4

The high frequency small signal analysis can be used to calculate the unity-gain bandwidth of the OTA. Poles of the gain stage appear at drains of M3, M4, M9, and M10 [107]. However, total resistance seen at the drains of transistors M3, M9, and M10 are approximately 1/gm, and the total capacitance at these nodes are small. A load capacitance connected at the output of the circuit sets the dominant pole of the circuit. Thus, there is no need for extra compensation capacitance for the folded-cascode OTA, since a load capacitance connected at the output performs the compensation, which is not the case for other types of OTA structures. Considering the dominant pole of the circuit at the output node, unity-gain frequency of the circuit is expressed as [107];

$$f_o = \frac{gm_1}{2\pi C_L} \tag{5.5}$$

where C_L is the capacitance connected to the output of the OTA.

Slew rate of the OTA defines the maximum operation frequency. It depends on current passing from the output branch of the OTA, and can be calculated as;

$$S_r = \frac{I_o}{C_L} \tag{5.6}$$

where I_o is the DC current at the output branch.

One disadvantage of the folded-cascode topology is the reduced output voltage swing. The effect of this disadvantage is decreased by using high-swing current mirror type folded load which maximizes the output voltage swing of OTA. This load consists of transistors M5, M6, M7, and M8 of Figure 5.6. If these transistors are biased at the edge of saturation, output voltage swing of the OTA is maximized to $Vdd\text{-}2Vds_{sat}$. Figure 5.7 shows the circuit, which biases the high-swing current mirror load. On the other hand, the main consideration is not the output voltage swing. Therefore, W/L ratio of the bias transistor of the high-swing current mirror load (M5 of Figure 5.7 corresponding to M14 of Figure 5.6) is selected to be smaller than the ideal value which maximizes the voltage swing, so that process variations will not affect the operation.

Simulations of the OTA are performed using the CADENCE design environment. Figure 5.8 shows the gain-bandwidth simulation of the folded-cascode OTA, and Table 5.2 presents the other simulation results. Necessary bias voltages are also included in Table 5.2. The layout of the design is drawn according to a 0.8

μm CMOS n-well process and occupies an area less than 280 μm x 200 μm. Substrates of all NMOS and PMOS transistors are connected to ground and positive supply voltage, respectively. Sealing the PMOS and NMOS transistor from each other with substrate connections decreases the latch-up effect. Moreover, common-centroid layout technique is used to increase the matching of the transistors having the same W/L ratios [108].

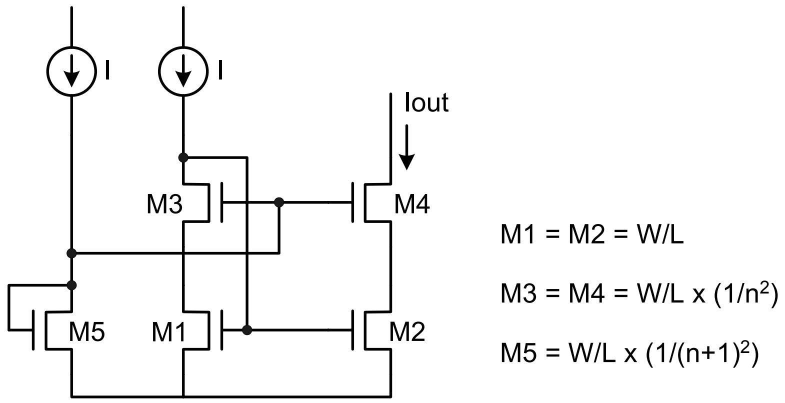

Figure 5.7 Bias scheme of the high-swing current mirror for highest output swing.

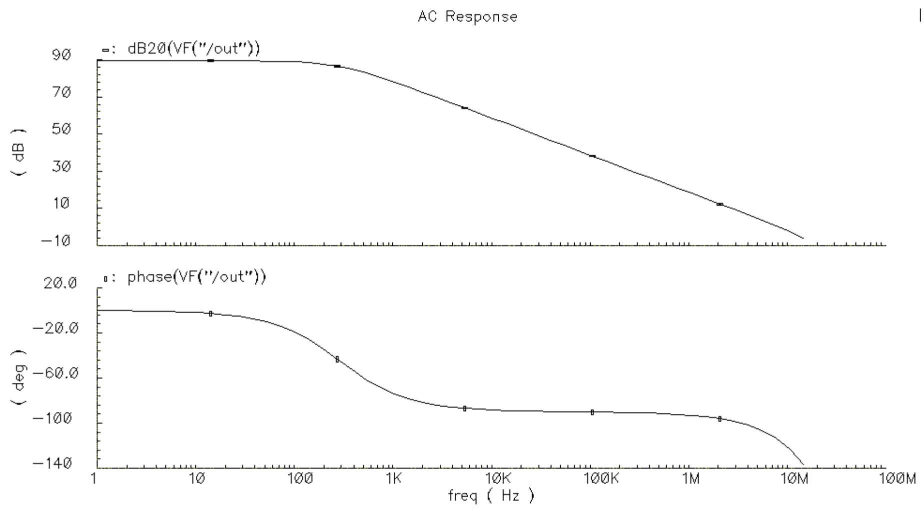

Figure 5.8 Gain-bandwidth simulation of the folded-cascode OTA.

Table 5.2 Simulated performance results of the folded-cascode OTA.

DC Supply Voltages	Vdd = 5 V, Vss = 0 V
Bias Voltage	4 V
Load Capacitance	7 pF
Low-Frequency Open Loop Gain	89 dB
Unity-Gain Frequency	8.16 MHz
Phase Margin	65.5º
Slew Rate	6.1 V/µs
Offset Voltage	40 µV
Input Referred Noise	26.7 $nV/\sqrt{Hz}$
CMRR	144 dB
Output Voltage Swing	4.3 V
Power Consumption	1 mW

5.2.2 Charge Integrator and CDS

The charge integrator circuit detects the seismic mass motion of the accelerometer via sensing the change in the sense capacitances. Figure 5.9 illustrates the operation of the charge integrator connected to the differential capacitance bridge. Operation of the circuit consists of reset and integration phases that are defined by the closed and open states of the switch φ, respectively. From the charge conservation rule, the output voltage of the integrator can be calculated. Assuming bias signal swing of 0-5 V and reference voltage of 2.5 V, then Q_1 and Q_2 can be written as;

$$Q_1 = -2.5(C - \Delta C) + 2.5(C + \Delta C) \tag{5.7}$$

$$Q_2 = \Delta V\, C_{\text{int}} + 2.5(C - \Delta C) - 2.5(C + \Delta C) \tag{5.8}$$

where Q_1 and Q_2 are the total charges, when switch φ is closed and open, respectively, and ΔV is the change of the output voltage from the reference voltage.

From the charge conservation rule, total charges at two different states must be equal. Hence, equating Equations 5.7 and 5.8 to each other, change of output voltage from the reference level can be written as;

$$\Delta V = V_{bias} \times \frac{2 \times \Delta C}{C_{\text{int}}} \tag{5.9}$$

where C_{int} is the integration capacitance, ΔC is the change of single sense capacitance, and V_{bias} is the peak-to-peak value of the complementary bias signals. However, the output voltage of the charge integrator generates error signals like amplifier offset. In order to get rid of these error signals, a correlated double sampling circuit is introduced in the charge integrator.

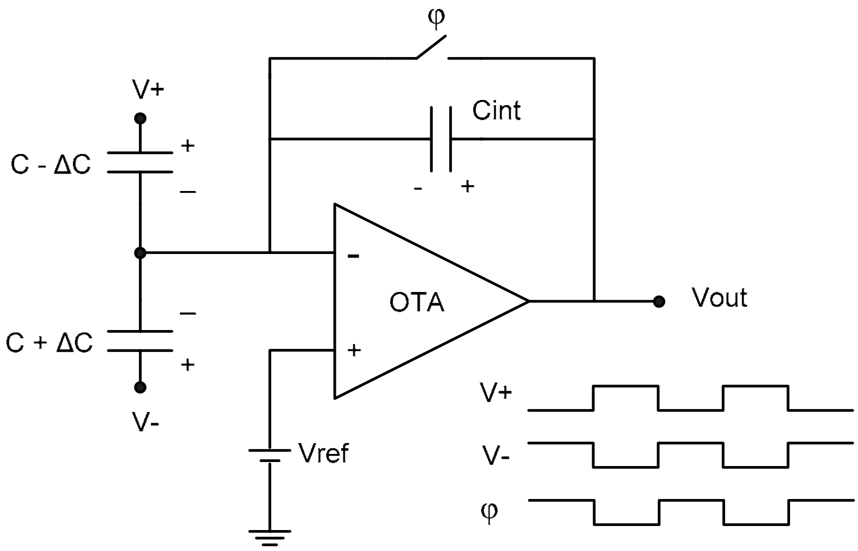

Figure 5.9 The charge integrator schematic and operation principle.

The basic structure of the implemented charge integrator with CDS is shown in Figure 5.10, which is similar to the structure explained in [103]. Operation of the circuit consists of two phases. In the first phase, OTA is buffer connected, and the error storage capacitance, Ccds, is connected to the reference voltage level. This generates an error voltage on the error storage capacitor. Then, in the second phase, the error storage capacitor is disconnected from the reference voltage level and connected to the output. OTA is in charge integrating mode at this phase. After the charge integration, the OTA output contains the signal including the error due to OTA offset. If the output voltage of the CDS circuit is considered, this error value is subtracted from the output of the OTA resulting in an error-free output voltage.

The charge integrator together with CDS circuit is simulated with a capacitance change, ΔC, of 10 fF, and integration capacitance of 1 pF. Figure 5.11 shows the simulation results of the output of the charge integrator and output of the CDS. The ideal output voltage of the integrator is 100 mV. Figure 5.11 shows that the integrator output is very close to 100 mV, so as the CDS output, showing that the designed OTA has a very low offset voltage. The small mismatch between the integrator output and the CDS output is due to charge injection from switches to the CDS capacitor.

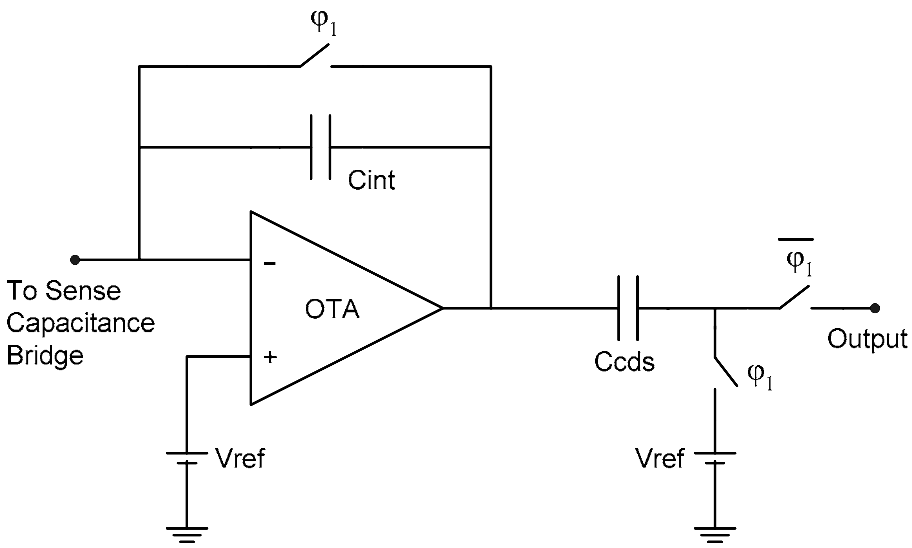

Figure 5.10 The charge integrator circuit with CDS [103].

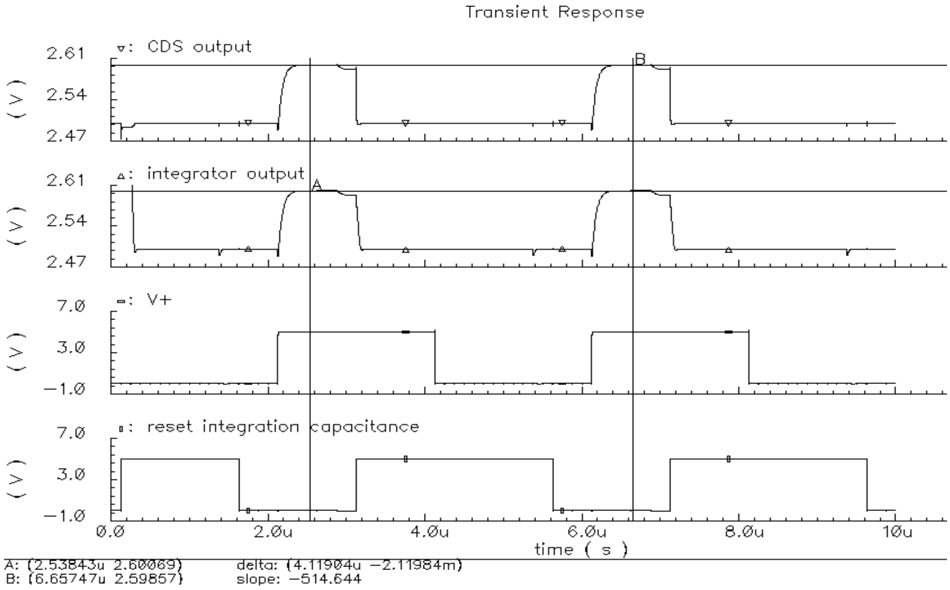

Figure 5.11 Simulation result of the charge integrator and CDS circuits for a sense capacitance change of 10 fF. Output of the charge integrator is 100.7 mV, and output of the CDS is 98.6 mV.

5.2.3 Fully Differential Latched Comparator

The comparator is the most important and limiting component of the readout circuit, due to its finite accuracy and comparison speed. Moreover, it sets the precision of the loop, since the output of the charge integrator is compared with a reference voltage, where offset of the comparator plays an important role in the loop error. Therefore, there is a need for a high-speed and high-precision comparator for proper operation of the readout circuit. The designed comparator is a differential comparator, but it can also be used as a single-ended one.

Figure 5.12 shows the schematic of the implemented comparator [109, 110], and Table 5.3 gives the W/L ratios of the transistors. The circuit consists of a PMOS differential input pair (M1, M2), NMOS and PMOS regenerative loops (M15, M16, and M5, M6), and an S-R latch (M8-M11, M17-M20). Note that the bulk nodes of the input pair transistors are connected to their sources in order to prevent the threshold variations due to bulk-to-source voltage variations. The circuit operates with two non-overlapping clock signals, namely, *reset* and *calculate*. In the reset phase, drains of M15, M16, and M5, M6 are shorted, which equalizes the voltages at these nodes from the previous state. After the reset signal goes low, regeneration starts on the NMOS regenerative pair, i.e. non-overlapping period of *reset* and *calculate* signals. This step is important for reducing the input offset voltage of the comparator [109]. Then, in the calculate phase, the voltage difference at the drains of the differential input pair is further amplified by the NMOS and PMOS regenerative loops to a value very close to the supply voltages. The latch preserves the state of the output till the start of the next calculate phase.

Simulation of the latched comparator is performed with a 1 mV sinusoidal signal applied to the inverting input, while non-inverting input is connected to 2.5 V. *Reset* and *calculate* signals have a frequency of 5 MHz and a non-overlapping period of 100 ns. The bias voltage of the comparator is 4 V. As can be seen from the simulation result, shown in Figure 5.13, the comparator operates properly with a 1 mV sinusoidal signal. The offset voltage of the comparator is 1 μV, and the settling time of 3.5 ns.

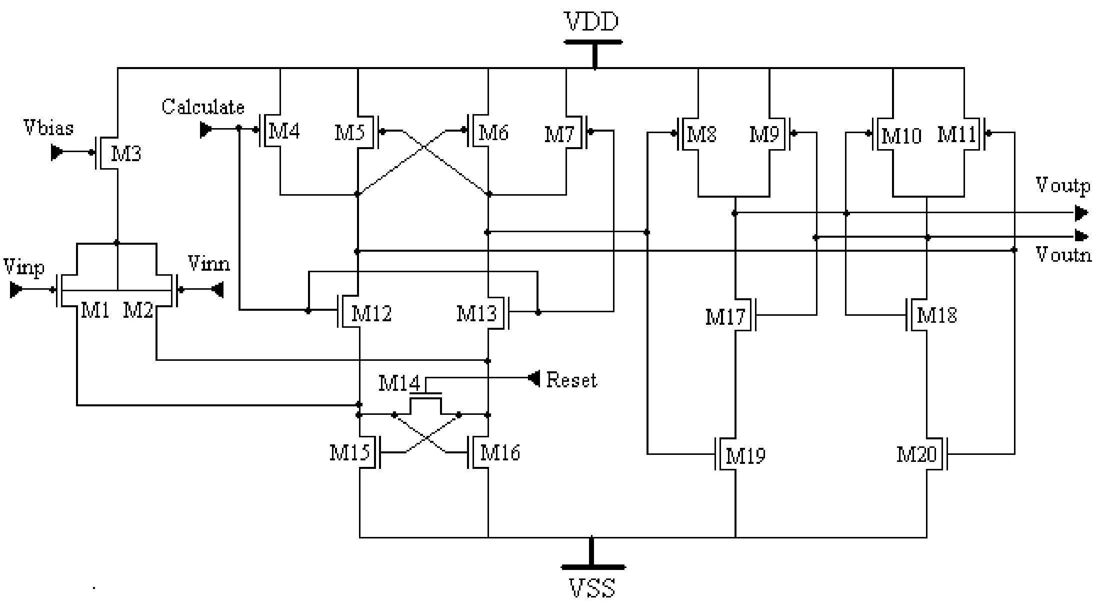

Figure 5.12 Schematic of the fully differential latched comparator.

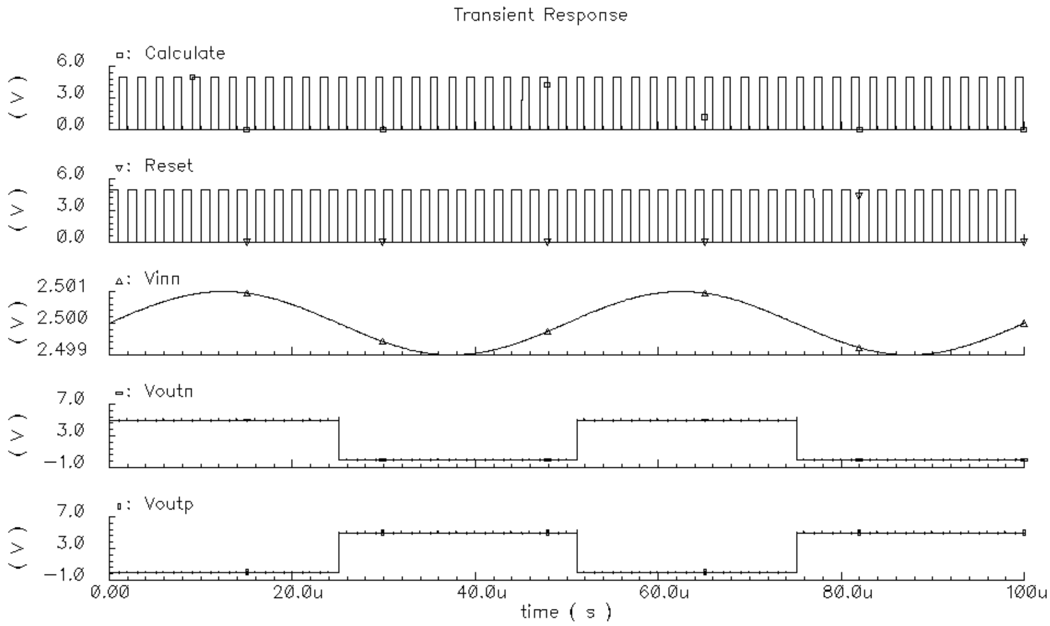

Figure 5.13 Simulation result of latched comparator with 1 mV sinusoidal wave.

Table 5.3 The W/L ratios of the designed latched comparator.

M1, M2	30 /4	**M10, M11**	10/4
M3	20/4	**M12, M13, M14**	4/4
M4, M5	10/4	**M15, M16**	15/4
M6, M7	10/4	**M17, M18**	4/4
M8, M9	10/4	**M19, M20**	4/4

5.2.4 Description of Complete Single-Ended Readout Circuit

Figure 5.14 shows the complete schematic of the single-ended readout circuit connected to an accelerometer, which requires eight clock signals that are shown in Figure 5.15. These clocks are for proper control of switches and complementary bias signals. These clock signals are generated internally from a 4-bit synchronous counter, through a combinational logic circuit. Details of this circuit are described in the next section. The operation of the circuit is based on the integration of the charge due to the mismatch of the sense capacitances. The charge imbalance is generated by complementary square waves. Operation of the circuit connected to an accelerometer is described below;

If the seismic mass of the accelerometer deflected downwards, it decreases the capacitance of the upper sense capacitor and increases the bottom. This capacitance change results in an increase at the output voltage of the integrator during integration time, as described in Section 5.2.2. Then, the comparator compares this voltage with the reference voltage and generates logic Low at its output. This voltage is applied to the seismic mass during the feedback time and creates a force pulling it to the upper electrode, as described in Figure 5.5.

Operation of the circuit starts with resetting the sense capacitances of the accelerometer. Switches operating with clock Q_1 are used for this purpose, so that charge imbalance on the sense capacitances due to the previous state is equalized.

Clock Q_2 is used to connect the sense capacitances to the complementary bias signals. Without switches operating with this clock signal, complementary bias signals are connected to ground during reset of the sense capacitances.

Clock Q_3 controls the switch between the readout node of the sense capacitance bridge and charge integrator. After this switch is closed, charge imbalance is integrated on the integration capacitance of the charge integrator during the transition of the V+ bias signal to high.

Clock Q_4 performs the reset operation of the integration capacitance of the charge integrator, and also controls the CDS operation. If switches controlled by this clock are closed, integration capacitance is reset, and CDS is in error sensing mode.

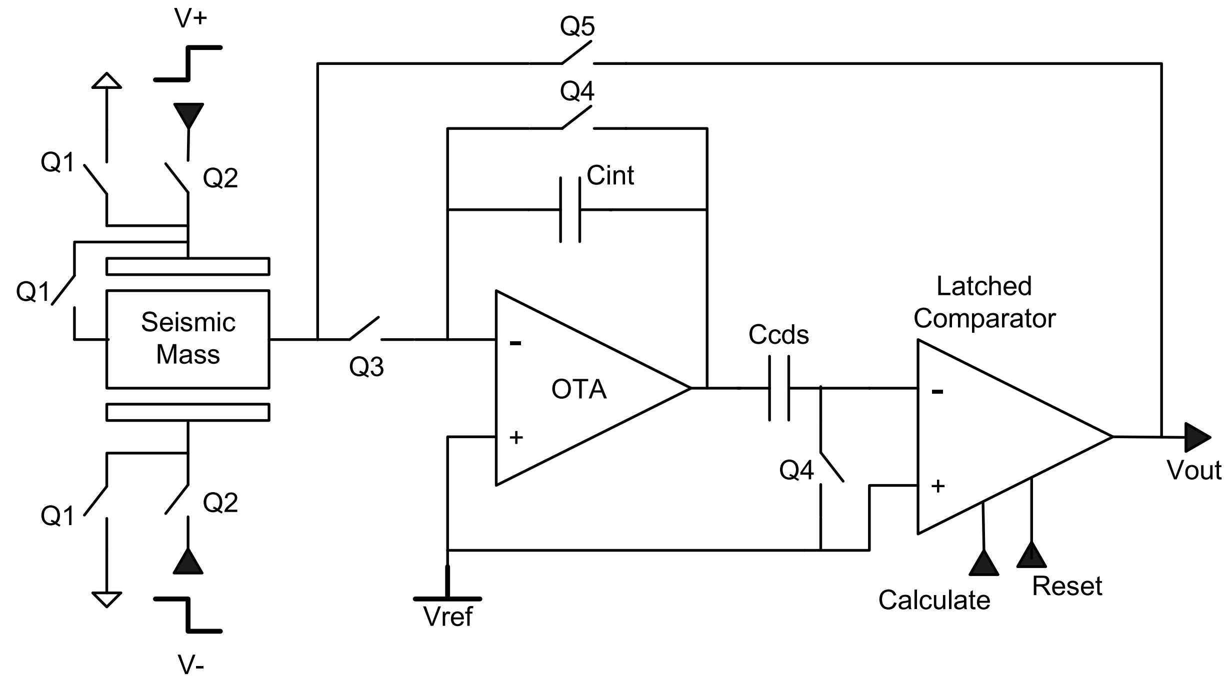

Figure 5.14 The complete schematic of the single-ended readout circuit connected to an accelerometer.

Reset and *calculate*, are used to control the operation of the latched comparator, as described in Section 5.2.3. After the error on the output signal of the charge integrator is cancelled by the CDS circuit, the comparator compares this signal with the reference voltage, in order to understand the direction of the seismic mass displacement. Then, comparator generates an output voltage that will counteract the deflection of the seismic mass. During clock Q_5, this output voltage is applied to seismic mass and nulls the deflection of the seismic mass.

Figure 5.15 shows the clock signals controlling the switches of the single-ended readout circuit. Open-loop simulations of the circuit are performed for two different capacitance values. Figure 5.16(a) shows the result of the simulation with the upper and lower capacitances are selected as 95 fF and 105 fF, respectively. Figure 5.16(b) shows the same simulation where values of these capacitances are reversed. Figure 5.16 (a) and (b) also show the comparator output.

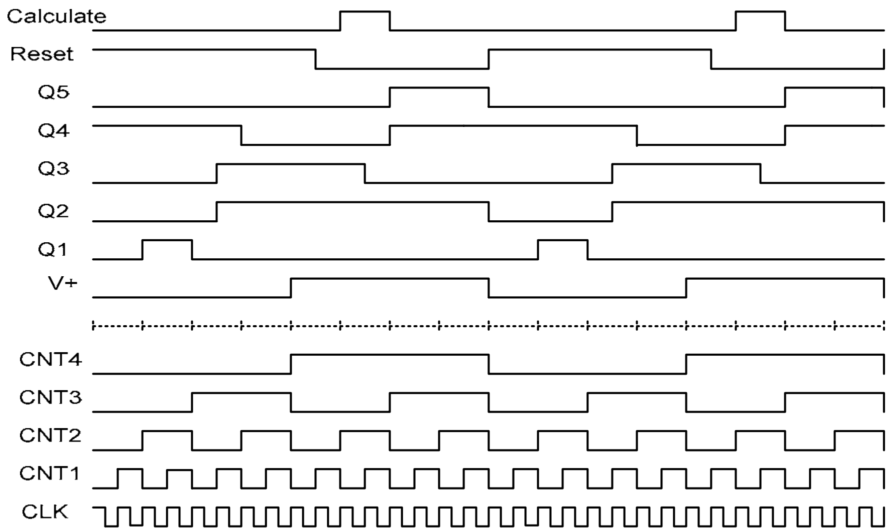

Figure 5.15 Control signals for the switches of single-ended sigma-delta interface circuit, and bias signal of the sense capacitance bridge.

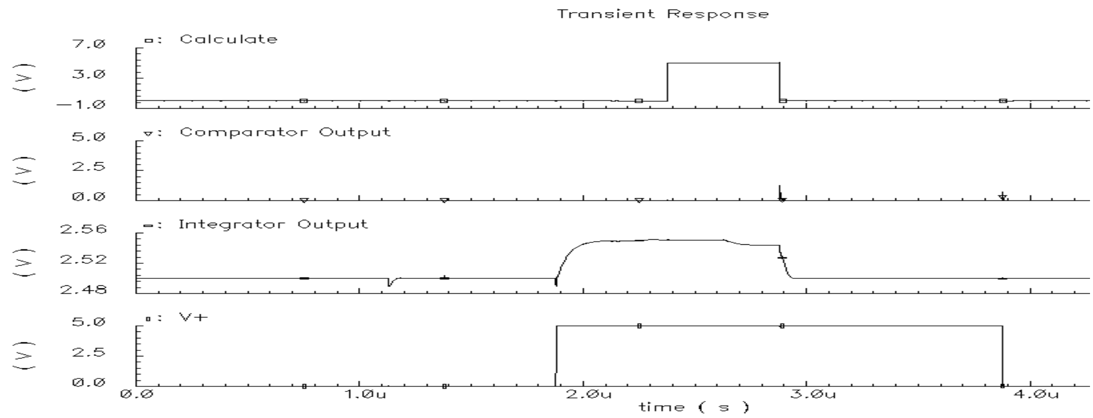

(a)

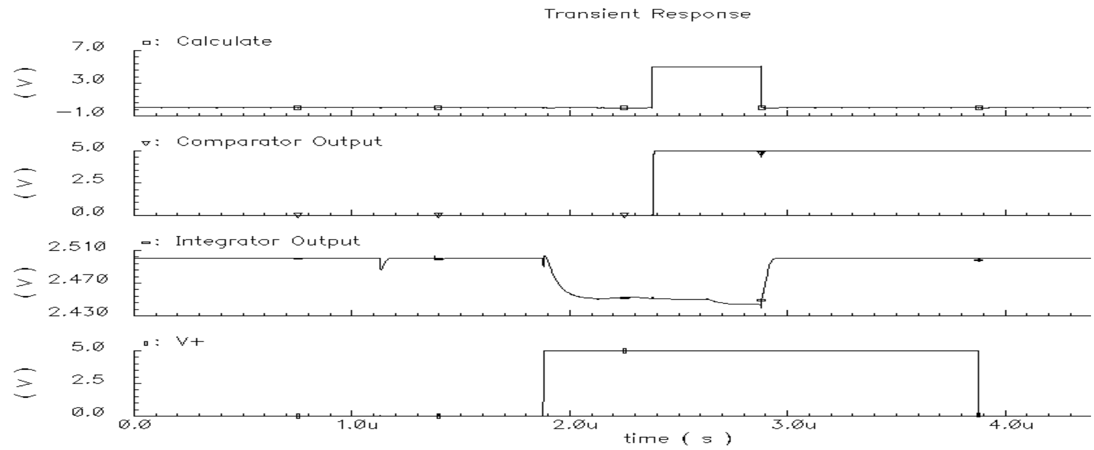

(b)

Figure 5.16 Open-loop simulation results of the single-ended readout circuit, (a) Top sense capacitance is 95 fF, and bottom in 105 fF, (b) values of capacitances are reversed.

5.2.5 Digital Control Signal Generation

A digital circuit generating the proper control signals is necessary for the proper operation of the readout circuit. The digital control signal generator uses a 4-bit synchronous counter having asynchronous reset. The circuit generates all the necessary control signals and their complements for switches and the bias signals for the sense capacitance bridge. Table 5.4 gives the logic functions of the control signals, whose diagram is shown in Figure 5.15. A common problem in the digital circuits is the output glitches that occur due to the delay between the inputs of the circuit. The output of the complementary logic circuit is sampled by a D flip-flop at the negative edge of the clock signal in order to overcome this problem. Output signals are free off glitches with this method since output of the complementary logic is changing at positive edge of the clock signal.

Table 5.4 The logic functions of the digital control signals.

Control Signals	Logic Function
V+	$CNT4$
Q1	$\overline{\left(\overline{CNT2}+CNT3+CNT4\right)}$
Q2	$\overline{\left(\overline{(CNT1+CNT2+CNT3)}+\overline{(CNT3+CNT4)}\right)}$
Q3	$\overline{\left(\overline{\left(\overline{(CNT3+\overline{CNT4})}\bullet\overline{(CNT1\bullet CNT2)}\right)}\bullet\overline{\left(\overline{(\overline{CNT3}+CNT4)}\bullet\overline{(\overline{CNT1}\bullet\overline{CNT2})}\right)}\right)}$
Q4	$\overline{\left((CNT3\oplus CNT4)\bullet\overline{(CNT3\bullet\overline{CNT2})}\right)}$
Q5	$\overline{\left(\overline{CNT3}+\overline{CNT4}\right)}$
Calculate	$\overline{\left(\overline{CNT2}+CNT3+\overline{CNT4}\right)}$
Reset	$\overline{\left(CNT4\bullet\overline{(\overline{CNT1}\bullet\overline{CNT2}\bullet\overline{CNT3})}\right)}$

5.3 Fully-Differential Readout Circuit

Different from the single-ended readout circuit, fully differential approach uses fully-differential charge integrator as the front-end circuit. This approach is very popular for several reasons. Most important advantage of the fully differential approach is its immunity to common mode errors, like the switch-introduced noise and the noise on the power rails [102]. Many different accelerometers utilizing fully differential readout technique are reported in the literature [21, 29, 39, 87, 102, 105, 111, 112]. Figure 5.17 shows the simplified structure of the fully-differential readout circuit. The circuit utilizes the fully-differential capacitance bridge interface for acceleration detection. For the accelerometer prototypes presented in this thesis, this structure can be constructed with two accelerometers having very similar resonant frequencies and sense capacitances, where each accelerometer constructs one of the sense capacitance of the differential bridge. Another approach is to use a single accelerometer and two reference capacitances instead of capacitance C_3 and C_4 [21, 102]. For the two accelerometer case, the operation of the circuit is as follows: Under acceleration, the middle nodes of the two differential bridges generate complementary charge packets. These complementary charge packets are integrated by the fully-differential charge integrator, resulting in complementary output voltage shifts. After the amplifier offset cancellation and further reduction in the common mode errors by the CDS circuit, the latched comparator generates a single-bit according to the differential output. Then, these voltage levels are feedback to the seismic masses of the accelerometers for forcing the seismic masses to null position. Digital output of the circuit can be obtained from one of the outputs of the latched comparator.

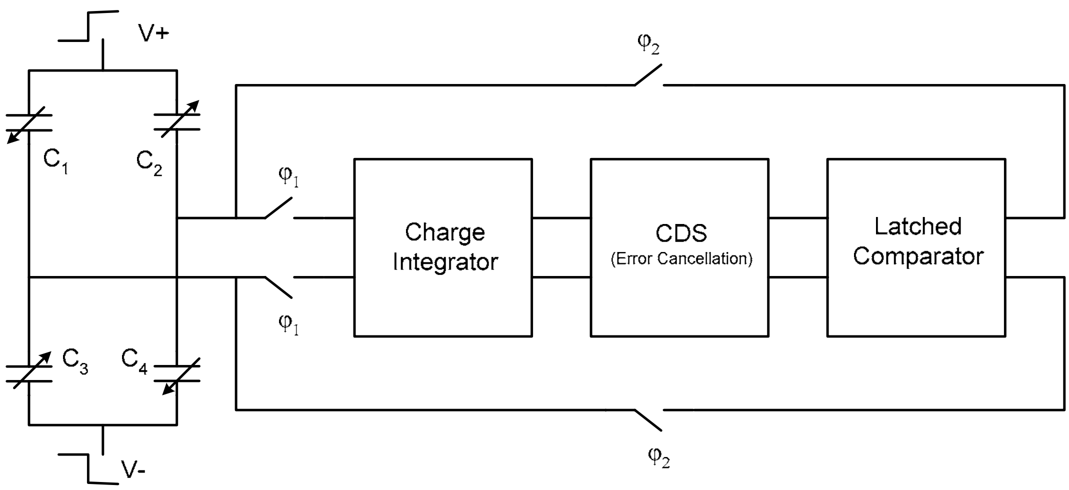

Figure 5.17 Basic structure of the fully-differential readout circuit.

The basic component of the fully-differential readout circuit is the fully-differential OTA that is used for the fully differential charge integrator circuit. The differential comparator described in Section 5.2.3 is used as the latched comparator. Rest of this section describes the components used for the construction of the fully differential readout circuit and the detailed operation of the loop.

5.3.1 Fully-Differential Folded-Cascode Operational Transconductance Amplifier

Fully-differential OTA is very advantageous in terms of rejection of the common mode errors for switched-capacitor applications [102]. Figure 5.18 shows the schematic of the fully-differential folded-cascode OTA structure [112], and Table 5.5 shows the W/L ratios of the transistors. The circuit consists of two main blocks: the bias circuit and the main OTA part. The bias circuit generates necessary bias voltages for the folded branch of the OTA and also for the drive current of the differential input pair from a single voltage supply. Note that the CMFB (common mode feedback) terminal in Figure 5.18 is not connected to the bias circuitry, whose bias is separately generated by the CMFB circuit.

Although the fully-differential approach is advantageous in terms of reducing the common mode errors, it needs a CMFB circuit. The output common mode level of the output voltage is undefined since the input voltage of the OTA is differential and common mode gain is very low [107]. Ideally, the CMFB circuit tries to set the common mode level of the output, preferably to the half-way between the power supply voltages in order to maximize the output voltage swing. This is achieved by controlling the current passing through the folded branch of the OTA.

Figure 5.19 shows the implemented CMFB circuit for setting the output common voltage level of the fully-differential OTA [109, 114]. The circuit operates with two non-overlapping clocks. Expression relating the total charge in the two phases (φ_1 and φ_2) can be written from the charge conservation rule as [109];

$$(C_1 + C_2)\left[V_{com}(\varphi_2) - V_{cmfb}(\varphi_2)\right] = C_1(V_{bias} - V_{cm}) + C_2\left[V_{com}(\varphi_1) - V_{cmfb}(\varphi_1)\right] \tag{5.10}$$

where V_{com} is the common mode output voltage level and defined as;

$$V_{com} = (V_{outp} + V_{outn})/2 \tag{5.11}$$

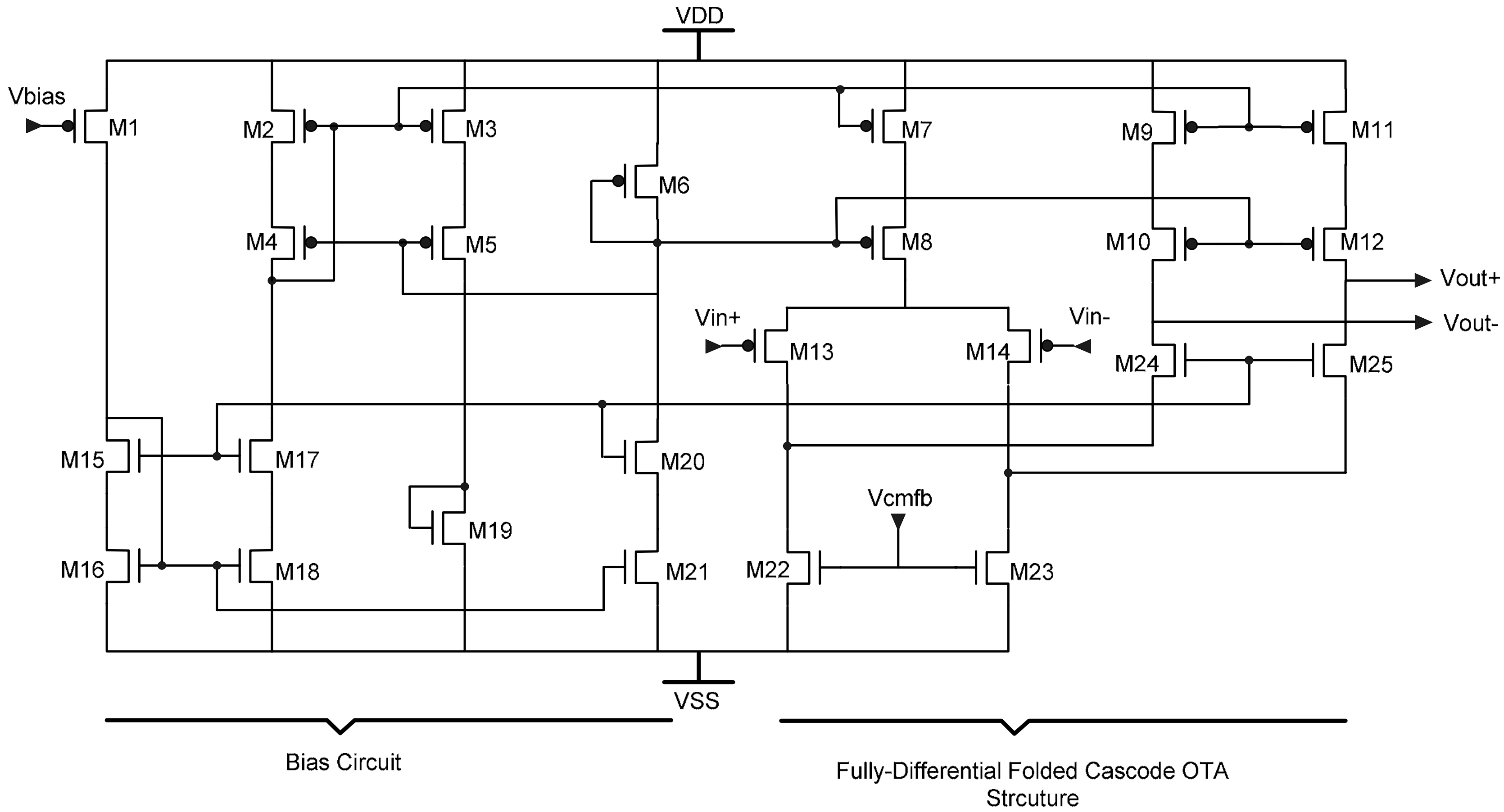

Figure 5.18 Schematic of the fully-differential folded-cascode operational transconductance amplifier (OTA).

Equation 5.10 states that, in order to have stable common mode output voltage level, (V_{com} - V_{cmfb}) at two clock phases should be equal to each other and also should be equal to (V_{bias} - V_{cm}) [109]. V_{bias} is selected as 3.95 V and V_{cm} is selected as 2.5 V, considering the necessary CMFB voltage in order to set the output common mode voltage level close to 2.5 V.

Figure 5.20 shows the simulation result of the common mode output voltage level of the fully differential folded-cascode OTA with the switch capacitor CMFB circuit. The common mode output voltage level of the OTA comes closer to the desired output voltage level of 2.5 V with every clock pulse. The common mode voltage level can be fine trimmed to 2.5 V by properly adjusting the V_{bias} voltage.

Table 5.5 The W/L ratios of the transistors of the fully-differential folded-cascode OTA.

M1	100/4	**M13, M14**	140/2
M2, M3	80/2	**M15, M17**	40/4
M4, M5	80/4	**M16, M18**	40/2
M6	16/4	**M19**	10/4
M7	240/2	**M20**	40/4
M8	240/4	**M21**	40/2
M9, M11	120/2	**M22, M23**	120/2
M10, M12	120/4	**M24, M25**	120/4

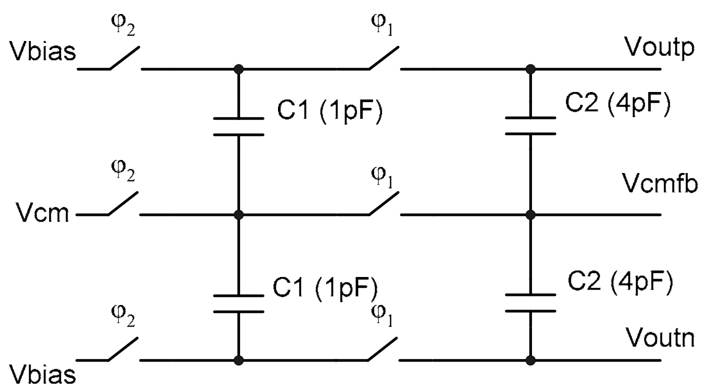

Figure 5.19 Schematic of the common mode feedback circuit for the fully-differential folded cascode OTA [114].

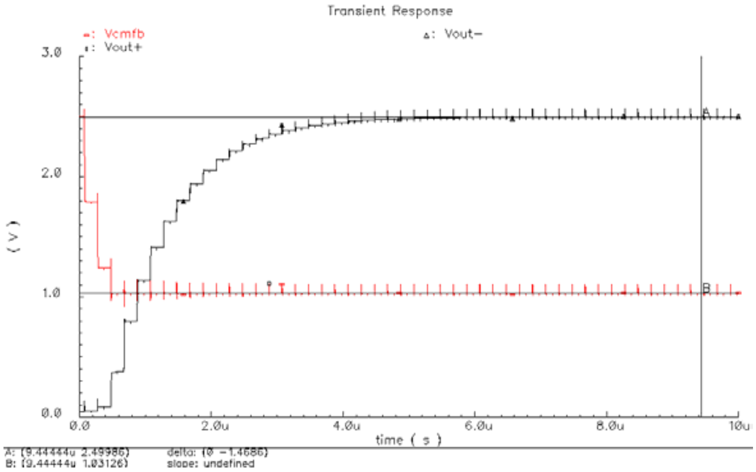

Figure 5.20 Simulation of the fully differential OTA with CMFB circuit. CMFB circuit sets the output of the fully-differential OTA to 2.5 V.

Table 5.6 gives the performance values and summary of the designed fully-differential folded-cascode OTA structure. Figure 5.21 illustrates the differential gain-bandwidth simulation of the OTA. The OTA has a relatively large low frequency open-loop gain with a high phase margin, and it is used to implement the fully-differential charge-integrator front-end of the fully-differential readout circuit. Since operation of the fully-differential charge-integrator is very similar to the single-ended one, it is not described separately. Instead, the overall operation of the fully-differential topology is described in the next section.

Table 5.6 Performance values and necessary parameters of the designed fully-differential folded-cascode OTA.

Supply Voltages	Vdd = 5V, Vss = 0V
OTA Bias Voltage	4 V
CMFB bias (Vbias)	3.95 V
Vcm	2.5 V
Load Capacitance	4 pF
Slew Rate	5.6 V/μs
Differential Offset	~ 0V
Power Consumption	2.1 mW
Low-frequency Differential Gain	90.7 dB
Phase Margin	68.5 deg
CMRR	310 dB
Unity Gain Frequency	29.7 MHz

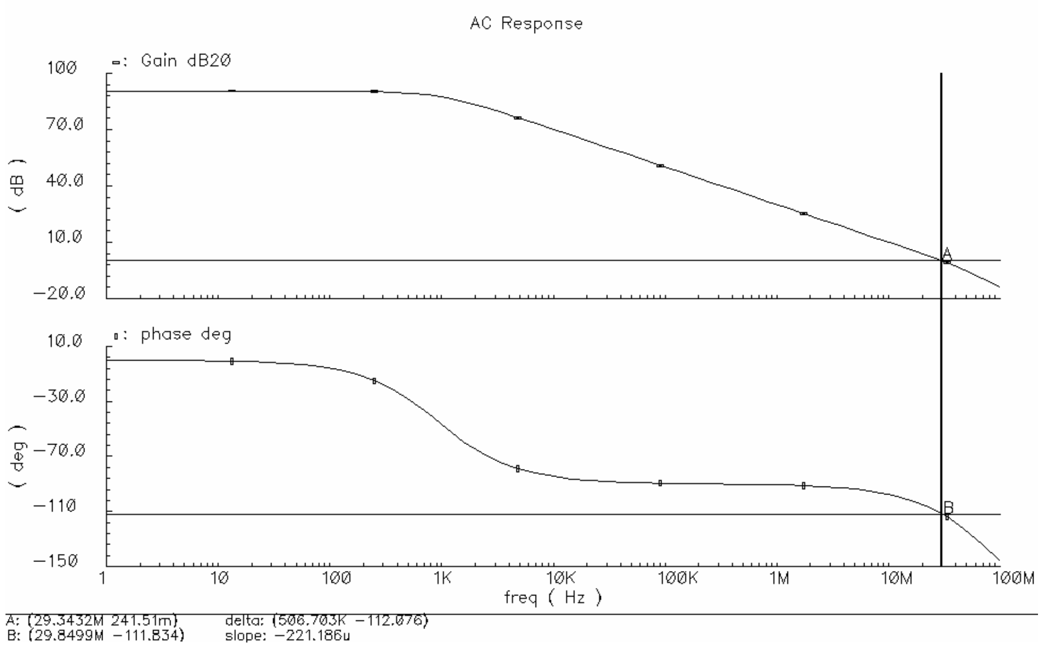

Figure 5.21 Open-loop gain-bandwidth simulation of the fully-differential folded-cascode OTA.

5.3.2 Description of the Fully-Differential Readout Circuit

Figure 5.22 shows the schematic of the fully-differential readout circuit. The operation principle is very similar to the single-ended readout circuit. In addition to the seven clock signals that are shown in Figure 5.15, there are two additional non-overlapping clock signals for the CMFB circuit. Note that the switches of fully-differential readout circuit have the same functions with those of the single-ended readout circuit.

Operation of the circuit starts with resetting the sense capacitances of the fully-differential sense capacitance bridge. Integration capacitances are reset by the Q4 switches before applying the bias signals to the sense capacitance bridge. Meanwhile the CMFB circuit sets the output and input common mode voltage levels of the fully-differential OTA close to 2.5 V, since input and output common mode levels of the OTA are not stable without this operation. If the amount of deviation is large, bias signals applied to the sense capacitance bridge for sensing seismic mass motion can exert force to the seismic mass, which results in oscillation of the seismic mass. After setting the common mode level, and resetting the integration capacitances, complementary bias signals are applied to the fully differential sense capacitance bridge. Due to these bias signals, the charge mismatch is integrated on the fully-differential charge integrator resulting in complementary output shifts at the differential outputs of the charge integrator. The differential comparator senses the shift and generates the complementary output for the force-feedback operation of the seismic mass (masses).

Note that the CMFB circuit does not operate during the integration time of the charge-integrator. This is because of the glitches that are appearing at the output of the fully-differential OTA during the switch-capacitor CMFB circuit operation as shown in Figure 5.20. Another cause is to prevent CMFB circuit to affect the charge integration operation of the fully-differential OTA.

Figure 5.23 (a) shows the simulation result for a capacitance mismatch of 2 fF for each differential bridge (C2 is higher for the left differential bridge and C3 for the right differential bridge). The calculated differential output voltage is -20 mV where as the simulated is -19.94 mV. Figure 5.23 (b) shows the simulation for the same capacitance mismatch but values of the capacitors of each differential bridge are reversed. The differential output voltage is 19.93 mV.

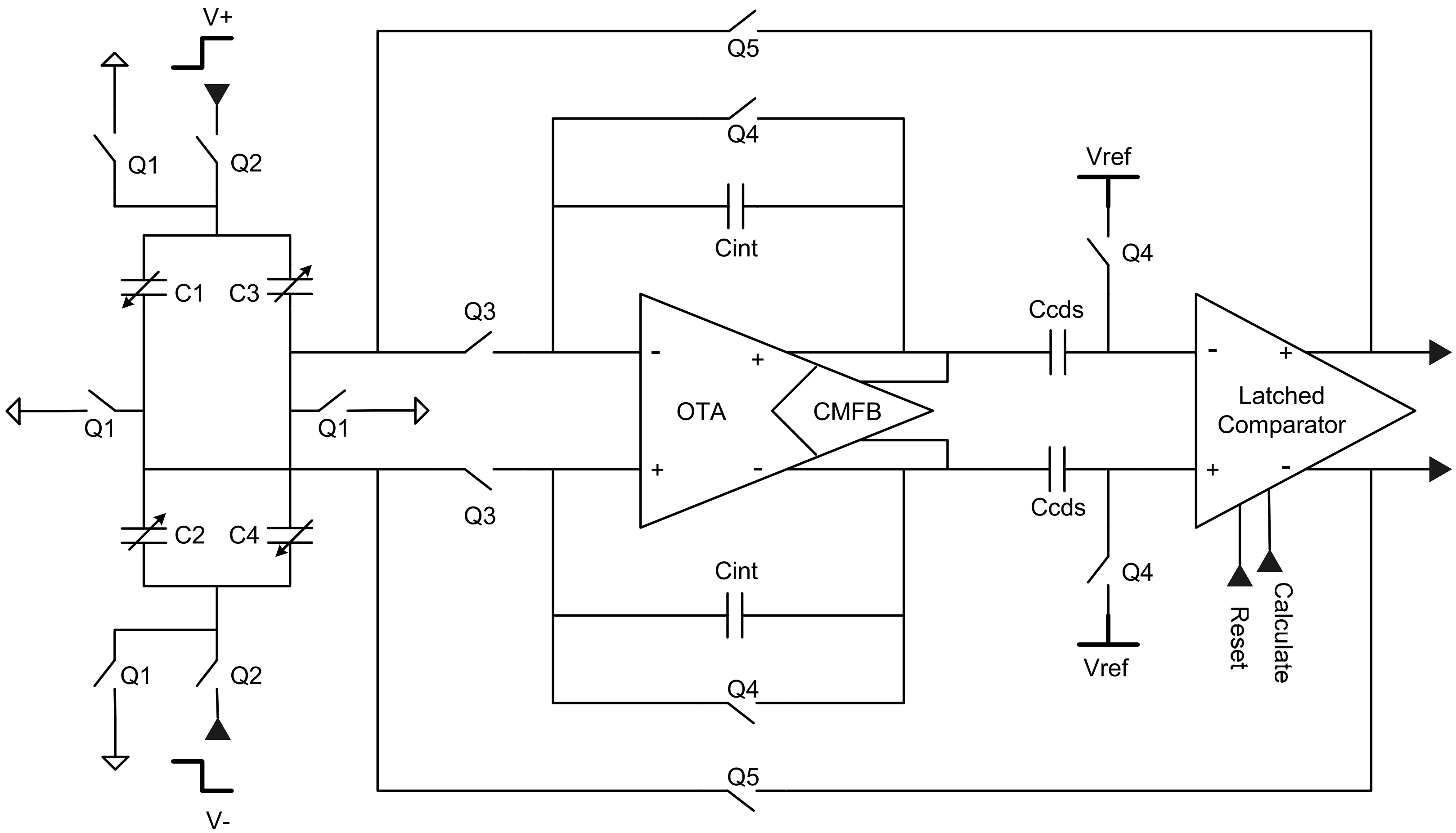

Figure 5.22 The schematic of the fully-differential readout circuit.

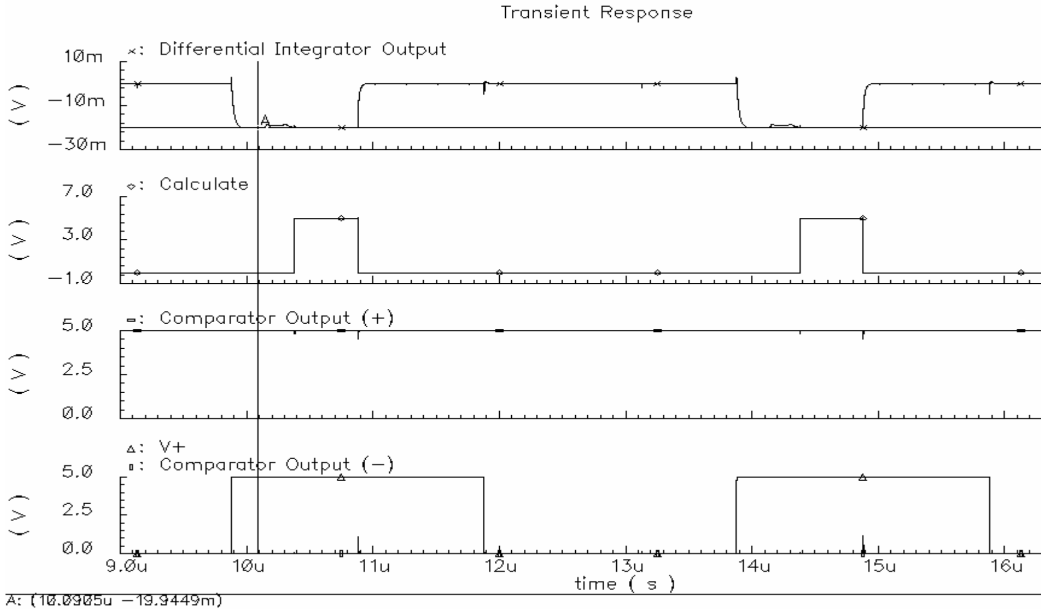

(a)

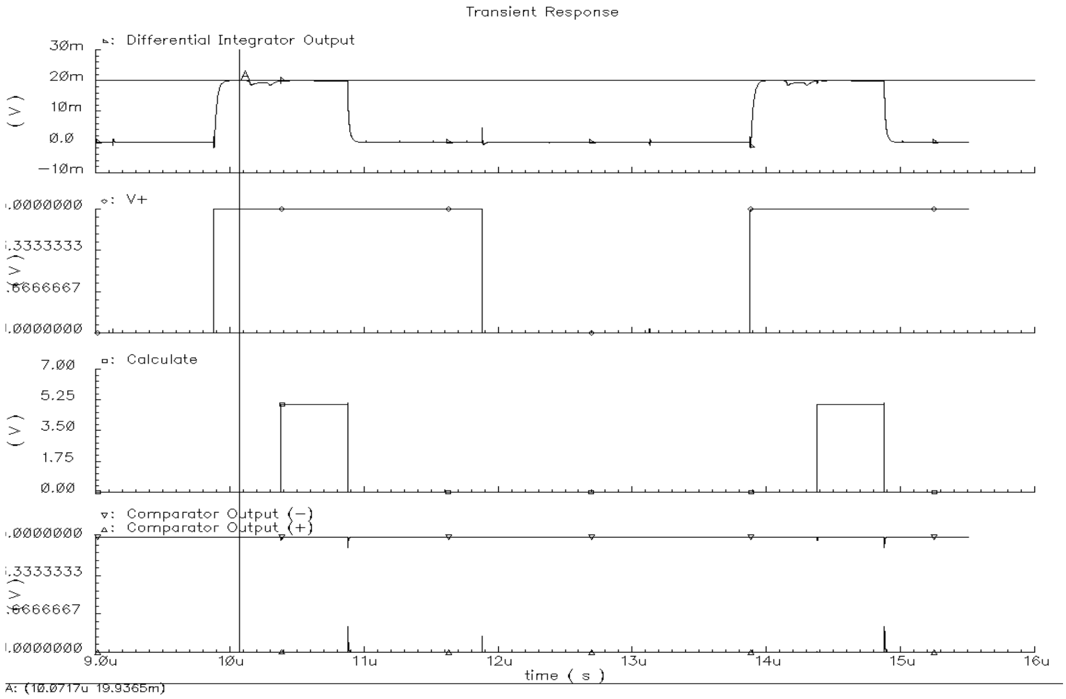

(b)

Figure 5.23 The open-loop simulation of the fully-differential readout circuit for a capacitance mismatch of 2 fF for each differential bridge. (a) C2 is higher for the left differential bridge and C3 for the right differential bridge, (b) values of the capacitances are reversed.

5.3.3 Digital Control Signal Generation

Digital signals controlling the operation of the fully-differential readout circuit is the same with that of the single-ended readout circuit, which are described in Section 5.2.5. There is an additional digital circuit that is generating the necessary non-overlapping clock signals for the operation of the CMFB circuit. Figure 5.24 shows the circuit that is used for non-overlapping clock generation. The circuit consists of two cross-coupled NOR gates with delay elements connected to their outputs. Delay element consists of small sized inverters with dummy inverters as capacitive loads. Non-overlapping clock outputs are synchronized with reset operation of the charge integrators (refer to Section 5.3.2), and therefore the CMFB circuit operates only when the fully-differential OTA is connected in negative feedback mode.

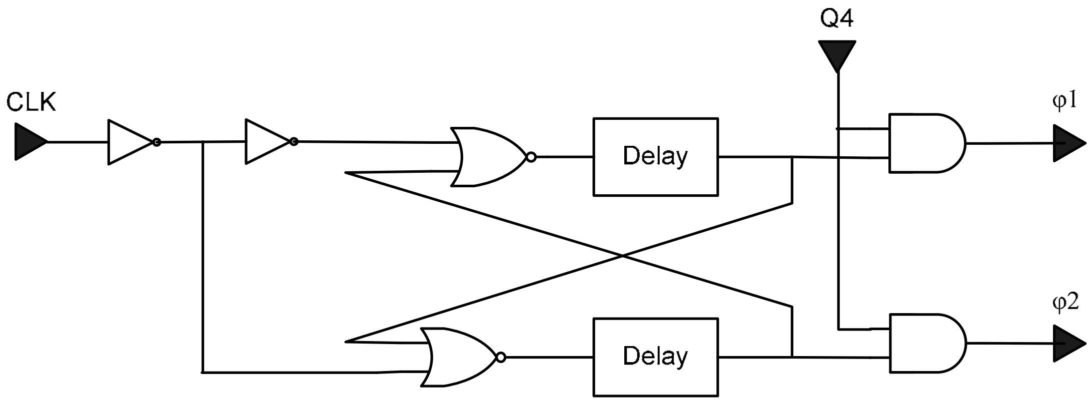

Figure 5.24 The schematic of the non-overlapping clock signal generator circuit.

5.4 On Chip Testing of Charge Integrators

On-chip test capacitances are included in the designed chip for testing the proper operation of the charge integrators. These capacitances consist of imbalanced capacitive bridges simulating the sense capacitances of the accelerometers. These capacitance bridges are connected to the input of the charge integrators through switches. These switches are controlled with a decoder circuit. Figure 5.25 shows the structure of the test capacitance bridges, and Table 5.7 gives the values of these test capacitances. There are three differential bridges for the single-ended charge integrator and four for the fully-differential charge integrator. An eight-bit decoder is necessary for controlling the connection of these bridges to the inputs of the charge integrators including the external accelerometer connection.

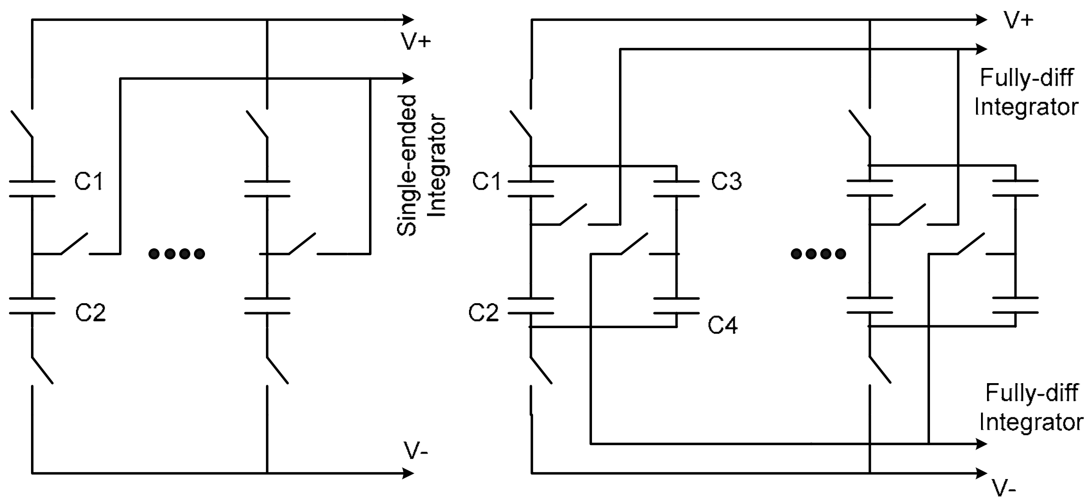

(a) (b)

Figure 5.25 The structure for connecting test capacitances to (a) the single-ended and (b) fully-differential readout circuit. Each capacitance bridge is connected to the charge integrators by closing the switches.

Table 5.7 Values of the test capacitances with notation used in Figure 5.25.

		C1 (fF)	**C2 (fF)**	**C3 (fF)**	**C4 (fF)**
Fully Differential Bridge	1	204.91	195.8	195.8	204.91
	2	549.3	450.7	450.7	549.3
	3	210.3	190.4	190.4	210.3
	4	525.1	474.5	474.5	525.1
Differential Bridge	5	195.9	204.9		
	6	190.4	210.3		
	7	450.6	549.2		

5.5 Unity-Gain Improved Buffer Capacitive Interface Circuit Design

In addition to the readout circuits designed for the MEMS capacitive accelerometer, another interface circuit for sensing the motion of a capacitive gyroscope is designed and fabricated with a 0.8 μm n-well CMOS process. This circuit can be used in the future while implementing an inertial measurement unit (IMU), where three accelerometers and three gyroscopes are used.

The operation principle of a capacitive MEMS gyroscope is given in [115]. The structure of the MEMS gyroscope that is developed at METU is shown in Figure 5.26 [116]. The gyroscope operates according to the Coriolis coupling principle. The proof mass is vibrated along drive mode (Figure 5.26 (a)). When the gyroscope is rotated around substrate plane, the proof mass starts to vibrate along the sense mode (Figure 5.26 (b)) due to Coriolis coupling [115]. Since sense and drive mode capacitances of the structure is very small, and these nodes are highly capacitive, there is a need for a capacitive interface, such as a buffer with high input impedance. Such an improved buffer structure is proposed in [100], where it has very high input impedance. A modified version of this structure is implemented in this work, where both the gain and the input impedance of the structure are improved further.

Figure 5.27 shows the flipped version of the improved buffer structure proposed in [100], when drawn in the n-well CMOS process. The circuit is biased with an external resistor through a diode connected PMOS transistor. There are two outputs of the circuit. The first one is the shield output, which is used for bootstrapping. The other one is the off-chip output, capable of driving resistive loads. C_L represents the capacitance that is driven by the shield output. The key issue in the design is the minimization of the input capacitance and achieving a buffer gain close to unity.

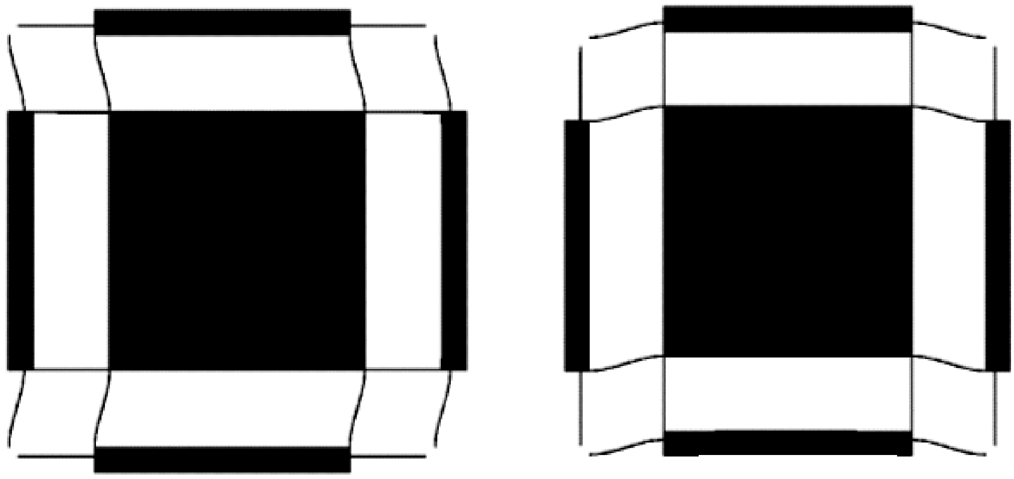

(a) (b)

Figure 5.26 Structure of the MEMS gyroscope developed in METU. (a) Drive mode of the gyroscope, (b) sense mode of the gyroscope.

There are three components of the total input capacitance, which are due to the input transistor, M1. These components are gate-to-source (C_{gs}), gate-to-drain (C_{gd}), and gate-to-bulk (C_{gb}) capacitances. These capacitances can be minimized by forcing the source, bulk, and drain voltages to track the gate voltage of the input transistor [100]. The small-signal gate-to-source voltage of the input transistor, M1, is inversely proportional with the open-loop gain of the amplifier, which provides desired reduction in the C_{gs}. On the other hand, connecting the bulk terminals to the source terminals (n-well process) and utilizing the open-loop gain of the amplifier on the reduction of the gate-to-source capacitance can reduce C_{gb}. Transistors M3 and M4 are included for the reduction of the gate-to-drain capacitances,. These transistors are copying the drain voltage of M2 to the drain of M1, thus forcing the drain voltage of the M1 to track the gate voltage [100]. This lowers the C_{gd} component of the total input capacitance.

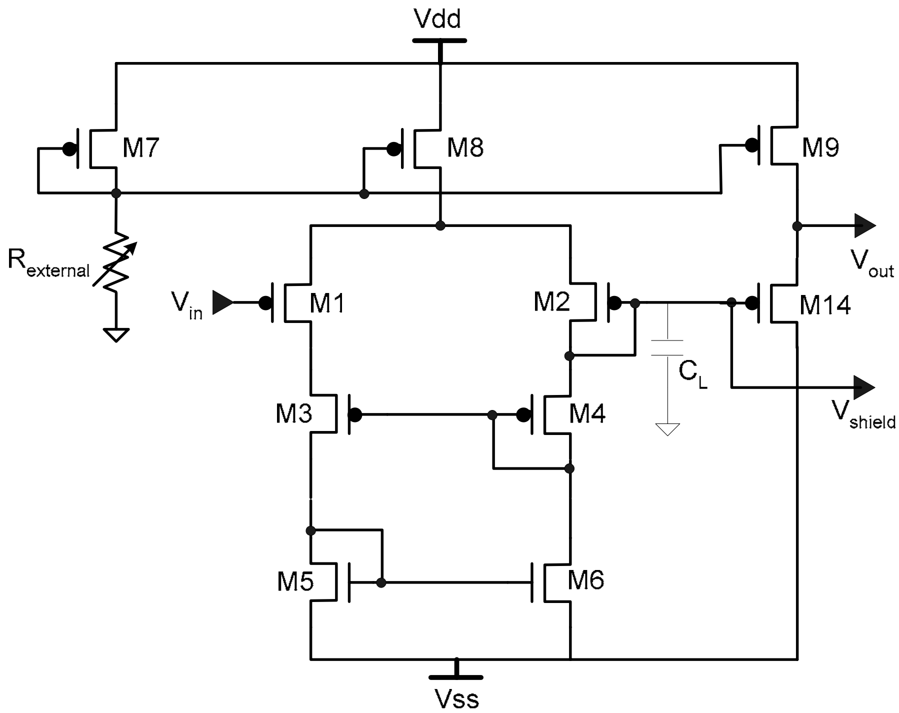

Figure 5.27 Schematic of the improved buffer structure proposed by [100].

Figure 5.28 shows the proposed buffer structure, which is the modified version of the buffer structure shown in Figure 5.27. Circuit operates with +2.5 V and -4.0 V, with a biasing resistor of 15 kΩ. Current mirrors M3, M4, and M5, M6 are replaced with cascode current mirrors in this structure. This both increases the open-loop gain and decreases the input capacitance of the buffer. Table 5.8 compares the gain transfer functions and input impedances of the two improved buffer structures, where r_o is the output resistance of a transistor and g_m is the transconductance. Common source output stages are excluded in the calculations. The new buffer design has a lower input capacitance and also higher gain than the buffer structure of [100].

One drawback of the new circuit is the decreased output voltage swing due to the high number of cascaded transistors. Fortunately, this does not have the primary importance, since output voltage of the circuit is expected to be in the order of millivolts.

Besides the capacitances associated with the input transistor of the improved buffer structure, there are also routing capacitances that directly adds to the input capacitance of the improved buffer structure. In order to minimize the capacitance due to the routing lines, a technique called bootstrapping is used. Figure 5.29 describes this technique. The metal-2 line is carrying the signal coming from the capacitive gyroscope. This metal-2 line is shielded from the conductive substrate with the metal-1 line, which is carrying the shield output of the buffer. Forcing the shield output to have the same potential with the buffer input suppresses much of parasitic capacitance from the signal carrying routing metal to the substrate. The shield output of buffer must be identical with the input voltage for effective shielding, which can be achieved with buffer gain very close to unity.

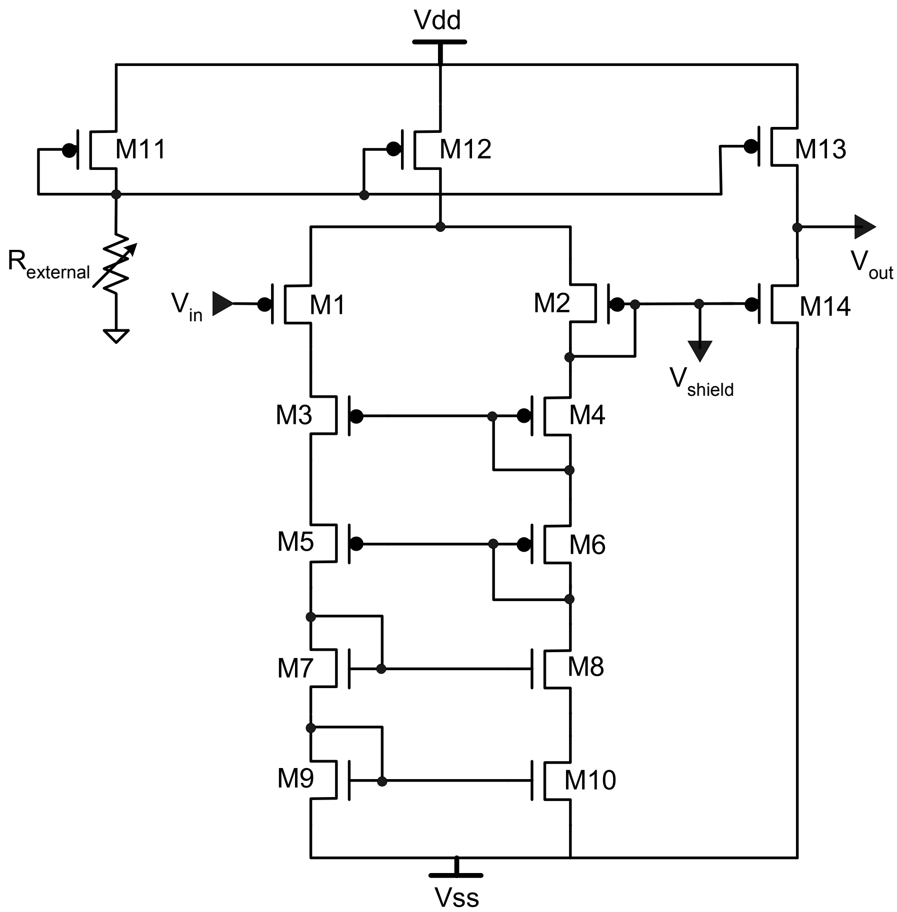

Figure 5.28 The schematic of the proposed improved buffer structure.

Table 5.8 The gain-transfer function and input impedance formulas of buffer circuit in [100] and proposed structure.

	Reference [100]	Proposed
Gain Transfer Function	$\left(1+\dfrac{1}{g_{m,M1}r_{o,M6}}+\dfrac{sC_L}{g_{m,M1}}\right)^{-1}$	$\left(1+\dfrac{1}{g_{m,M1}g_{m,M8}r_{o,M8}r_{o,M10}}+\dfrac{sC_L}{g_{m,M1}}\right)^{-1}$
Input Impedance	$\left[\dfrac{sC_{gs,M1}}{2g_{m,M1}}\left(\dfrac{1}{r_{o,M8}}+\dfrac{1}{r_{o,M6}}+sC_L\right)\right]^{-1}$	$\left[\dfrac{sC_{gs,M1}}{2g_{m,M1}}\left(\dfrac{1}{r_{o,M12}}+\dfrac{1}{g_{m,M8}r_{o,M8}r_{o,M10}}+sC_L\right)\right]^{-1}$

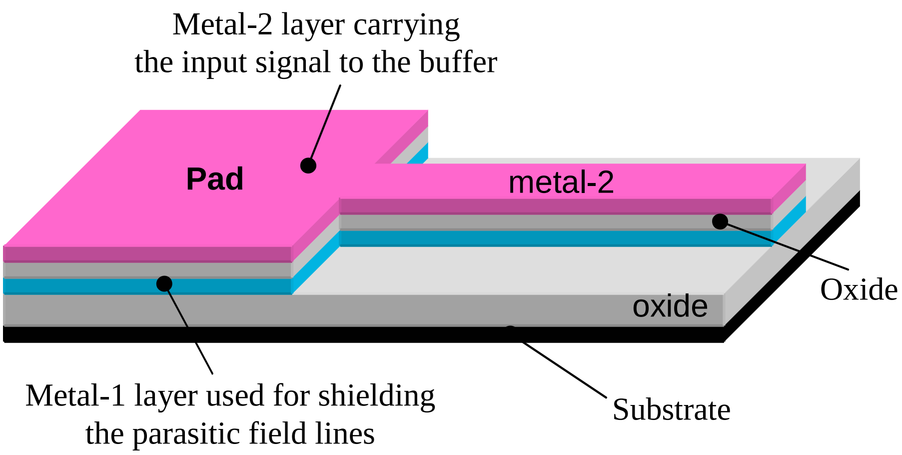

Figure 5.29 Bootstrapping of the signal metal-2 line with metal-1 line carrying the shield output of the improved buffer structure.

The improved buffer structure is designed for sensing the drive and sense mode motions of a capacitive MEMS gyroscope. Connecting the high impedance buffer input to a capacitive gyroscope addresses a need for DC biasing of the high impedance input node of the improved buffer. This is achieved with a minimum size PMOS transistor operating in sub-threshold region connected between the input node of the improved buffer and ground. The DC level of the input node is not defined, and the output of the buffer saturates without this DC biasing. Simulations of the circuit is performed assuming a capacitance of 0.035 fF/μm^2 between the metal-1 and metal-2, and also 0.03 fF/μm^2 between metal1 and field oxide, in order to calculate the capacitance that the shield output drives [117]. Table 5.9 gives the simulation results of the proposed improved buffer structure. As can be seen from the results, gain of the buffer circuit is very close to unity.

Table 5.10 compares the simulation results with the results of [100]. As expected, the gain is increased and also input capacitance of the buffer is reduced with the new improved buffer structure design. Also the rms noise of the circuit is an order of magnitude lower than the rms noise of [100], which is due to the replacement of the diode biasing technique with the transistor biasing technique.

Table 5.9 Simulation results of the proposed improved buffer structure.

Shield Output Gain	0.999997
Output Gain	0.9804
Offset Between Shield and Input	~ 0 V
Input Capacitance w/o biasing Tr	2.2637 fF
Input Capacitance with biasing Tr	22.0 fF
Bandwidth	13.7 MHz
Rms output Noise (50 kHz)	6.32 μVrms
Output Voltage Swing	2.0 Vpp
Power Dissipation	1.5 mW

Table 5.10 Comparison of the simulation results of proposed improved buffer with improved buffer structure of [100].

	Reference [100]	**Proposed**
Input Capacitance	4.32 fF	2.2637 fF
Shield Output Gain	0.9965 V	0.999997 V
Rms Noise (50 kHz)	81 μV	6.32 μV

5.6 CMOS Chip Designed for the Readout Circuits

Designed single-ended and fully-differential readout circuits, and improved buffer structure are fabricated in the AMS 0.8 µm n-well CMOS process. Test results of these designs are presented in the next chapter. Figure 5.30 shows the complete photograph of the fabricated chip including the readout circuits. The bonding pad list for the readout circuits are given in Appendix B.

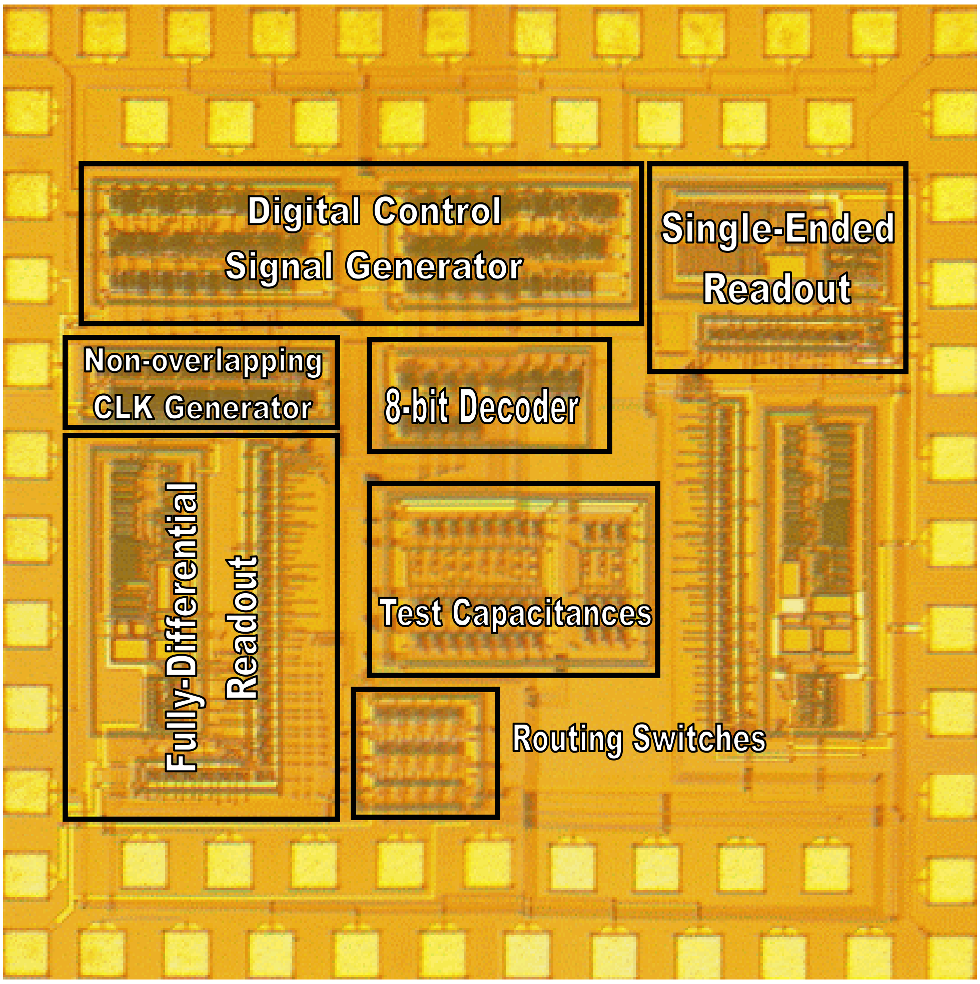

Figure 5.30 The photograph of the fabricated chip designed for readout circuit. The circuit occupies an area of 4 mm^2.

5.7 Summary

Performance of capacitive accelerometers majorly depends on the minimum detectable capacitance change. Therefore, there is a need for a high performance readout circuit capable of detecting capacitance changes in the order of attofarads. This chapter describes the design and implementation of two different readout circuits capable of operating in both open and close loop and detecting small capacitance changes. Moreover, these readout circuits are capable of performing the force-to-rebalance operation.

Two different readout circuits are designed, namely, the single-ended readout circuit and the fully-differential readout circuit. The fully-differential approach is advantageous in terms of reducing the common-mode errors at the output of the charge integrator circuit. Both circuits use CDS in order to cancel the charge integrator offset. The latched comparator at the output of the charge integrator defines the feedback voltage that will be applied to the seismic mass of the accelerometer for the force-feedback operation.

In addition to these readout circuits, an improved buffer having very high input impedance is designed for sensing the drive and sense mode motions of a capacitive MEMS gyroscope. This circuit can be used with gyroscopes, when an inertial measurement unit is required to be implemented in the future.

CHAPTER 6

FABRICATION AND TEST RESULTS

This chapter presents the fabrication and test results of the MEMS accelerometers, fabricated CMOS readout and interface circuits, as well as the open-loop tests of the hybrid-connected accelerometer and single-ended readout circuit. This chapter also includes the tests of the improved buffer capacitive interface circuit hybrid connected to a capacitive microgyroscope sample. Section 6.1 presents the testing methods and test results of the individual accelerometer prototypes. Section 6.2 gives the test results of the capacitive readout and interface circuit. Section 6.3 presents the test results of the improved buffer circuit hybrid-connected to a gyroscope sample. Section 6.4 gives the test results of the single-ended readout circuit hybrid connected to an accelerometer prototype. Finally, Section 6.5 presents the summary of the chapter and discusses the test results.

6.1 Fabrication and Test Results of Individual Accelerometers

Capacitive MEMS accelerometers are fabricated with the process steps described in Chapter 3. Optimization of the structural mold resist is difficult due to the sensitivity of the SJR 5740 resist to cleanroom temperature and humidity. Therefore, an important step in the process is the development of the SJR 5740 resist. During development of the resist, feature size of the structural resist increases and gap spacing of the comb fingers decreases due to the lateral development of the unexposed resist. This also results in wider spring widths from the original design. From the SEM views, this expansion is estimated to be 1.5-2.5 µm, changing due to the curved surface of the hotplate which results in different soft bake temperatures throughout the wafer. The effect of this expansion on the performance of the accelerometers is the change in the resonant frequency due to the expansion in springs, as well as, the change in the total sense capacitance. For lateral springs, the spring constant is proportional to the third power of the width, thus expansion in the width of the springs results in an increase in the resonant frequency of the structures, as described in Section 2.3.

In addition to the feature size and gap spacing change due to the structural mold resist, the thickness of the fabricated devices also vary throughout the wafer. Thickness of the nickel structural layer is estimated between 15 µm and 17 µm. This is due to the variation of electroplating thickness through out the wafer surface. It is a well known fact that electroplating occurs much faster at the edges of the wafer than the center of the wafer due to the increased number of field lines at the edges of the wafer. This affects both the total sense capacitance of the structures and also weight of the seismic mass.

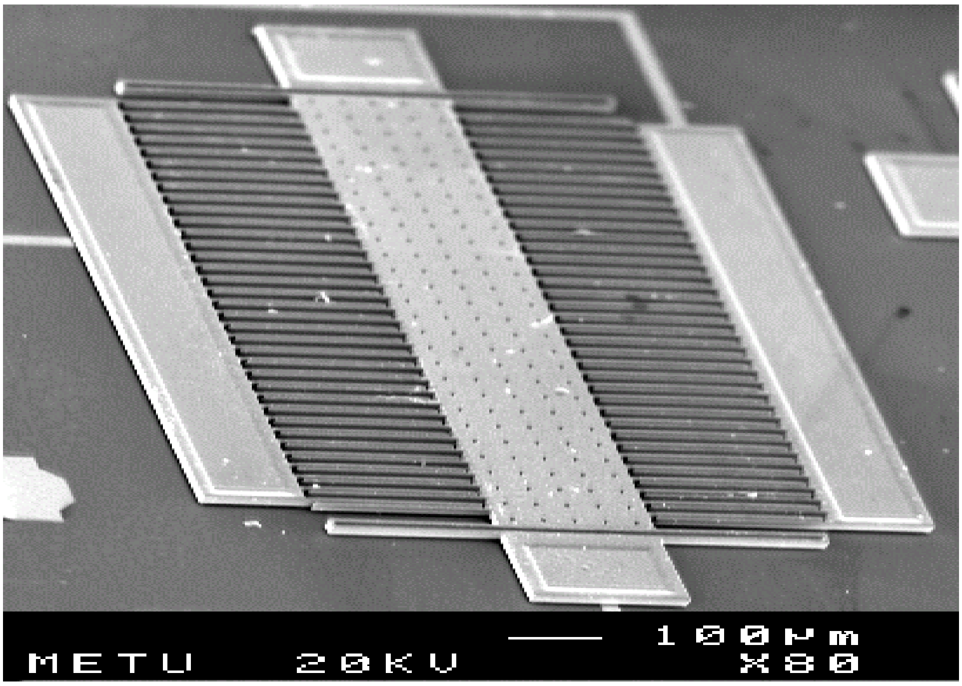

Figure 6.1 SEM picture of a fabricated accelerometer with optimized fabrication process.

Figure 6.1 shows the SEM picture of a fabricated accelerometer with the optimized fabrication process, and Figure 6.2 shows the spring, comb fingers, and etch holes of the same accelerometer, as well as, demonstrating the gap between the seismic mass and substrate.

A test structure is used for stress characterization of the electroplated nickel, whose deflected photograph is shown in Figure 6.3. The deflection direction of the test structure shows the type of the residual stress, which is compressive.

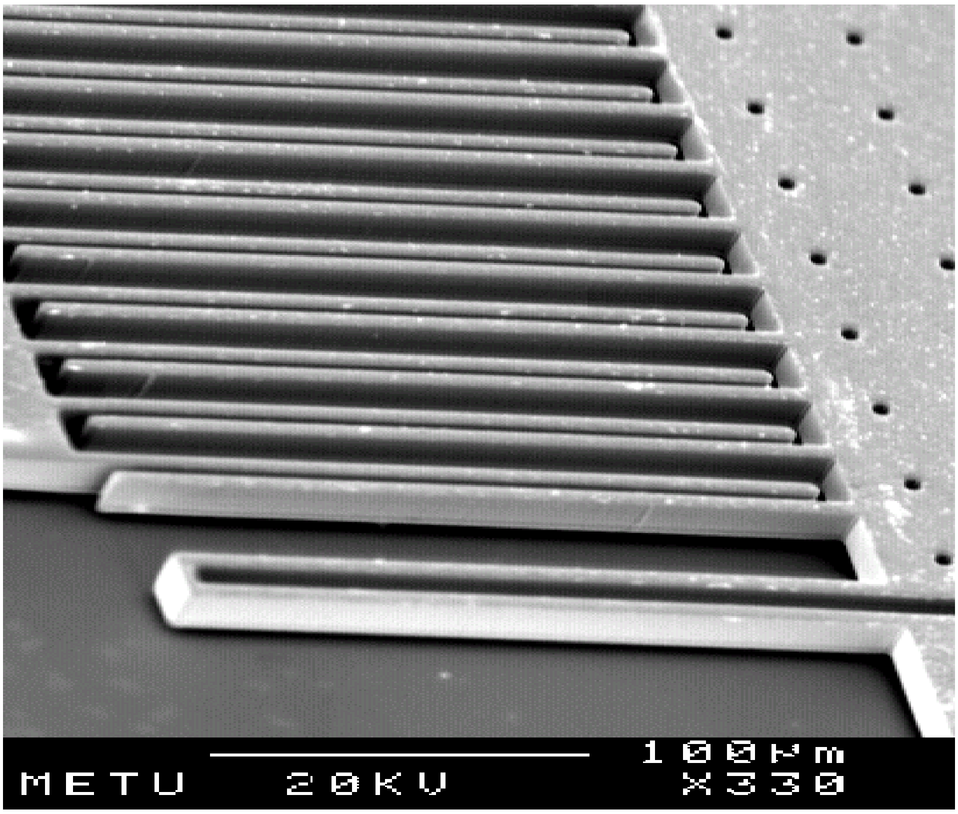

Figure 6.2 SEM picture of comb fingers, etch holes on the seismic mass, and spring of the accelerometer of Figure 6.1.

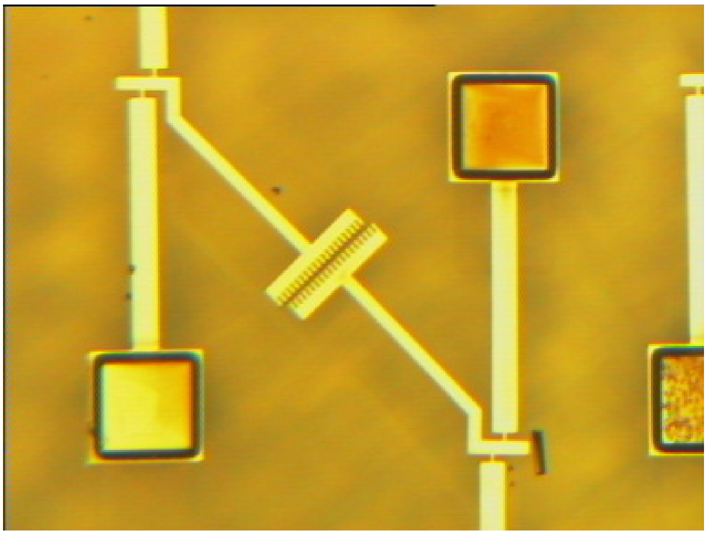

Figure 6.3 Characterization structure for the nickel electroplating. There is compressive residual stress in the electroplated nickel structural layer.

Test methods and tests of individual accelerometers are presented in the following parts of this section. Moreover, these test results are compared with the calculated results in the following sections, which are updated according to the achieved process results. The calculated results are updated assuming that the structural thickness is 16 µm, the finger gaps decrease 2 µm compared to the original gaps on the designed mask, and the spring widths increase 2 µm compared to the widths on the designed mask.

6.1.1 Tests Performed on the Accelerometer Prototypes

Various tests are performed on the fabricated micromachined accelerometers for determining their performance values and also evaluating the fabrication steps. There are mainly four different tests that are performed on the designed prototypes: the stiction test, the short circuit test, the sense capacitance measurement test, and the resonant frequency test.

First test, namely the stiction test, is performed using a probe station. Aim of this test is to evaluate the releasing of the accelerometer structure with sacrificial layer etching. In this test, the sample is placed under the microscope of the probe station, and a probe tip is used to move the seismic mass of the accelerometer through the sensitive axis of the structure. It is important to move the structure in its sensitive axis, otherwise possible deformations in the springs of the accelerometer can occur, resulting in a damaged accelerometer sample. Fortunately, we have not encountered in a stiction problem throughout the releasing of many accelerometers.

The second test is the short circuit test, the aim of which is, to check the possible shorts between the rotor fingers and stator fingers of the accelerometer. The sample is placed under the microscope of the probe station. With the help of the probe tips and a multimeter, any short circuits between the rotor fingers connected to the seismic mass and stator fingers are checked. There were some accelerometers, which failed in this test, and therefore, they are eliminated from the further tests.

The third test for the samples having passed above two tests is the sense capacitance measurement test. Two sense capacitances of the accelerometer forming the differential bridge are measured and compared. This test also shows the mismatch between the two sense capacitances. The sense capacitance measurement is also performed with the help of a probe station. An impedance analyzer is used for measuring the capacitance between the rotor and stator fingers. However, measuring capacitances in the order of femtofarads need special attention because parasitic capacitances due to the probes of the probe station can affect the measurement results. For this reason, the impedance analyzer must be calibrated before each measurement. For the short circuit calibration, probe tips that are connected to the impedance analyzer are first short circuited on the anchor of the accelerometer. Then, for the open circuit calibration, one of the probes is moved to the other anchor, where the measurement will be taken, and the other probe is not moved from its location. Then, before touching anchor with the probe, the open circuit calibration is performed. With these measurements much of the parasitic capacitances between the probes are eliminated. It should also be noted here that the calibration must be renewed, if the probe tips are moved from their locations.

The last test for the accelerometer prototypes is the resonant frequency measurement tests. This test is performed with a network analyzer and with the help of a probe station. The measurement technique for the resonant frequency test is illustrated in Figure 6.4. Sweeping AC output of the network analyzer is connected to one of the stator electrodes, and the sensing input probe of the network analyzer is connected to the other electrode. If there is a DC bias connected to the seismic mass of the accelerometer, this creates an alternating force on the seismic mass of the accelerometer, Section 2.4.2. This force resonates the seismic mass, when its frequency sweeps through the mechanical resonance frequency of the accelerometer.

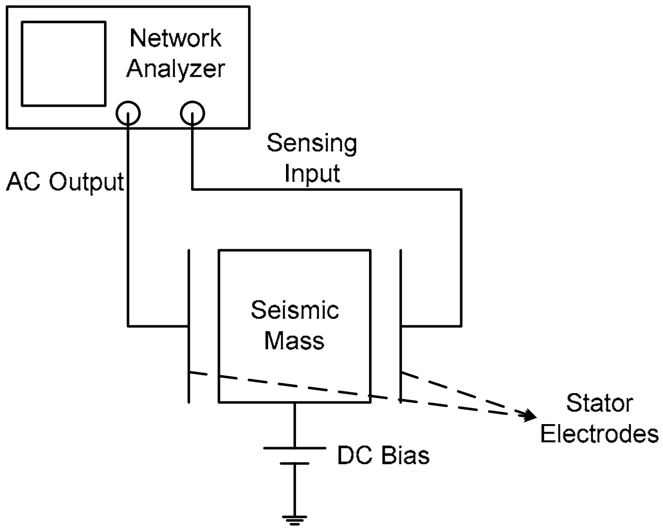

Figure 6.4 Connections of the network analyzer for the resonant frequency tests of the accelerometer samples.

A capacitance variation between the seismic mass electrode and stator electrode, where sensing input of the network analyzer is connected, occurs due to the resonating seismic mass. This capacitance variation creates an alternating current as;

$$I = \frac{\partial Q}{\partial t} = C\frac{dV}{dt} + V\frac{dC}{dt} \tag{6.1}$$

where C represents the capacitance between the seismic mass and stator electrode, and Q is the total charge on the sensing capacitance. Note that the voltage between the seismic mass and sensing electrode is constant, so only the second term contributes to the alternating current. This alternating current is converted to voltage by the resistance and capacitance of the probe of the network analyzer and compared with the drive signal for the magnitude plot. Since vibration of the seismic mass is maximum at resonance, this results in the highest output current. Therefore, we observe a peak at the network analyzer. This peak represents the resonant frequency of the accelerometer.

6.1.2 Test Results of Prototype-1

This prototype has three different versions according to their spring length, and each version has subgroups according to their finger length and fingers gaps. For all versions, only 5 µm spaced fingers could be fabricated. Moreover, accelerometers having cross-over type sense fingers could not be fabricated since the development of the small anchors could not be completed. This makes the adhesion of the small anchors to the substrate weaker. Thus, during releasing, fingers having small anchors are pealed off from the substrate.

Figure 6.1 and 6.2 show the SEM picture for a sample having 200 µm length fingers and also having 200 µm. Table 6.1 indicates the devices passing all the tests which are described in Section 6.1.1 (Note that originally finger spacing is 5 µm for all devices that could pass the tests). Moreover this table gives the calculated values of each fabricated accelerometer type according to the optimized process conditions.

Figure 6.5 shows the total sense capacitance measurement versus percentage error between the two sense capacitances for several samples. Devices are divided into two groups during sense capacitance measurements, with comb fingers having 90 µm overlap length and 200 µm overlap. Measurement results show large variation from sample to sample due to different photolithography resolution throughout the wafer. Moreover, measured capacitance values are higher than the expected sense capacitance values. That is due to the parasitic capacitances between the comb fingers. Section 6.4 presents the simulation of these parasitic capacitances, while characterizing the performance of accelerometer hybrid-connected to the readout circuitry.

Table 6.1 Updated performance values for prototype-1 according to optimized process conditions. "SW" corresponds to spring width, "FOL" corresponds to finger overlap length, "FS" corresponds to finger spacing. Detailed description of each version can be found in Section 4.3.1.

	Resonant Frequency (kHz)	SW (μm)	Finger Type	FOL (μm)	FS (μm)	Total SC (fF)	Capacitance Sensitivity (fF/g)
Version1	6.8	5	1	90	3	297	0.53
				200	3	660	1.18
Version2	3.7	5	1	90	3	297	1.79
				200	3	660	3.98
Version3	2.4	5	1	90	3	297	4.26
				200	3	660	9.84

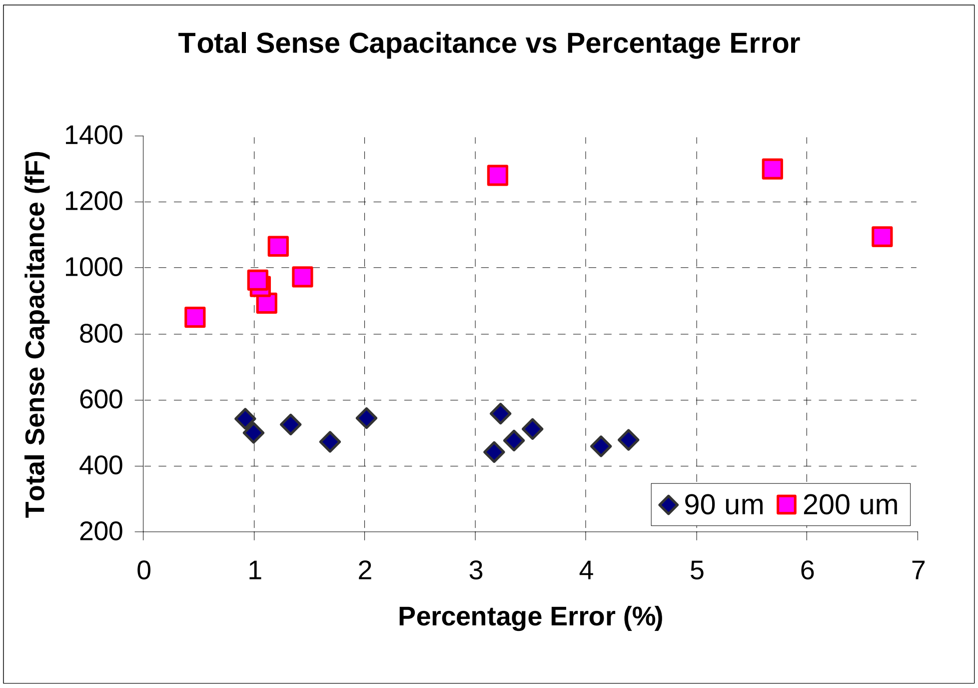

Figure 6.5 The measured total sense capacitance versus mismatch between the sense capacitances for prototype-1. Increase in the sense capacitance is due to the parasitic capacitances.

Resonant frequency measurements are performed for each sample as described in Section 6.1.1. Resonant frequencies of samples are measured under same condition, for an AC excitation voltage of 1.25 Vrms and DC bias voltage of 5 V. It is important to apply the smallest possible DC voltage to the mass to prevent the electrostatic spring constant effect for varying gap sense fingers. Figure 6.6 shows a resonant frequency measurement result for an accelerometer. Figure 6.7 shows the measurement results for each version of accelerometers. The measured frequencies are close to the calculated values considering the thickness variation throughout the wafer. Variation in the resonant frequencies for each version is again due to varying spring widths for each sample.

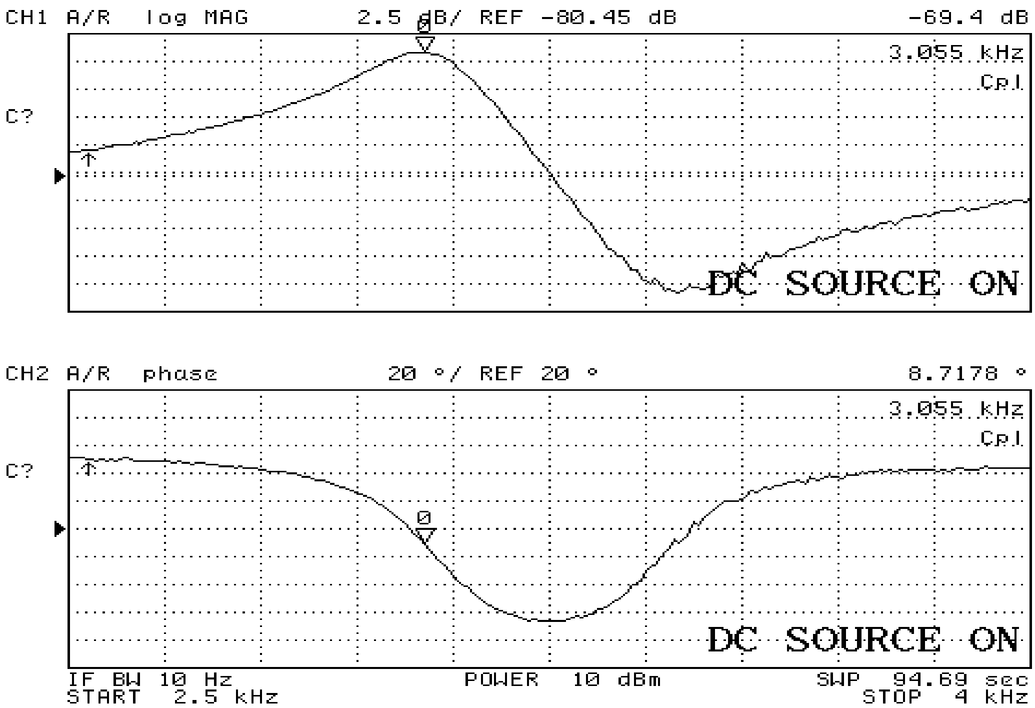

Figure 6.6 The output of the resonant frequency measurement for an accelerometer sample.

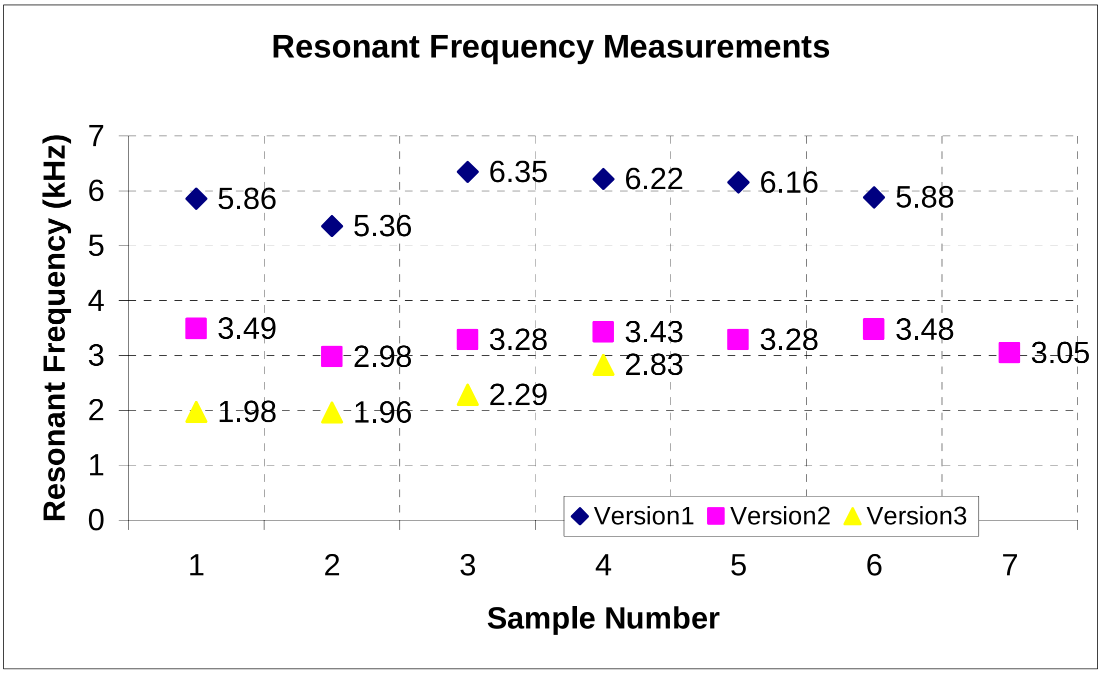

Figure 6.7 The resonant frequency measurements for several samples from each version of prototype-1. Variation in the resonant frequency is due to the varying spring width, related width the photolithography resolution change throughout the wafer.

6.1.3 Test Results of Prototype-2

Figure 6.8 shows the SEM picture of the fabricated prototype-2 accelerometer. Table 6.2 shows the updated performance values of two versions of this prototype according to the optimized fabrication conditions. Fabricated devices have 5µm and 4µm drawn sense finger gaps, but there is a reduction of 2 µm in the finger gap on average. Some devices have more and some have less change in the gaps due to the changing photolithography resolution throughout the wafer. Therefore, resonant frequencies and sense capacitances of the samples are not matching well with each other.

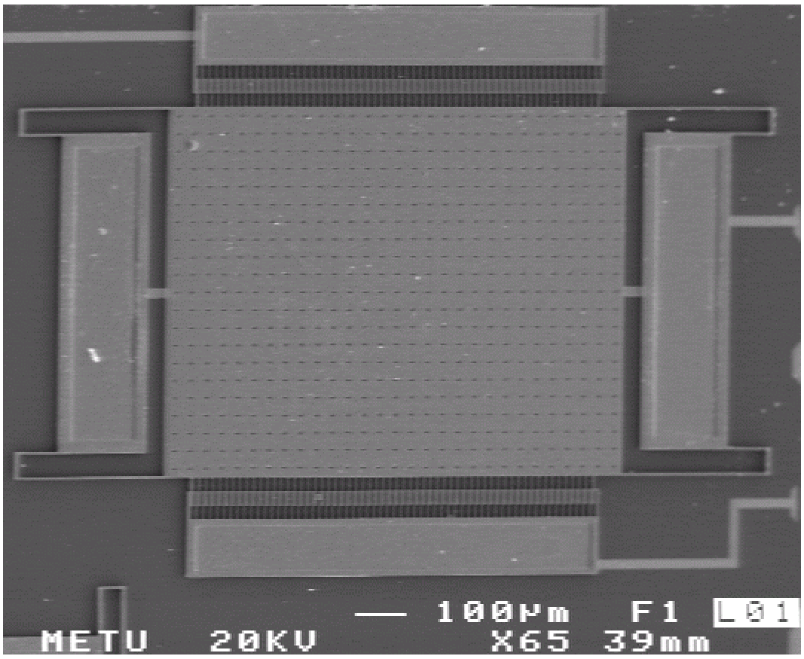

Figure 6.8 SEM picture of the fabricated prototype-2 accelerometer.

Table 6.2 Updated performance values for prototype-2 according to the optimized process conditions. “FL” corresponds to finger length, “FOL” corresponds to finger overlap length, “FN” corresponds to finger number, and “FS” corresponds to finger spacing.

	Resonant Frequency (kHz)	FL (μm)	FOL (μm)	FN (μm)	FS (μm)	Total SC (fF)	Capacitance Sensitivity (fF)
Version1	2.03	30	10	138	2	195	1.17
				120	3	113	0.68
Version2	2.03	60	30	138	2	586	1.17
				120	3	339	0.68

Figure 6.9 shows the percentage error between the sense capacitances versus total sense capacitance of the two versions of prototype-2, and Figure 6.10 shows the measured resonant frequencies of the prototype-2 samples. Measured results are close to the calculated ones. Finally, Figure 6.11 gives resonant frequency test result of a sample. Note that Q factor of this prototype is much higher than the prototype-1 due to varying-area type comb fingers.

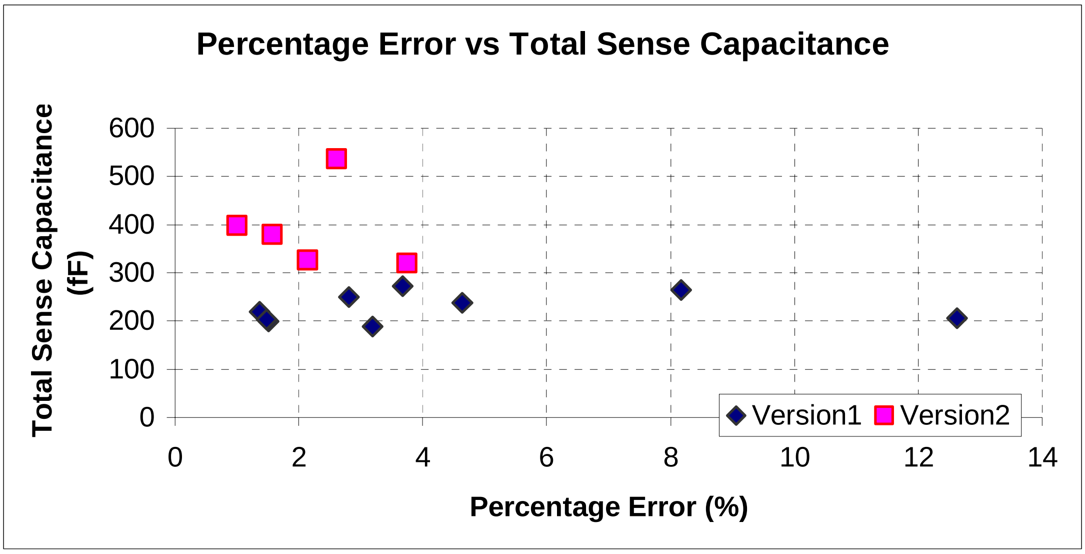

Figure 6.9 The percentage error versus measured total sense capacitance values for prototype-2.

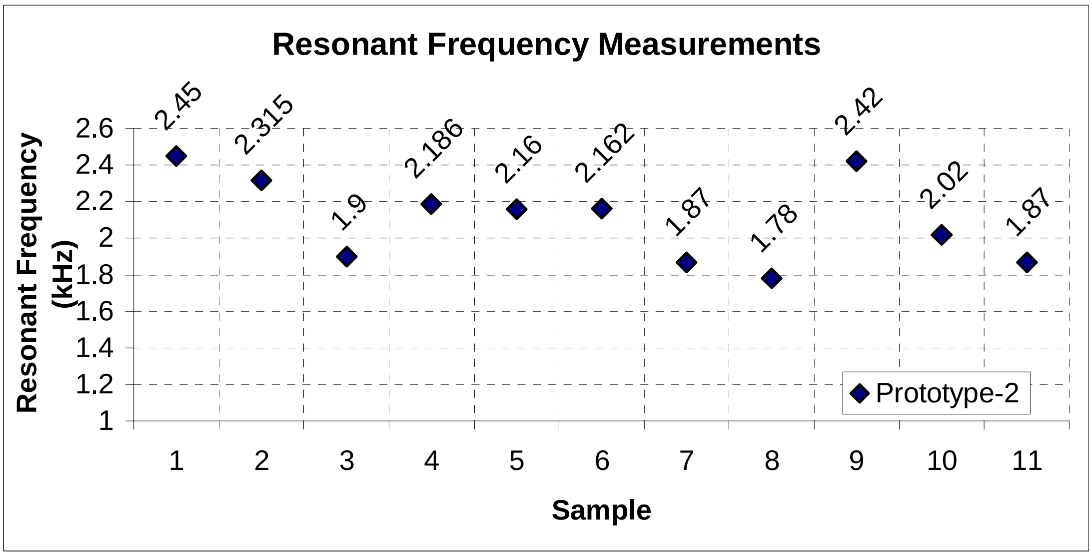

Figure 6.10 The measured resonant frequencies for prototype-2.

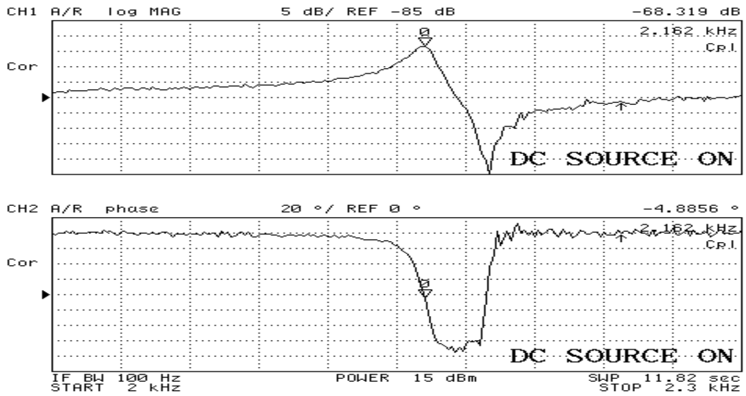

Figure 6.11 A resonant frequency measurement for prototype-2 with 20 Vdc bias and 1.25 Vrms AC excitation.

6.1.4 Test Results of Prototype-3

This structure suffers from the compressive residual stress of the electroplated structural nickel layer. Due to the large seismic mass of the structure, center of the seismic mass curls up, while edges curl down touching to the substrate. Therefore, these structures could not be effectively released. Figure 6.12 shows the fabricated device, where the seismic mass is deflected along its sensitive axis, and Figure 6.13 shows the edge of the seismic mass touching the substrate.

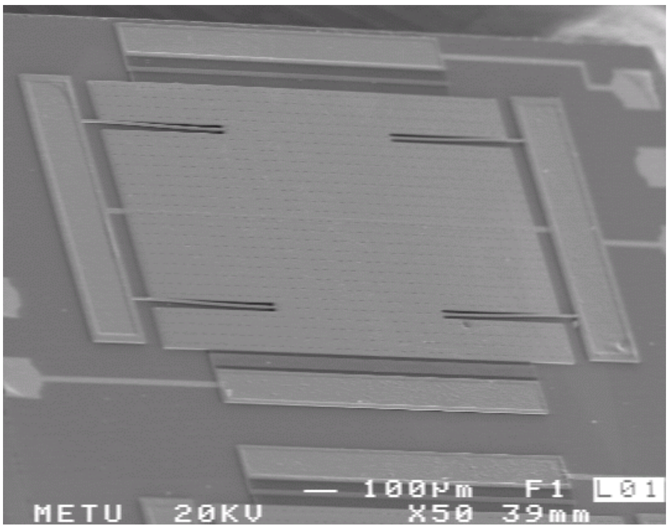

Figure 6.12 SEM picture of the fabricated prototype-3, where the seismic mass is deflected along its sensitive axis.

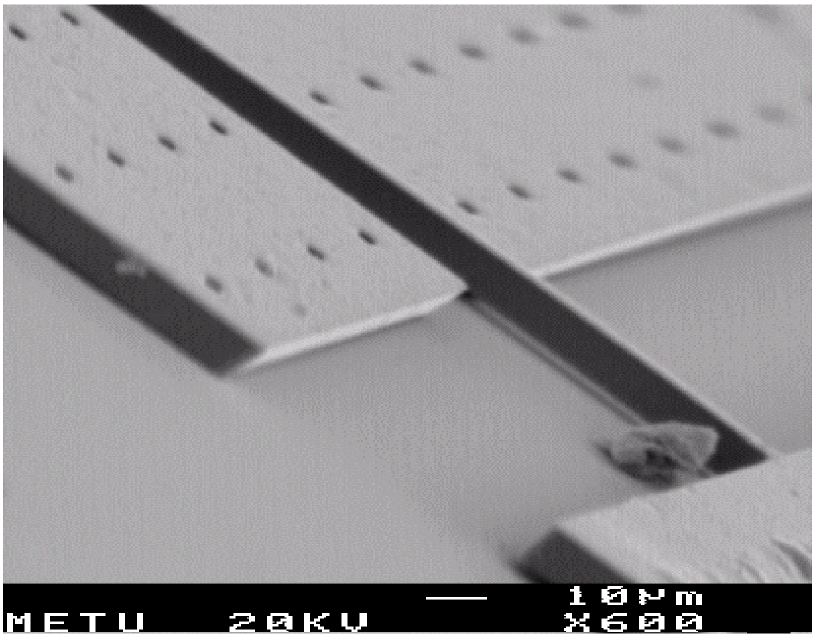

Figure 6.13 SEM picture of seismic mass of prototype-3. Edge of the seismic mass is touching the substrate.

6.1.5 Test Results of Prototype-4 and Prototype-5

From these two prototypes, samples having only 5μm finger spacing could be fabricated. Table 6.3 shows the updated performance values for prototype-4 and prototype-5 according to optimized process conditions. During these calculations 3 μm reduction is assumed specific for these two prototypes based on the SEM observations. Figure 6.14 shows the fingers of these devices, where finger gaps are around 2 μm. Measured capacitance and resonant frequencies for these two prototypes are given in Table 6.4. Moreover, resonant frequency measurement for a sample is given in Figure 6.15 for prototype-4. Note that Q factor of the device is higher than the prototype-1 due to lower overlap length of the sense fingers.

Table 6.3 Updated performance values of prototypes 4 and 5 according to optimized process conditions. "FOL" corresponds to finger overlap length, "FN" corresponds to finger number, "FS" corresponds to finger spacing, and "SC" corresponds to sense capacitance.

	Resonant Frequency (kHz)	FOL (µm)	FN (µm)	FS (µm)	Total SC (fF)	Capacitance Sensitivity (fF/g)
Prototype-4	3.26	50	76	2	269	3.14
Prototype-5	2.31	50	76	2	269	6.25

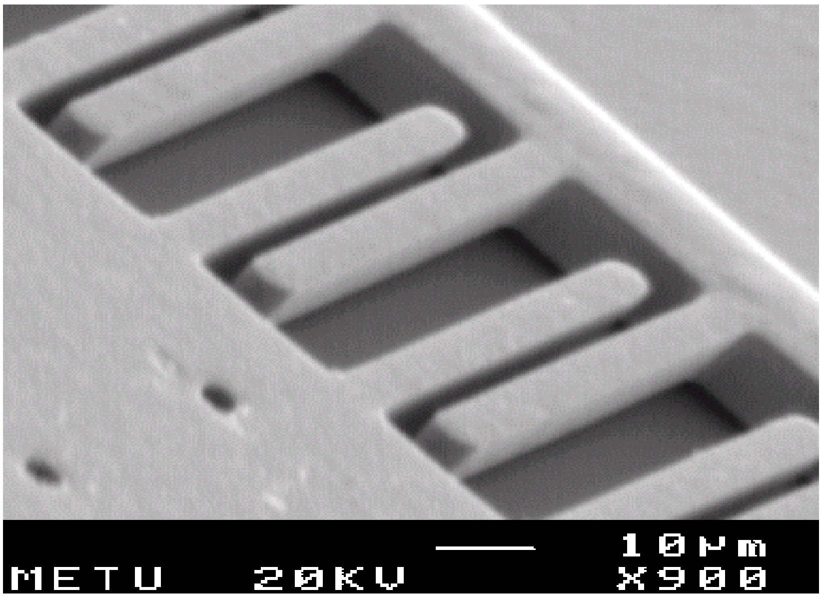

Figure 6.14 SEM shows the 2µm finger gaps for prototype-4.

Table 6.4 Measurement results for the prototypes 4 and 5.

	Sample	Resonant Frequency	Total Sense Capacitance	Sense Capacitance Mismatch (%)
Prototype-4	1	3.705	347	4.68
	2	3.69	322	1.51
Prototype-5	1	2.28	285	1.14

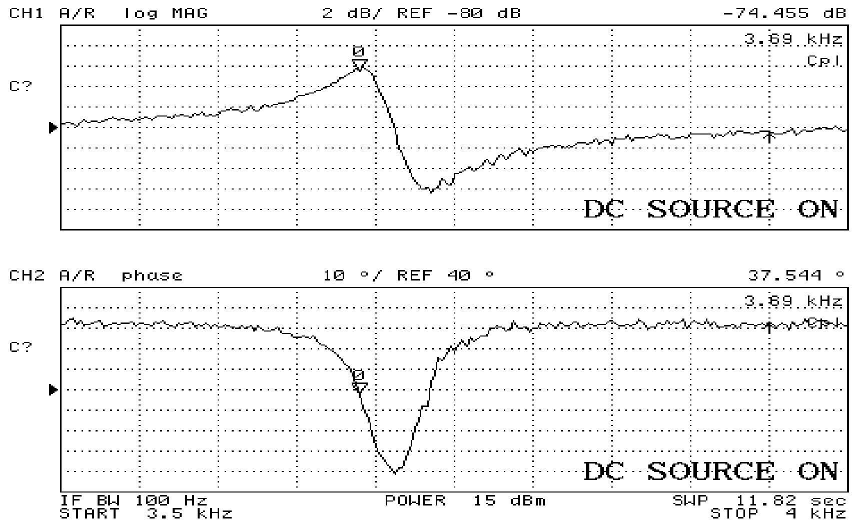

Figure 6.15 Resonant frequency measurement result for an accelerometer sample of prototype-4. DC bias is 5V and AC excitation voltage is 1.25 Vrms.

6.1.7 Test Results of Prototype-6

Figure 6.16 shows the SEM picture of the fabricated prototype-6 accelerometer. This prototype utilizes metal lines underneath the seismic mass instead of comb fingers. Table 6.5 gives the updated performance values of the structure according to the optimized fabrication. During these calculations, a 2 μm increase in the width of the springs is used based on the SEM observations.

Table 6.5 Updated performance values of prototype-6 according to optimized process conditions, assuming a 2 μm increase in the width of the springs. "SW" corresponds to spring width, "BW" corresponds to bar width, and "SC" corresponds to sense capacitance.

	Resonant Frequency (kHz)	SW (μm)	BW (μm)	Metal Line #	Total SC (fF)	Capacitance Sensitivity (fF/g)
Ver.1	3.148	5	15	2x42	948	4.75
			30	2x21	474	2.37
Ver.2	4.138	6	15	2x42	948	2.75
			30	2x21	474	1.37
Ver.3	5.214	7	15	2x42	948	1.73
			30	2x21	474	0.86

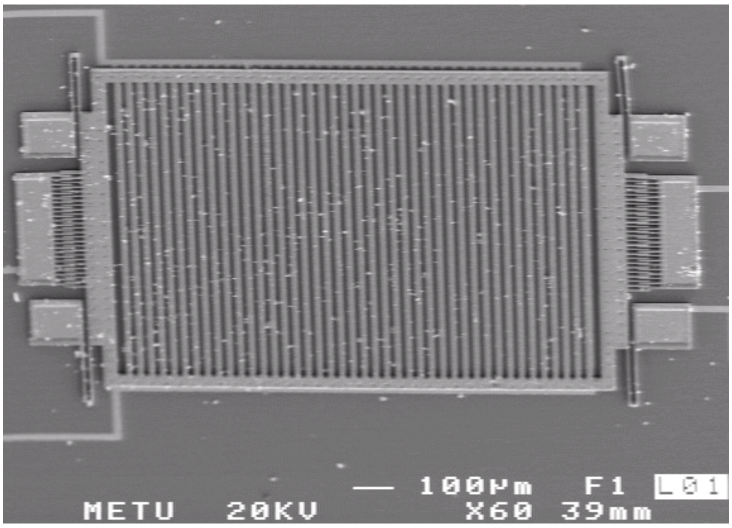

Figure 6.16 SEM picture of the fabricated prototype-6 accelerometer.

Test results show that measured sense capacitances of the structures does not match with the calculated capacitance values. This is most probably due to the fringing field between the metal lines beneath the mass and column-shaped electrodes of the mass. During the capacitance calculations only the overlap area is considered. A capacitance increase of 30 % due to fringing fields is acceptable for a two parallel plate capacitor; however, since parallel plate capacitors in this design is misaligned (Figure 4.17), the increase in the capacitance due to fringing fields is much higher. Table 6.6 gives the measured resonant frequencies for each version of prototype-6, and Figure 6.17 gives the plot of the sense capacitance measurements for two different types of bar widths. Figure 6.18 gives a resonant frequency measurement result for a sample of prototype-6.

Table 6.6 Measured resonant frequencies for prototype-6

	Sample 1	**Sample 2**
Version1	4.3 kHz	
Version2	4.72 kHz	4.54 kHz
Version3	5.3 kHz	5.73 kHz

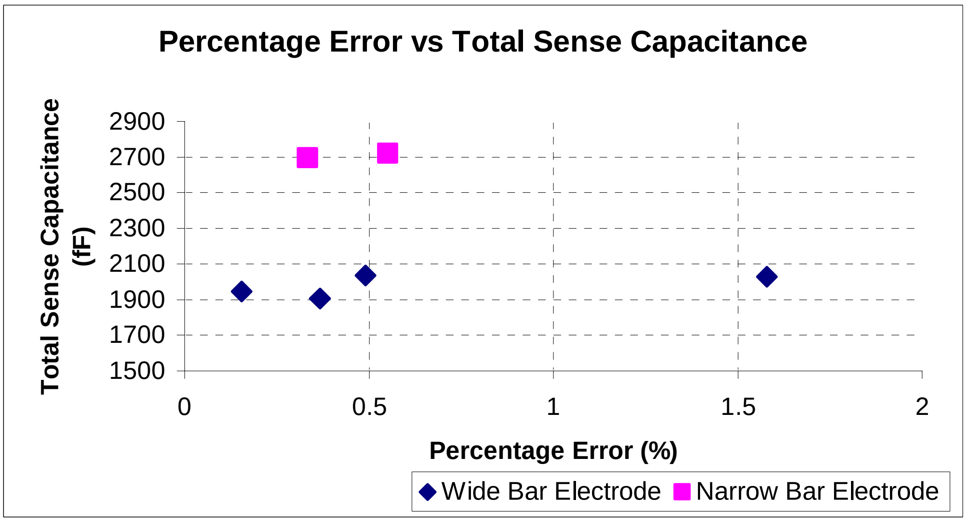

Figure 6.17 Percentage error versus total sense capacitance plot of the prototype-6.

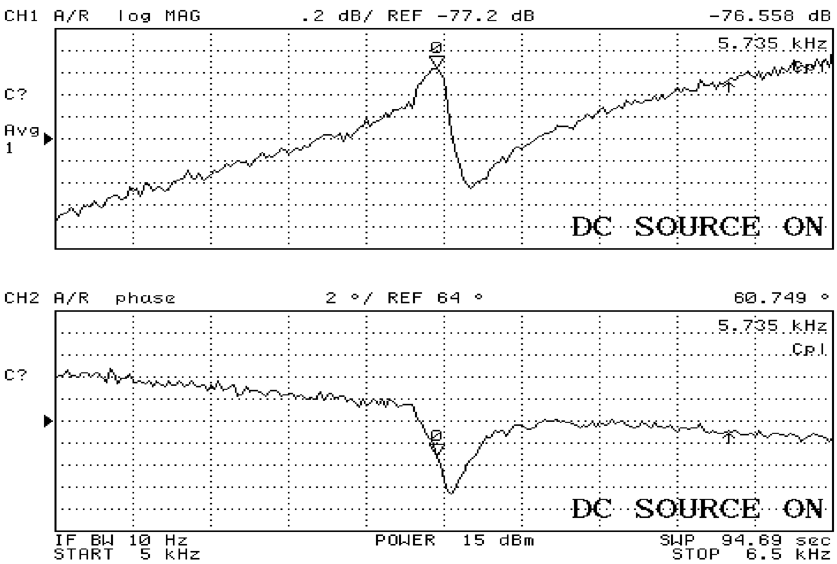

Figure 6.18 Resonant frequency measurement of prototype-6 with 40 Vdc bias and 1.25 Vrms AC excitation.

6.1.8 Test Results of Prototype-7

Structures in this category consist of a single variable sense capacitance and a fixed reference capacitor, so resonant frequencies of these structures is measured by applying both AC excitation and DC bias signal to the seismic mass of the device and measuring the output signal from the lower electrode. However, only one of the two samples could be characterized with this technique. Figure 6.29 shows the SEM picture of the fabricated device, and Table 6.7 gives the measured sense capacitance, reference capacitance values, and resonant frequency of this prototype.

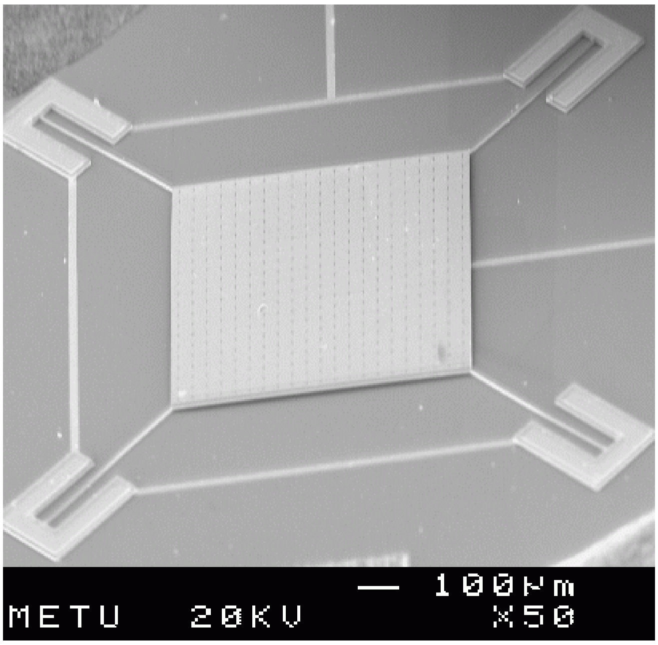

Figure 6.19 SEM picture of fabricated prototype-7.

Table 6.7 Measured sense and reference capacitance values, and resonant frequencies for prototype-7.

	Sense Cap.	**Ref. Cap.**	**Meas. Res. Freq**
Version-1	460 fF	1200 fF	8.34 kHz
Version-2	800 fF	1570 fF	

There is a large difference between the sense capacitance and reference capacitance of the structure. This is due to the fact that compressive stress causes the springs to buckle upwards, so the seismic mass, decreasing the sense capacitance of the structure. Figure 6.20 shows this situation. Moreover, reference capacitances are higher than expected. This could be due to the fringing fields or due to the thin sacrificial layer.

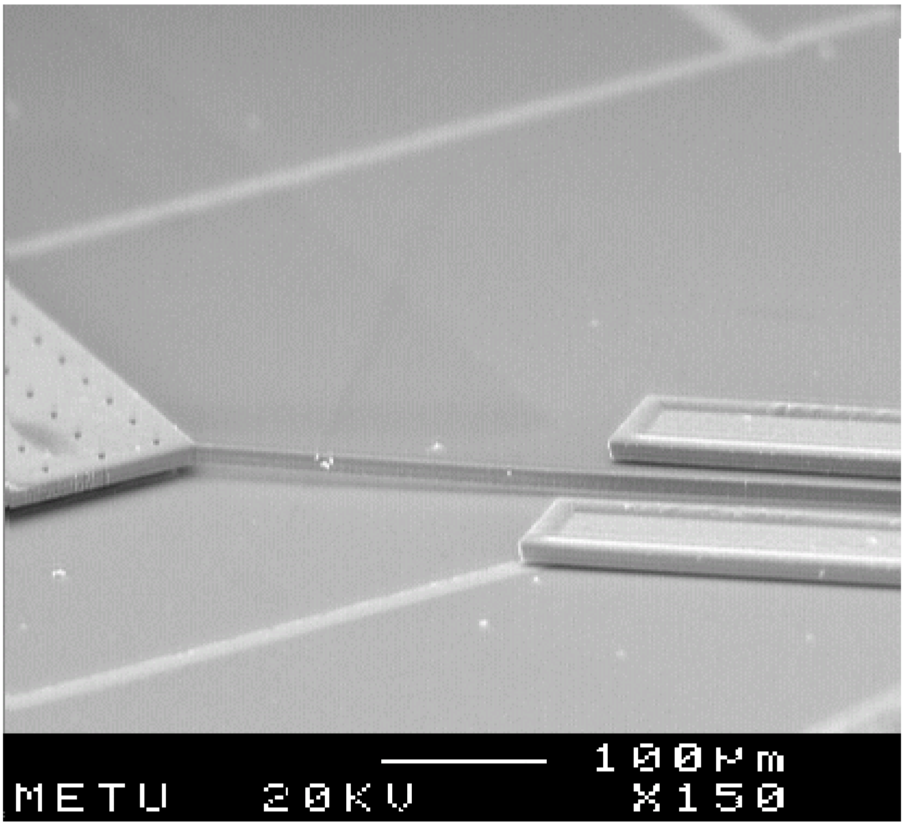

Figure 6.20 Buckling of the spring of prototype-7. This buckling increases the separation between the mass and metal electrode underneath. Thus, the sense capacitance of the structure decreases.

6.1.9 Test Results of Prototype-8

Since this structure has also one variable sense capacitance, the resonant frequency measurement is performed as described for prototype-7. Although these structures have folded type spring that helps to prevent the buckling of the springs, there are still buckling showing the internal stress is very high. Sense capacitance of these structures and reference capacitor have also large mismatches. Table 6.8 gives the measured sense and reference capacitance values, and measured resonant frequencies for prototype-8. Reference capacitances are higher than expected like the reference capacitances of prototype-7, which have the same structure. Figure 6.20 shows the SEM picture of the fabricated device, and Figure 6.21 shows the SEM picture of the buckled spring.

Table 6.8 Measured sense and reference capacitances, and resonant frequencies of prototype-8.

	Sample	Sense Capacitor (fF)	Reference Capacitor (fF)	Measured Resonant Freq. (kHz)
Version 1	1	550	1160	4.03
Version 2	1	615	1200	4.42
Version 3	1	860	1430	NA
	2	780	1650	10.01
Version 4	1	1000	1500	NA
	2	804	1570	NA

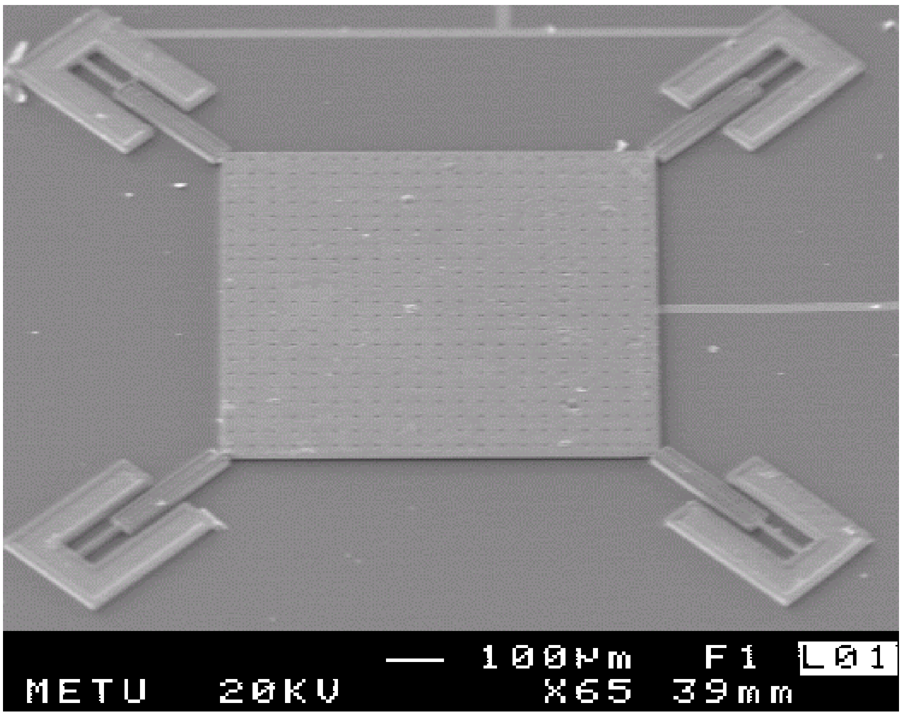

Figure 6.21 SEM picture of fabricated prototype-8. There is buckling in the structure, which prevents its proper operation.

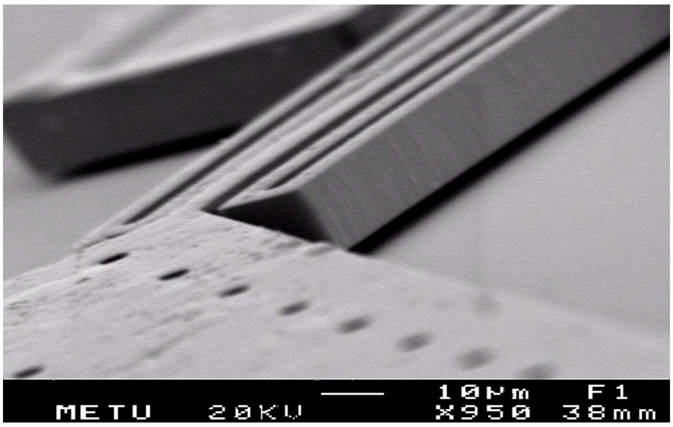

Figure 6.22 SEM picture of the buckled spring. Buckling is reduced, but still affects the sense capacitance of the sensor.

6.2 Tests of Readout and Interface Circuits

The building blocks of the readout and interface circuits are tested, before connecting them to the accelerometers and gyroscopes. For this purpose a single-ended OTA, a fully-differential OTA, and a latched comparator are separately placed in the designed chip. Since the CMFB circuit of the fully-differential OTA is not implanted in the test structure, only basic characteristics of the fully differential OTA are tested.

There are on-chip test capacitances placed in the layout for the characterization of single-ended and fully differential charge integrator circuits. These test capacitances are also connected to the charge integrator circuits for the characterization of the charge integrators.

6.2.1 Characterization of the Single-Ended OTA

Main component of the readout circuit is the OTA. The input offset voltage, slew rate, and output voltage swing of the OTA is measured in unity-gain configuration, and open-loop gain of the OTA is measured in the open loop configuration.

OTA is operating with a 5 V supply and bias circuit generates the necessary voltage for biasing of the internal nodes from an external bias voltage of 3.93 V. This external bias voltage was originally designed to be 4V, but adjusted to 3.93 V to set the current drawn from the 5 V supply to 205 μA for proper gain.

The input offset voltage measurement of the OTA was performed by applying 2.5 V to the non-inverting input of the OTA, while it is in unity-gain configuration. Then the output of the OTA was measured, and difference was taken as the input offset voltage of the OTA. Measured difference between the input voltage and the output voltage is 10 mV.

The measurement of the slew-rate was performed by applying a 3-Vpp square wave on the top of 2.5 V DC to the non-inverting input of the OTA. To prevent the effect of probe capacitance on slew rate, an LF353 Opamp is connected at the output of the circuit in unity gain configuration. Figure 6.23 shows the input and output voltages of the OTA. The slew rate of the OTA is measured from the rise and fall times of the output square wave. Figure 6.23 shows the input and output of the buffer connected OTA. The slew rate of the OTA for rising and falling edges were measured as 4.5 V/μs and 5.43 V/μs, respectively, which were around 6 V/μs in simulations.

Output voltage swing measurements were performed by applying a 5-Vpp sine wave on top of a 2.5 Vdc bias to the non-inverting input of the buffer connected OTA. The output voltage swing is measured about 4.2 V, where the transistors start to saturate beyond this level, reducing the gain of OTA. Output voltage swing of the OTA was simulated as 4.3 V.

The open-loop gain measurement of the OTA was performed by applying a triangular wave to the non-inverting input. Slopes of the input wave and output wave are measured. Figure 6.24 illustrates the measurement technique of the open-loop gain of the OTA. For the measurement, a triangular wave having an amplitude of 200 Vpp and 200 mVdc offset is applied to the non-inverting input, and inverting input is biased with 200 mVdc. Moreover, an LF353 Opamp is connected at the output of the OTA to prevent the effect of the finite probe resistance of the oscilloscope on the open-loop gain of the OTA. The slope of the input triangular wave is 0.4 V/s, and the slope of the rising edge of the OTA is measured as 6250 V/s resulting in an open-loop gain of 83.87 dB, which simulated as 89 dB.

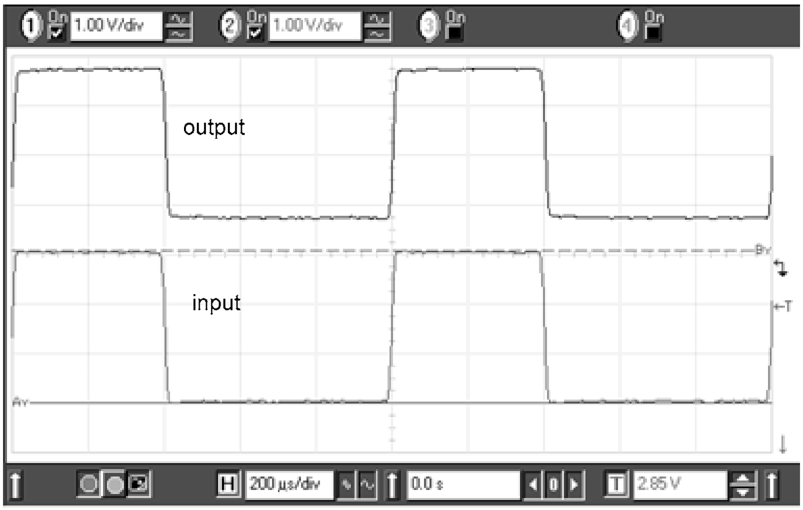

Figure 6.23 The input and output voltages of the OTA for measuring the slew rate. The slew rate is determined as 4.5 V/μs and 5.43 V/μs for rising and falling edges respectively, which are close to the simulated slew rate of 6 V/μs.

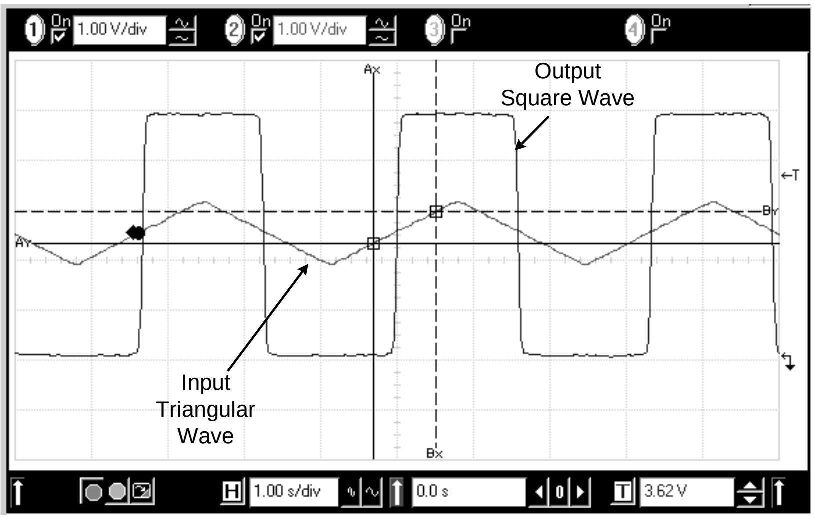

Figure 6.24 The open-loop gain measurement technique for OTA. The gain is measured as 83.87 dB, which is very close to the simulation value of 89 dB.

6.2.2 Characterization of Differential Latched Comparator

Tests of the differential latched comparator are performed with two non-overlapping clock signals that are generated from a two-bit counter operating at 5 MHz. A 1.3 Vpp triangular wave at 5 Hz is applied to the positive input of the comparator, and negative input is biased with 2.5 V. Figure 6.25 shows the input triangular wave and positive output of the comparator. This measurement shows that the comparator has an offset of 40 mV.

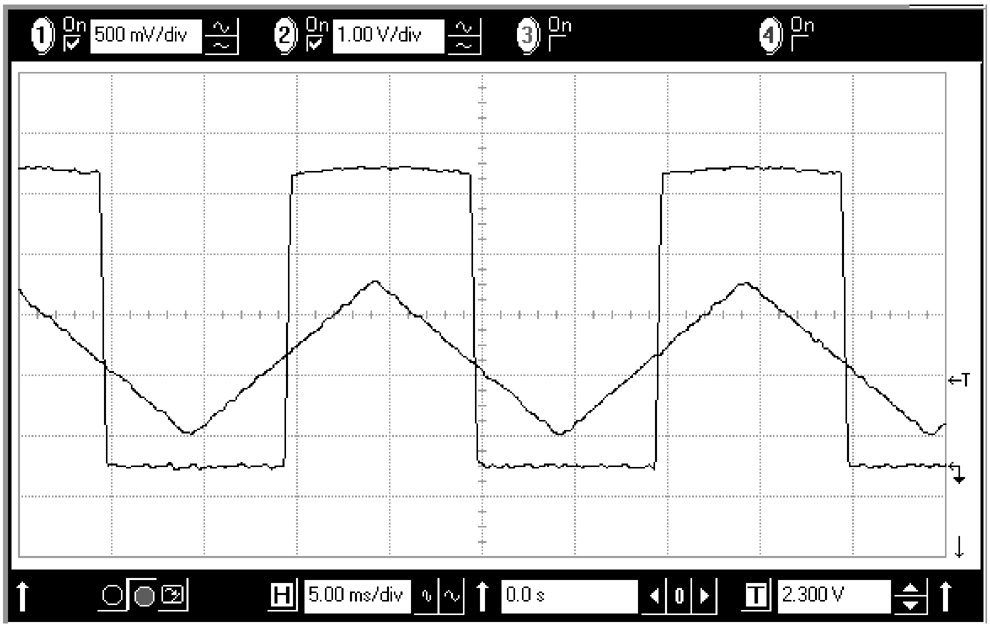

Figure 6.25 The test result of the latched comparator. Input is a 1.3 Vpp triangular wave with 5 Hz frequency applied to the positive input of the comparator. This measurement shows that the comparator has an offset voltage of 40 mV.

6.2.3 Tests of On Chip Digital Control Signals

Figure 6.26 shows the measurement result of the on chip control signals. All signals are correctly generated except the reset signal. However this does not affect the close loop operation of the readout circuit, because the reset signal, as well as all of the digital control signals, can be supplied externally with an FPGA chip.

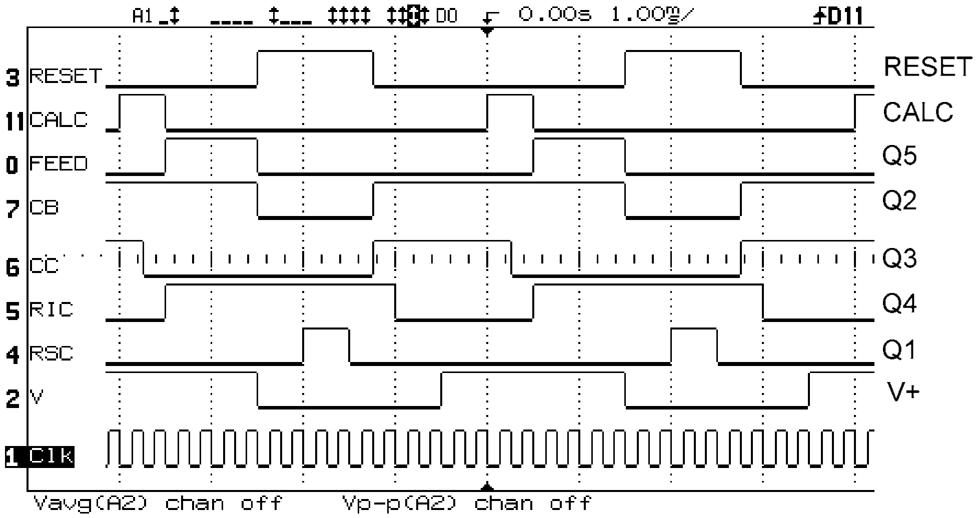

Figure 6.26 The measurement result of the on chip digital control signals.

6.2.4 Tests of the Single-Ended Charge Integrator

The single-ended charge integrator circuit is tested with the help of on-chip test capacitances. Connection of these test capacitances to the charge integrators are controlled by an 8-bit decoder circuit. Details of connecting these test capacitances to the integrator circuit are described in Appendix B. These three capacitances are connected to the input of the circuit at a time, and the output of the charge integrator is measured. Table 5.7 gives the values of these capacitances.

Figure 6.27 shows the output of the charge integrator, when the test capacitance #5 is connected at the input of the circuit. This capacitance bridge has a capacitance mismatch of 9.05 fF. Note that change at the output of the charge integrator is 50 mV, where ideal voltage change is 45.25 mV which is very close to the calculated output voltage change. Considering the measurement errors, capacitance change due to the fabrication, and routing capacitances, this measurement is very close to what is expected.

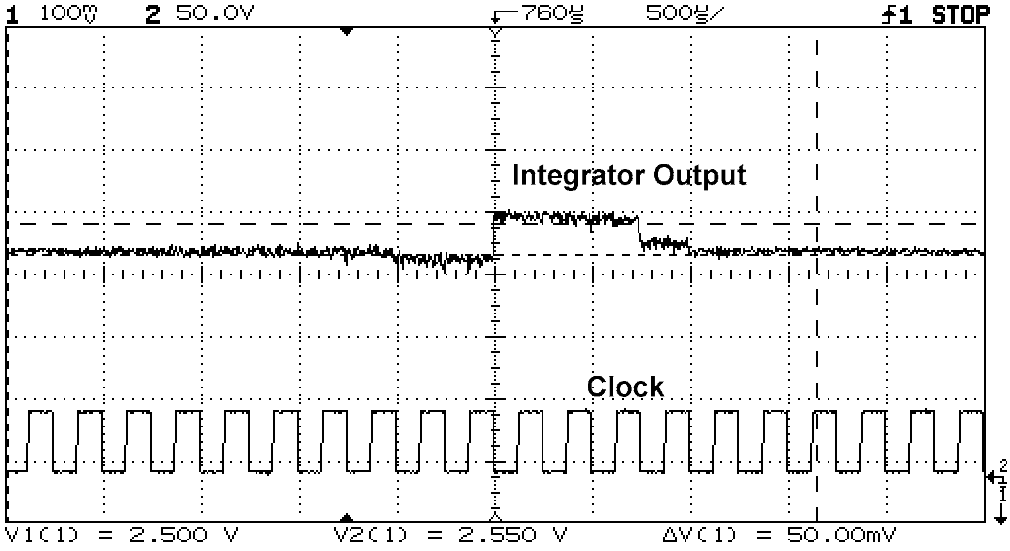

Figure 6.27 The output of charge integrator when test capacitance #5 is connected to the input. Mismatch of the capacitances is 9.05 fF. Calculated integrator output change is 45.25 mV. Test result show that integrator output change, due to this capacitance mismatch, is 50 mV.

Figure 6.28 shows the output of the charge integrator when test capacitance #6 is connected to the input of the charge integrator circuit. This capacitance bridge has a capacitance mismatch of 19.51 fF. Calculated output voltage change for this capacitance mismatch is 99.55 mV. Measured output voltage change is 112.5 mV. Measured value is very close to calculated output voltage considering the measurement errors, routing capacitances, and capacitance change due to fabrication.

Figure 6.29 shows the output of the charge integrator to the last test capacitance bridge connected to the input of the circuit. This test capacitance bridge has a capacitance mismatch of 98.53 fF. Calculated output voltage change for this capacitance mismatch is about 493 mV, and measured output voltage change is 493.7 mV, which is very close to what is expected.

These tests verify that the single-ended charge integrator operates properly as designed.

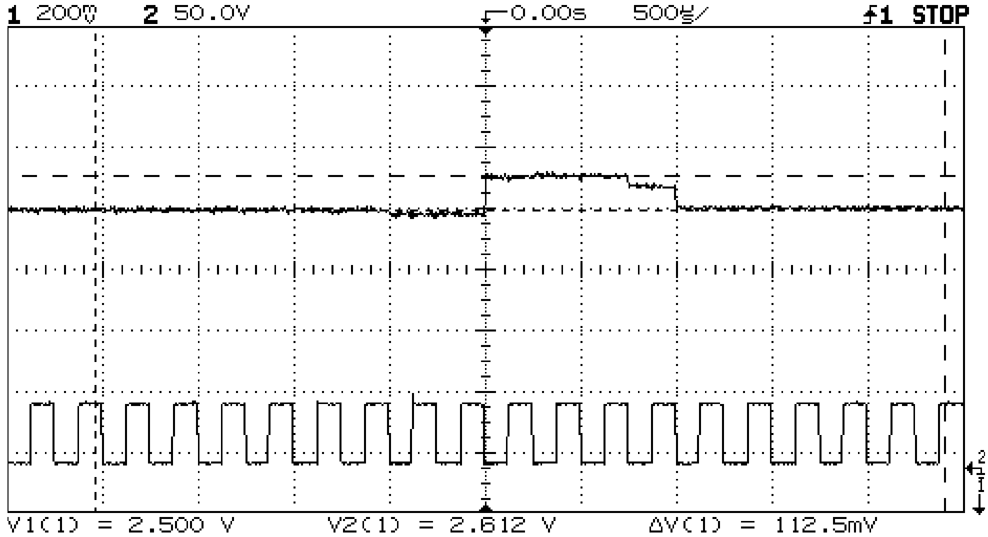

Figure 6.28 The output of the charge integrator when test capacitance #6 is connected to the input. Mismatch of the capacitances is 19.51 fF. Calculated integrator output is 99.55 mV. Test result show that integrator output change due to this capacitance mismatch is 112.5 mV.

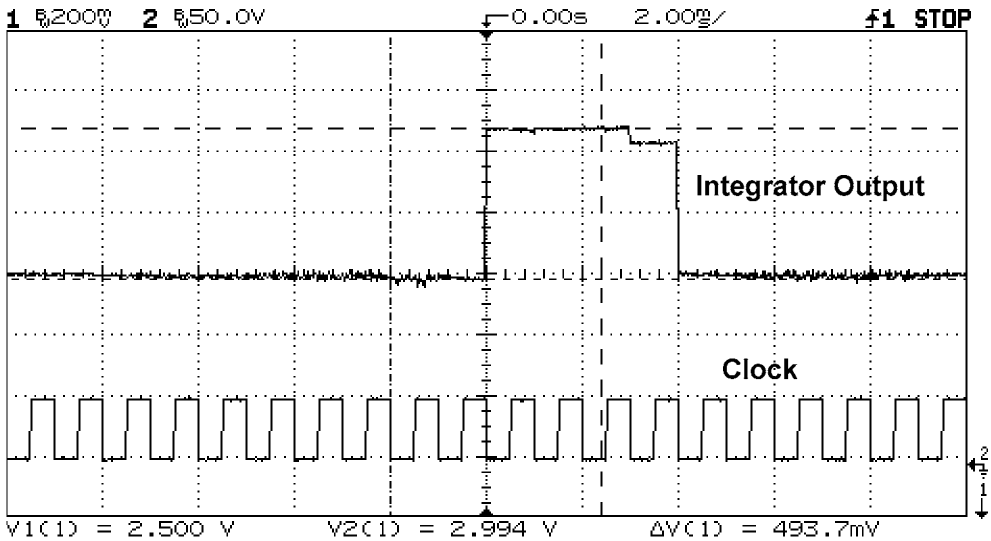

Figure 6.29 The output of the charge integrator, when test capacitance #7 is connected to the input. Mismatch of the capacitances is 98.53 fF. Calculated integrator output is about 493 mV. Test result show that integrator output change due to this capacitance mismatch is 493.7 mV.

It should be noted that there is a reduction in the integrator output during the end of integration time. This reduction coincides with the opening of switch Q3 of Figure 5.13, which connects the sense capacitances to the input of the charge integrator circuit. However, this does not affect the operation of the comparator circuit because latched comparator generates its output before this reduction at the output of the charge integrator.

Another observed result of this test is the affect of the 1 MΩ probe resistance on the gain of OTA. Resistive loads degrade the open-loop gain of OTA. However, as proved with the charge integrator test results, degraded open-loop gain of the OTA does not affect the charge integrator operation of the OTA. This means that open-loop gain of the OTA is still high enough for the charge integration operation.

6.2.5 Characterization of Fully-Differential OTA

Only open-loop operation of the fully-differential OTA could be observed since the switch-capacitor common mode feedback (CMFB) circuit is not present in the test structure of the fully-differential OTA. Figure 6.30 illustrates the open-loop configuration of the fully-differential OTA. For observing the differential output of the fully-differential OTA, a 4-Vpp triangular wave at 1 kHz is applied to the inverting input of the OTA and 0.966 V is applied to the CMFB input terminal of the OTA. The bias voltage of the OTA is adjusted by measuring the total current that OTA draws from the 5 V supply voltage.

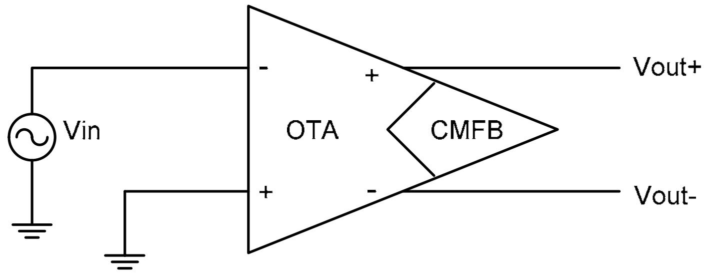

Figure 6.30 Open-loop configuration of the fully-differential OTA.

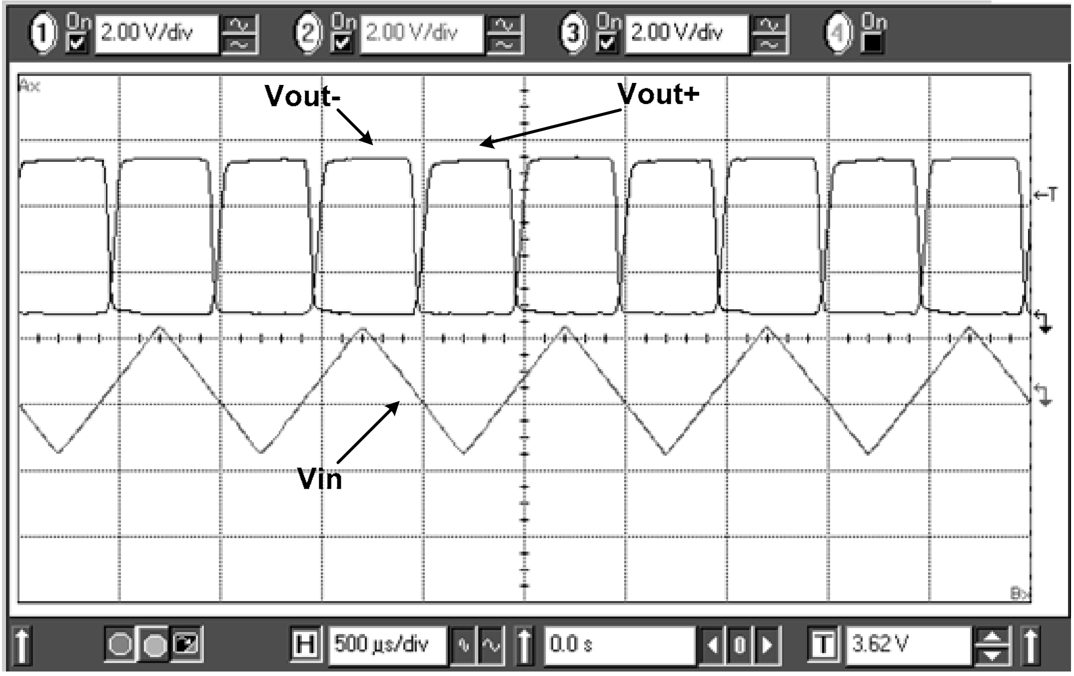

Figure 6.31 The input and output waveforms for the open-loop test of the fully-differential OTA. Input is 4 Vpp triangular wave with 1 kHz frequency.

Figure 6.31 shows the output of the OTA for the triangular wave input. Although this test proves the operation of the full-differential OTA, measurement of the open-loop gain is not possible since open-loop gain of the OTA is sensitive to the CMFB voltage.

6.2.6 Tests of Non-Overlapping Clock Generator Circuit

Figure 6.32 shows the test result of the non-overlapping clock generator circuit for the CMFB circuit of the fully differential OTA. Two non-overlapping clocks are generated, when positive and negative inputs of the OTA are connected to the negative and positive outputs of the OTA, respectively.

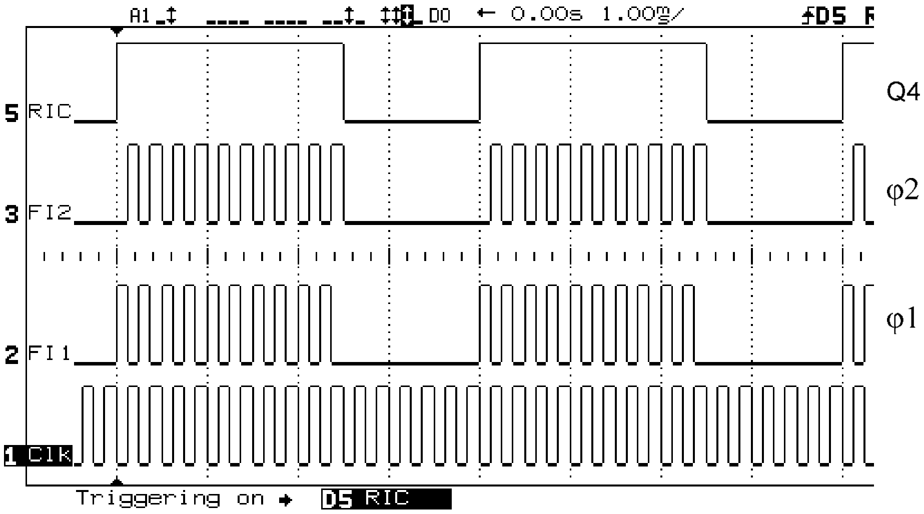

Figure 6.32 The test result of the non-overlapping clock generator circuit for CMFB circuit of fully differential OTA.

6.2.7 Tests of Fully-Differential Charge Integrator

The fully-differential charge integrator circuit is used for the tests of the fully-differential charge integrator circuit. Moreover, this test also proves the proper operation of the switch capacitor CMFB circuit. There are 4 test capacitances on the designed chip for testing the performance of the fully-differential charge integrator circuit.

Figure 6.33 (a) shows the output voltage of the fully-differential charge integrator for test capacitance # 2 and Figure 6.33 (b) shows the differential output voltage of the charge integrator for four test capacitances. Offset between the outputs of the fully-differential OTA is around 8 mV. Also note that this test validates the operation of the CMFB circuit because the common mode level of the output voltage is very close to 2.5 V. The calculated differential output voltage values for four test capacitances are -91.1 mV, -985.33 mV, -199.1 mV, and -505.9 mV, respectively. Measured differential output voltage for these capacitances are -93.75 mV, -1.01 V, -220 mV, and -537 mV. These results are matching well with the calculated values, considering the capacitance changes due to process variations, and routing metals.

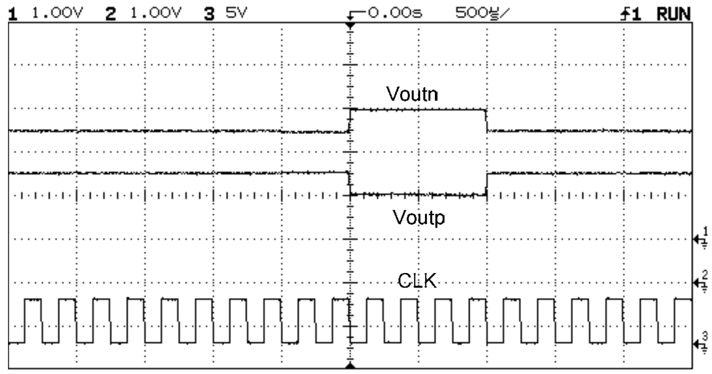

(a)

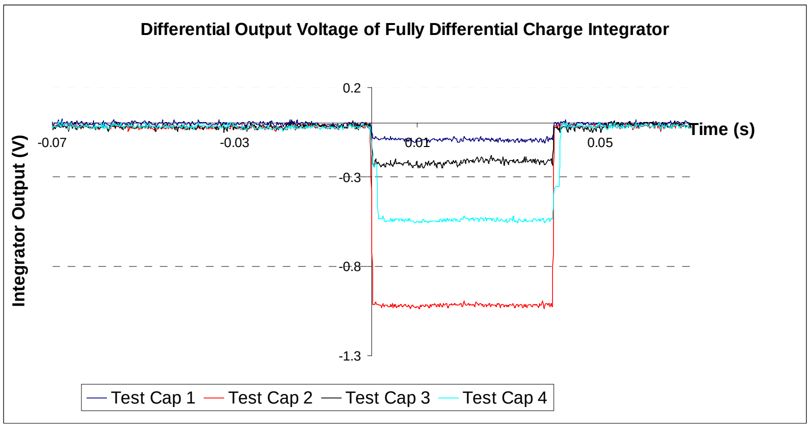

(b)

Figure 6.33 (a) Output voltage of the fully-differential charge integrator, when test capacitance bridge #2 is connected to the input, (b) Differential output voltage of the fully-differential charge integrator for all the test capacitance bridges.

6.2.8 Characterization of the Improved Buffer Interface Circuit

The improved buffer circuit is designed to be used with capacitive MEMS gyroscopes. This circuit is first tested separately, before connected to a gyroscope. The buffer capacitive interface circuit operates with +2.5 V and -4.0 V supply. Biasing of the buffer is performed with a potentiometer. This potentiometer is adjusted for a bias current of 66 μA.

First test, for the improved buffer structure include the measurement of the output offset voltage and the output voltage swing. For these tests, a sinusoidal wave having peak-to-peak voltage of 500 mV and a frequency of 100 kHz is applied to the input of the buffer. Figure 6.34 shows the input and output waveforms of the improved buffer structure. The offset voltage of the output waveform is measured as 1.44V, which is due to the source follower output stage of the improved buffer. Output voltage swing of the circuit is measured as 1.9 Vpp limited by the positive voltage supply. Output voltage gain of the buffer circuit can be calculated as 0.987, which agrees well with the simulation results of 0.981.

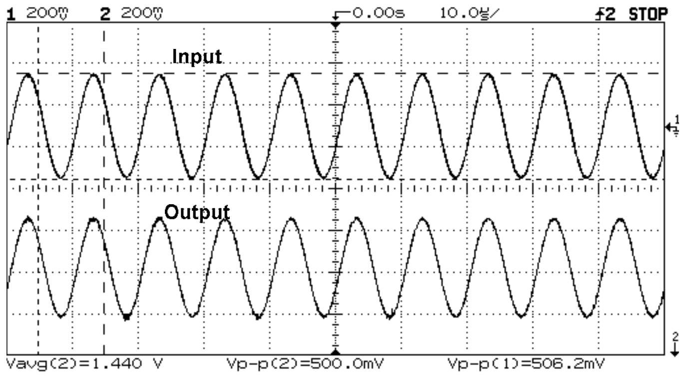

Figure 6.34 Output voltage of the improved buffer structure for a sinusoidal input of 500 mVpp and 100 kHz.

Second test for the characterization of the improved buffer circuit is the validation of the high impedance input node biasing. A square wave of amplitude 100 mVpp and frequency 1 kHz, and an offset of 50 mV is applied to the ground terminal of the input node biasing transistor for this purpose. Figure 6.35 illustrates the test setup, and Figure 6.36 shows the voltage at the input node of the improved buffer structure.

Final test is the measurement of the gain bandwidth of the improved buffer structure. This test is performed by using HP 4395A network analyzer is used for this test. Source power of the network analyzer was set to 708 μVrms for the measurement. Figure 6.37 shows the gain bandwidth measurement result of the improved buffer circuit. Output gain of the buffer at 100 kHz is 0.981, which is totally consistent with the simulation results of 0.9804. Moreover, the 3 dB bandwidth of the buffer is 14.8 MHz, which is slightly large than the simulated value of 13.7 MHz.

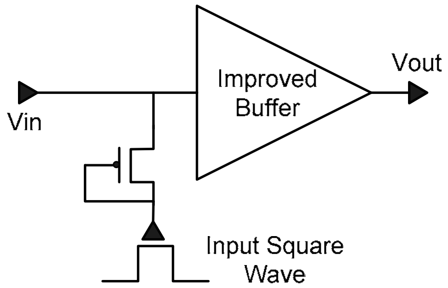

Figure 6.35 Test setup for testing the high impedance input node biasing of the improved buffer structure.

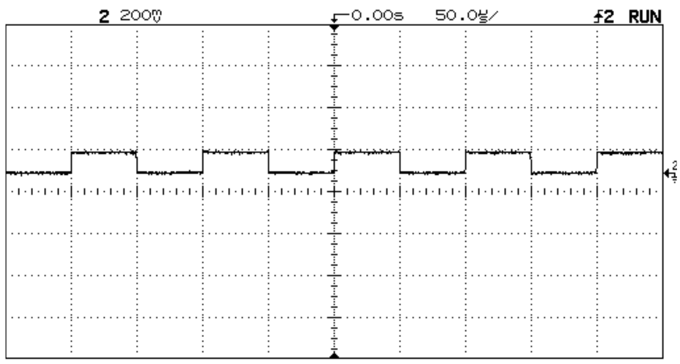

Figure 6.36 Changing input DC voltage when a square wave of 100 mVpp amplitude, 50 mV offset, and 1 kHz frequency is applied to the drain of the input node biasing transistor.

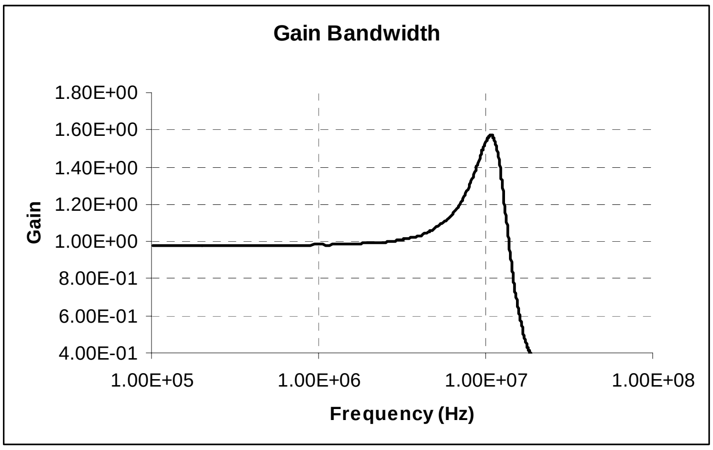

Figure 6.37 Gain bandwidth measurement of the improved buffer structure. Gain is 0.981 at 100 kHz and 3 dB bandwidth is 14.8 MHz.

6.3 Tests of Improved Buffer Circuit Hybrid Connected to a Capacitive Gyroscope Sample

For the overall test of the improved buffer structure and also for determining the input capacitance, the buffer circuit is connected to sense mode electrode of a gyroscope, whose structure and operation principle is described in Section 5.5. Figure 6.38 shows the connection diagram of the gyroscope and the buffer circuit. Two different tests are performed on the hybrid connected gyroscope and the buffer interface circuit.

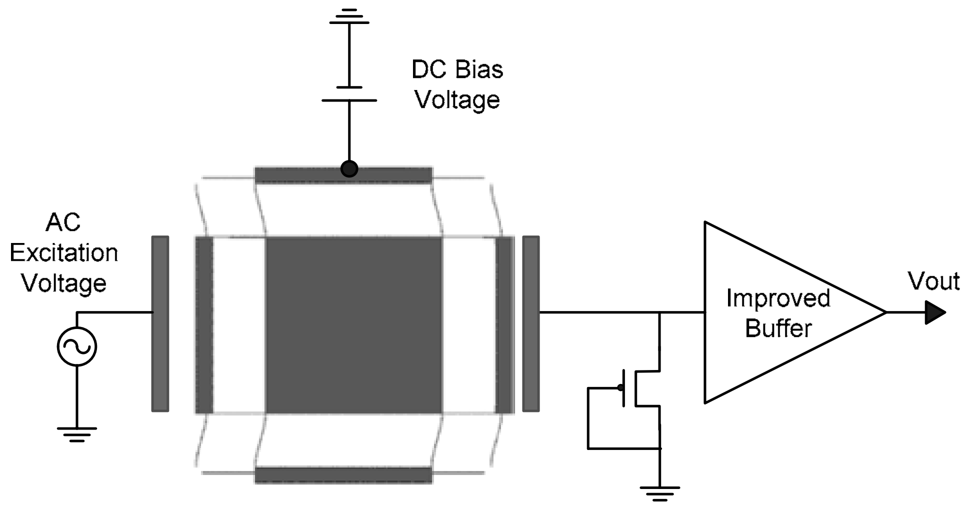

Figure 6.38 The connection of the improved buffer interface circuit to the gyroscope sample.

The first test on the hybrid system is to compare the resonant frequency measurements of the buffer circuit. Figure 6.39 shows the resonant frequency measurement with and without the buffer circuit with an excitation voltage of 1.25 Vrms and a bias voltage of 40 Vdc. Figure 6.39 (a) shows the resonant frequency measurement without the buffer circuit and Figure 6.39 (b) shows the same measurement with the improved buffer circuit connected at the output of the gyroscope. Note that, with the buffer circuit, the peak value of the buffer circuit appears at -19.53 dB, where as without buffer circuit it appears at -41.09 dB. The improvement at the output of the gyroscope is about 21 dB, which is very significant.

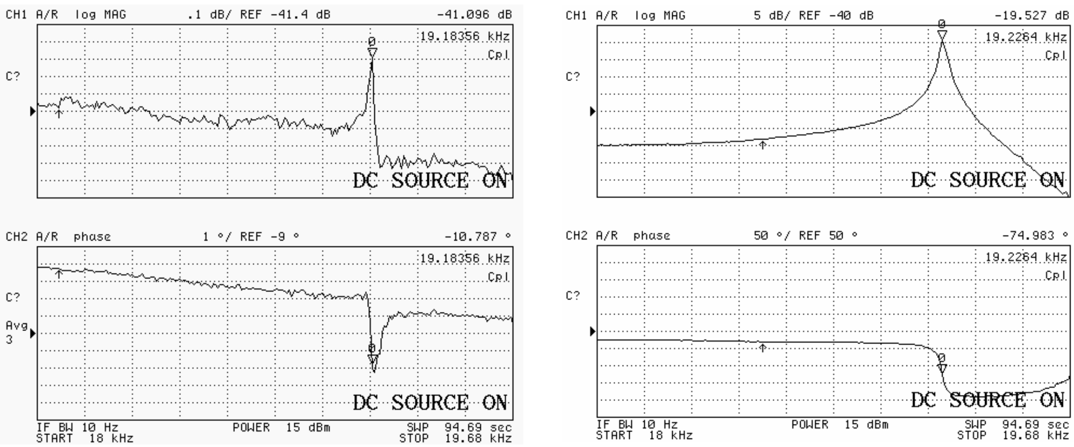

(a) (b)

Figure 6.39 The difference between the resonant frequency measurements of the gyroscope with and without buffer circuit with an AC excitation of 1.25 Vrms and DC bias of 40 V. Improvement with buffer circuit corresponds to about 21.6 dB.

The second test that was performed on the hybrid system is to calculate the input capacitance of the improved buffer circuit. For this test, the gyroscope was excited with a 5 Vpp sinusoidal wave at the resonant frequency of the sense mode and 30 Vdc bias voltage is applied to the mass of the gyroscope. Figure 6.40 shows the input excitation voltage and sensed output voltage with the improved buffer circuit. With 5 Vpp excitation voltage improved buffer circuit can generate 500 mVpp output voltage. If the excitation voltage is changed to square wave then the buffer circuit can generate 770 mVpp output voltage for the same DC biasing. Figures 6.40 (a) and (b) shows the output of the improved buffer circuit for the sinusoidal and square wave drive signals. Note that the output of the improved buffer is still sinusoidal, even when gyroscope is excited with square wave. This is due to the low-pass characteristics of the mechanical resonators.

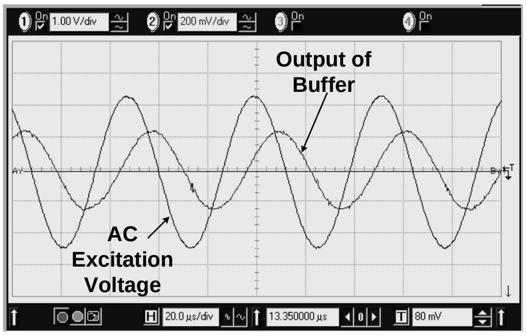

(a)

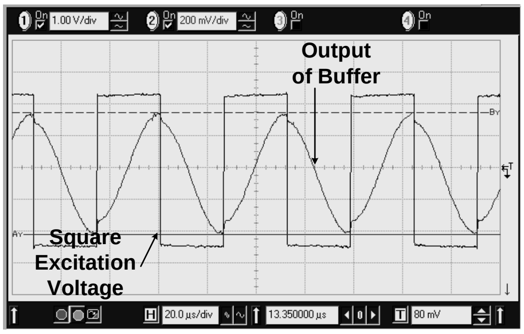

(b)

Figure 6.40 The AC excitation signal of the gyroscope and output of the improved buffer circuit to this excitation voltage. (a) Gyroscope is excited with 5 Vpp sinusoidal wave at the resonant frequency of the sense mode. Sensed output voltage is 500 mVpp, (b) Gyroscope is excited with 5 Vpp square wave at the resonant frequency of the sense mode, sensed output voltage is sinusoidal and has a peak-to-peak amplitude of 770 mV.

SIMULINK model of the sense mode of the gyroscope was constructed for calculating the resonant amplitude of the gyroscope, with excitation voltage of 5 Vpp and DC bias of 30 V. Quality factor of the resonant characteristics of the gyroscope is measured from the resonant frequency test of the gyroscope as 800, which is shown in Figure 6.39 (b). Figure 6.41 shows displacement of the proof mass of the gyroscope for a sinusoidal excitation of 5 Vpp at resonant frequency of the sense mode with a 30 Vdc bias voltage.

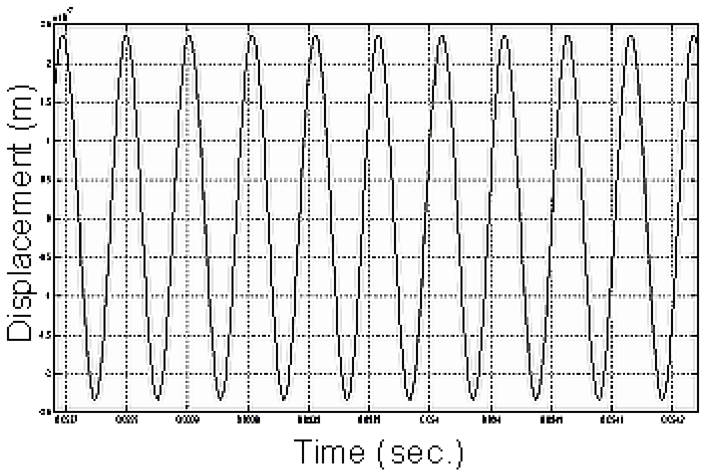

Figure 6.41 Simulink simulation result showing the displacement of the sense mode of the gyroscope for an AC excitation of 5 Vpp and DC bias voltage of 30 V. Displacement of the proof mass is around 0.23 µm for this bias voltage.

Knowing the displacement of the proof mass of the gyroscope, the current generated due to the movement of the seismic mass can be calculated using Equation 6.1. Then, the total parasitic input capacitance at the sense node of the gyroscope can be calculated by integrating the current generated by the capacitance change and dividing it to the generated sinusoidal voltage amplitude at the input node of the buffer, which is known from Figure 6.40 (a). With this technique, the total parasitic capacitance at the input node of the buffer is calculated as 219 fF. Note that this capacitance measurement includes the parasitic capacitance due to the hybrid connection of the gyroscope sample and improved buffer circuit. This demonstrates the reduction in the input capacitance of the buffer circuit. Monolithic integration is necessary in order to effectively utilize the low input capacitance of the buffer circuit because wirebonding increases the total capacitance at the input of the improved buffer circuit.

6.4 Tests of Accelerometer and Single-Ended Readout Circuit Hybrid System

Prototype-1 accelerometer is selected for hybrid system connection. Reason for selecting this prototype is due its high sense capacitance, its relatively low resonant frequency, and its fabrication yield. The selected sample for the hybrid connection with the readout circuit is version-2 type of prototype-1. Properties of this sample are shown in Table 6.9.

Table 6.9 The properties of the accelerometer selected for hybrid connection with the single-ended readout circuit.

Spring Length	300 µm
Resonant Frequency	3.05 kHz
Sense Capacitance 1	476 fF
Sense Capacitance 2	486 fF

COVENTORWARE simulations were performed for extracting the capacitance change of the accelerometer with changing finger gap. Figure 6.42 shows the simulation model of the sense capacitance of the accelerometer prototype. Simulation is performed by changing the gap between the stator fingers from 3 µm to 5 µm with 1 µm steps. Figure 6.43 shows the comparison of the calculated and simulated sense capacitance value for prototype-1.

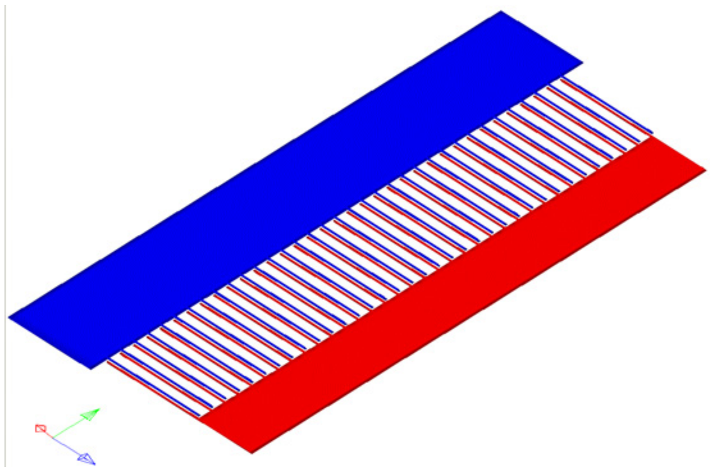

Figure 6.42 Simulation model of prototype-1 for extracting the parasitic capacitances of the sensor. Rotor fingers are shown with blue and stator fingers are shown with red.

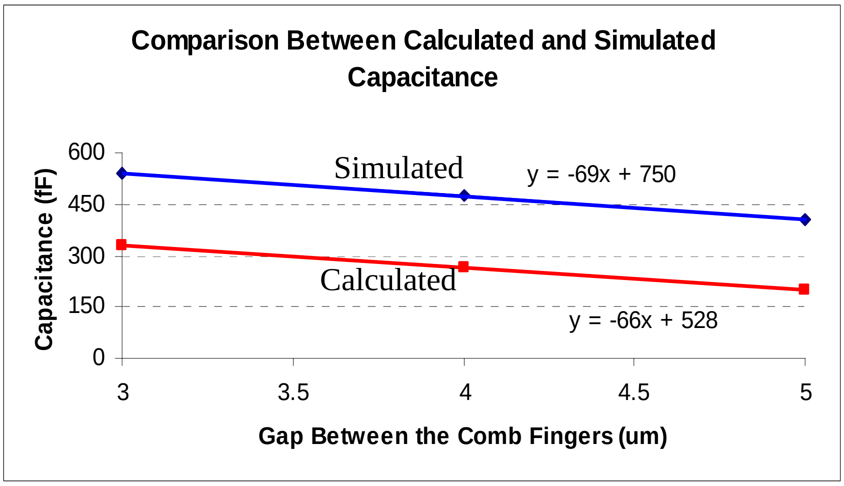

Figure 6.43 Comparison of the calculated and simulated capacitance change with varying finger gap.

This simulation shows the affect of the fringing fields on the sense capacitance of the accelerometer. Capacitance sensitivity of the accelerometer is related with the slope of the capacitance change curve, shown in Figure 6.43. Although there is a high offset between the simulated and calculated capacitance change, slopes of the curves are very similar. Capacitance sensitivity of the accelerometer can be calculated as 3.68 fF/g from the slope of the simulated capacitance change. Sensitivity difference between the calculated and simulated capacitance change is only 160 aF/g, which is negligible. Moreover, this simulation also explains the difference between the calculated sense capacitances in Table 6.1 and measured sense capacitances in Figure 6.5.

After determining the capacitance sensitivity of the sensor, close-loop SIMULINK model of the hybrid system was constructed for evaluating the close-loop performance. Figure 6.44 shows the SIMULINK model of the close-loop system [118, 119]. Output of the system is in pulse-density-modulated form and can be converted to analog by low-pass filtering. Various simulations are performed on the close loop model in order to estimate the close-loop performance of the hybrid system. Maximum operation range of the close-loop system can be calculated from the maximum force that the feedback system can apply to the accelerometer through stator and rotor comb fingers with the 5 V feedback voltage. Considering the duty cycle of the feedback operation, the maximum average force that can be exerted to the seismic mass of the accelerometer can be calculated as 1.86 g. Thus, accelerations beyond this value results in a saturation of the feedback system.

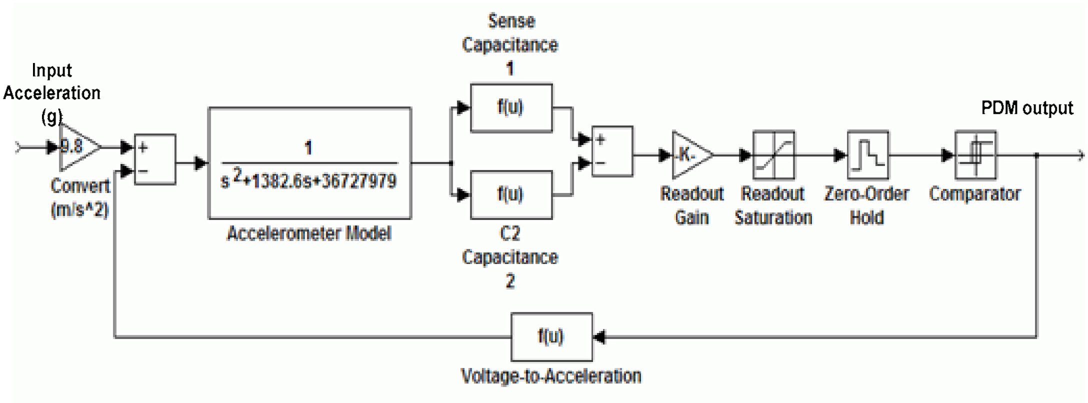

Figure 6.44 The SIMULINK model of the close-loop hybrid accelerometer system.

First simulation on the system is the step response test in order to see the stability of the system. Figure 6.45 shows the input acceleration, and low-pass filtered output of the system to a 1g acceleration input. This figure shows the stability of the system; however, for high Q accelerometers compensation is necessary. Second simulation is to determine the response of the system to an AC input acceleration. Figure 6.46 shows the sinusoidal input acceleration, pulse-density-modulated output, and low-pass filtered output of the system to a sinusoidal acceleration having amplitude of 1g and frequency of 200 Hz.

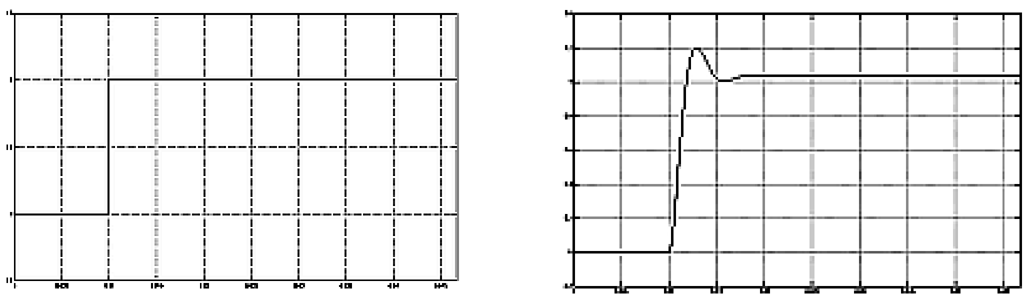

(a) (b)

Figure 6.45 The simulation of the close-loop hybrid system to a 1g step input. (a) 1g step input, (b) low-pass filtered output of the accelerometer showing the stability of the system.

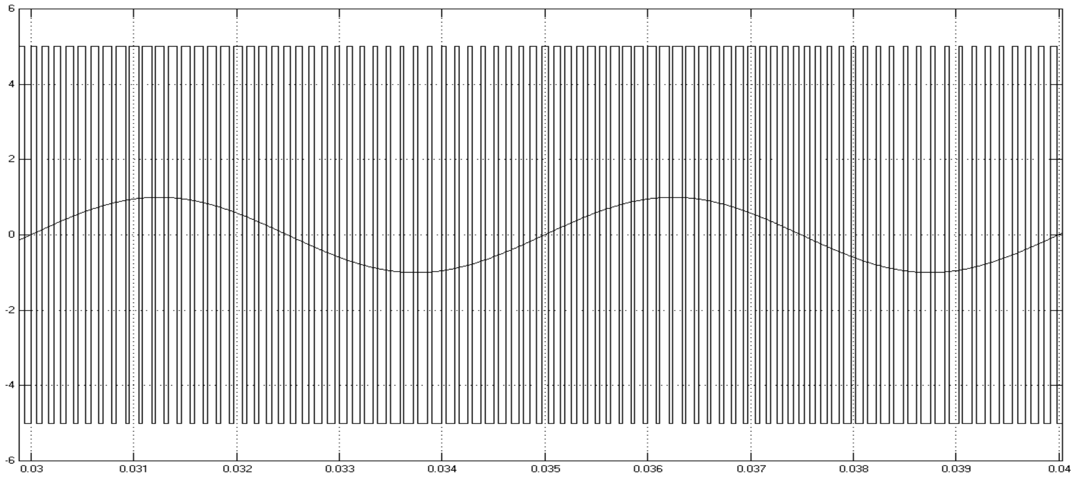

(a)

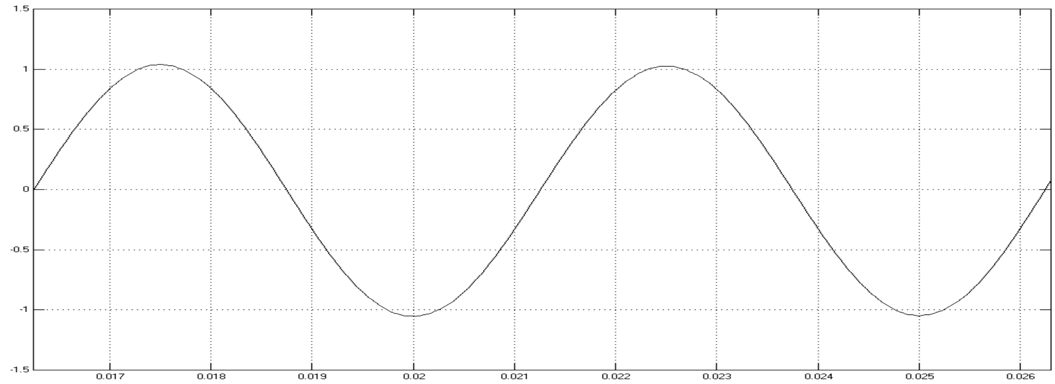

(b)

Figure 6.46 AC simulation of the close-loop hybrid system, (a) 1g sinusoidal input acceleration at 200 Hz and pulse density modulated output, (b) Low-pass filtered output of the accelerometer system.

Close loop tests of the accelerometers could not be performed using the currently fabricated devices. There are two main reasons for that. First one is the offset of the comparator circuit, which is about 40mV; and the second and more important one is the sense capacitance mismatch of the accelerometers. Simulations and calculations show that close-loop system can not null the 10 fF capacitance mismatch, which sets the limit for the close-loop operation. The mismatch of the capacitances can be decreased by optimizing the fabrication process further. Also, some attention should be paid to reduce the parasitic capacitances that occur during hybrid connection of the readout circuit and accelerometer.

6.4.1 Open-Loop Tests of Hybrid System

Figure 6.47 shows the photograph of the accelerometer and readout circuit wire bonded to each other. There are 4 main tests for the open-loop characterization of the hybrid system. These tests are voltage sensitivity, nonlinearity, noise, and bias instability tests.

Voltage sensitivity and nonlinearity tests of the accelerometer are performed with an index table having a 1^{o} resolution. Response of the hybrid system to the acceleration is measured by a spectrum analyzer observing the peak amplitude at fundamental frequency of the output square wave of the charge integrator. Figure 6.48 shows the measured output voltage change of the hybrid accelerometer from the spectrum analyzer. As a result of the test, nonlinearity of the system is determined as 0.29 % and voltage sensitivity of the accelerometer is determined as 15.7 mV/g. This corresponds to 3.14 fF total sense capacitance change per applied gravitational acceleration, which is very close to the simulated capacitance sensitivity of 3.68 fF/g. Also note that the offset voltage of the system is 79 mV corresponding to capacitance mismatch of 15.8 fF, consistent with the sense capacitance measurements.

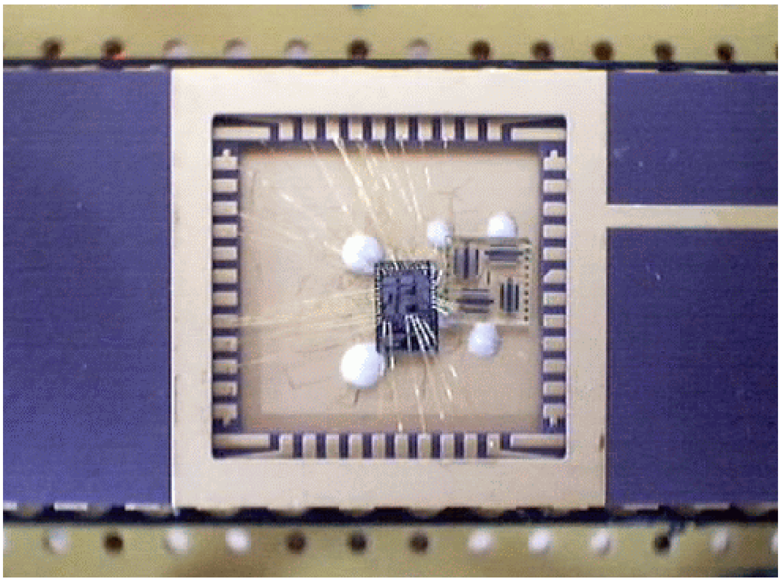

Figure 6.47 The photograph of the accelerometer and readout circuit wire bonded to each other in a DIL-48 package.

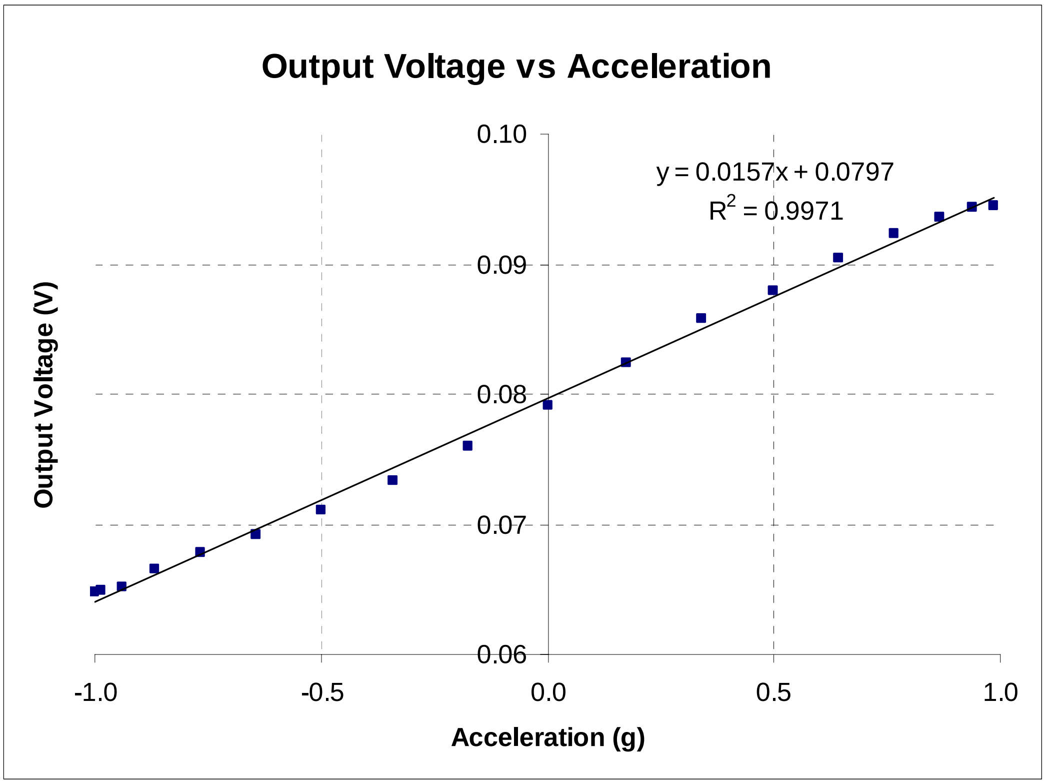

Figure 6.48 Output voltage change of the accelerometer with changing acceleration. Voltage sensitivity of the hybrid accelerometer system is 15.7 mV/g and nonlinearity is 0.29 %.

Figure 6.49 shows the measured squared rms voltage output noise of the hybrid system up to the resonant frequency of the accelerometer with a spectrum analyzer. Noise floor of the hybrid system is $7.65\,\mu\text{V}/\sqrt{\text{Hz}}$. This noise floor corresponds to an equivalent acceleration noise floor of $487\,\mu\text{g}/\sqrt{\text{Hz}}$. As a result, hybrid system is capable of resolving a capacitance mismatch of $1.52\,\text{aF}/\sqrt{\text{Hz}}$.

Finally, the bias instability of the accelerometer was tested for 3 hours. This test was performed by applying 0g to the accelerometer and measuring the output voltage change of the accelerometer over time. Figure 6.50 shows the output voltage change of the accelerometer for a 3 hour period. Bias instability of the accelerometer is measured as 13.9 mg. The output voltage in Figure 6.50 slightly increases with time. However, this is mostly due to the changing bias voltages of the readout circuit, which are generated from a battery.

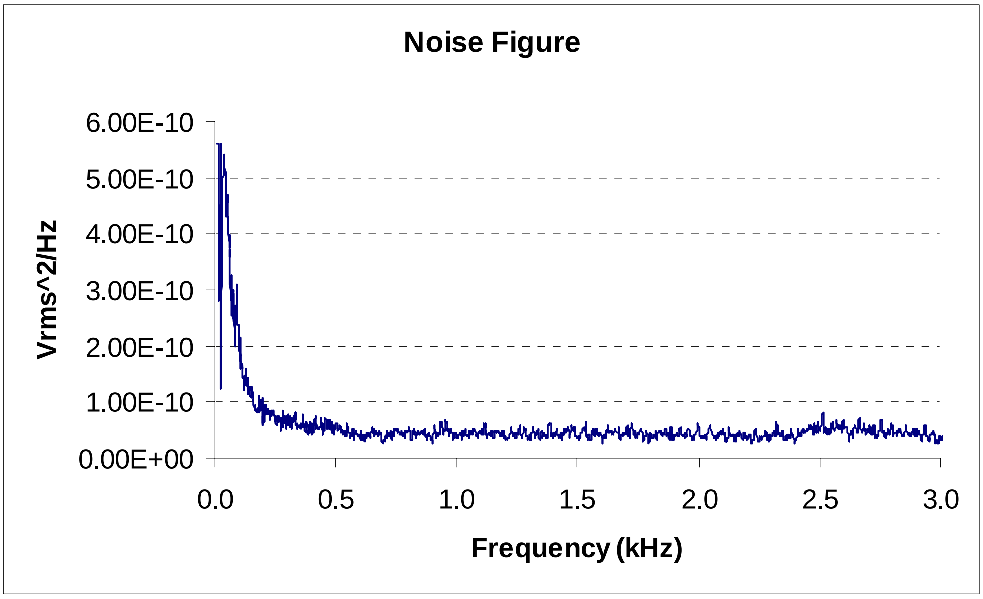

Figure 6.49 Squared rms output noise of the hybrid accelerometer system. Noise floor of the hybrid accelerometer system is $7.65\,\mu\mathrm{V}/\sqrt{\mathrm{Hz}}$, corresponding to equivalent acceleration noise floor of $487\,\mu\mathrm{g}/\sqrt{\mathrm{Hz}}$.

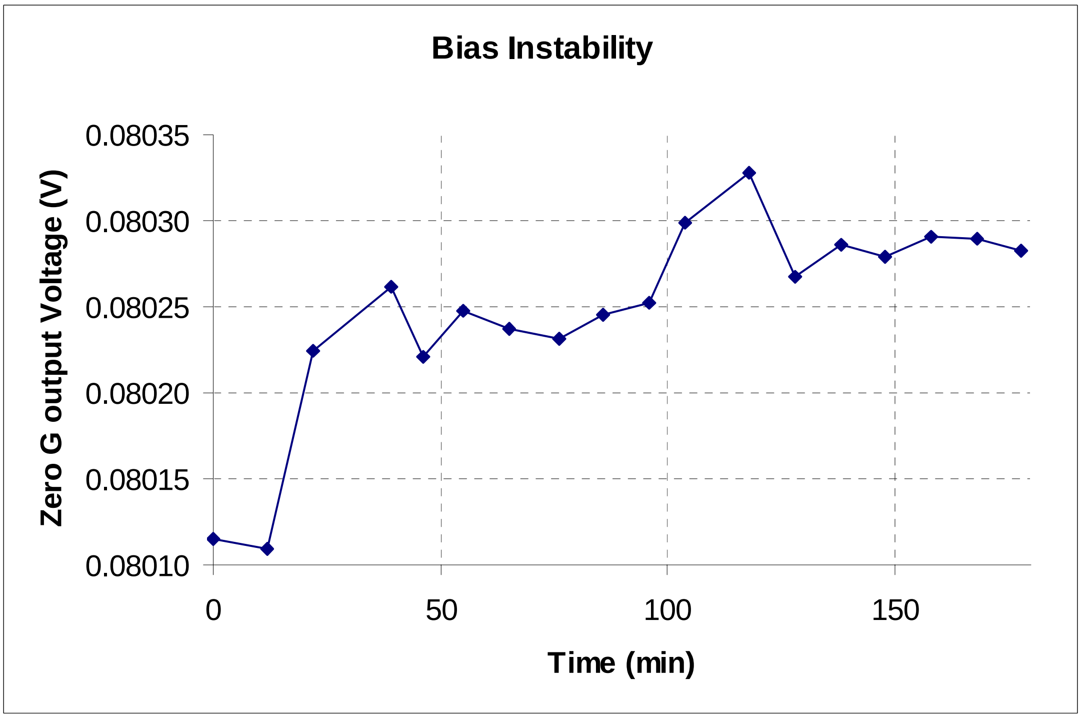

Figure 6.50 Result of the bias instability test. The bias instability of the accelerometer is 13.9 mg.

As a result, the tests prove that hybrid accelerometer system works properly. Table 6.10 gives the summary of the measured performance values of the accelerometer and readout hybrid system. Further tests that can be performed on the hybrid system are summarized in Section 6.5.

Table 6.10 Summary of the test results for accelerometer and readout hybrid system

Voltage Sensitivity	15.7 mV/g
Noise Floor	$487\ \mu g/\sqrt{Hz}$
Nonlinearity	0.29 %
Bias Instability	13.9 mg
Power Dissipation	20 mW
Operation Range (Calculated)	± 20 g

6.5 Summary and Discussion of the Tests

All the necessary tests and characterizations are completed for the development of the accelerometer prototypes, capacitive readout circuits, and hybrid-connected system. Moreover, an improved buffer structure is tested for use with a capacitive gyroscope. This section summarizes and discusses the test results, and reports future work.

- Resolution of the structural mold resist depends on the environmental conditions, especially relative humidity of the air, affecting the resolution uniformity throughout the wafer. This problem prevents the proper fabrication of most of the accelerometer prototypes. In addition, it causes non-uniform sense capacitances, which prevents the test of the close-loop system

- Resolution of the structural mold resist is also changing highly throughout the wafer due to the hotplate, having a non-flat surface. This results in a non-uniform soft bake time for different parts of the wafer. Development of the structural resist starts from the middle of the wafer for our case. Therefore, after completing the development of the resist, structures in the middle of the wafer has a very bad resolution due to overdevelopment. Using oven for soft bake may overcome this problem.

- Structures do not suffer from the stiction problem due to the high out-of-plane stiffness of the accelerometer prototypes. We have not encountered even a single stiction problem during the release of the accelerometer prototypes. However, some structures, especially the z-axis structures having clamped beams, suffer from buckling. this results in a high mismatch between the sensor and reference capacitance, which saturates the readout circuit output for z-axis structures.

- Measured resonant frequencies of the prototypes are close to the calculated resonant frequencies, even though the resolution change throughout the wafer affecting the spring widths. This is also valid for the sense capacitance measurements, if the capacitances due to fringing fields are excluded from the measurement results. Capacitance simulations are performed showing the capacitance due to fringing fields for the prototype that is connected to the readout circuit.

- Characterization of the readout and interface circuits shows that all the components of the circuits are working properly excluding the offset of the latched comparator. This offset could be due to the mismatch of the input differential pair.

- Improved buffer circuit has a total input capacitance of 219 fF, when hybrid connected to a capacitive gyroscope. This capacitance also includes the parasitic wire bonding capacitances. In order to effectively utilize the low-input capacitance of the improved buffer structure, it should be monolithically integrated with the gyroscope.

- Accelerometer and single-ended sigma-delta interface hybrid system could not be operated in close loop mode. This has two major reasons: first one is the offset of the comparator which is around 40 mV; the second and more important one is the sense capacitance mismatch of the accelerometer. SIMULINK model of the accelerometer-readout hybrid system shows that close-loop system has a stable operation. However, the feedback force can not null this capacitance mismatch, resulting in saturation of the comparator output.

- Test results of the open-loop operation of the single-ended readout circuit show that readout circuit can detect the capacitance mismatch of 1.52 $\mathrm{aF}/\sqrt{\mathrm{Hz}}$ of the sense capacitances. All the necessary tests for evaluating the operation of the accelerometer system are performed. Achieved results after the test of the hybrid system are as follows: voltage sensitivity is 15.7 mV/g, nonlinearity is 0.29 %, noise floor is $487\,\mu\mathrm{g}/\sqrt{\mathrm{Hz}}$ **,** and bias instability is 13.9 mg.

Further tests can be performed in the future on the accelerometer-readout circuit hybrid system. These tests can be listed as follows;

- Response of the system to AC acceleration can be tested by a shaker table. This test is necessary to evaluate the bandwidth of the accelerometer system.

- Characterization of the system for a higher input acceleration must be performed to determine the operation range of the accelerometer. This test can also be performed with a shaker table.

- Temperature test of the system is necessary for determining the operation temperature range of the accelerometer system.

CHAPTER 7

CONCLUSIONS AND SUGGESTIONS FOR FURTHER RESEARCH

Research presented in this thesis can be categorized into four main groups;

- Design and fabrication of micromachined accelerometer prototypes.
- Design of readout circuits for micromachined accelerometers (single-ended and fully-differential approach).
- Hybrid connection of the fabricated accelerometers and readout circuits and testing of the system.
- Design of a capacitive interface circuit for micromachined gyroscopes.

Micromachined accelerometers convert the input acceleration to seismic mass motion, which results in a capacitance change. Readout circuit detects this capacitance change and converts it into electrical signal. Single-ended and fully-differential readout circuits are capable of operating in open and close loop form. These readout circuits are fabricated with the AMS 0.8 µm n-well CMOS process. Close-loop operation has the advantages of force-feedback and digital output in pulse density modulated form. The fully-differential approach has advantages in terms of reducing common-mode errors, like the switch introduced noise. Micromachined capacitive accelerometers are fabricated with 3 mask surface micromachining process, where electroplated nickel is used as the structural layer.

The capacitive interface circuit which is developed for micromachined capacitive gyroscopes is used for detecting the proof mass motion of the gyroscopes. The developed interface circuit uses feedback together with bootstrapping for reducing its input capacitance, and It can be used as a bridge between the micromachined gyroscope and its control circuit.

Based on the results obtained during this research, the following conclusion can be made;

1) Several different kinds of micromachined accelerometers that are proposed in the literature are investigated through MATLAB and COVENTORWARE simulations. Most appropriate ones for our fabrication process are selected and optimized from these accelerometers. Designed accelerometers occupy areas ranging from 0.2 mm^2 to 0.9 mm^2.

2) Accelerometer prototypes are fabricated with 3-mask surface micromachining process, where electroplated nickel is used as the structural material. Fabrication of the accelerometer consists of 4 main steps; fabrication of the metallization layer, fabrication of the sacrificial layer, fabrication of the structural layer, and release of the structure by etching the sacrificial layer. Humidity sensitivity and soft bake non-uniformity of the structural mold photoresist (SJR5740), and deposition conditions of the electroplated nickel affect the resolution of the fabrication process during the fabrication of the structural layer. The structural layer thickness of the fabricated accelerometer prototypes changes from 15 µm to 17 µm due to the difference of the electroplating rate at the center and edges of the wafer. A more uniform structural layer thickness can be obtained with a pulsed-plating setup [120]. Moreover, there is a reduction between 1.5 µm and 2.5 µm in the finger gaps of the accelerometer prototypes, due to the lateral development of the unexposed structural photoresist. Therefore, only accelerometers having 5 µm finger gaps could be fabricated. In addition to these problems, residual stress of

the electroplated structural causes buckling problem for the accelerometers having clamped type springs, i.e., the accelerometers designed for sensing the z-axis movements.

3) Stiction, short circuit, sense capacitance measurement and resonant frequency tests are performed on all the designed and fabricated micromachined accelerometer prototypes. None of the structures suffers from the stiction problem. The structures that pass the short circuit tests are used in further tests. Capacitance measurements are performed on the structures with an impedance analyzer. Capacitance measurements show that sense capacitance values of the fabricated structures are changing through out the wafer indicating the resolution and thickness change of the structural layer. Moreover, most of the devices suffer from the sense capacitance mismatch. This is related with the resolution of the structural mold photoresist. After the sense capacitance measurements of the micromachined accelerometers, resonant frequency tests are performed on the prototypes with a network analyzer. Measured resonant frequencies are compared with expected resonant frequencies, which are determined according to the optimized process conditions. Variations of the resonant frequencies for each prototype are related with the spring width change of the devices.

4) The single-ended readout circuit that can operate in both open and close loop is fabricated with AMS 0.8 µm n-well CMOS process. The fabricated circuit occupies an area less than 0.25 mm^2 including all the digital and the analog blocks. Circuit operates with a 5V supply and dissipates less than 20 mW power. All the blocks of single-ended readout circuit are tested with the test structures placed on the fabricated chip. Except the comparator, all of the blocks are operating properly, except the comparator, which has an offset voltage of 40 mV. A possible cause of this is offset is the mismatch of the input transistor pairs. The single-ended charge integrator is tested with the on chip test capacitance bridges, by connecting

these capacitances to the input of the circuit. Test results show that output of the circuit is very close to the simulated values considering the capacitance change due to fabrication. Moreover, they also show that the circuit can detect very small capacitance changes, in the order of attofarads, and it has a sensitivity of 10 mV/fF.

5) Fully-differential readout circuit that can operate in both open and close loop is fabricated with AMS 0.8 μm n-well CMOS process. Fabricated circuit occupies an area less than 0.38 mm^2 and dissipates less than 30 mW power from a 5 V supply, while operating at 100 kHz. Operation of the fully-differential charge integrator is verified with the on chip test capacitance bridges. All the on chip test capacitances are connected to the input of the circuit and differential output of the charge integrator is measured. Test results show that fully-differential charge-integrator circuit operates properly and has a very promising performance. This circuit needs two on chip reference capacitance in order to implement a fully-differential accelerometer system. However, these reference capacitances were not included in the fabricated chip since fabrication process of the micromachined accelerometers were not optimized during the design of the readout circuit.

6) Most successful micromachined accelerometer prototype is hybrid connected to the single-ended readout circuit operating in open loop. Hybrid system occupies an area less than 13 mm^2 and dissipates less than 20 mW power, while operating from a 5 V supply with a frequency of 100 kHz. Nonlinearity, voltage sensitivity, noise floor, and bias instability tests are performed on the hybrid system. First two tests are performed with a rotation table having 1^o resolution. Voltage sensitivity of the system is 15.7 mV/g with 0.29 % nonlinearity. This sensitivity value corresponds to 3.14 fF/g capacitance change, which is close to the theoretical calculation of 3.68 fF/g. Noise measurement of the hybrid system shows that readout circuit is capable of detecting a capacitance mismatch of $1.52\,\mathrm{aF}/\sqrt{\mathrm{Hz}}$,

which corresponds to minimum resolvable acceleration of $487\,\mu g/\sqrt{Hz}$. Bias instability test is performed by measuring the output voltage change of the hybrid system, while applying 0g. Bias instability is measured as 13.9 mg. Table 7.1 compares the performance goals at the beginning of this work and achieved results.

Table 7.1 Comparison of the achieved accelerometer performance values with the performance goals at the beginning of this work.

Parameter	Performance Goals	Achieved
Nonlinearity	< 1%	0.29 %
Noise Floor	$1.5\ mg/\sqrt{Hz}$	$487\ \mu g/\sqrt{Hz}$
Bias Instability	< 20 mg	13.9 mg
Cross-Axis Sensitivity	< 5%	5.8%*

*This is the simulated mechanical cross-axis sensitivity of the accelerometer. Cross-axis sensitivity of the hybrid system is expected to be much lower than this value, since at secondary resonant mode of this accelerometer, which is shown in Figure 4.4 (b) ,there is no differential capacitance change. Therefore, this motion of the accelerometer does not change the output voltage of the accelerometer system.

Close loop operation could not be performed, which is due to the capacitance mismatch of the accelerometers. Operation range of the close loop system is 1.86 g for the selected prototype, which has the lowest capacitance mismatch. However, mismatch of the sense capacitances corresponds to 5 g.

7) A new improved buffer circuit having very high input impedance (very low input capacitance) necessary for capacitive interface is designed and fabricated with AMS 0.8 µm n-well CMOS process. The circuit occupies an area less than 0.05 mm^2 and dissipates less than 2 mW power. The circuit utilizes feedback and bootstrapping in order to decrease the input capacitance of the improved buffer circuit. This buffer circuit is an improved version of a buffer structure in the literature [100]. Table 7.2

compares the performance values of the designed buffer structure and the buffer structure proposed in [100]. The new buffer structure is hybrid connected to a capacitive micromachined gyroscope prototype in order to evaluate its performance. Test results show that buffer circuit can generate 500 mVpp output, when the gyroscope prototype is resonated with a 5 Vpp sinusoidal wave and with a DC bias of 30 V at its resonant frequency. Total parasitic capacitance at the input node of the buffer structure is calculated to be 219 fF from this test. However, this capacitance is mostly due to wire bonding capacitances. Reduction in the total input capacitance of the buffer can be further understood, if the parasitic capacitance only due to a pad structure is calculated, which is expected to be as high as 350 fF if bootstrapping is not used.

Table 7.2 Comparison of the proposed improved buffer structure with the buffer structure of [100].

	Reference [100]	**Proposed**
Input Capacitance	4.32 fF	2.2637 fF
Shield Output Gain	0.9965 V	0.999997 V
Rms Noise (50 kHz)	81 µV	6.32 µV

Although much of the work has been accomplished for the development of micromachined accelerometer, various other steps need to be taken for the further development and characterization of the micromachined accelerometers. Some of the steps can be summarized as follows;

1) For the further characterization of the accelerometers, higher acceleration values must be applied to the hybrid accelerometer system. This can be achieved with a shaker table.

2) Response of the hybrid accelerometer system to AC accelerations must be characterized. A shaker table is also needed for this test.

3) Bias instability test must be performed several times, in order to obtain a more accurate bias instability value.

4) Cross-axis sensitivity of the accelerometer must be tested. This test can be performed with an index table.

5) The hybrid accelerometer system must be packaged to improve the EMI immunity. This also improves the resistance of the accelerometer system to environmental conditions. Packaging can be made on the chip level by sealing the system with a metal can, however, this increases both the size and the cost of the system. Wafer level packaging is desirable for the high volume production of the accelerometers.

6) In this work, close loop operation of the system is limited by the mismatch of the sense capacitances. Perfect matching of the sense capacitance is impossible. Therefore, one possible solution to this problem is to reduce the resonant frequency of the accelerometer. This can be achieved by increasing the seismic mass size of the accelerometers. SU-8 is a good candidate for increasing the seismic mass size of the accelerometer. Initial work for development of an SU-8 process started in this research, however, fabricated SU-8 in this work suffers from adhesion problem. Fortunately, newer version of SU-8, which is called SU-8 2000, has improved adhesion property, and the SU-8 2000 is ordered for future studies. In addition to lower resonant frequency, a thicker structural layer also increases the sense capacitance. Another possible solution to overcome the sense capacitance mismatch is to construct a startup circuit. Details of this startup circuit can be found in [109].

7) A fully-differential readout circuit, which is proposed in this work, can be used with for the next generation accelerometers. This improves both the noise floor and common mode errors at the readout front end. For this

purpose, after the optimization of the fabrication process, two reference capacitances equal to the rest sense capacitances of the accelerometer must be placed on the readout chip.

8) A z-axis accelerometer must be developed for the fabrication of the three-axis accelerometers. This can be achieved either fabricating an in-plane accelerometer and aligning its sensitive axis to z-axis or using torsional z-axis accelerometer structures.

In conclusion, the most significant contribution of this research is the development of an accelerometer system for the first time in Turkey. Furthermore, improved and new readout techniques are implemented and tested. This work also contributes to the development of the micromachined gyroscopes via proposing a new high performance interface circuit. It is hoped that this research will be the first step to develop tactical and inertial grade high performance micromachined accelerometer system, in METU.

REFERENCES

[1] M. Kraft, "Micromachined Inertial Sensors: The State of the Art and a Look into Future," IMC Measurement and Control, Vol. 33, No. 6, pp. 164-168, 2000.

[2] C. Song, "Commercial Vision of Silicon Based Inertial Sensors," in Tech. Dig. 9^{th} Int. Conf. Solid-State Sensors and Actuators (Transducers'97), pp. 839-842, June 1997.

[3] J. Marek, "Microsystems for Automotive Applications," Proc. 13th Eur. Conf. Solid-State Transducers (EuroSensors XIII), pp. 1-8, 1999.

[4] H. Kuisma, "Inertial Sensors for Automotive Applications," Tech. Dig. 11^{th} Int. Conf. Solid-State Sensors and Actuators (Transducers'01), pp. 430-433, June 2001.

[5] D. S. Eddy, and D. R. Sparks, "Application of MEMS Technology in Automotive Sensors and Actuators," Proc. of the IEEE, Vol. 86, No. 8, pp. 1747-1755, August 1998.

[6] K. Kumar, N. Barbour, and J. M. Elwell, "Emerging Low(er) Cost Inertial Sensors," Proc. AIAA GN&C Conf., Hilton Head, pp. 11-24, August 1992.

[7] N. Barbour and G. Schmidt, "Inertial Sensor Technology Trends," IEEE Workshop Autonomous Underwater Vehicles, pp. 1-10, August 1998.

[8] A. D. King, "Inertial Navigation – Forty Years of Evolution," GEC Review, Vol. 13, No. 3, pp. 140-149, 1998.

[9] H. Chen, M. Bao, H. Zhu, and S. Shen, "A Piezoresistive Accelerometer with a Novel Vertical Beam Structure," Sensors and Actuators, vol. 63, pp. 19-25, 1997.

[10] S. McNamara, and Y. B. Gianchandani, "A Bridge-Type Piezoresistive Accelerometer using Merged Epitaxial Lateral Growth for Thin Silicon Beam Formation," Sensors and Actuators, Vol. 56, pp. 267-271, 1996.

[11] G. Li, Z. Li, Y. Jin, Y. Hao, D. Zhang, and G. Wu, "Design and Simulation of Capacitive, Piezoresistive and Piezoelectric Triaxial Accelerometers Using a Highly Symmetrical Quad-Beam Structure," Tech. Dig. 11th Int. Conf. Solid-State Sensors and Actuators (Transducers'01), pp. 304-307, June 2001.

[12] A. Partridge, J. K. Reynolds, B. W. Chui, E. M. Chow, A. M. Fitzgerald, L. Zhang, and N. I. Maluf, "A High-Performance Planar Piezoresistive Accelerometer," J. Microelectromechanical Sys., Vol. 9, No. 1, pp. 58-66, March 2000.

[13] H. Takao, Y. Matsumoto, and M. Ishida, "Stress-sensitive Differential Amplifiers Using Piezoresistive Effects of MOSFETs and Their Application to Three-Axial Accelerometers," Sensors and Actuators, Vol. 65, pp. 61-68, 1998.

[14] J. A. Plaza, M. A. Benitz, and E. Lora-Tamayo, "New FET accelerometer Based on Surface Micromachining," Sensors and Actuators, Vol. 61, pp. 342-345, 1997.

[15] H. Takao, H. Fukumoto, and M. Ishida, "Fabrication of a Three-Axis Accelerometer Integrated with Commercial 0.8µm-CMOS Circuits," Proc. IEEE Micro Electro Mechanical Systems Workshop (MEMS'00) , pp. 781-786, 2000.

[16] A. Partridge, A. E. Rice, T. W. Kenny, and M. Lutz, "New Thin Film Epitaxial Polysilicon Encapsulation for Piezoresistive Accelerometers," 14th IEEE Int. Conf. on Micro Electro Mechanical Systems (MEMS'00), pp. 54-59, Jan. 2001.

[17] H. Chen, S. Shen and M. Bao, "Over-range Capacity of a Piezoresistive Microaccelerometer," Sensors and Actuators, Vol. 58, pp. 197-201, 1997.

[18] N. Yazdi, F. Ayazi, and K. Najafi, "Micromachined Inertial Sensors," Proc. of the IEEE, Vol. 86, No. 8, pp. 1640-1659, August 1998.

[19] Y. Matsumato, M. Iwakiri, H. Tanaka, M. Ishida, and T. Nakamura, "A Capacitive Accelerometer using SDB-SOI Structure," Sensors and Actuators, Vol. 53, pp. 267-272, 1996.

[20] D. Lapadatu, M. D. Cooman, and R. Puers, "A Double-Sided Capacitive Miniaturized Accelerometer based on Photovoltaic Etch-Stop Technique," Sensors and Actuators, Vol. 53, pp. 261-266, 1996.

[21] A. Salian, H. Kulah, N. Yazdi, G. He, and K. Najafi, "A High-Performance Hybrid CMOS Microaccelerometer," Tech. Dig. Solid-State Sensor and Actuator Workshop, pp. 285-288, June 2000.

[22] C. Hierold, A. Hildebrandt, U. Naher, T. Scheiter, B. Mensching, M. Steger, and R. Tielert, "A Pure CMOS Surface-Micromachined Integrated Accelerometer," Sensors and Actuators, Vol. 57, pp. 111-116, 1996.

[23] H. Xie, and G. K. Fedder, "A CMOS Z-Axis Capacitive Accelerometer with Comb-Finger Sensing," Proc. IEEE Micro Electro Mechanical Systems Workshop (MEMS'00), pp. 496-501, 2000.

[24] H. Luo, G. K. Fedder, and L. R. Carley, "A 1mG Lateral CMOS-MEMS Accelerometer," Proc. IEEE Micro Electro Mechanical Systems Workshop (MEMS'00), pp. 502-507, 2000.

[25] K. H.-L. Chau, S. R. Lewis, Y. Zhao, R. T. Howe, S. F. Bart, and R. G. Marcheselli, "An Integrated Force-Balanced Capacitive Accelerometer for low-g Applications," Sensors and Actuators, vol. 54, pp. 472-476, 1996.

[26] T. Yamamoto, N. Kato, M. Matsui, Y. Takeuchi, Y. Otsuka, and S. Akita, "Capacitive Accelerometer with High Aspect Ratio single crystalline Silicon Microstructure using the SOI Structure with Polysilicon-Based Interconnect Technique," Proc. IEEE Micro Electro Mechanical Systems Workshop (MEMS'00), pp. 514-519, 2000.

[27] W. Qu, C. Wenzel, and G. Gerlach, "Fabrication of a 3D Differential-Capacitive Accelerometer by UV-LIGA," Sensors and Actuators, Vol. 77, pp. 14-20, 1999.

[28] X. Jiang, F. Wang, M. Kraft, and B. E. Boser, "An Integrated Surface Micromachined Capacitive Lateral Accelerometer with 2 μG/rt-Hz Resolution," Tech. Dig. Solid State Sensor and Actuator Workshop, Hilton Head, pp. 202-205, June 2002.

[29] J. Chae, H. Kulah, and K. Najafi, "A Hybrid Silicon-on-Glass (SOG) Lateral Micro-Accelerometer with CMOS Readout Circuitry," in Proc. IEEE Micro Electro Mechanical Systems Workshop (MEMS'02), pp. 623-626, January 2002.

[30] K.-Y. Park, C.-W. Lee, H.-S. Jang, Y. Oh, and B. Ha, "Capacitive type Surface-Micromachined Silicon Accelerometer with Stiffness Tuning Capability," Sensors and Actuators, Vol. 73, pp. 109-116, 1999.

[31] L. S. Johansen, J. T. Ravnkilde, A. D. Yalicinkaya, and O. Hansen, "Electroplated Ni Comb Accelerometers for CMOS Post Processing," Proc. 13th Eur. Conf. Solid-State Transducers (EuroSensors XIII), pp. 799-802, 1999.

[32] J. W. Wiegold, K. Najafi, and S. W. Pang, "Design and Fabrication of Submicrometer, Single Crystal Si Accelerometer," Journal of Microelectromechanical Systems, Vol. 10, pp. 518-524, Dec. 2001.

[33] L.Spangler and C. J. Kemp, “ISAAC: Integrated Silicon Automotive Accelerometer,” Sensors and Actuators, vol. 54, pp. 523-529, 1996.

[34] Analog Devices, “High Accuracy ±1g to ±5g Single Axis iMEMS Accelerometer with Analog Input,” ADXL 105, Datasheet, Rev. A.

[35] Puers and S. Reyntjens, “Design and Processing Experiments of a new Miniaturized Capacitive Triaxial Accelerometers," Sensors and Actuators, vol. 68, pp. 324-328, 1998.

[36] Z. Xiao, M. Chen, G. Wu, C. Zhao, D. Zhang, Y. Hao, G. Zhang, and Z. Li, “Silicon Micro-Accelerometer with mg Resolution, High Linearity and Large Frequency Bandwidth Fabricated with two Mask Bulk Process,” Sensors and Actuators, Vol. 77, pp. 113-119, 1999.

[37] S. Valoff and W. J. Kaiser, “Presettable Micromachined MEMS Accelerometers,” Proc. IEEE Micro Electro Mechanical Systems Workshop (MEMS’99), 1999.

[38] K. H. Han and Y. H. Cho, “Self-Balanced High-Resolution Capacitive Microaccelerometers Using Branched Finger electrodes with High-Amplitude Sense Voltage,” in Proc. IEEE Micro Electro Mechanical Systems Workshop (MEMS’02), pp. 714-717, January 2002.

[39] J. Chae, H. Kulah, and K. Najafi, "An All-Silicon In-Plane High-Sensitivity Low-Noise Micro-G Micromachined Accelerometer," Proc. IEEE Micro Electro Mechanical Systems Workshop (MEMS’03), pp 466-469, January 2003.

[40] C. Yeh, “A Low-Voltage Bulk-Silicon Tunneling-Based Microaccelerometer with CMOS Interface Circuitry,” Ph.D. Dissertation, The University of Michigan, 1996.

[41] C. Yeh and K. Najafi, “A Low-Voltage Bulk-Silicon Tunneling-Based Microaccelerometer,” Tech. Dig. IEEE IEDM, Washington, pp. 593-596, Dec. 1995.

[42] C. Yeh and K. Najafi, “CMOS Interface Circuitry for a Low-Voltage Micromachined Tunneling Accelerometer,” J. Microelectromechanical Sys., Vol. 7, No. 1, pp. 6-15, March 1998.

[43] C.-H. Lui and T. H. Kenny, “A High-Precision, Wide-Bandwidth Micromachined Tunneling Accelerometer,” J. Microelectromechanical Sys., Vol. 10, No. 3, pp. 425-433, Sept. 2001.

[44] Y. Nemirovsky, A. Nemirovsky, P. Muralt, and N. Setter, “Design of a Novel Thin-Film Piezoelectric Accelerometer,” Sensors and Actuators, Vol. 56, pp. 239-249, 1996.

[45] D. L. DeVoe and A. P. Pisano, “Surface Micromachined Piezoelectric Accelerometers (PiXLs),” J. Microelectromechanical Sys., Vol. 10, No. 2, pp. 180-186, June 2001.

[46] J. Kalanik and R. Pajak, “A Cantiliver Optical-Fiber Accelerometer,” Sensors and Actuators, Vol. 68, pp. 350-355, 1998.

[47] B. Guldimann, P. Dubois, P.-A. Clere, and D. de Rooij, “Fiber Optic-Mems Accelerometer with High Mass Displacement Resolution,” Tech. Dig. 11th Int. Conf. Solid-State Sensors and Actuators (Transducers’01), pp. 438-441, June 2001.

[48] B. Guldimann, P. Thiebauld, N. F. de Rooji, and R. A. Turpin, “Micromachined, Fiber-Optic Based Accelerometer with Shutter Modulation,” Proc. IEEE Micro Electro Mechanical Systems Workshop (MEMS’00), 2000.

[49] G.Schropfer, W. Elflein, M. de Labachelerie, H. Porte, and S. Ballandras, “Lateral Optical Accelerometer Micromachined in (100) Silicon with Remote Readout Based on Coherence Modulation,” Sensors and Actuators, Vol. 68, pp. 344-349, 1998.

[50] U. A. Dauderstadt, P. M. Sarro, and P. J. French, “Temperature Dependence and Drift of a Thermal Accelerometer,” Sensors and Actuators, Vol. 66, pp. 244-249, 1998.

[51] U.A. Dauderstädt and P.J. French, "A Thermal Accelerometer," Proc. of SAFE98, Mierlo, pp.14, Nov. 1998.

[52] V. Milanovi, E. Bowen, N. Tea, J. Suehle, B. Payne, M. Zaghloul, and M. Gaitan, “Convection-Based Accelerometer and Tilt Sensor Implemented in Standard CMOS,” Proc. Int. Mech. Eng. Conf. and Exp., MEMS Symposium, Anaheim, Nov. 1998.

[53] A. A. Seshia, M. Palaniapan, T. A Roessing, R. T. Howe, R. W. Gooch, T. R. Schimert, and S. Montague, “A Vacuum Packaged Surface Micromachined Resonant Accelerometer,” J. Microelectromechanical Sys., Vol. 11, No. 6, pp. 784-793, Dec. 2002.

[54] P. Ohlckers, R. Holm, H. Jakobsen, T. Kvisteroy, G. Kittisland, A. Larsen, M. Nese, S. M. Nilsen, and A. Ferber, “An Integrated Resonant Accelerometer Microsystem for Automotive Applications,” Sensors and Actuators, vol. 66, pp. 99-104, 1996.

[55] M. Aikele, K. Bauer, W. Ficker, F. Neubauer, U. Prechtel, J. Schalk, and H. Seidel, “Resonant Accelerometer with Self-Test,” Proc. 14th Eur. Conf. Solid-State Transducers (EuroSensors XIV), pp. 385-386, 2000.

[56] D. W. Burns, R. D. Horning, W. R. Herb, J. D. Zook, and H. Guckel, "Sealed-Cavity Resonant Microbeam Accelerometer," Sensors and Actuators, Vol. 53, pp. 249-255, 1996.

[57] B. Lee, C. Oh, S. Lee, Y. Oh, and K. Chun, "A Vacuum Packaged Differential Resonant Accelerometer using Gap Sensitive Electrostatic Stiffness Changing Effect," Proc. IEEE Micro Electro Mechanical Systems Workshop (MEMS'00), 2000.

[58] J. Noetzel, T. Tonnesen, W. Benecke, J. Binder, and G. Mader, "Quasianalog Accelerometer Using Microswitch Array," Sensors and Actuators, Vol. 54, pp. 574-578, 1996.

[59] S. Michaelis and H. Time, "Acceleration Threshold Switches from an Additive Electroplating MEMS Process," Proc. 13th Eur. Conf. Solid-State Transducers (EuroSensors XIII), pp. 785-788, 1999.

[60] R. Houlihan, A. Kukharenka, M. Gindila, and M. Kraft "Analysis and Design of a Capacitive Accelerometer Based on a Electrostatically Levitated Micro-Disk," Proc. SPIE Conf. on Reliability, Testing and Characterization of MEMS/MOEMS, San Francisco, pp. 277-286, 2001.

[61] M. Kraft and A. Evans, "System Level Simulation of an Electrostatically Levitated Disk," Proc. 3rd Conf. on Modeling and Simulation of Microsystems, San Diego, pp. 130-133, March 2000.

[62] R. Toda, N. Takeda, T. Murakoshi, S. Nakamura, and M. Esasi, "Electrostatically Levitated Spherical 3-Axis Accelerometer," 15th IEEE Int. Conf. on Micro Electro Mechanical Sys., pp. 710-713, Jan. 2002.

[63] N. Takeda, "Ball Semiconductor Technology and its Applications," 13th Int. Conf. on Micro Electro Mechanical Sys. (MEMS'00), pp. 11-16, Jan. 2000.

[64] F. P. Beer and E. R. Johnston, *Vector Mechanics for Engineers: Statics*, McGraw-Hill, 1990.

[65] F. P. Beer and E. R. Johnston, *Mechanics of Materials*, McGraw-Hill, 1985.

[66] S. D. Senturia, *Microsystem Design*, Kluwer Academic Publishers, 2001.

[67] A. S. Salian, "Design, Fabrication and Testing of High-Performance Capacitive Microaccelerometers," Ph.D. Dissertation, The University of Michigan, 2001.

[68] W. T. Thomson and M. D. Dahleh, *Theory of Vibration with Applications*, Prentice Hall, 1998.

[69] A. Burstein, “High Aspect Ratio Accelerometers with a CMOS Precision Interface Circuit,” Ph.D. Dissertation, Univ. of California, Los Angeles, 1999.

[70] W. Kuehnel, “Modeling of the Mechanical Behavior of a Differential Capacitor Accelerometer Sensor,” Sensors and Actuators A, vol. A36, pp. 79-87, March 1993.

[71] T. Viejola, H. Kuisma, J. Ladenpera, and T. Rayhanen, “Equivalent-Circuit Model of the Squeezed Gas Film in a Silicon Accelerometer,” Sensors and Actuators, A: Physical, Vol. A48, pp. 239-248, 1995.

[72] M. A. Lemkin, “Micro Accelerometer Design with Digital Feedback Control,” Ph.D. dissertation, University of California, Berkeley, 1997.

[73] M. Bao, H. Yang, and Y. Sun, “Modified Reynolds’ Equation for Squeeze-Film Air Damping of Hole-Plate,” Proc. 13th Eur. Conf. Solid-State Transducers (EuroSensors XIII), Prague, Sept. 2002.

[74] M. Handtmann, R. Aigner, A. Meckes, and G. Wachutka, “Sensitivity Enhancement of MEMS Inertial Sensors Using Negative Springs and Active Control,” Sensors and Actuators, A: Physical, A97-98 Special Issue, pp. 153-160, 2002.

[75] P. J. French and P. M. Sarro, “Surface versus Bulk Micromachining: The Contest for Suitable Applications,” J. Micromech. Microeng., pp. 45-53, August 1998.

[76] G. T. A. Kovacs, N. I. Maluf, and K. E. Petersen, “Bulk Micromachining of Silicon,” Proc. IEEE, Vol. 86, No. 8, pp. 1536-1551, August 1998.

[77] H. Rodjegard and G. Andersson, “A Monolithic Three-Axis Accelerometer with Symmetric Properties,” Tech. Dig. 11th Int. Conf. Solid-State Sensors and Actuators (Transducers’01), pp. 442-445, June 2001.

[78] S. Bütefisch, A. Schoft, and S. Büttgenbach, “Three-Axes Monolithic Silicon Low-g Accelerometer,” J. Microelectromechanical Sys., Vol. 9, No. 4, pp. 551-556, December 2000.

[79] J. C. Lotters, J. H. Bomer, A. J. Verloop, E. A. Droog, W. Olthuis, P. H. Veltink, and P. Bergveld, “Design, Fabrication and Characterization of a Highly Symmetrical Capacitive Triaxial Accelerometer,” Sensors and Actuators, Vol. 66, pp. 205-212, 1998.

[80] G. Li, Z. Li, C. Wang, Y. Hao, T. Li, D. Zhang, and G. Wu, “Design and Fabrication of a Highly Symmetrical Capacitive Triaxial Accelerometer,” J. Micromech. Microeng., Vol. 11, No. 1, pp. 48-54, January 2001.

[81] J. M. Bustillo, R. T. Howe, and R. S. Muller, “Surface Micromachining for Microelectromechanical Systems,” Proc. of the IEEE, Vol. 86, No. 8, pp. 1552-1574, August 1998.

[82] J. Y. Park, G. H. Kim, K. W. Chung, and J. U. Bu, “Electroplated RF MEMS Capacitive Switches,” in Proc. IEEE Micro Electro Mechanical Systems Workshop (MEMS 2000), pp. 639-644, January 2000.

[83] W. Qu, C. Wenzel, and A. Jahn, "One-mask Procedure for the Fabrication of Movable High-Aspect-Ratio 3d Microstructures," J. Micromech. Microeng. Vol. 8, No. 4, pp. 279-283, December 1998.

[84] J. Gobet, F. Cardot, J. Bergqvist, and F. Rudolf, "Electrodeposition of 3D Microstructures on Silicon," J. Micromech. Microeng. Vol. 3, No. 3, pp. 123-130, September 1993.

[85] W. Ruythooren, K. Attenborough, S. Beerteen, P. Merken, J. Fransaer, E. Beyne, C. Van Hoof, J. De Boeck, and J. P. Celic, "Electrodeposition for the Synthesis of Microsystems," J. Micromech. Microeng. Vol. 10, No. 2, pp.101-107, June 2000.

[86] S. E. Alper and T. Akin, "A Symmetrical and Decoupled Microgyroscope with Electroforming Process on Insulating Substrate," The 16th European Conf. on Solid-State Transducers (Eurosensors XVI), Prague, Czech Republic, Sept. 2002.

[87] C. Lu, M. Lemkin, and B. E. Boser, “A Monolithic Surface Micromachined Accelerometer with Digital Output,” IEEE Journal of Solid-State Circuits, Vol. 30, No. 12, pp. 1367-1373, Dec. 1995.

[88] Shipley Microposit SJR 5000 Photo Resist Datasheet.

[89] X. Li, S. Kiyawat, H. J. Santos, and C. J. Kim, “High-Aspect-Ratio Electroplated Structures with 2µm Beamwidth,” Proc. MEMS (MEMS-Vol. 1), ASME Int. Mechanical Eng. Congress and Exposition, Nashville, TN, pp. 25-30, Nov. 1999.

[90] MicroChem, Nano™ SU-8, Negative Tone Photoresist Formulations 50-100.

[91] MicroChem, Nano™ SU-8, Negative Tone Photoresist Formulations 2035-2010.

[92] J. R. Vig and Y. Kim, “Noise in Microelectromechanical System Resonators,” IEEE Trans. On Ultrasonics, Ferroelectrics, and Frequency Control, Vol. 46, No. 6, pp. 1558-1565, Nov. 1999.

[93] J. Bernstein, R. Miller, W. Kelley, and P. Ward, “Low-Noise MEMS Vibration Sensors for Geophysical Applications,” Tech. Dig. Solid-State Sensor and Actuator Workshop, Hilton Head, pp. 55-58, June 1998.

[94] K. Ishihara, C. Yung, A. A. Ayon, and M. A. Schmidt, “An Inertial Sensor Technology Using DRIE and Wafer Bonding with Interconnecting Capability,” J. Microelectromechanical Sys., vol. 8, no. 4, pp. 403-408, December 1999.

[95] M. A. Lemkin, B. E. Boser, D. Auslander, and J. H. Smith, "A 3-Axis Force Balanced Accelerometer Using a Single Proof-Mass," in Tech. Dig. 9th Int. Conf. Solid-State Sensors and Actuators (Transducers’97), pp. 1185-1188, June 1997.

[96] B. E. Boser and R. T. Howe, "Surface Micromachined Accelerometers," IEEE J. Solid-State Cct, Vol. 31, No.3, pp. 366-375, March 1996.

[97] B. E. Boser, “Electronics for Micromachined Inertial Sensors,” in Tech. Dig. 9th Int. Conf. Solid-State Sensors and Actuators (Transducers’97), pp. 1169-1172, June 1997.

[98] M. Lemkin and B.E. Boser, “A Three-Axis Micromachined Accelerometer with a CMOS Position-Sense Interface and Digital Offset-Trim Electronics,” IEEE J. Solid-State Cct., Vol. 34, No. 4, pp. 456-468, April 1999.

[99] Ph. Menini, Ph. Dondon, G.Blasquez and P.Pons, “Modeling of a Capacitance-to-Period Converter Dedicated to Capacitive Sensors,” Proc. of the 13th European Conf. on Solid-State Transducers (EUROSENSORS XIII), Netherlands, pp.549-552, Sept 1999.

[100] G. K. Fedder, “Simulation of Microelectromechanical Systems,” Ph.D. Dissertation, Univ. of California, Berkeley, 1994.

[101] T. Kajita, U. Moon, and G. C. Temes, “A Two-Chip Interface for a MEMS Accelerometer,” IEEE Trans. Instr. and Meas., Vol. 51, Is. 4, pp. 853-858, Aug. 2002.

[102] N. Yazdi, “Micro-G silicon Accelerometers with High Performance CMOS Interface Circuitry,” Ph.D Dissertation, Univ. of Michigan, 2000.

[103] N. Wongkomet, D. A. Horsley, and B. E. Boser, “Correlated Double Sampling in Capacitive Position Sensing Circuits for Micromachined Applications,” Proc. IEEE Asia-Pacific Conf. on Circuits and Systems, pp. 723-726, November 1998.

[104] S. Wuestling, O. Fomhein, H. Gemmeke, M. Tschuch, and O. Wollersheim, “Planar-Assembly Triaxial Microaccelerometer with Electromechanical Sigma-Delta ADCs,” Sensors and Actuators, vol. 61, pp. 436-440, 1997.

[105] M. Lemkin, B. E. Boser, D. M. Auslander, and J. H. Smith, "A 3-Axis Surface Micromachined Sigma-Delta Accelerometer," 9th Int. Conf. on Solid-State Sensors and Actuators (Transducers'97), Chicago, June 1997.

[106] M. Lemkin and B.E. Boser, "A Three-Axis Micromachined Accelerometer with a CMOS Position-Sense Interface and Digital Offset-Trim Electronics," IEEE J. Solid-State Crt., Vol. 34, No. 4, pp. 456-468, April 1999.

[107] R. Gregorian, *Introduction to CMOS OP-AMPS and Comparators*, John Wiley & Sons, 1999.

[108] A. Hastings and R. A. Hastings, *Art of Analog Layout*, Prentice Hall, 2000.

[109] A. Haberli, "Compensation and Calibration of IC Microsensors," Ph.D thesis, ETH Zurih, 1997.

[110] P. Malcovati, "CMOS Thermoelectric Sensor Interfaces," Ph.D thesis, ETH Zurih, 1996.

[111] H. Kulah, "Closed-Loop Electromechanical Sigma-Delta Microgravity Accelerometers," Ph.D Dissertation, The University of Michigan, 2003.

[112] J. Wu, G. K. Fedder, and R. L. Carley, "A Low-Noise Low-Offset Chopper-Stabilized Capacitive Readout Amplifier for CMOS MEMS Accelerometers," IEEE Tech. Dig. Solid-State Circuits Conf., Vol.1, pp. 428-478, Feb. 2002.

[113] Z. Cheng, "VLSI Implementation of a High-Speed Delta-Sigma Analog to Digital Converter," M.Sc. Thesis, Ohio Univ., 1997.

[114] H. Recoules, R. Bouchakour, P. Loumeau, and F. T. Braz, "Two SC-CMFB Networks Used in Fully Differential OTA: Measurements and Improvements," Proc. Circuits and Systems, Midwest Symposium, pp. 352-35, Aug. 19985.

[115] S. E. Alper, "Silicon Surface Micromachined Gyroscopes Using MEMS Technology," Ph.D. Thesis, Middle East Technical Univ., 2000.

[116] S. E. Alper and T. Akin, "A Single-Crystal Silicon Symmetrical and Decoupled Gyroscope on Insulating Substrate," The 12th Int. Conf. on Solid-State Sensors and Actuators (TRANSDUCERS'03, Eurosensors XV), Boston, June 2003.

[117] AMS (Austria Micro Systeme International AG), 0.8 µm Process Parameters, Doc. No. 9933006, Rev. B.

[118] M. Kraft and C.P. Lewis, "System Level Simulation of a Digital Accelerometer," 1st Int. Conf. On Modeling and Simulation of Microsystems (MSM 98), 1998.

[119] C. P. Lewis and M. Kraft, “Simulation of a Micromachined Digital Accelerometer in SIMULINK and PSPICE,” UKACC Int. Conf. on Control, Vol. 1, 1996, pp. 205–209.

[120] H. T. Yeh, “Fabrication and Cooling Test of High-Aspect-Ratio Electroplated Microchannels,” M. Sc. Thesis, Univ. of California, Los Angeles, 1998.

APPENDIX A

DEFINITIONS OF PERFORMANCE SPECIFICATIONS FOR ACCELEROMETERS

This appendix gives the definitions and formulas of the main performance specifications for accelerometers. Other names that are used for these specifications in the literature are also indicated.

Voltage Sensitivity (Scale-Factor): Voltage sensitivity of an accelerometer system is defined as the output voltage change at the output for 1g input acceleration and can be calculated as;

$$\text{Voltage Sensitivity} = \frac{\Delta \text{V}}{\Delta \text{a}} = \text{Capacitance Sensitivity} \times \frac{\Delta \text{V}}{\Delta \text{C}} \quad \text{(A.1)}$$

where $\frac{\Delta \text{V}}{\Delta \text{C}}$ is the gain of the readout circuit, and capacitance sensitivity is defined as;

$$\text{Capacitance Sensitivity} = \frac{\Delta C}{\Delta a} = \frac{\Delta x}{\Delta a} \times \frac{\Delta C}{\Delta x} \quad \text{(A.2)}$$

where $\Delta \text{x}/\Delta a$ is the displacement of the seismic mass for an input acceleration, and $\Delta \text{C}/\Delta \text{x}$ is the sense capacitance change of the accelerometer for a seismic mass displacement.

Noise Floor: Noise floor of an accelerometer is expressed in terms of $g/\sqrt{Hz}$. Sensitivity and output voltage noise floor of the accelerometer system defines the noise floor of the accelerometer, which can be calculated as;

$$\text{Noise Floor } \left(g/\sqrt{Hz}\right) = \frac{\text{Output Voltage Noise Floor}\left(V/\sqrt{Hz}\right)}{\text{Sensitivity}\left(V/g\right)} \qquad \text{(A.3)}$$

where output voltage noise floor represents the rms noise floor of the output voltage of the accelerometer system consists of accelerometer and readout circuit.

Resolution: This term corresponds to a minimum resolvable acceleration by the accelerometer depending on the operation bandwidth and noise floor. Resolution of an accelerometer can be calculated from the noise floor of the accelerometer as;

$$\text{Resolution } \left(g\right) = \text{Noise Floor}\left(g/\sqrt{Hz}\right) \times \sqrt{\text{Bandwidth}} \qquad \text{(A.3)}$$

Nonlinearity (Scale-Factor Nonlinearity): Nonlinearity is the deviation of the output of the accelerometer from the linear input-output curve which is plotted according to the sensitivity of the accelerometer. It is calculated in terms of percents (%).

Bias Instability: Output of the accelerometer must be repeatable. Bias instability of an accelerometer shows the change of the output of the accelerometer with constant input acceleration. It is generally performed with 0g constant input acceleration, and calculated in terms of gravitational acceleration (g).

Cross-Axis Sensitivity: Accelerometer output must be sensitive to input acceleration along its sensitive axis. Cross-axis sensitive is defined as the voltage sensitivity of the accelerometer to off-axis acceleration. Cross-axis sensitivity is calculated in terms of percents (%), which is the ratio of the sensitivity of the accelerometer to off-axis acceleration, to the sensitivity of the accelerometer.

APPENDIX B

BONDING PAD LIST FOR THE CAPACITIVE READOUT CIRCUIT CHIP

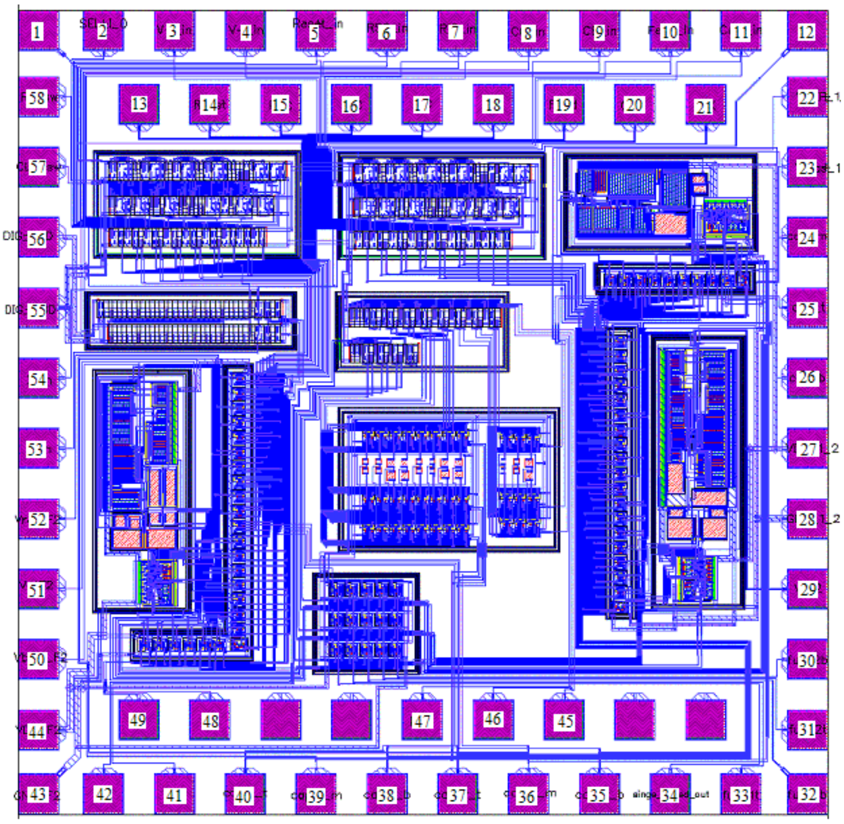

Figure B.1 Pad numbering convention for the single-ended and fully-differential capacitive readout circuits. Unused pads are not numbered.

Table B.1 Bonding pad list of the single-ended and fully-differential capacitive readout circuits.

Pad Number	Pad Name	Function
1	**Ti**	Active high toggle input of the counter (1 enables the count operation 0 freezes the output)
2	**SEL_I_O**	Select input for the selection of the internally generated digital signals or externally entered (1: internal, 0: external)
3	**V+_in**	External input pin of the V+ bias signal of the sense capacitances
4	**V-_in**	External input pin of the V- bias signal of the sense capacitances
5	**Reset_in**	External input pin of the Reset signal of the latched comparator
6	**RSC_in**	External input pin for the digital signal controlling the reset of the sense capacitances
7	**RIO_in**	External input pin for the digital signal controlling the reset of the integration capacitances and for the cds capacitances
8	**CC_in**	External input pin for the digital signal controlling the connection of the mid point of the sense capacitance array to the charge integrator
9	**CB_in**	External input pin for the digital signal controlling the switches that connects the bias signal of the sense capacitance array
10	**Feed_in**	External input pin for the digital signal controlling the feedback switch for the force –to-rebalance operation
11	**Calc_in**	External input pin for the digital signal calculate of the latched comparator
12	**RN**	Active low reset pin of the digital control signal generator for single-ended sigma-delta modulator
13	**V+**	Output pin of the digital signal biasing the sense capacitances, this is the output of the digital circuit controlling necessary digital signals for single-ended and fully-differential sigma-delta modulator with cont.-time CMFB
14	**Reset**	Output pin of the digital control signal for the reset operation of the latched comparator
15	**RSC**	Output pin of the digital signal controlling the reset sense capacitance operation
16	**RIC**	Output pin of the digital signal controlling the reset operation of the integration capacitances
17	**CC**	Output pin of the digital signal controlling the connection of the sense capacitances to the charge integrator
18	**CB**	Output pin of the digital control signal controlling the connection of the sense capacitances to the bias signals
19	**Feed**	Output pin of the digital control signal controlling the force-to-rebalance operation
20	**Calc**	Output pin of the digital control signal for the calculate operation of the latched comparator
21	**CLK**	Input pin for the clock signal of the digital circuit generating necessary clock signals for the single-ended sigma-delta.
22	**Vref_1**	2.5 v bias signal necessary for the operation of the single-ended sigma-delta.

Table B.1 (continued)

Pad Number	Pad Name	Function
23	**Vbias_1**	4 V Bias signals of the OTA and latched comparator used in single-ended.
24	**cap_m**	Input pin for the connection of the middle node of the sense capacitance bridge for single-ended sigma-delta
25	**cap_t**	Input pin for the connection of the top node of the sense capacitance bridge for the single-ended sigma-delta
26	**cap_b**	Input pin for the connection of the middle node of the sense capacitance bridge for the single-ended sigma-delta
27	**VDD_1**	5 V Vdd input pin for single-ended and fully differential sigma-delta with cont.-time CMFB
28	**GND_1**	0 V gnd pin for the single-ended and fully-differential sigma-delta with cont.-time CMFB
30	**Full_2b**	Output pin for the bottom branch of the fully-differential sigma-delta with SC CMFB according to the selection input from pins S1S0 (outputs are bottom branch of comparator output (00), bottom branch of CDS output (01) and bottom branch of integrator output (10))
31	**Full_2_t**	Output pin for the top branch of the fully-differential sigma-delta with SC CMFB same selection as Full_2_b
32		Not Used
33		Not Used
34	**Single_ended_out**	Output pin for the outputs of the single-ended sigma-delta selection are same as fully-differential circuit
35	**Cap_r_b**	Connection pin for the fully-differential sense capacitance array (right-bottom)
36	**Cap_r_m**	Connection pin for the fully-differential sense capacitance array (right-middle)
37	**Cap_r_t**	Connection pin for the fully-differential sense capacitance array (right-top)
38	**Cap_l_b**	Connection pin for the fully-differential sense capacitance array (left-bottom)
39	**Cap_l_m**	Connection pin for the fully-differential sense capacitance array (left-middle)
40	**Cap_l_t**	Connection pin for the fully-differential sense capacitance array (left-top)
41	**S0**	LSB bit of the decoder generating select signals for the output pins 30-34
42	**S1**	MSB bit of the decoder generating select signals for the output pins 30-34
43	**GND_F2**	0 v gnd voltage for the fully-differential sigma-delta circuit with SC CMFB
44	**VDD_F2**	5 v vdd voltage for the fully-differential sigma-delta circuit with SC CMFB
45	**BS2**	MSB of the decoder generating necessary control signals for the selection of the test capacitances
46	**BS1**	2^{nd} bit of the decoder generating necessary control signals for the selection of the test capacitances
47	**BS0**	LSB bit of the decoder generating necessary control signals for the selection of the test capacitances

Table B.1 (continued)

48	**Fi2**	Output pin for the output of the non-overlapping clock signal generator
49	**Fi1**	Output pin for the non-overlapping clock signal generator
Pad Number	**Pad Name**	**Function**
50	**Vbias_F2**	4 v bias signal for the fully-differential sigma-delta circuit with SC CMFB
51	**Vr_F2**	4v bias signal for the top branch and bottom branch of the SC CMFB circuit
52	**Vref_F2**	2.5 v reference signal for the fully-differential sigma-delta with SC CMFB for CDS and CMFB operations
53	**Y_in**	Input pin for the non-overlapping clock signal generator for SC CMFB
54	**X_in**	Input pin for the non-overlapping clock signal generator for SC CMFB
55	**DIG_GND**	0 v gnd signal for digital circuits
56	**DIG_VDD**	5 v vdd signal for digital circuits
57	**CLK_sw**	Clock signal for the digital circuit generating necessary control signals for fully-differential sigma-delta with SC CMFB
58	**Rn_sw**	Active low reset input for the digital-circuit generating necessary control signals for the fully-differential sigma-delta with SC CMFB

Table B.2 Test capacitance connection to the input of the charge integrators

BS2	**BS1**	**BS0**	**TEST CAPACITANCE #**
0	0	0	For Output Connection
0	0	1	1
0	1	0	2
0	1	1	3
1	0	0	4
1	0	1	5
1	1	0	6
1	1	1	7

Table B.3 Connection of the circuit outputs to the output pads.

S1	**S0**	**Single_ended_out**	**Full_2_t**	**Full_2_b**
0	0	Comp-out	Comp (+)	Comp (-)
0	1	CDS-out	CDS (+)	CDS (-)
1	0	Int-out	Int (+)	Int-bot (-)